AD-A134 836 PRECIPITATION MECHANISMS IN ALUMINUM-LITHIUM ALLOYS(U) 1/3
PURDUE UNIV LAFAYETTE IND DEPT OF MATERIALS ENGINEERING
T H SANDERS SEP 83 0303-53-1289 N00019-81-C-0471
UNCLASSIFIED F/G 11/6 NL

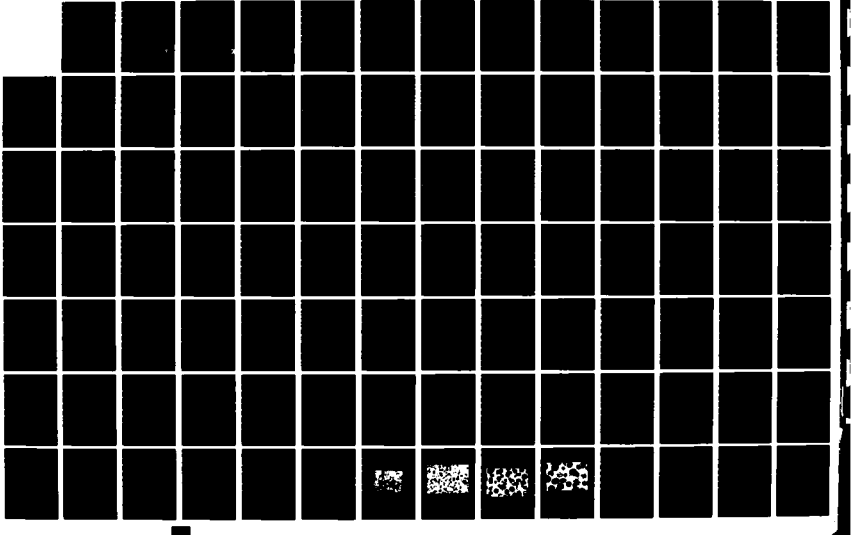

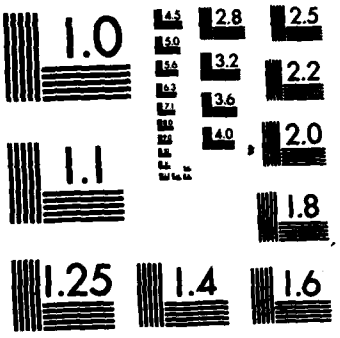

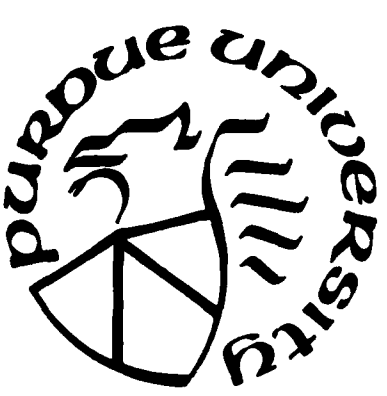

PURDUE UNIVERSITY

West Lafayette, Indiana

PRECIPITATION MECHANISMS IN ALUMINUM-LITHIUM ALLOYS

FINAL REPORT
(unclassified)

NAVAL AIR SYSTEMS COMMAND
Contract No. N00019-81-C-0471

T. H. Sanders, Jr.
Principal Investigator
Materials Engineering Department
Purdue University
West Lafayette, IN 47907

SCHOOL OF MATERIALS ENGINEERING

PRECIPITATION MECHANISMS IN ALUMINUM-LITHIUM ALLOYS

FINAL REPORT
(unclassified)

NAVAL AIR SYSTEMS COMMAND
Contract No. N00019-81-C-0471

T. H. Sanders, Jr.
Principal Investigator
Materials Engineering Department
Purdue University
West Lafayette, IN 47907

September 1983

CONTENTS

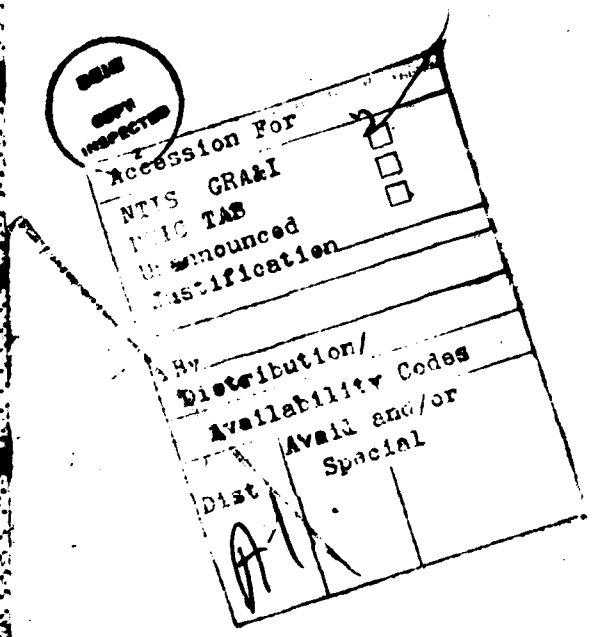

SECURITY CLASSIFICATION OF THIS PAGE (When Data Entered)

REPORT DOCUMENTATION PAGE		READ INSTRUCTIONS BEFORE COMPLETING FORM
1. REPORT NUMBER	2. GOVT ACCESSION NO. AD-A134836	3. RECIPIENT'S CATALOG NUMBER
4. TITLE (and Subtitle) Precipitation Mechanisms in Aluminum-Lithium Alloys		5. TYPE OF REPORT & PERIOD COVERED FINAL
		6. PERFORMING ORG. REPORT NUMBER 0303-53-1289
7. AUTHOR(s) T. H. Sanders, Jr.		8. CONTRACT OR GRANT NUMBER(s) N00019-81-C-0471
9. PERFORMING ORGANIZATION NAME AND ADDRESS School of Materials Engineering Purdue University West Lafayette, IN 47907		10. PROGRAM ELEMENT, PROJECT, TASK AREA & WORK UNIT NUMBERS
11. CONTROLLING OFFICE NAME AND ADDRESS Naval Air Systems Command Department of the Navy Washington, D.C. 20361		12. REPORT DATE September 1983
		13. NUMBER OF PAGES
14. MONITORING AGENCY NAME & ADDRESS (if different from Controlling Office)		15. SECURITY CLASS. (of this report) UNCLASSIFIED
		15a. DECLASSIFICATION/DOWNGRADING SCHEDULE

16. DISTRIBUTION STATEMENT (of this Report)

Approved for public release; distribution unlimited.

17. DISTRIBUTION STATEMENT (of the abstract entered in Block 20, if different from Report)

18. SUPPLEMENTARY NOTES

19. KEY WORDS (Continue on reverse side if necessary and identify by block number)

Aluminum-Lithium alloys, aluminum-lithium-silver alloys, $\delta'(Al_3Li)$, $\delta(AlLi)$, δ' coarsening, precipitation processes, precipitate free zones (PFZ)

20. ABSTRACT (Continue on reverse side if necessary and identify by block number)

Coarsening kinetics of δ' in Al-Li and Al-Li-Ag alloys were studied. The influence of deformation on the growth of δ' was also investigated.

DD FORM 1 JAN 73 1473 EDITION OF 1 NOV 65 IS OBSOLETE
S/N 0102-LF-014-6601

SUMMARY

Precipitation in Al-Li and Al-Li-Ag Alloys

Excellent consistency exists between DSC and TEM analysis for the characterization of precipitation microstructure in the alloys studied.

The presence of dislocation and grain boundary to be more important in the nucleation of δ rather than that of δ′. Formation of δ phase was found to be significantly enhanced by the presence of the grain boundaries as well as dislocations, suggesting that δ nucleates heterogeneously at the grain boundaries and the dislocations. It has been proposed that a certain amount of δ′ precipitates nucleate at the dislocations during subsequent ageing, even though most δ′ precipitates are formed during quenching in Al alloys containing sufficient Li content (>2 wt%).

Precipitation sequence of Al-Li alloys containing 1 wt% Ag can be summarized as follows:

$$\text{Supersaturation} \rightarrow Al_3Li(\delta') \rightarrow AlLi\ (\delta)$$

$$\rightarrow \text{Silver-rich G.P. Zone}$$

Spherical δ′ precipitates occurring in binary Al-Li alloy are responsible for the majority of strengthening in the Al-Li alloys

containing Ag. The microstructure of Al-Li alloys containing Ag is similar to that of Al-Li binary alloy in the early stage of ageing. The effect of the addition of Ag appears to be in the reduction of the solubility of Li, thus enhancing δ′ precipitation, and in the retardation of the growth of δ′. In the later stage, however, Ag atoms promote the nucleation of plate-shape δ precipitates, causing the rapid deterioration in strength and corrosion resistance, compared to the equivalent Al-Li alloys free from Ag. Analogous to Al-Li system, continued artificial ageing below the δ′ solvus results in the preferential coarsening of δ′ at the grain boundaries and the development of PFZ along the grain boundaries.

FOREWORD

This investigation was conducted for the U.S. Naval Air Systems Command under Contract No. N00019-81-C-0471. Mr. Michael D. Valentine was the contract monitor. The research was conducted at Purdue University.

The principle investigator would like to acknowledge Messers J. H. Kulwicki and H. J. Kim for their experimental work incorporated in this document. These gentlemen were supported under this contract as graduate research assistants.

The principle investigator would also like to acknowledge Mr. A. P. Divecha of the Naval Surface Weapons Center (NSWC) and the staff of NSWC for their assistance in preparing some of the alloys used in this investigation.

LIST OF TABLES

LIST OF FIGURES

APPENDIX A

APPENDIX B

APPENDIX I

1. BACKGROUND

1.1 Introduction

Aluminum-lithium alloys, based upon compositions where homogeneous decomposition of coherent $Al_3Li(\delta')$ can occur, offer attractive possibilities for aerospace applications (1-2). When lithium is added to aluminum, there is an increase in strength and elastic modulus, and a decrease in density. The sole technical drawback to widespread application of aluminum-lithium alloys appears to be their unacceptably low fracture toughness (2-3). Consequently, the primary emphasis of recent programs has been to understand the fundamental microstructural aspects of the deformation and fracture of Al-Li-X alloys (4-5). However, because of the reactive nature of lithium, alloying aluminum with lithium may also result in an alloy which, in a moist or salt fog environment, may be subject to extensive corrosion attack. A recent paper has discussed the relationship between microstructure and corrosion susceptibility (6). A number of the key microstructural features which are deleterious to corrosion resistance also contribute to the low ductility and fracture toughness of Al-Li-X alloys. The microstructural features which adversely affect both toughness and corrosion resistance will be discussed.

1.2 The Decomposition of Al-Li-X Alloys

When Al-Li alloys are quenched from the single-phase field and subsequently aged into the two-phase field, decomposition of the supersaturated solid solution occurs by continuous precipitation of δ′ throughout the matrix (7-9). Once the nucleation process has occurred, the growth rate appears to be governed by the transport of solute to the precipitates. Consequently, the particle size distribution function continuously shifts to larger sizes following a $t^{1/3}$ behavior. However, along with the growth of the δ′ precipitates within the grains, preferential coarsening of precipitates at the grain boundaries and the development and growth of a precipitate free zone (PFZ) have been observed (9). The growth of the PFZ has been approximated by a $t^{1/3}$ behavior which was interpreted as being the result of preferential coarsening of δ′ in the grain boundary regions by enhanced diffusion along the boundaries. Eventually, the δ′ precipitates are thought to transform to δ(AlLi) with prolonged aging below the δ′ solvus (9). Thus, depending upon aging time and temperature, a variety of microstructures having different distributions of δ′ and δ can be achieved.

The microstructure of an Al-Mg-Li alloy in the early stages of aging is similar to an Al-Li alloy (3-4,10). The only effect appears to be in the reduction of the solubility of lithium. Thus, for a given level of lithium, increasing the amount of magnesium results in an increase in the volume fraction of δ′. In the later stages of aging, magnesium enters into the

precipitation reaction and forms Al_2MgLi. However, since some of the magnesium is retained in solid solution, the modified precipitation scheme in the Al-Mg-Li system can be summarized as the following:

$$\alpha \text{ (supersaturated)} \rightarrow \delta' \rightarrow Al_2MgLi$$

Analogous to the Al-Li system, continued artificial aging below the δ' solvus results in preferential coarsening at grain boundaries, the transformation of δ' to Al_2MgLi, and the development and growth of PFZ's (4).

Precipitation in the Al-Cu-Li system is more complicated than in either the Al-Li or Al-Mg-Li systems. The precipitation sequence can be summarized as follows (4,11-12):

$$\alpha \text{ (supersaturated)} \rightarrow \begin{matrix} GPI \rightarrow \theta'' \rightarrow \theta' \rightarrow \theta\ (Al_2Cu) \\ T\ (Al_2CuLi) \\ \delta' \rightarrow \delta \end{matrix}$$

Depending upon composition and temperature, the relative size and volume fraction and type of precipitate systematically varies. Thus, the major influence of copper on the precipitation of lithium in the early stages of aging is similar to that of magnesium in that the copper reduces the lithium solubility and in the later stages postpones the formation of AlLi.

1.3 Strength of Al-Li-X Alloys

In an alloy system such as Al-Li which contains shearable particles, the critical resolved shear stress, τ, due to the interaction of gliding dislocations with the dispersion, can be represented by an equation of the form (13-15):

$$\tau = cf^m r^p$$

where c is an alloy constant that depends on the particular strengthening mechanism, (i.e., in Al-Li: surface, order, and/or modulus mechanisms appear to be most important), f is the volume fraction, and r is the particle radius. The exponents m and p are always positive and the strength increases with both volume fraction and particle size.

Regardless which strengthening mechanism dominates, the implication of precipitate shearing is that once deformation has occurred on a particular glide plane, deformation on that plane is favored. Thus, the localization of slip becomes an important characteristic in the Al-Li system.

In the Al-Mg-Li alloys, magnesium contributes to the strength in two ways. It adds a component of solid solution strengthening (8) and decreases the solubility of lithium in aluminum which results in an increase in the volume fraction of δ'. Since the δ' controls the deformation behavior, the previous discussion of the strengthening in Al-Li alloys also applies.

The development of high strength in an Al-Cu-Li alloy is a consequence of the co-precipitation of an Al_2Cu-type and δ′ precipitates. The Al_2Cu precipitates are primarily responsible for strengthening, while Al_3Li not only adds to the strength, but affects the deformation process and controls properties such as elastic modulus.

1.4 Ductility in Al-Li-X Alloys

The primary phenomenon which appears to dominate the ductility and fracture characteristics is the tendency toward strain localization (9,16). In underaged and peak aged Al-Li-X alloys, the shearable nature of the δ′ precipitates tends to localize the strain in intense bands of deformation which act as stress concentrations at grain boundary triple points. Cracks can then nucleate at these triple points and propagate intergranularly. On the other hand, overaging results in a microstructure which contains PFZ's with coarse grain boundary precipitates. Strain localization occurs at the PFZ's, and cracks can then nucleate at grain boundary precipitates and propagate intergranularly within the PFZ.

The degree of softening that occurs when dislocations shear the coherent precipitate, the magnitude of the stress concentrations produced at grain boundaries due to the intense slip bands, and deformation within the precipitate free zone, all depend on the number of dislocations that can be accommodated on a given slip plane. Consequently, reducing the grain size has been shown

to be a very effective method of preventing early crack nucleation due to strain localization (17). The reduced grain size limits the slip distance and lowers the stress concentrations across grain boundaries and at grain boundary triple points. The fracture mode can likewise change from a low-energy intergranular to a higher-energy transgranular mode.

Since strain localization depends on the presence of soft regions resulting from either dislocations shearing coherent precipitates, or PFZ's, it may be minimized by strengthening the matrix and reducing the width of the PFZ. When magnesium is added to an aluminum-lithium alloy, it adds a small component to the strength of the matrix.

Alternatively, elements such as manganese are added to form non-shearable precipitates that tend to disperse slip (18). In an alloy containing copper or magnesium and copper, metastable, transition phases co-precipitate with the δ'. These co-precipitating phases appear to be effective in improving corrosion resistance in two ways. First, they increase the strength of the matrix and secondly, reduce the size of the PFZ, thus promoting transgranular failure.

The extent of the strain localization will thus depend upon the volume fraction of δ', solid solution effects, volume fraction and distribution of shearable and non-shearable precipitates, degree of recrystallization, and grain size.

1.5 Corrosion of Al-Li-X Alloys

The primary microstructural feature which appears to dominate the corrosion response of Al-Li-X alloys in a 3.5% NaCl solution is the volume fraction of the anodic δ(AlLi) phase (6). The presence of sufficient quantities of δ to affect the corrosion resistance in binary Al-Li alloys has been observed only in overaged tempers. Thus, the susceptibility to attack can be controlled by:

1. the degree of overaging,
2. the number of heterogeneous nucleation sites available for precipitation, and
3. the amount of lithium available to form the anodic phase.

Increasing any of these increases corrosion susceptibility.

Al-Li alloys containing elements which reduce grain size and degree of recrystallization, such as manganese or zirconium, result in an alloy which is more susceptible to attack at a given aging condition than the corresponding binary Al-Li alloy. These alloying additions increase the number of heterogeneous nucleation sites available for precipitation (i.e., high angle grain boundaries, matrix/particle interfaces in the case of Mn containing alloys, and subgrain boundaries in the case of Zr containing alloys) thus rendering these alloys susceptible to corrosion.

Compared with binary Al-Li alloys or those containing Mg or Zr, Al-Li alloys containing Mg and/or Cu have superior aging related corrosion characteristics. Mg and Cu alter the aging sequence and promote the nucleation and growth of Al_2MgLi or Al_2CuLi rather than AlLi. These phases appear to be less active than AlLi(δ), resulting in better corrosion resistance in over-aged tempers than binary Al-Li alloys.

Based upon the preceding discussion, it is apparent that the morphologies, distributions and types of precipitates in Al-Li-X alloys can have profound effects on the properties of these alloys. Although a qualitative understanding of the precipitation sequences is known, a quantitative understanding of the transformations, kinetics, and the exact roles of individual phases in determining the properties of Al-Li-X alloys are not available. The purpose of this research is to be a comprehensible study of the transformation kinetics in Al-Li-X alloys.

1.6 Theories of Ostwald Ripening

The precipitation process may be divided into two stages: 1) nucleation directly from the supersaturated matrix, and 2) growth of the precipitate particles. The phenomenon known as Ostwald ripening characterizes the change in precipitate radius after nucleation is complete, thus occurring exclusively in the latter process. During the ripening process, the volume fraction of precipitate is constant. The solute necessary for continued growth during Ostwald ripening is supplied by the dissolution

mechanism described by Gibbs-Thomson effect (19).

Based on experimental results, Zener (20) laid the groundwork for a general ripening theory by defining a solution to the problem of diffusional growth of a spherical precipitate. Greenwood (21) tied together a number of different ideas on precipitate growth, but was unable to solve exactly the growth equations. Greenwood did, however, identify a relationship between the aging time and the cube of the particle radius, R. The work was based on experimental observations in the U-Pb system. The failure to find a theoretical growth equation represented a great problem.

Using these results, the first major Ostwald ripening theory came in the work of Lifshitz and Slyozov (22-23), and simultaneously in the work of Wagner (24). Their theory unified the ideas presented in previous theories. The LSW (Lifshitz-Slyozov-Wagner) theory of Ostwald ripening recognizes that the precipitation process can be divided into two stages as described before. From this, the theoretical particle size distribution function (PSD) is found by the solution of three simultaneous equations: a kinetic equation, a continuity equation and a mass balance equation.

The kinetic equation governs the diffusion of solute from one particle to another through the matrix, changing particle sizes. It has the form

$$\frac{d\rho^3}{dt} = 3\left(\frac{\rho}{X} - 1\right) \qquad [1]$$

with $\rho = \frac{R}{R_{Cr}}$ a dimensionless parameter where R is the actual particle radius, R_{Cr} is the critical radius related to the degree of supersaturation. X is a function of t, the dimensionless critical radius, with the boundary condition X(0) = 1.

The continuity equation describes the changes in size of particles in a given volume and has the form

$$\frac{\partial f}{\partial t} + \frac{\partial}{\partial \rho}(fV_\rho) = 0 \qquad [2]$$

with V_ρ the rate of grain travel in the space of grain sizes where

$$V_\rho = \frac{\partial \rho}{\partial t} \qquad [3]$$

and $f(\rho,t)$ is the unknown function which must be found. This equation accounts for particle growth above the critical size and particle dissolution below the critical size.

The mass balance equation accounts for the constant amount of matter in the system. This equation has the form

$$1 = \frac{\Delta}{Q_0} + \chi \int_0^\infty f\rho^3 d\rho \qquad [4]$$

with

$$\chi = \frac{4\pi R_{CrO}^3}{3Q_0} \qquad [5]$$

where,

$$R_{CrO} = \frac{\alpha}{\Delta_0} . \qquad [6]$$

α is associated with the interphase surface tension, and Δ_0 is the initial supersaturation of the system. Also Q_0 is the total initial supersaturation including the initial volume of matter in

the grains and Δ is the degree of supersaturation.

The simultaneous asymptotic solution of equations (1), (2) and (4) with the condition $f(\rho,0) = f_0(\rho)$ gives

$$\phi(Z,\gamma_0) = \begin{cases} n(\tau)\ p(Z,\gamma_0) & \text{when } Z < Z_0 \\ 0 & \text{when } Z > Z_0 \end{cases} \qquad [7]$$

with

$$n(\tau) = \int_0^\infty \phi(Z,\tau)dZ \qquad [8]$$

the number of grains per unit volume and

$$\rho(Z,\gamma_0) = \begin{cases} 3^3 2^{-5/2} e^{\cdot}(z^{1/3}+3)^{-11/3} \exp[-(1-\frac{2}{3}Z^{1/3})^{-1}], & \text{when } Z < Z_0 \\ 0 & \text{when } Z > Z_0 \end{cases} \qquad [9]$$

the probability that a particle will have a reduced volume between Z and Z + dZ. $\phi(Z,\gamma_0)$ is related to the unknown function $f(\rho,f)$ by

$$\phi(Z,t) = f(\rho^3,t)d\rho^3 \qquad [10]$$

Z, γ and τ are also dimensionless parameters like ρ, where $Z = \frac{\rho^3}{X^3(t)}$ a measure of particle size, $\gamma = 3\frac{dt}{dX^3}$, and $\tau = \ln X^3(t)$, a measure of time. The limit $Z_0 = \frac{27}{8}$ from (7) and (9) is directly related to the asymptotic limit of particle size, as required for the solution of this problem.

The ultimate result of this lengthly solution is the form of the particle size distribution function (PSD) shown in Figure 1, with this ρ is directly proportional to $Z^{1/3}$. As shown in the figure, no values of ρ greater than 1.5 will occur, and the PSD is asymmetrical with the maximum frequency value near $\rho = 1.1$.

This analysis has a number of other built in assumptions: 1) the volume fraction of precipitate is zero, 2) the particles are spherical, and 3) anisotropic effects are negligible. The first assumption assures that the distance between particles is large enough such that each particle does not affect the diffusion of solute to another particle.

As mentioned before, a linear relationship between average particle size versus time$^{1/3}$ results. This relationship was identified by Greenwood (21) in his work. This relationship has the form

$$\bar{R}^3 - R_{CO}^3 = -Kt \qquad [11]$$

with $\bar{R}$ the average particle size, R_{CO} the initial critical size for growth and K a rate constant incorporating temperature, surface tension between particle and matrix, and diffusivity. Lifshitz and Slyozov do not extrapolate their model to short growth times, since nucleation is most likely occurring during the early stages of aging.

The results of Lifshitz and Slyozov for very low volume fractions of particles and the results of Wagner (24) for interface controlled coarsening constitutes the full LSW theory. The

LSW theory represented a significant breakthrough in the theoretical understanding of the Ostwald ripening process. However, little agreement between experimental PSD's and theoretically calculated PSD's was found to occur; consequently, modifications to the LSW theory have been attempted.

The first major modification to the LSW theory was presented by Ardell, based on considerable work in the Ni-Al system (25-28). The MLSW (Modified Lifshitz-Slyozov-Wagner) theory redefines the diffusion geometry by considering the dissolution of particles in a region near a growing precipitate. This changes the expression developed by Zener which was used in the LSW theory for the concentration gradient at the particle-matrix interface from

$$\left.\frac{dc}{dR}\right|_{R=r} = \frac{c' - c_r}{r} \qquad [12]$$

to the new expression

$$\left.\frac{dc}{dR}\right|_{R=r} = \frac{c' - c_r}{r}(1 + \beta\rho) \qquad [13]$$

where c is the concentration of solute at a distance R, c′ the concentration where $R \to \infty$, and c_r the concentration at the interface of particle with radius r. The added term has the parameter β which is a function of the all important volume fraction of precipitate. This change of diffusion characteristics modifies the kinetic equation, producing

$$\frac{d\rho^3}{dt} = \frac{1}{r^{*3}}\left(3\alpha D\Omega(\rho - 1)(1 + \beta\rho) - \rho^3 \frac{dt}{dr^{*3}}\right) \qquad [14]$$

with r^* the critical radius, Ω the molar volume of precipitate, D

the solute diffusion coefficient and α a constant related to the interfacial energy. Compared to Equation (1), Equation (14) is a good deal more complicated.

The theoretical PSD has the form

$$g'(\rho') = \frac{A\rho^3}{d\rho^3/d\tau} \exp\left(\int_0^{\rho} \frac{3\rho^2 d\rho}{d\rho^3/d\tau}\right) \qquad [15]$$

which produces a PSD as shown in Figure 2, for varying values of volume fraction of precipitate. The PSD's are broader than expected from the LSW theory, giving a better fit to the experimental data, especially in the γ/γ' system. The calculated PSD's remain asymmetrical for all values of volume fraction, but the PSD's do approach a normal curve as the volume fraction approaches one.

The MLSW model also assumes spherical particles as did the LSW theory, but the geometry of the problem can be modified to fit the correct shape of the growing particles. In the limit of zero volume fraction the MLSW theory reduces to the LSW theory.

Like the LSW theory, the MLSW theory had some difficulty in explaining some growth systems, while describing other systems fairly accurately. This model has had problems where the volume fraction of the precipitating phase Q is greater than 0.08. Nevertheless, the MLSW theory introduces the effect of volume fraction on the PSD function.

A recently developed theory which involves the use of the volume fraction parameter in a significant way is a theory

developed by Brailsford and Wynblatt (29). The Brailsford-Wynblatt model also modifies the diffusion geometry of the problem, but reduces the significance of the volume fraction. This further alteration of the diffusion geometry produces a distribution function of the form

$$g(\rho) = A\rho^2 \exp \frac{[-3\rho\rho_c/(\rho_0 + \rho_c)(\rho_c - \rho)]}{(1 + \rho/\rho_0)^a (1 - \rho/\rho_c)^b} \qquad [16]$$

where

$$a = 1 + 3\rho_0^2/(\rho_0 + \rho_c)^2 \qquad [17]$$

and

$$b = 2 + 3\rho_c(2\rho_0 + \rho_c)/(\rho_0 + \rho_c)^2 \qquad [18]$$

with ρ_0 inversely related to the square of ρ_c. ρ_c is a parameter dependent upon the mean particle radius. This theoretical distribution function produces results very similar to the results of the MLSW theory found in Figure 2. The PSD's are asymmetrical at all volume fractions, thus the shape of the PSD function is much less sensitive to the volume fraction.

The Brailsford-Wynblatt model, as does the previously discussed theories, allows for different shapes of growing particles to be compensated within the theory. The Brailsford-Wynblatt theory also agrees with other theories by identifying the linear dependence of $\bar{R}^3$ versus aging time. The theory also reduces to the results of the LSW theory when Equation (16) is reduced to the zero volume fraction of precipitate.

An entirely different approach is presented in the LSEM (Lifshitz-Slyozov Encounter Modified) theory, as developed by Davies, Nash and Stevens (30). Unlike the previously discussed modifications to the original theory, the LSEM theory modifies not the kinetic equation, but the continuity equation. This alternative approach is based on the assumption that encounters can occur between separate particles. This new continuity equation has the form

$$\frac{d}{dZ}(fg) + f = \frac{-3Q}{4\pi}I \qquad [19]$$

where g is equivalent to Equation (1) and I is known as the encounter integral

$$I = 1/2\int_0^Z Zf(Z - Z')f(Z')dZ' - f(Z)\int_0^\infty (Z + Z')f(Z')dZ' \qquad [20]$$

with $Z = \frac{R^3}{R_c^3}$, a dimensionless parameter of volume. In comparison to Equation (2) the difference is slight, but the encounter integral allows consideration of particle coalescence, which is considered briefly in the LSW theory, while not considered at all in the MLSW or the Brailsford-Wynblatt model.

Using Equation (20), the theoretical PSD result is illustrated in Figure 3, with varying values of volume fraction of precipitate. Two important consequences must be noted. First, symmetrical PSD's are very much possible at smaller volume fractions, which is different than other theories discussed. None of these other theories predict a symmetrical PSD at volume fractions ranging from .15 to .75. Secondly, values of particle sizes near two times the mean particle size are very much

possible in this model, while impossible or highly improbable in the previously discussed models.

The LSEM model, as the other models, reduces to the LSW model at zero volume fraction. Also, a linear dependence for diffusion controlled growth of the mean particle size $\bar{R}^3$ versus time is predicted. The consideration of particle encounters within the theory represents a considerable change in approach than previously developed theories. Continued work is being done to incorporate the two approaches into a unified theory.

The detailed background presented here has been developed in order to provide an understanding on what ideas the form of particle size distribution function is based. Each model has certain assumptions and ideas which must be presented for the understanding of these models. Without this background, the similarities or differences of models of Ostwald ripening may be unclear.

2. EXPERIMENTAL PROCEDURE

2.1 Kinetics of Precipitation of δ′ in an Al-Li Alloy

An aluminum-lithium alloy of composition described in Table 1 was cast, hot and cold rolled to a thickness of 2.5mm. The rolled sheet was then sectioned into 1cm x 1cm pieces. The sectioned samples were solution heat treated (SHT) for 1/2 hour at 550°C in a noncorrosive salt bath and then cold water quenched (CWQ).

The samples were isothermally aged for periods of time ranging from 12 hours to 12 weeks at three temperatures: 168°C, 200°C, and 225°C. The heat treating conditions are summarized in Table 2. The samples were prepared for both optical and transmission electron microscopy (TEM).

To determine the grain structure, as-quenched samples were prepared for optical metallography. The samples were polished through 600 grit, 6 μm diamond paste and 0.5 μm chromium(III) oxide. The specimens were electropolished in a solution of 948ml H_2O, 55ml HBF_4 and 7g H_3BO_3 at 18 volts for one minute. The grains could then be observed optically using plane polarized light.

For TEM, the samples were thinned through 600 grit to 0.2mm and foils were made by jet-polishing with a 25% HNO_3 - 75% CH_3OH (by volume) solution. The central dark field (CDF) imaging was found to give good contrast between images of the δ′ precipitates and the matrix. In addition, lattice images were formed on selected samples to determine the nature of the δ′ precipitates.

Particle sizes were determined by hand measuring individual δ′ precipitates on several negatives for a given aging condition. The negatives were examined through a photographic enlarger. Numerous fields of view photographed at each aging condition formed the experimental basis of the PSD. An arbitrary minimum of approximately 600 precipitate particles was considered significant in the analysis of the PSD's. These data appear in Appen-

dix A, for 200°C and 225°C.

The hand measurement of PSD's proved to be time consuming so a semi-automatic Image Analyzing System (IAS) was programmed to aid in the measurement of particle sizes directly from the negatives. This EyeCom II IAS has an interface controller for the DEC PDP-11 minicomputer in place of the microprocessor. The IAS can read pictorial, graphical and alphanumerical data. The IAS has also been programmed to run directly from the terminal with the joy stick acting as a pen light. The IAS is represented in a simple schematic illustrating the integral parts of the system in Figure 4. The steps necessary to adapt the IAS to complete the task are presented in Appendix B and the program to calculate the PSD's is given in Appendix C. The program duplicated the calculations given in Appendix A.

2.2 Precipitation Mechanisms in Al-Li and Al-Li-Ag Alloys

Four alloys containing lithium and silver were cast at the Naval Surface Weapons Center (NSWC) and were either hot rolled to 0.5cm thick sheet or extruded to round rod 2.5cm in diameter. The nominal compositions are listed in Table 3.

Samples of the different alloys approximately 2.5cm x 1cm were SHT for 1/2 hour at 550°C in a salt bath, CWQ and artificially aged at 175, 200 and 225°C in molten salt.

Hardness curves were generated at each aging temperature for the four alloys. Rockwell hardness measurements with two scales

were used to cover the wide range of hardness values found for the different alloys.

Optical and TEM specimens were prepared using standard techniques.

Single crystals of Al-3.Li were grown using the strain-anneal technique. The as-received extruded bar was annealed at 550°C in molten salt for 15 minutes, CWQ and cold swaged approximately 75% and cut to approximately 23cm lengths. The swaged rods were then annealed at 550°C for 3 minutes, CWQ and strained 1.25% in a tensile machine. The deformed samples were macroetched to remove the surface layer.

Each rod was then annealed in a furnace designed to produce a steep thermal gradient (>100°C/cm). Figure 5 is a schematic of the apparatus used to grow the crystals. The specimens were lowered vertically into molten salt at 610°C at a rate of 0.45cm/hour.

The as-grown crystals were etched using concentrated Keller's etch to initially screen the crystals. Those which appeared from etching to be single crystals were examined using the Laue method.

The preparation of a polycrystal specimen for thermal analysis was carried out as follows.

A plate-shaped sample was cut and ground resulting in 34mg sample. The weighed sample was SHT, and CWQ as described for

hardness samples and immediately mounted in the DSC cell. For single crystals, a single crystal rod was carefully cut and ground on 320, 400 and 600 grit-emery paper and then severely etched in order not only to remove surface deformation but also to reduce weight to 34mg.

The weighed crystal was given the same heat treatment as the polycrystals.

Thermal analysis was conducted using DuPont 910 Differential Scanning Calorimeter (DSC) system. The specific experimental conditions chosen in this experiment were the following:

Temperature range:	$20^{o}C$ - $570^{o}C$
Programmed Heating Rate:	$5^{o}C$/min
Sample Size:	34 mg
Atmosphere:	air
Reference Material:	Pure Aluminum
	34 mg

2.3 Casting and Fabricating Al-Li-Cu-Mg

A series of Al-Li-Cu-Mg alloys were cast and extruded into rectangular sections. The alloys had compositions in the range (compositions are given in weight percent).

Li: 0.5 - 3.0%

Cu: 0.5 - 4.5%

Mg: 0.0 - 3.5%

The above compositions were chosen such that each alloy could be SHT in the single phase field.

The alloys were cast at the Naval Surface Weapons Center (NSCWS) in a glove box containing circulated and scrubbed helium. Oxygen, nitrogen, and water levels were each monitored and maintained at values less than 1ppm.

The glove box and support equipment provide about 1.6 meters^3 (55 cubic feet) of working space in a helium atmosphere. The "floor" of the glove box is 2.3 meters wide and 0.75 meters deep (7.5′ x 2.5′). The oxygen content of the helium is ≃1-5ppm. The water content of the helium ranges from ≃1ppm (furnace off) to ≃3-10ppm with the furnace on. Variations are the result of water diffusing from the furnace insulation and the crucible. Although crucibles are dried before inserting them into the glove box, some moisture always remains in the crucibles to diffuse out when they are re-heated in the glove box's furnace. One milligram of water raises the water content of the glove by ≃0.8ppm.

To arrest any increase in moisture content, the helium is continually dehydrated by drawing it from the glove box and blowing it through a bed of xeolite. The gas then travels over copper chips to remove oxygen (which diffuses into the box through the gloves). Next the gas is blown through a bed of sponge titanium at 930°C to remove nitrogen. An external air conditioner cools the gas before it re-enters the glove box. Helium is cleansed at a rate of about 1.4 meters^3/minute (50 feet^3/minute).

A second air conditioner is installed in the ceiling of the glove box to protect operators from excessive temperatures during melting and pouring operation.

The various alloys were melted and poured into a brass mold with a hot top to minimize the pipe in the ingot. The alloys were homogenized for 12 hours at 400°C followed by 12 hours at 425°C in an air circulating furnace. Each alloy was then machined into a cylinder 7.33cm diameter by 10.8 cm long. These billets were hot extruded at 412°C into rectangular sections (3.21cm x 1.00cm).

3. RESULTS

3.1 Kinetics of Precipitation of δ′ in an Al-Li Alloy

The structure as determined by optical microscopy, was fully recrystallized with a grain size of approximately ASTM 5 (3910 grains/mm^3), as shown in Figure 6. TEM revealed the presence of

the ordered Al_3Li precipitates (δ') and also the larger, incoherent Al_6Mn dispersoids. Representative TEM's for different aging conditions are shown in Figures 7-9. The precipitates are easy to identify with clear precipitate-matrix interfaces. During artificial aging the δ' precipitates grow retaining their spherical morphology. For example, Figure 9 contains TEM's of δ' precipitates aged 8 weeks at 200°C, the longest aging time investigated, yet these particles are still spherical.

By taking a number of TEM micrographs at a particular aging condition and compiling all the measurements, a PSD curve can be constructed. An example of a PSD curve is shown in Figure 10. All other PSD's for the various aging times, at 200°C and 225°C can be found in Appendix A. The number of particles counted per aging condition are summarized in Tables 4-6. The minimum number of particles counted at a particular aging condition was 346.

In order to compare the experimental data to a normal distribution, a program was written to fit a normal curve to the data. The results and the program are presented in Appendix D. An example is shown in Figure 11. The figure shows the experimental data with the fitted curve superimposed. The normal curve appears to provide a reasonable approximation of the data.

The statistical significance of the average particle size and the shape of the PSD function for a given aging condition depend on the number of particles comprising the population examined and the accuracy of the measurement as determined by the

size of the intervals making up the total range of sizes for a given aging condition. In an attempt to determine the minimum number of particles necessary to produce a reasonable estimate of $\overline{R}$, the two aging conditions having the most particles were used, 2 weeks at 200°C and 36 hours at 225°C, Tables 4 and 5 respectively. The values of $\overline{R}$ determined by varying the number of particles counted for the two aging conditions are summarized in Tables 7 and 8. A detailed description of the results is given in Appendix E. The interval size can also have an influence on the average size. As the interval size increased, there was a slight increase in the value of the calculated $\overline{R}$, summarized in Appendices F and G.

In addition to having an effect on $\overline{R}$, the number of measurements and the interval of the measurements can affect the shape of the distribution. A correlation exists between the number of measurements and the measurement interval size. As the interval size becomes small, a great number of measurements are needed to produce the same result. Using a constant number of measurements, use of an interval size which is too small will produce discontinuous results, while a large interval size will produce results which may not be meaningful for analysis. The results of varying the number of particles counted on the shape of the PSD's are given in Appendix E, and the effect of interval size are also presented in Appendix F.

A population of 400 particles was tested using the image analyzer. The results are presented in Appendix B. The results

agreed with those determined by using the enlarger and measuring by hand.

3.2 Precipitation Mechanisms in Al-Li and Al-Li-Ag Alloys

3.2.1 Differential Scanning Calorimetric Analysis Specific heat changes (ΔC_p) associated with precipitation reactions involving either an endothermic (heat absorption) or exothermic (heat evolution) process were automatically recorded as a function of temperature (T) by a DSC recorder. For the quantitative measurement of the energy of a heat evolution or absorption process, the area enclosed by the specific heat change vs. temperature (C - T) curve and the base line were measured with a plainmeter. The DSC was calibrated according to the method outlined in Appendix I.

To examine the effect of structural defects such as dislocations and grain boundaries on the precipitation process, calorimetric heat measurements were initially made on single crystals, polycrystals, deformed single crystals and deformed polycrystals of the Al-3wt%Li alloy immediately after quenching. However, about 15 minutes was required to begin the heating of alloys for heat measurement after quenching. The typical results are shown in Figures 12-14. These results suggest that the shape of C-T curve is considerably affected by the presence of structural defects in the sample. The base slope line (indicated by dotted line) does not show a linear dependence on temperature probably due to a small contamination in the DSC cell, however, it was reproducible in every experiment.

Calorimetric heat measurements were also made on the various as-quenched alloys. These results are presented in Figures 15 and 16. Neither an endothermic nor an exothermic reaction was detected for the low lithium alloys, the Al-1.5Li and Al-1.5%Li-1Ag, Figure 15. However, two types of endothermic reactions, one marked 'B' and the other 'D', and two types of exothermic reactions, one marked 'A' and the other 'C' occur red over a wide range of temperatures in the Al-3% Li and Al-3% Li-1% Ag alloys as shown in Figure 16. Normally in the heat measurement of age-hardening alloys, an exothermic reaction is associated with precipitation and an endothermic reaction is associated with redissolution.

In Figure 16 the similarity of overall shape of C-T curve between Al-3%Li and Al-3%Li-1%Ag implies that the general precipitation behavior of Al-3%Li-1%Ag alloys follows that of Al-3%Li alloys.

3.2.2 Precipitation Characteristics of Al-Li Alloys Containing Ag All the alloys investigated were fully recrystallized and a typical microstructures are presented in Figure 17. To reveal the aging response of Al-Li alloys containing Ag, isothermal hardness curves versus aging time at various temperatures were determined and are given in Figures 18-21. The curves for the equivalent binary Al-Li alloy are also included so that the effect of the Ag can be appreciated. In all cases, a logarithmic time scale has been used in order that hardness changes at short aging times may be conveniently shown.

Hardness curves for Al-3%Li alloys containing Ag follow the classical pattern. That is, the harness increases to a maximum and then decreases as overaging begins. The rate of hardening increases as the temperature of the aging increases. The addition of Ag to the 1.5% Li alloy caused a greater hardening and a reduction in the incubation period compared to the hardness curve of the Al-1.5Li alloy, Figure 21.

In order to characterize the microstructure of Al-Li alloys containing silver, TEM, in conjunction with optical microscopy, was utilized.

The presence of ordered precipitates in as-quenched Al-3%Li-1%Ag was indicated by the presence of superlattice reflections on SAD's and superdislocations in bright field (BF), Figure 22a. Neither superlattice reflections nor superdislocations were observed in the as-quenched Al-1.5%Li-1%Ag alloys, Figure 22b. A typical central dark field (CDF) image for Al-3%Li-1%Ag and Al-1.5%Li-1%Ag aged 96 hours at 175°C and corresponding SAD patterns are shown in Figures 23 and 24. These micrographs demonstrate that in both alloys spherical δ' precipitates exist and that the morphology of the δ' phase did not appear to be affected by the presence of silver. However, it was impossible to identify the existence of silver-rich G. P. Zones possibly introduced by the Ag addition from either the micrographs or electron diffraction pattern, because of the similarity in the morphology the Ag-rich G. P. Zones (6-8).

Ashby-Brown contrast [31] observed in BF (Figure 25) indicates that Ag did not appear to have a significant effect on the spherical strain contrast of the δ′ precipitates occurring in Al-Li binary alloy. However, a comparison of CDF image of Al-3%Li and Al-3%Li containing Ag with identical heat treatment (Figure 26) reveals that the addition of Ag has a slight effect on the size of the δ′ precipitates as plotted in Figure 27.

The microstructure of overaged Al-Li alloys containing Ag is characterized by the appearance of plate-shaped equilibrium precipitates. The microstructure of an overaged sample was first observed by optical microscopy because the reactivity of the equilibrium phase makes the preparation of a good thin foil difficult. A typical microstructure is presented in Figure 28. A number of plate-shaped equilibrium precipitates lying in a certain direction were observed in Al-3Li alloy containing Ag aged 322 hours at 200°C. This typical precipitate microstructure of overaged Ag containing alloy present a contrast to that of identically heat treated Ag-free alloy which consists of no equilibrium precipitates, suggesting that the presence of silver encourages the formation of the equilibrium phase. In fact, the presence of the equilibrium phase within the matrix was never observed for any investigations of an Al-Li alloy free from silver. The appearance of coarse plate-shaped equilibrium phase of silver containing alloy might account for the accelerated softening on hardness curve and extremely corrosive nature of overaged alloys containing silver. These results also correspond

with the results of the DSC study which shows that the addition of Ag noticeably increases the amount of equilibrium phase.

TEM was utilized to identify the equilibrium precipitates. For the preliminary survey for equilibrium precipitates, δ(AlLi) equilibrium precipitates produced in Al-3%Li alloy aged 2 hours at 300°C and were observed as illustrated in Figure 29. The δ precipitates consisted of long, coarsely dispersed rod-shaped precipitates surrounded by a misfit dislocations in agreement with the observations of Noble and Thompson [7].

The length of rods was approximately 1 μm. A large amount of equilibrium precipitates were produced and readily observed in Al-1.5%Li alloy containing 1%Ag when slightly deformed (≃5% in compression) and aged for one week at 175°C. The morphology and size of precipitates were approximately the same as that noted in binary Al-Li alloys, as shown in Figure 30. SAD's taken from the plate-shaped precipitates were indexed in terms of cubic structure with lattice parameter 6.37A. This is in close agreement with the value for the δ phase for Al-Li binary alloy determined by Silcock [11] using X-ray technique indicating that the addition of 1%Ag does not change the equilibrium phase (δ) which occurs in Al-Li binary alloy. Trace analysis on the δ precipitates gave a {111} habit plane. These results are consistent with the habit plane proposed by Silcock [11] and confirmed by Noble and Thompson [7] for binary Al-Li alloys.

Higher number density of δ precipitates were observed at the grain boundary, demonstrating that grain boundary are favorable sites for the formation of δ precipitates as shown in Figure 24. The δ precipitates took a rather irregular form with the average size of 0.3μm. Preferential location of precipitates in one side of grain might be due to the grain boundary migration associated with deformation before aging. Grain boundaries observed were very irregular suggesting that nucleation of δ at the grain boundary may cause the rotation of the grain boundary plane. However, any sign of discontinuous precipitation at the vicinity of grain boundary that was reported by Williams and Eddington [32] was not observed in any of the foils examined in the present work. A high density of interface dislocations was observed even around the grain boundary-nucleated δ precipitates.

3.3 Casting and Fabricating Al-Li-Cu-Mg

These alloys have been cast and fabricated during this contract period and will be examined as part of next years' program.

4. DISCUSSIONS

4.1 Ripening Theory

Examination of the TEM foils at the different conditions revealed that the precipitates remained coherent and spherical through the aging conditions investigated. These qualities make this system ideal for examining in detail the phenomenon of Ostwald ripening and for relating the data to theories in the

literature.

While models for ripening may disagree on the form of the theoretical PSD, there is complete agreement on the functional dependence of the mean particle size $\bar{R}$ versus aging time for diffusion controlled growth. This equation is of the form

$$\bar{R}^3 - R_{CO}^3 = Kt \qquad [21]$$

with $\bar{R}$ the mean particle size, R_{CO} the initial critical size for growth, and K a rate constant. K is defined as

$$K = \frac{8\ \sigma\ D\ C_e\ V_m^2}{9RT} \qquad [22]$$

where D is the diffusion coefficient of solute within the matrix, C_e the equilibrium solute concentration at temperature T, σ the interfacial free energy of the precipitate, and V_m the molar volume of the precipitate.

Plotting the experimental values for the cube of the radii versus aging time, as required in Equation [21], produces a plot as shown in Figure 31. The results of data taken by hand at 200° and 225°C are presented, along with the results utilizing the IAS data taken on the samples aged at 168°C and 200°C. The values for the constants K and R_{CO} are found for each condition in Table 9.

Examining the extrapolated values of R_{CO}, no systematic positive or negative values were observed. The values of R_{CO} are located around $R_{CO} = 0$, which has been identified by other workers in this system (14-15) to be a reasonable value for R_{CO}. When R_{CO} equals zero, Equation [21] reduces to the form:

$$\bar{R} = k\ t^{1/3} \qquad [23]$$

The average particle size versus $t^{1/3}$ for the different experimental conditions are plotted in Figures 32-33. A "least-squares" line is included on the plot. The slopes of the "least-squares" line, equal to k, are summarized in Table 10 along with the extrapolation to t = 0. The intercept values are approximately zero suggesting that the assumption:

$$\bar{R} \propto t^{1/3} \qquad [24]$$

is reasonable, implying that the precoarsening regime is very short or does not exist at all.

The critical ordering temperature of Al_3Li, based upon measured superdislocation spacings and the associated calculated APB energy of 195 ergs/cm^2, has been estimated to be 810K for an Al-3.3 wt% Li alloy (33). This temperature is above the accepted δ' solvus temperature (34). As a consequence of the predicted high critical ordering temperature one would predict that Al_3Li should decompose directly from the supersaturated solid solution as an ordered structure and would not disorder upon heating, but rather dissolve. When considering quenching and aging in light of the stability of the structure, one would expect the clusters to be initially ordered and they would grow during aging. This idea is supported by the observation that the $\bar{R}$ vs $t^{1/3}$ behavior extrapolates to very short aging times. The origin of the clusters, whether they exist in the solid solution as clusters, nucleate during the quench, or nucleate at very short aging times is a

subject of a separate investigation.

TEM analysis appears to be satisfactory over the range of particle sizes examined in this research, where the matrix/particle interface is well resolved and the precipitate overlap is small. Further work at shorter aging conditions cannot be conveniently accomplished using TEM, but will require small angle scattering techniques.

For a given composition and temperature, K is a function of the diffusion coefficient and the interfacial free energy. Consequently, in order to determine one of these variables the other must be determined by an independent measurement or a reasonable estimate must be assumed.

In the aluminum-lithium system two opposite approaches dealing with the separation of K have been taken. Values of experimental K from previous workers can be found in Table 11. Noble and Thompson (7) extrapolated the high temperature diffusion data (34) to find values of D, found in Table 12, for their aging temperatures, then calculated σ. The calculated σ is one order of magnitude larger than the value one might expect in a system which has coherent, spherical precipitates with small strain (34). The approach of Williams and Eddington (8), on the other hand, was to assume a value for σ and calculate D. Their results were based on an interfacial free energy value found by Parker and West published in reference 36. Parker and West used Ni-X alloys to find the mismatch between an ordered $L1_2$ structure in a

fcc matrix. δ′ within the α matrix acts similarly to Ni_3X in a nickel matrix, so William and Eddington used a value $2.5 \times 10^{-2} J/m^2$ for the interfacial free energy of δ′ in the α matrix, a value found by Parker and West. The calculated diffusion coefficients from Williams and Eddington are found in Table 12.

The extrapolation of diffusion data to low temperatures is not completely valid an alloy which is SHT, CWQ, and isothermally aged. The rate of diffusion depends not only on the temperature but the vacancy concentration. The vacancy concentration is approximately the equilibrium concentration at the solution heat treatment temperature. Thus one would expect during artificial aging the diffusion coefficient would be higher than that calculated by extrapolation. Examination of Equation [22] reveals:

$$K \alpha D\sigma \qquad [25]$$

thus, for a given value of K under estimating D would tend to overestimate σ.

The δ′/α interfacial free energy values of Noble and Thompson and of Williams and Eddington were compared to other similar systems for agreement, system which also exhibit, for example, small misfit strain and coherency within the matrix. Table 13 (36) contains a summary of interfacial free energy values for a number of different systems. Precipitates which are coherent with small strain have low interfacial free energies. Thus, assuming a value of the interfacial free energy and calculating

diffusivity is more realistic than the approach of Noble and Thompson. The value of 2.5×10^{-2} J/m^2 was utilized in this investigation to calculate the diffusivity at each of the three aging temperatures. The calculated diffusivity values may be found in Table 14.

All the experimental PSD's could be approximated by a normal curve. By finding the peak width at half height of these normal PSD's and plotting these versus $\bar{R}$, as in Figure 34, it was found that the peak width at half height was independent of temperature, since both 200° and 225°C results were found to lie on a common line. This is to be expected, for the shape of the PSD should only be a function of the extent of aging. Changing aging temperature should only affect the rate of growth, not the distribution of particles.

Comparison of the experimental PSD's to various Ostwald ripening theories results in some interesting discrepancies. In all cases examined, the experimentally found PSD can be approximated by a normal distribution. This result is not predicted by all the theories.

The main foundation work of modern Ostwald ripening theory is the LSW (Lifshitz-Slyozov-Wagner) theory as proposed by Lifshitz and Slyozov (22-23). This theory united many ideas on ripening into a coherent unified theory. The PSD function solution generated by this theory is illustrated in Figure 1. This theoretically derived PSD is not symmetrical. More importantly,

the LSW theory fails to predict the existence of any precipitates at sizes greater than 3/2 the mean particle size, while the experimental results clearly show that the larger sizes do indeed exist.

A modification of the theory, the MLSW (Modified Lifshitz-Slyozov-Wagner) was proposed by Ardell(25-27). The MLSW theory produced a theoretical PSD which incorporated the volume fraction of precipitates as the controlling parameter, producing theoretical PSD's of the form shown in Figure 2 (28). In this model, the theoretically determined PSD does approach symmetric behavior at volume fractions approaching unity. The MLSW model predicts a slightly assymetric PSD, with a deviation of the maximum frequency value away from the mean particle size $\overline{R}$. Although this is a closer approximation to the experimental results presented in this investigation, the MLSW theory cannot be applied to this Al-Li alloy. According to the MLSW model values of $\overline{R}$ greater than approximately 1.75 $\overline{R}$ should not exist. Thus the MLSW model does not completely fit the experimental results

Similarly, the model proposed by Brailsford and Wynblatt (29), which also depends upon volume fraction as a controlling parameter, also predicts an asymmetrical PSD and is thus inconsistent with the experimentally found normal PSD's. All three models, on the other hand, do predict the linear relationship of aging time and the mean particle size which was found to occur in Figure 32. The asymmetry of the theoretical PSD represents a considerable problem which must be discussed.

Solute to aid the ripening process in these models comes from a mechanism as proposed by Gibbs and Thomson (19). The mechanism releases the excess surface energy by dissolution of smaller particles, providing the solute necessary for other precipitates to grow. The smaller precipitates have a larger ratio of surface area to volume then larger precipitates, so the continued growth of larger precipitates reduces the overall energy within the system.

The Gibbs-Thomson Effect is also included in the model which does predict symmetrical PSD's and values of R nearly two times the mean particle size. The LSEM (Lifshitz-Slyozov Encounter Modified) theory, as proposed by Davies, et al. (30), does predict a symmetrical PSD function. The LSEM model takes into account the encounters between close precipitates to combine and form mean particles of volume fraction equal to the sum of the individual particle volume fractions. Lifshitz and Slyozov acknowledge encounters in their work, while MLSW and Brailsford-Wynblatt models do not consider these events to be significant. The LSEM theory describes the change in theoretical PSD with the inclusion of encounters, broadening the PSD. This broadening of the curves can be seen in Figure 3, as compared to the theoretical PSD's of the previously discussed theories. It is especially important that values near two times the mean particle size are more probable in the LSEM theory, which is not possible in other theories.

Since the idea of encounters is central to the LSEM theory, it must be considered in more detail. Encounters between precipitates may be identified in two different ways. One method is to examine the overall shape of individual particles. δ′ precipitates are spherically shaped, producing an aspect ratio near 1.00, where the aspect ratio is defined as the ratio of the minor axis and the major axis. If an encounter occurs between two precipitates, this aspect ratio will deviate significantly from unity, producing a value of .50 when two identical dimension precipitates meet. The occurrence of particles with aspect ratios between .50 to .80 may indicate the possibility of an encounter. If an aspect ratio < .80 is used as a criterion of encounter events the number of encounters is small and perhaps not significant, Figures 35 and 36.

The idea of encounters may also be examined in a different light. Consider two precipitates, as in Figure 37, having an $L1_2$ structure like δ′, with the aluminum in the face center and the lithium in the corners, as shown in Figure 38. During aging, the precipitates will grow forming spherical precipitates. If aging continues, the precipitates will continue to grow and the two separate precipitates will meet and form a new, larger precipitate. Unless there is a lattice registry between the two precipitates, an antiphase domain boundary (APB) will form, shown in Figure 39. In the FCC structure there is a 50-50 probability that an APB will form. The existence of some encounters should, therefore, be identified by the presence of an APB within a pre-

cipitate. If the LSEM model indeed fits the ripening of δ′ precipitates, antiphase boundaries will be found in some δ′ precipitates.

Lattice images of the δ′ precipitates as in Figure 40 were taken. In examining these lattice images, the δ′ precipitates were found to be uniform with no APB's. In fact, no APB's were found in any of the precipitates examined, suggesting that encounters between precipitates must be limited to those precipitates which are in crystallographic registry.

4.2 Statistical Analysis

The 600 particle minimum, which was arbitrarily set for the hand measured PSD, was indeed very generous as fewer particles were needed for accurate results. The 400 particle minimum established by experiment will give an accurate description of the overall shape of the PSD. It is important to note, however, this 400 particle minimum does not need to be kept if the overall shape of the PSD is unimportant but the mean particle size $\bar{R}$ is the desired value.

The use of the IAS, while not sacrificing statistical accuracy, proved to be a great time saver, cutting hours off particle measurement and analysis time. The results from the IAS proved to be just as accurate for $\bar{R}$ as the hand measurements. The closeness of the class intervals, however, presented a small problem with the overall shape of the PSD. Too small class interval sizes from a constant population size, will produce results which

may not be sufficient for accurate analysis of the data. Interval sizes on the IAS must be carefully watched for clear and accurate shapes of PSD's.

4.3 Differential Scanning Calorimetric Analysis

To understand the change in shape on the energy-temperature curve associated with the structural defects, it is necessary to compare the area of each endothermic or exothermic step and analyze the value on the basis of the knowledge of the process of precipitation occurring in Al-Li alloys. In each energy-temperature curve (Figures 12-14), the area of D (dissolution of δ phase) is larger than that of C (formation of δ phase) in disagreement with Nozato et al.[37] results. This difference in area implies that the shape of C is governed not only by the formation of δ but also by the dissolution of δ' because if the shape of 'C' were solely governed by the formation of δ, in other words all δ' phase dissolve until the temperature reaches 312^{o}C (δ' solvus) and above 312^{o}C δ precipitates started to form without further dissolution of δ' the area of heat evolution associated with δ', formation should be equal to that of heat absorption associated with redissolution of δ phase. It can therefore be suggested that below the 312^{o}C (δ' solvus) dissolution of δ' is predominant over the formation δ, causing the heat absorption marked B, however, above 312^{o}C rapid formation of δ phase makes the heat of evolution dominate the heat of absorption associated with the dissolution of δ' and therefore causes the heat absorption marked C on energy-temperature curve. This

interpretation can be supported by corresponding TEM observation which shows the presence of a significant amount of δ precipitates in the Al-3%Li aged 2 hours at 300°C (≃12°C below the δ′ solvus), Figure 29. The presence of δ precipitates at the matrix (Figure 41a) and along the grain boundary (Figure 41b) has been also observed in the sample heated to 275°C in the DSC cell.

These competing reactions make it difficult to interpret the energy-temperature curves, in the 'B' and 'C' regions curve unambiguously. However, the D region will be governed only by the dissolution of δ′ phase, assuming all δ phase dissolves before the temperature reaches the D region. This assumption is reasonable because the temperature range of 'D' is far above the δ′ solvus. Therefore, the energy (area) of heat absorption 'D' may be proportional to the volume fraction of the δ precipitates undergoing dissolution. This relationship can be expressed as follows:

$$\Delta HR = \frac{\Delta Hp}{MWp} \frac{lp}{ls} V_f$$

where

ΔHp = molar heat of dissolution of precipitate

MWp = molecular weight of precipitate

lp = density of precipitate

ls = density of sample

V_f = volume fraction of precipitate

The energy of 'D' in Figures 12-14 plotted versus the amount of deformation is shown in Figure 42. Figure 42 shows that the polycrystalline material produces more of the δ phase (60% increase) than the single crystal. The increase in the amount of δ phase by the presence of grain boundaries can be explained in terms of lower surface energy of grain boundary than that of matrix which may release the strain energy developed by large lattice misfit of δ phase more easily. A comparison of the energy-temperature curves for a single crystal and a polycrystal in Figure 12 reveals that the corresponding curves for polycrystals moves upward compared to that for single crystals at a temperature range of 137°C ~ 312°C, indicating that the grain boundary increases the rate of the dissolution of δ′ since the heat evolution in this temperature range is associated with the dissolution of δ′ phase as described earlier.

Figures 13 and 14 demonstrate the importance the dislocation introduced by deformation on the precipitation process in the Al-3%Li alloys. Figure 42 also reveals that the amount of δ phase is increased by increasing the amount of deformation, further demonstrating that dislocations introduced by deformation also promote the formation of the δ precipitates. An interesting feature in Figures 13 and 14 is that heat evolution 'A' increases while heat absorption 'B' decreases with increasing the deformation. This shift in the energy-temperature curves associated with the presence of dislocations can be explained as follows.

As described earlier, heat evolution 'A' is associated with the formation of δ′ phase, however, small area of 'A' (formation of δ′) especially compared to 'B' (dissolution δ′) implies that most δ′ phase forms during quenching and just a very small amount of δ′ is nucleated during aging. These results are consistent with the electron microscopy which shows the presence of δ′ in the as-quenched Al-3%Li alloys.

The small increment of 'A' with deformation implies that only a small amount of δ′ nucleates near at the dislocations after quenching. However, the increase in the area of 'A' is very small compared to that of 'D'. This indicates that dislocations are much more favorable sites for the nucleation of the δ phase rather than the δ′ phase. This is quite probable because large strain energy generated by the nucleation of δ with large lattice misfit with the matrix can be relieved by dislocation. On the other hand, the strain energy factor is not important for the nucleation of δ′ phase possessing very small lattice misfit with the matrix. This can be confirmed by Williams' TEM observation[8] showing that δ′ precipitate is not affected by the presence of grain boundaries or dislocations. Thus the nucleation of δ′ can be explained in terms of the segregation of Li atoms along the dislocation leading to the nucleation of δ′, rather than an accommodation of strain energy generated by nucleation of δ′.

As can be seen in Figures 13 and 14, the area of 'B' is increased with deformation, indicating that dislocations also promote the dissolution of the δ′ phase. The enlargement of area

B with deformation implies that δ′ precipitates nucleated in the vicinity of dislocations grow rapidly by drawing Li atoms from the regions adjacent to the dislocations, causing the preferential dissolution of δ′ precipitates around the dislocations. To illustrate the effect of dislocations on the distribution of δ′ in a dilute alloy (Al-1.5Li) Figure 43 contains a TEM showing δ′ in the vicinity of dislocations.

As a result, it can be proposed that even though the precipitation of δ′ is not affected by the presence of dislocation during quenching, preferential diffusion of Li atoms along dislocation during aging may cause extra nucleation of δ′ at dislocation and that rapid coarsening of δ′ phase on dislocation causes the large amount of δ′ dissolution around the dislocation.

The absence of any endothermic or exothermic reaction on the energy-temperature curves for Al-1.5%Li and Al-1.5%Li-1%Ag in Figure 15 can be interpreted as being the results of the incubation time in these alloys on the basis of the Al-Li phase diagram (Figure 44), which shows that 1.5%Li lies just inside two phase regions below the δ solvus temperature of about 200°C. That is, even though samples containing 1.5wt%Li are supersaturated at room temperature up to ≃200°C (δ solvus temperature) the small driving force for precipitation due to low supersaturation is correspondingly low. This explanation can be verified by the presence of a long incubation period on the hardness curve (Figure 21) for Al-1.5%Li alloy aged at 200°C and 175°C.

4.4 Precipitation Characteristics of Al-Li Alloy Containing Ag

An addition of a small amount (1 wt.%) of Ag did not appear to alter the precipitation sequence occurring in Al-Li binary system. The δ′ phase which occurs in binary Al-Li alloys is also responsible for the strengthening in the Al-Li alloys containing Ag. However, the presence of Ag had a marked effect on the rate of precipitation process. Reduction in the size of δ′ particles together with the delay of peak hardness aging time when compared with Ag-free alloys can be explained in terms of the reduction of growth rate of δ′ precipitates associated with the addition of Ag. This result is not surprising since many workers[39] have reported that the trace element reduces the rate of zone formation by retarding the diffusion in many aluminum alloys. Kimura et al.,[39] proposed the following explanation. The role of trace element is to trap excessive vacancies and thereby reduce the rate of zone formation. We might be able to adapt their proposal for the explanation of the reduction of the growth rate of δ′.

Sanders, et al., [3] and Williams, et al., [8] have demonstrated that elimination of excessive vacancies by step quenching in Al-Li alloys cannot suppress the formation of δ′ precipitate. Therefore, even though silver atoms trap the excessive vacancies during aging, it may not be able to suppress the δ′ precipitation. However, the presence of silver atoms may diminish the growth rate of the δ′ precipitates by trapping the vacancies during subsequent aging.

To explain the apparent hardening generated by the addition of Ag there exist several feasible proposals. First is the solid solution hardening analogous to the addition of Mg to Al-Li alloys [10]. This is not probable, however, because Haessner and Schreiber[40] has reported that there is no solid solution hardening when Ag is in true solid solution in Al.

Another possible explanation will be a hardening associated with the Ag-rich G.P. zone possibly introduced by the addition of Ag since 1 wt.% Ag is over the solid solubility limit of Ag in Al.

In spite of the difficulty in identifying the existence of GP zones by TEM microscopy, its presence can be recognized by interpreting the slope change of the hardness curve for Al-Li alloy containing Ag by reference to the results of extensive studies of Al-Ag alloys. Koster and Braumann[41], and Beton and Rollason[42] have reported that the most Al-Ag alloys aged in the temperature range of 100 ~ 200°C have hardness-time curves which exhibit a clear double peak. The first peak early in the aging process occurs at approximately 1 hour aging time as illustrated in Figure 45. Baur and Gerold[43] have proposed that the peak can be attributed to the reversion of the first strengthening phase occurring with the transformation from ordered G.P. zone (r-state) to disordered G.P. zone (ε state). More recently, Gragg, et al.[44], have substantiated that the ε-state G.P. zone is indeed a disordered structure with an octahedral morphology.

On the basis of these reports, it is believed that a rapid decrease in the slope of the hardness together with an apparent drop at 1hr. aging time for Al-3%Li-1%Ag and Al-1.5%Li-1%Ag, respectively (Figures 18-21) are indicative of the existence of silver-rich G.P. zone in the Ag-bearing alloys. However, from the phase diagram of Al-Ag with the metals stable miscillility gap of G.P. zone as shown in Figure 46, it is conceivable that after the reversion of strengthening expected disordered G.P. zone (ε-state) might be very small or dissolved entirely into solid solution and thereby making little contribution to the strengthening of this alloy. Even though the hardness behavior of Al-1%Ag, which would verify this explanation, is not available, the indirect information can be obtained from the data reported by Hardy[45], showing that the addition of 0.97 wt% Ag to pure Al cause the strengthening from 1.8 tons/in^2 to 2.3 ton/in^2 by 0.1% proof - stress after aging 2~3 weeks at room temperature, while the strength of the sample aged 16 hours at 165^{o}C is nearly the same as pure Al (1.9 tons/in^2). As a result, it is unlikely that the G.P. zone make a significant contribution to the strengthening in Al-Li alloy containing silver after hardness reversion.

The most obvious benefits of Ag is that the addition of Ag reduces the solid solubility of Li in Al, thus enhancing the formation of δ' precipitates which is responsible for the strengthening in the Al-Li alloys. This explanation is in good agreement with the DSC results which showed that Ag addition

increase the solvus temperature indicating that Ag addition shifts the solvus line to left thus reducing the solid solubility of Li in Al as indicated in Figure 44. Furthermore, the hardening associated with the addition of Ag in the Al-1.5%Li alloy lends further support to this explanation because Al-1.5%Li alloy which lies just inside the metastable gap for δ′ precipitation is much more affected by aging than the binary 1.5%Li alloy.

The reduction of incubation time by adding Ag to the Al-1.5%Li alloys can also be explained in terms of the reduction of solid solubility of Li. However, both TEM and DSC results have shown that there is no nucleation of δ′ during quenching in the Al-1.5%Li-1%Ag alloys.

The nucleation of equilibrium δ phase appears to be enhanced by the addition of Ag. This observation is consistent with Hardy's rule[46], that is, if a specific precipitate is accelerated by the cold work, that precipitate is expected to be increased by the addition of trace element. On the basis of Hardy's rule, it is conceivable that δ precipitation, which is accelerated by deformation as demonstrated in DSC and TEM, is also be accelerated by the addition of Ag atom.

The precise mechanism for Ag atom to facilitate the nucleation of δ has not been determined. Presumably, Ag atoms reduce the precipitate-matrix interface energy and hence reduce the critical size for the nucleation of δ at a particular supersaturation as in the case of In additions to Al-Cu alloys[37].

5. SUMMARY AND CONCLUSIONS

5.1 Kinetics of Precipitation of δ′ in an Al-Li Alloy

Summarizing, it was observed for an Al-3Li alloy the growth of δ′ precipitates was found to obey an Ostwald ripening growth mechanism. The PSD function of δ′ at different aging conditions was found to be symmetrical and centered around the mean particle size $\bar{R}$, with the normal curve reproducable at the three aging temperatures and all aging times investigated. Plotting the mean particle size $\bar{R}$ versus (aging time)$^{1/3}$ produced a linear dependence, confirming the work of previous investigators. As time approached zero, the mean particle size $\bar{R}$ approached 0 Angstroms, suggesting that nucleation occurred spontaneously during the quench and that growth with no further nucleation occurred once artificial aging begins.

In comparing the experimental results to various theories of Ostwald ripening, it was found that none of the theories represent an accurate picture of what occurred in the Al-Li system. The LSW, MLSW and Brailsford-Wynblatt models were unable to predict a spherical PSD, but while the LSEM model could predict a symmetrical PSD, from the lattice images and an analysis of the precipitate shape of the δ′ particles the significance of the encounter phenomenon in the Al-Li system was small. Since the symmetric PSD's of the LSEM theory is based upon the importance of encounters, this might indicate that for the Al-Li system the similarities in the LSEM model and this data is fortuitous.

Statistically, the initial assumption of 600 precipitate particles was well in excess of the approximately 400 particle population needed to determine the overall shape of a PSD. The determination of $\bar{R}$ could be found with a much smaller populations, however, if the shape of the PSD is not needed. Varying class interval size will produce smoother PSD's with little static, but the class interval size must be watched carefully. The use of the image analyzer confirmed these results, allowing the use of the time-saving IAS for accurate determination of PSD's with little difficulty.

More theoretical work must be done to explain the results presented in this report. The development of a unified, consistent Ostwald ripening theory is necessary for accurate determination and prediction of precipitate growth. With the use of accurate statistical samples, comparison with experiment is possible so that a final, comprehensive ripening theory may be developed.

5.2 Precipitation in Al-Li and Al-Li-Ag Alloys

Excellent consistency exists between DSC and TEM analysis for the characterization of precipitation microstructure in the alloys studied.

The presence of dislocation and grain boundary to be more important in the nucleation of δ rather than that of δ'. Formation of δ phase was found to be significantly enhanced by the presence of the grain boundaries as well as dislocations,

suggesting that δ nucleates heterogeneously at the grain boundaries and the dislocations. It has been proposed that a certain amount of δ′ precipitates nucleate at the dislocations during subsequent aging, even though most δ′ precipitates are formed during quenching in Al alloys containing sufficient Li content (>2 wt%).

Precipitation sequence of Al-Li alloys containing 1 wt% Ag can be summarized as follows:

$$\text{Supersaturation} \rightarrow Al_3Li(\delta') \rightarrow AlLi\ (\delta)$$

$$\rightarrow \text{Silver-rich G.P. Zone}$$

Spherical δ′ precipitates occurring in binary Al-Li alloy are responsible for the majority of strengthening in the Al-Li alloys containing Ag. The microstructure of Al-Li alloys containing Ag is similar to that of Al-Li binary alloy in the early stage of aging. The effect of the addition of Ag appears to be in the reduction of the solubility of Li, thus enhancing δ′ precipitation, and in the slight retardation of the growth of δ′. In the later stage, however, Ag atoms promote the nucleation of plate-shape δ precipitates, causing the rapid deterioration in strength and corrosion resistance, compared to the equivalent Al-Li alloys free from Ag. Analogous to Al-Li system, continued artificial aging below the δ′ solvus results in the preferential coarsening of δ′ at the grain boundaries and the development of PFZ along the grain boundaries.

6. REFERENCES

1. R. E. Lewis, D. Webster and I. G. Palmer, "A Feasibility Study for Development of Structural Aluminum Alloys from Rapidly Solidified Powders for Aerospace Structural Applications," Lockheed Palo Alto Research Laboratory Final Report, Contract F33615-77-C-5186, Technical Report No. AFML-TR-78-102, July, 1978.

2. T. H. Sanders, Jr. and E. A. Starke, Jr., eds., Aluminum-Lithium Alloys (Proceedings of the First International Aluminum-Lithium Conference, Stone Mountain, Georgia, May 19-21, 1980), The Metallurgical Society of AIME, Warrendale, PA, 1981, 377 pages.

3. T. H. Sanders, Jr., "Development of an al-Mg-Li Alloy," NADC Contract No. N62269-74-C-0438, Final Report, June, 1976.

4. T. H. Sanders, Jr., "Factors Influencing Fracture Toughness and Other Properties of Aluminum-Lithium Alloys," Naval Air Development Center Contract No. N62269-76-C-0271, Final Report, June 1979.

5. E. A. Starke, Jr. and T. H. Sanders, Jr., "The Effect of Microstructure of the Properties of High Strength Aluminum Alloys," AFOSR Annual Scientific Report, Research Grant No. AFOSR-78-3471, February 1981.

6. P. Niskanen, T. H. Sanders, Jr., M. Marek and J. G. Rinker, "The Influence of Microstructure on the Corrosion of Al-Li, Al-Li-Mn, Al-Li-Mg, and Al-Li-Cu Alloys in 3.5% NaCl Solution," in Aluminum-Lithium Alloys, T. H. Sanders, Jr. and E. A. Starke, Jr., eds., AIME, Warrendale, PA, 1981, p. 347.

7. B. Noble and G. E. Thompson, "Precipitation Characteristics of Aluminum-Lithium Alloys," Metal Sci. J., 5 (1971), 114.

8. D. B. Williams and J. W. Eddington, "The Precipitation of (Al_3Li) in Dilute Aluminum-Lithium Alloys," Metal Science, 9 (1975), 529.

9. T. H. Sanders, Jr., E. A. Ludwiczak, and R. R. Sawtell, "The Fracture Behavior of Recrystallized Al-2.8% Li-0.3% Mn Sheet," Mat. Sci. Eng., 43 (1980), 247.

10. G. E. Thompson and B. Noble, "Precipitation Characteristics of Aluminum-Lithium Alloys Containing Magnesium," Journal of the Institute of Metals, 101 (1973), 111.

11. J. M. Silcock, "The Structural Aging Characteristics of Aluminum-Copper-Lithium Alloys," Journal of the Institute of Metals, 88, (1959-60), 357.

12. B. Noble and G. E. Thompson, " T_1 (Al_2CuLi) Precipitation in Aluminum-Copper-Lithium Alloys," Met. Sci. J., 9, (1972), 167.

13. P. M. Kelly, "The Quantitative Relationship Between Microstructure and Properties in Two Phase Alloys," Inter. Met. Reviews, 18, (1973) 31.

14. R. F. Decker, "Alloy Design, Using Second Phases," Metallurgical Transactions, 4, (1973), 2495.

15. E. A. Starke, Jr., "Aluminum Alloys of the 70's: Scientific Solutions to Engineering Problems," Materials Science and Engineering, 29, (1977) 99.

16. T. H. Sanders, Jr. and E. A. Starke, Jr., "The Effect of Slip Distribution on the Monotonic and Cyclic Ductility of Al-Li Binary Alloys," Acta Met., in press.

17. E. A. Starke, Jr. and G. Lutjering, "Cyclic Plastic Deformation and Microstructure," in Fatigue and Microstructure, M. Meshii, ed., ASM, Metals Park, Ohio (1979), 205.

18. K. K. Sankaran, S. M. L. Sastry, and J. E. O'Neal, "Microstructure and Deformation of Rapidly Solidified Al-3Li Alloys Containing Incoherent Dispersoids," in Aluminum-Lithium Alloys, T. H. Sanders, Jr. and E. A. Starke, Jr., eds., AIME, Warrendale, PA, (1981), 189.

19. D. A. Porter and K. E. Easterling, Phase Transformations in Metals and Alloys, Van Nostrand Reinhold, New York, (1981), 46.

20. C. Zener, Journal of Applied Physics, 20, (1949), 950.

21. G. W. Greenwood, Acta Metallurgica, 4, (1956) 243.

22. I. M. Lifshitz and V. V. Slyozov, Soviet Physics JETP, 35 (8), (1959), 331.

23. I. M. Lifshitz and V. V. Slyozov, Journal of the Physical Chemistry of Solids, 19, (1961) 35.

24. C. Wagner, Z. Electrochemie, 65, (1961) 581.

25. A. J. Ardell and R. B. Nicholson, Acta Metallurgica, 14, (1966), 1295.

26. A. J. Ardell and R. B. Nicholson, Journal of the Physical Chemistry of Solids, 27, (1966) 1793.

27. D. J. Challman and A. J. Ardell, Acta Metallurgica, 22, (1974) 577.

28. A. J. Ardell, Acta Metallurgica, 20, (1972) 61.

29. A. D. Brailsford and P. Wynblatt, Acta Metallurgica, 27, (1979) 489.

30. C. K. L. Davies, P. Nash and R. N. Stevens, Acta Metallurgica, 28, (1980) 179.

31. M. F. Ashby and L. M. Brown, "Diffraction Contrast From Spherically Symmetrical Coherency Strains," Phil. Mag., 1963, 18, p. 1083.

32. D. B. Williams and J. W. Eddington, "The Discontinuous Precipitation Reaction in Dilute Al-Li Alloys," Acta Met., 1976, 24, p. 323.

33. M. Tomura, T. Meri, and T. Nakamura, Journal of the Japanese Institute of Metals, 34, (1970) 919.

34. D. B. Williams, Aluminum-Lithium Alloys, T. H. Sanders, Jr. and E. A. Starke, Jr., eds., AIME, Warrendale, PA, (1981), 89.

35. L. P. Costas, U.S. Atomic Energy Commission Report, (DP-813), 1963.

36. J. W. Martin and R. D. Doherty, Stability of Microstructure in Metallic Systems, Cambridge University Press, Cambridge, U.K. (1980) 176.

37. R. Nozato and G. R. Nakai, "Thermal Analysis of Precipitation in Al-Li Alloys," Trans. J. I. M., 1977, 18, p. 678.

38. D. B. Williams, "Microstructural Characteristics of Al-Li Alloys," in Aluminum-Lithium Alloys, T. H. Sanders, Jr. and E. A. Starke, Jr., eds., AIME, Warrendale, PA., 1981, p. 87.

39. H. Kimura and R. R. Hasiguti, "Interaction of Vacancies with Sn Atoms and the Rate of G. P. Zone Formation in an Al-Cu-Sn Alloys," Acta Met., 1961, 9, p. 1076.

40. F. Haessner and D. Schreiber, "Uber die Verfestigung von Aluminium-Emkristallen mit Geringer Silberzusatzen," Z. Metalkunde, 1956, 48, p. 263.

41. W. Koster and F. Braumann, "Uber die Aushartung von Aluminium-Silver-Legierungen," Z. Metalkunde, 1952, 43, p. 193.

42. R. H. Benton and E. C. Rollason, "Hardness Reversion of Aluminum-Silver Alloys," J. Inst. Met., 1957-58, 86, p. 85.

43. R. Baur and V. Gerold, "The Existence of a Metastable Miscibility Gap in Aluminum-Silver Alloys," Acta Met., 1962, 10, p. 637.

44. J. E. Gragg, Jr. and J. B. Cohen, "The Structure of Guinier-Preston Zones in Aluminum-5wt%Silver," Acta Met., 1971, 19, p. 507.

45. H. K. Hardy, "Aluminum-Copper-Cadminum Alloys," J. Inst. Met., 1954-55, 83, p. 337.

46. J. M. Silcock, T. J. Heal, and H. K. Hardy, "The Structural Aging Characteristics of Ternary Aluminum-Copper Alloys with Cadminum, Indium, or Tin," J. Inst. Met., 1955-56, 84, p. 23.

TABLES

TABLE 1.

COMPOSITION OF THE Al-Li ALLOY
(given in weight percent)

Li	Mn	Fe	Si	Al
2.78	0.32	0.06	0.04	Balance

TABLE 2.

AGING CONDITIONS USED FOR THE DETERMINATION OF PARTICLE SIZE DISTRIBUTION (PSD) FUNCTIONS

TIME (aging)	(seconds)	TEMPERATURE 168°C	200°C	225°C
12 hours	4.32×10^4	--	--	*
24 hours	8.64×10^4	--	--	*
36 hours	1.30×10^5	--	--	*
48 hours	1.73×10^5	--	*	*
72 hours	2.59×10^5	--	--	*
96 hours	3.46×10^5	--	*	*
144 hours	5.18×10^5	--	--	*
1 week	6.05×10^5	*	*	--
8 days	6.91×10^5	*	--	--
10 days	8.64×10^5	*	--	--
274 hours	9.86×10^5	--	*	--
2 weeks	1.21×10^6	*	*	--
3 weeks	1.82×10^6	*	--	--
4 weeks	2.42×10^6	*	*	--
5 weeks	3.03×10^6	*	--	--
6 weeks	3.63×10^6	*	*	--
7 weeks	4.24×10^6	*	--	--
8 weeks	4.84×10^6	*	*	--
9 weeks	5.44×10^6	*	--	--
10 weeks	6.05×10^6	*	--	--
11 weeks	6.65×10^6	*	--	--
12 weeks	7.26×10^6	*	--	--

* Denotes measurements made at these times.

TABLE 3

NOMINAL COMPOSITIONS OF Al-Li and Al-Li-Ag ALLOYS
(given in weight percent)

Alloy	Li	Ag	Al
I	1.5	0.0	Balance
II	1.5	1.0	Balance
III	3.0	0.0	Balance
IV	3.0	1.0	Balance

TABLE 4

PRECIPITATES EXAMINED UNDER VARYING AGING CONDITIONS AT 225°C

Aging Conditions (Time Aged)	Number of Films Examined	Total Number of Precipitates Analyzed
12 hours aging	6	726
24 hours aging	7	614
36 hours aging	9	1220
36 hours aging, II	5	619
48 hours aging	6	777
48 hours aging, III	8	724
72 hours aging	9	698
96 hours aging	7	697
96 hours aging, II	5	668
144 hours aging	8	879
144 hours aging,II	6	656

TABLE 5

PRECIPITATES EXAMINED UNDER VARYING AGING CONDITIONS AT 200°C

Aging Conditions (Time Aged)	Number of Films Examined	Total Number of Precipitates Analyzed
48 hours aging	5	665
96 hours aging	5	642
1 week aging	4	408
1 week aging, II	5	391
274 hours aging	5	600
2 weeks aging	8	1317
4 weeks aging	8	709
6 weeks aging	10	793
8 weeks aging	8	563

TABLE 6

PRECIPITATES EXAMINED UNDER VARYING AGING CONDITIONS AT 168°C

Aging Conditions (Time Aged)	Number of Films Examined	Total Number of Precipitates Analyzed
1 week aging	3	390
8 days aging	3	392
10 days aging	3	438
2 weeks aging	6	1160
2 weeks aging,II	4	504
3 weeks aging	2	465
4 weeks aging	3	530
5 weeks aging	4	529
6 weeks aging	4	587
7 weeks aging	5	448
8 weeks aging	3	424
9 weeks aging	4	421
10 weeks aging	4	408
11 weeks aging	4	408
12 weeks aging	3	346

TABLE 7

$\bar{R}$ VALUES FOR VARYING NUMBER OF PARTICLES AT 225°C, 36 HOURS AGING

Number of Films	Number of Particles	Average Size (mm)	Average Size (A)	Distribution Width (A)
1	114	15.90	482	126
2	260	5.25	462	126
3	400	15.52	470	129
4	483	5.41	467	128
5	711	15.81	479	120
6	838	15.66	475	122
7	930	15.65	474	124
8	1006	15.59	472	124
TOTAL	1220	15.62	473	124

TABLE 8

$\bar{R}$ VALUES FOR VARYING NUMBER OF PARTICLES AT 200°C, 2 WEEKS AGING

Number of Films	Number of Particles	Average Size (mm)	Average Size (A)	Distribution Width (A)
1	110	17.24	517	134
2	288	17.76	532	141
3	444	17.53	526	144
4	638	17.60	528	147
5	877	17.07	512	146
6	1009	17.71	531	145
7	1132	17.46	524	144
TOTAL	1317	17.52	525	146

TABLE 9

EXPERIMENTAL VALUES DETERMINED FROM FIGURE 17
BASED ON EQUATION 21

T (^{o}C)	K	R_{CO}(A)
168	2.28	53
200	21.52	-115
225	92.33	83
200 IAS	17.64	97

TABLE 10

VALUES DETERMINED FROM FIGURES 18-19
BASED ON EQUATION 23

T (^{o}C)	k	Intercept (A)
168	1.21	18
200	2.80	-10
225	4.35	13
200 IAS	2.51	14

TABLE 11

VALUES OF K FROM PREVIOUS WORKERS (7-8)

T(°C)	Noble & Thompson[3] (cm^3/sec)	Williams & Eddington[3] (cm^3/sec)
220	6.83×10^{-22}	---
200	1.25×10^{-22}	5.62×10^{-22}
170	---	8.91×10^{-24}

TABLE 12

VALUES OF D FROM PREVIOUS WORKERS (7-8)

T(°C)	Noble & Thompson[2] (cm^2/sec)	Williams & Eddington[2] (cm^2/sec)
220	9.52×10^{-15}	---
200	2.32×10^{-15}	7.24×10^{-15}
170	---	1.05×10^{-15}

TABLE 13

VARIOUS INTERFACIAL FREE ENERGY VALUES (32)

System	Interface Type	Misfit %	Energy Jm^{-2}
Ni-Si	Coherent	0.3	0.011
Ni-Al	Coherent	0.5	0.014
Ni-Ti	Coherent	0.9	0.021
Cu-Co	Coherent	1.8	0.20
Cu-Co	Coherent	1.8	0.23
Cu-Co	Coherent	1.8	0.18
Cu-Zn-Sn (β/γ)	Coherent	0.4	0.06-0.12
Cu-Zn (β/γ)		0.1	0.13
Cu-Zn (α/β)	Incoherent		0.5
Cu-Zn (α/β)	Incoherent		0.42
α-Fe-Fe_3C	Incoherent		0.74
α-Fe-γFe	Incoherent		0.56
α-Fe-Cu(fcc)	Incoherent		0.50
α-Fe-Cu(fcc) $\langle 111\rangle_\alpha \| \| \langle 110\rangle_{Cu}$	Coherent	3.0	0.125
Ni-ThO_2	Incoherent		1.5
Al-Zn $(111)_{Al} \| \| (0001)_{Zn}$	Coherent		0.07
Cd-Zn (both cph)	Coherent		0.11
Al-Al_2Cu	Coherent		0.34 0.09-0.11
Ag-Pb (both fcc)	Coherent		0.09-0.11 0.11-0.19

TABLE 14

CALCULATED DIFFUSIVITY VALUES BASED ON EQUATION 22

T	D(cm^2/sec)
168°	3.44×10^{-16}
200°	2.77×10^{-15}
225°	1.24×10^{-14}
200 IAS	2.05×10^{-15}

FIGURES

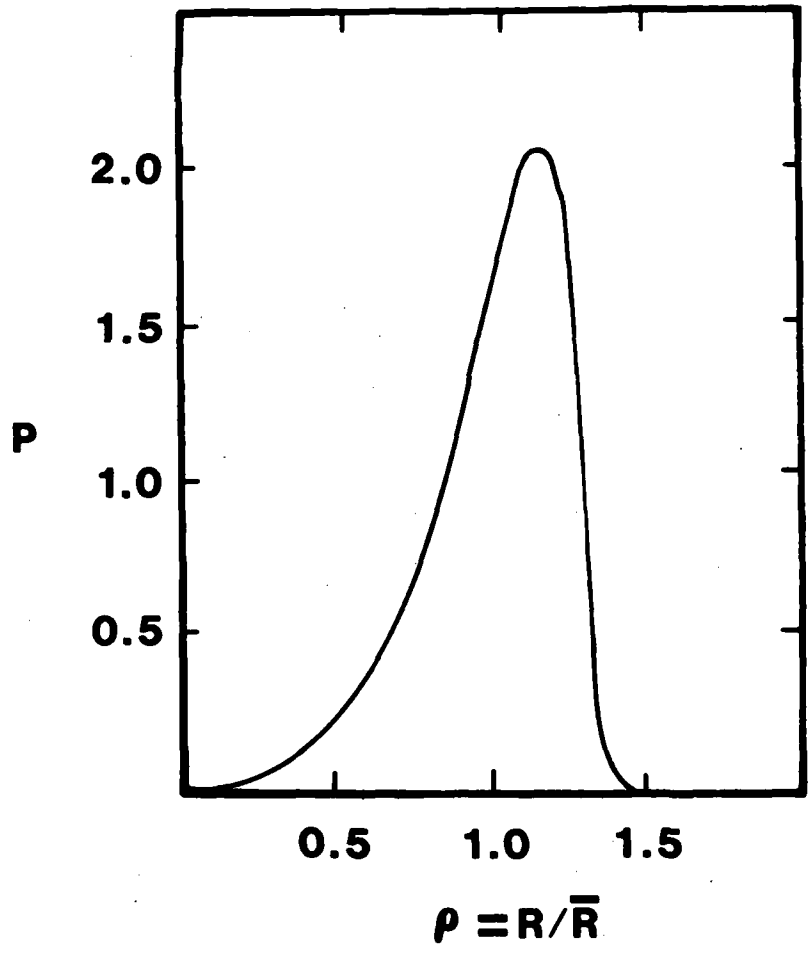

Figure 1. Theoretical particle size distribution function (PSD) based on the LSW theory, from (23).

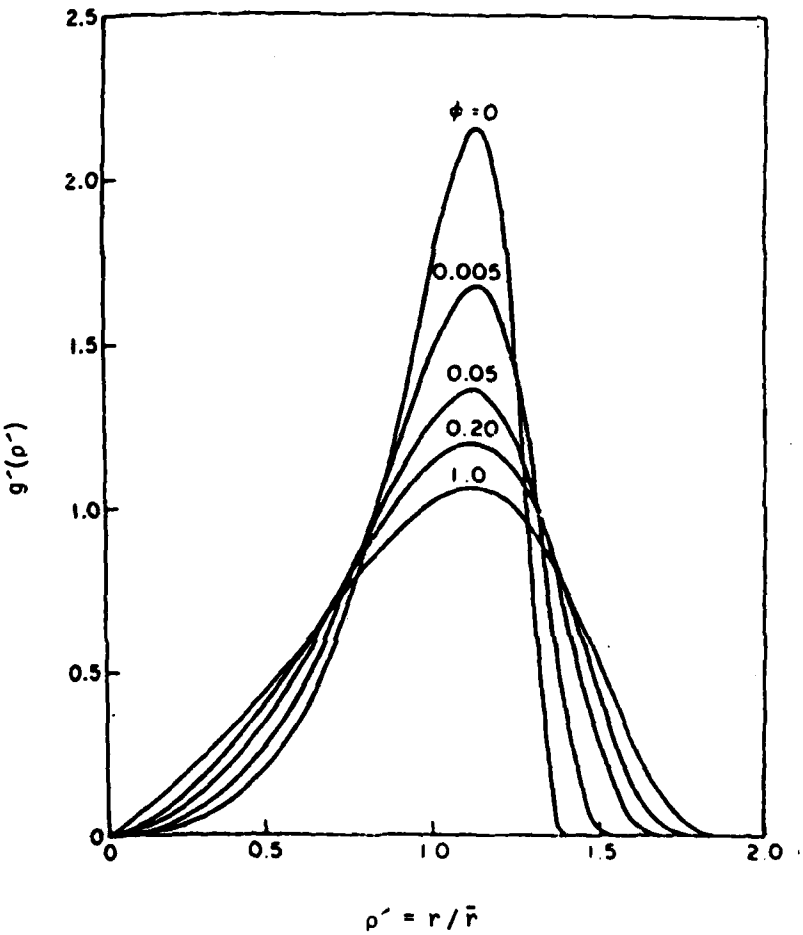

Figure 2. Theoretical PSD based on the MLSW theory with varying volume fraction of precipitate, from (28).

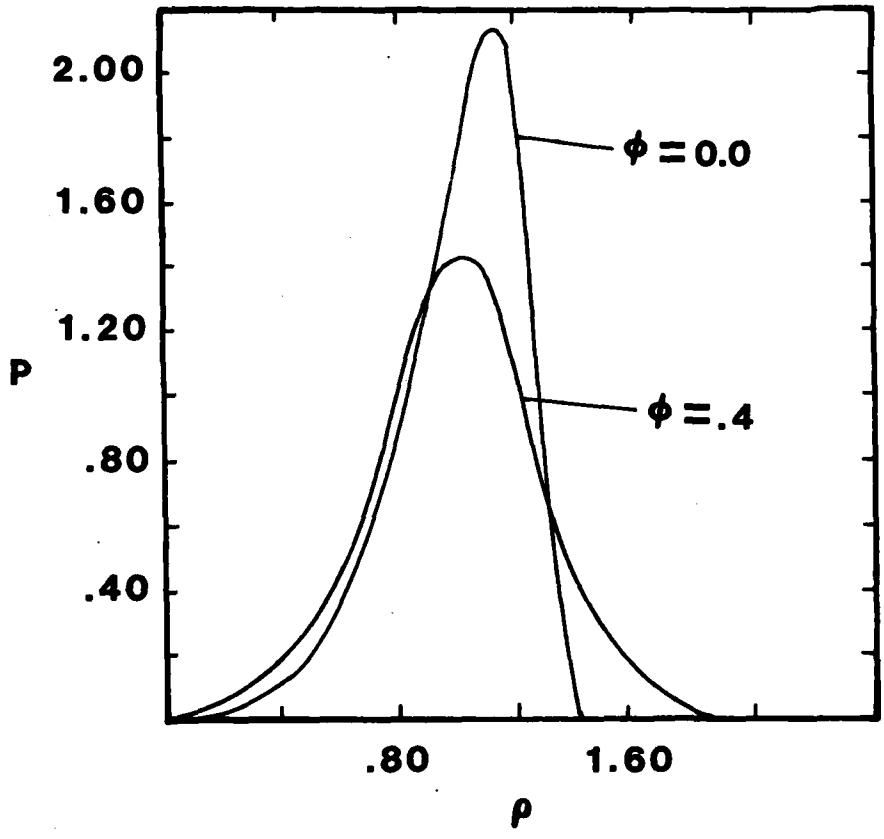

Figure 3. Theoretical PSD based on the LSEM theory with varying volume fraction of precipitate, from (30).

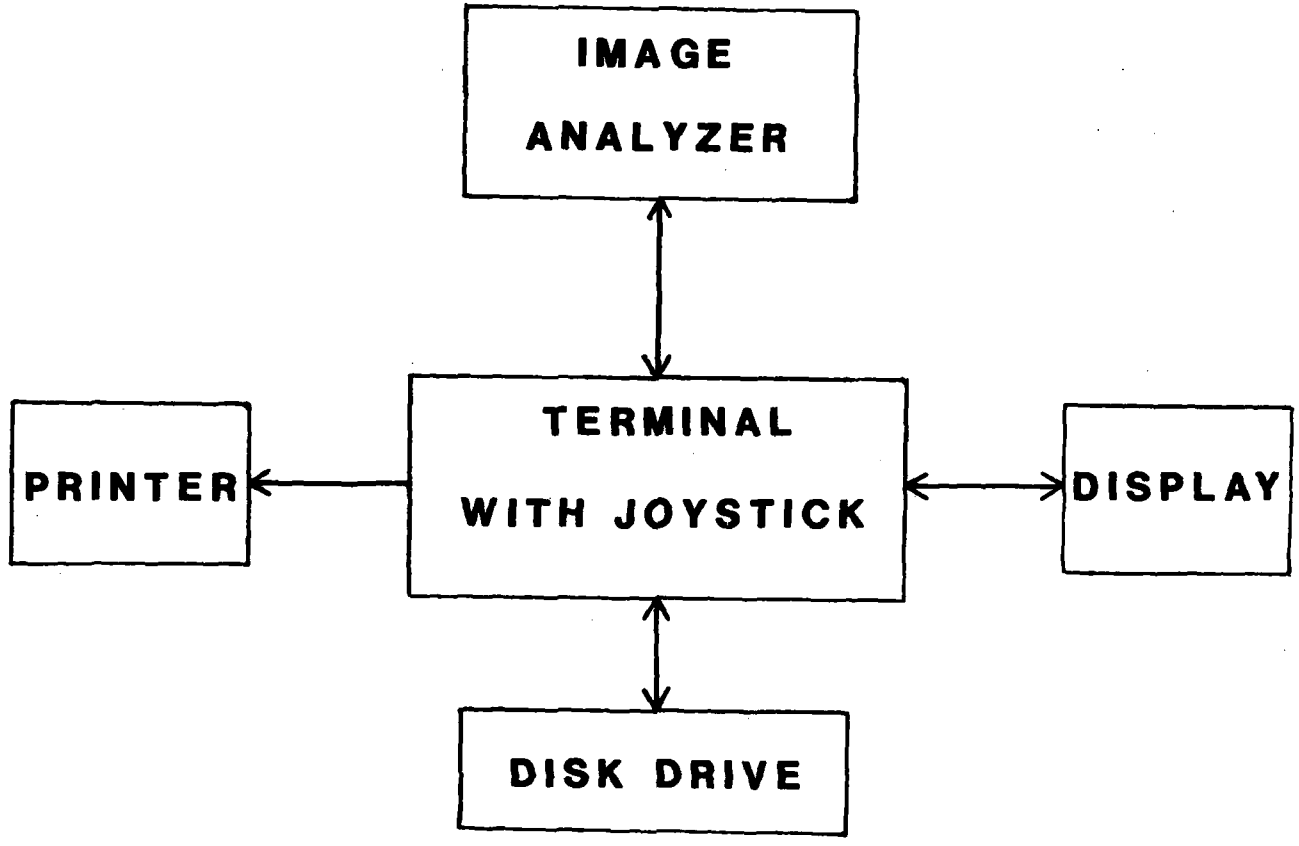

Figure 4. Schematic drawing of the Image Analyzing System (IAS).

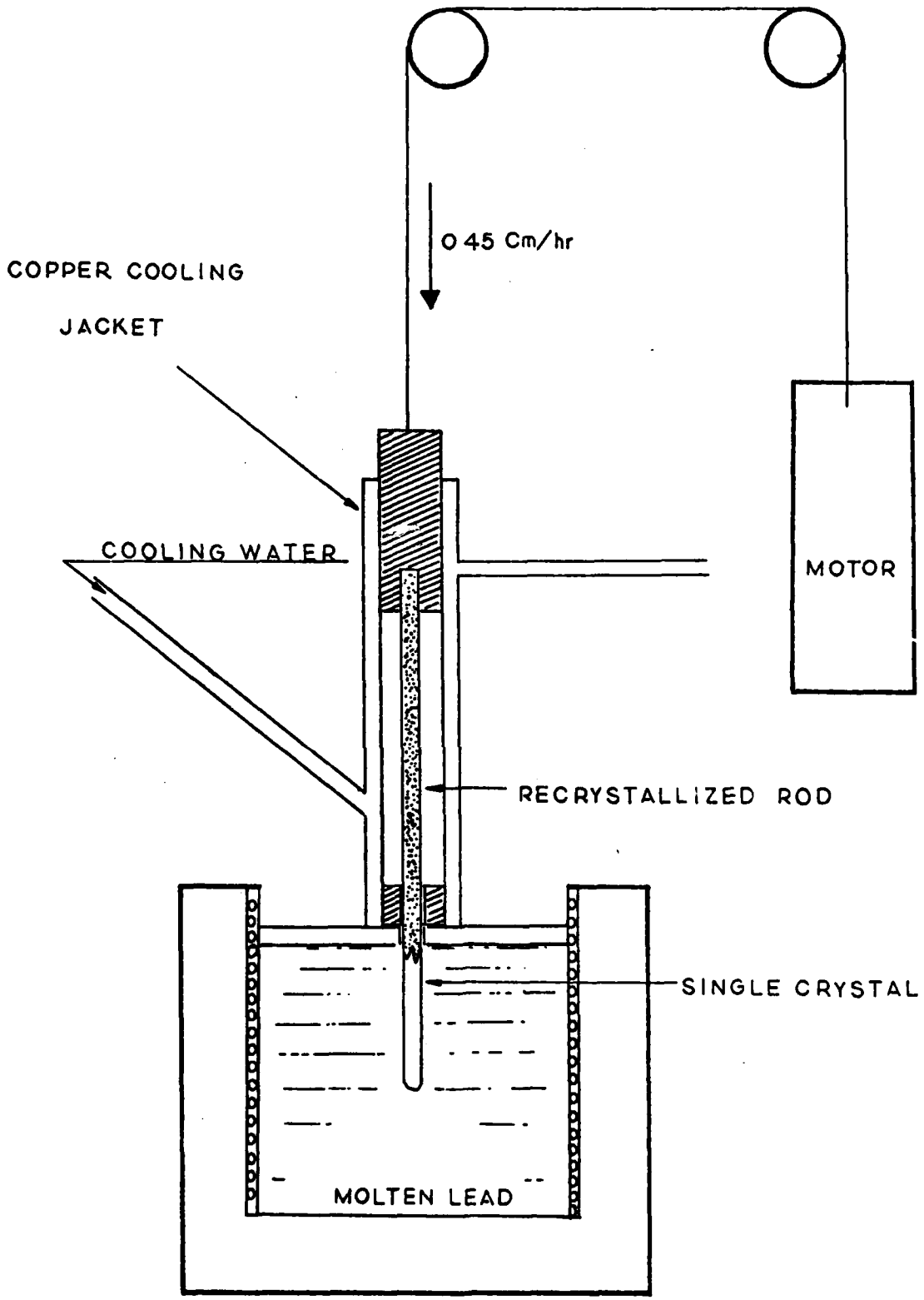

FIGURE 5. Schematic drawing of the temperature gradient furnace.

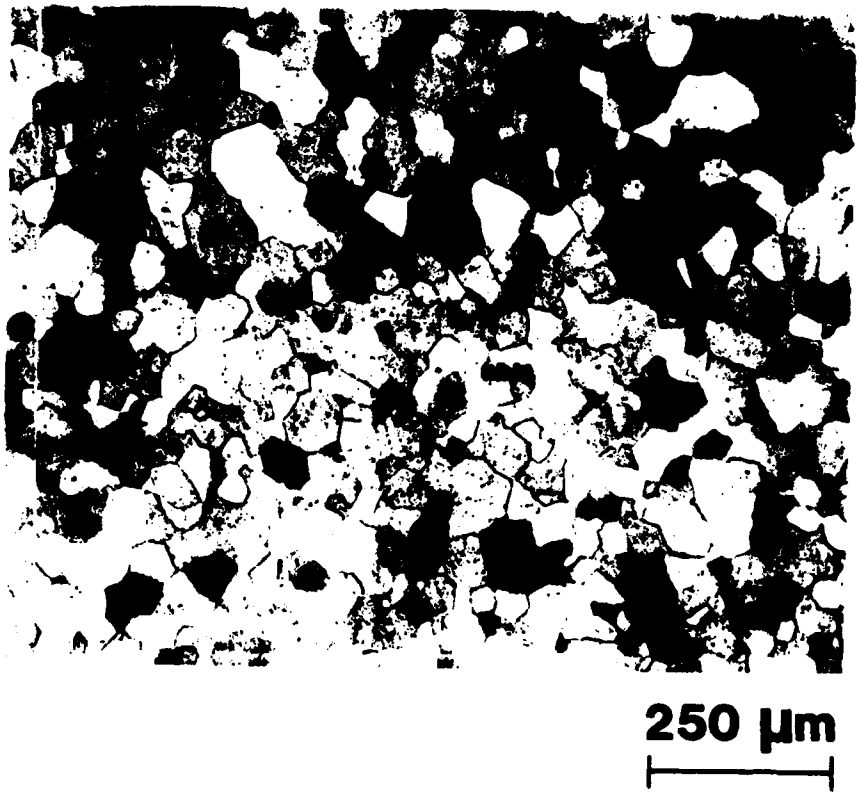

Figure 6. Grain structure of Al-Li alloy after recrystallization treatment.

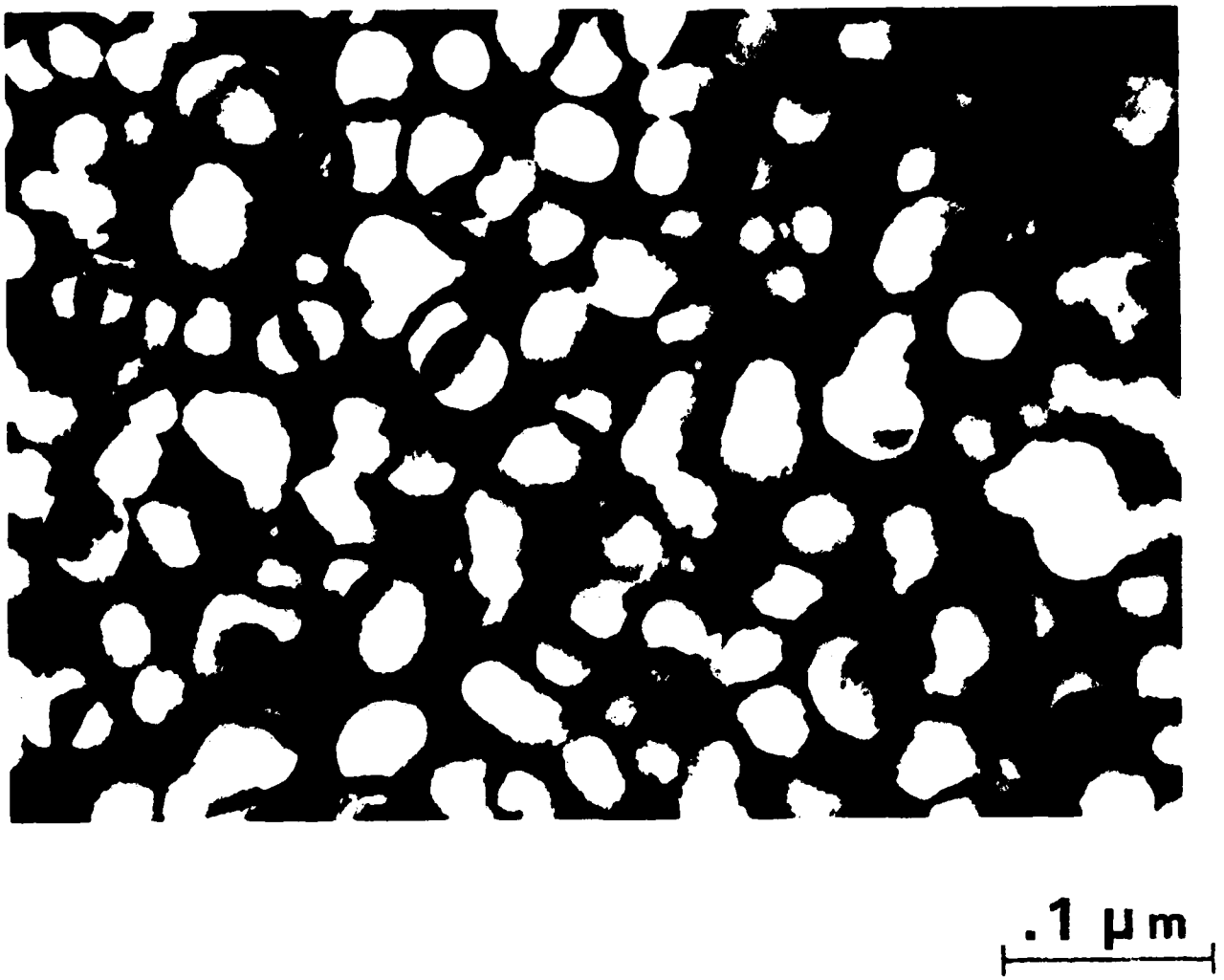

Figure 7. δ′ precipitates aged 48 hours at 200°C.

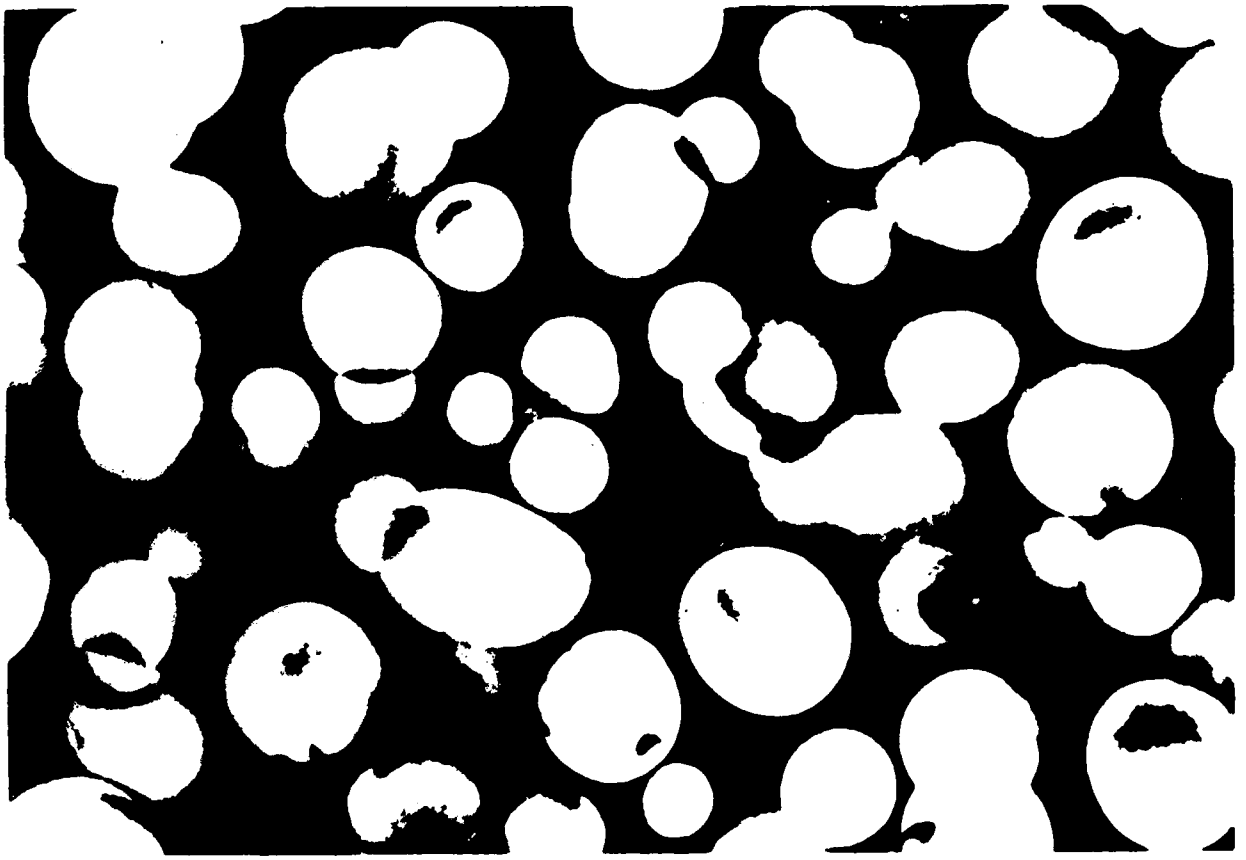

Figure 8. δ′ precipitates aged 8 weeks at 200°C.

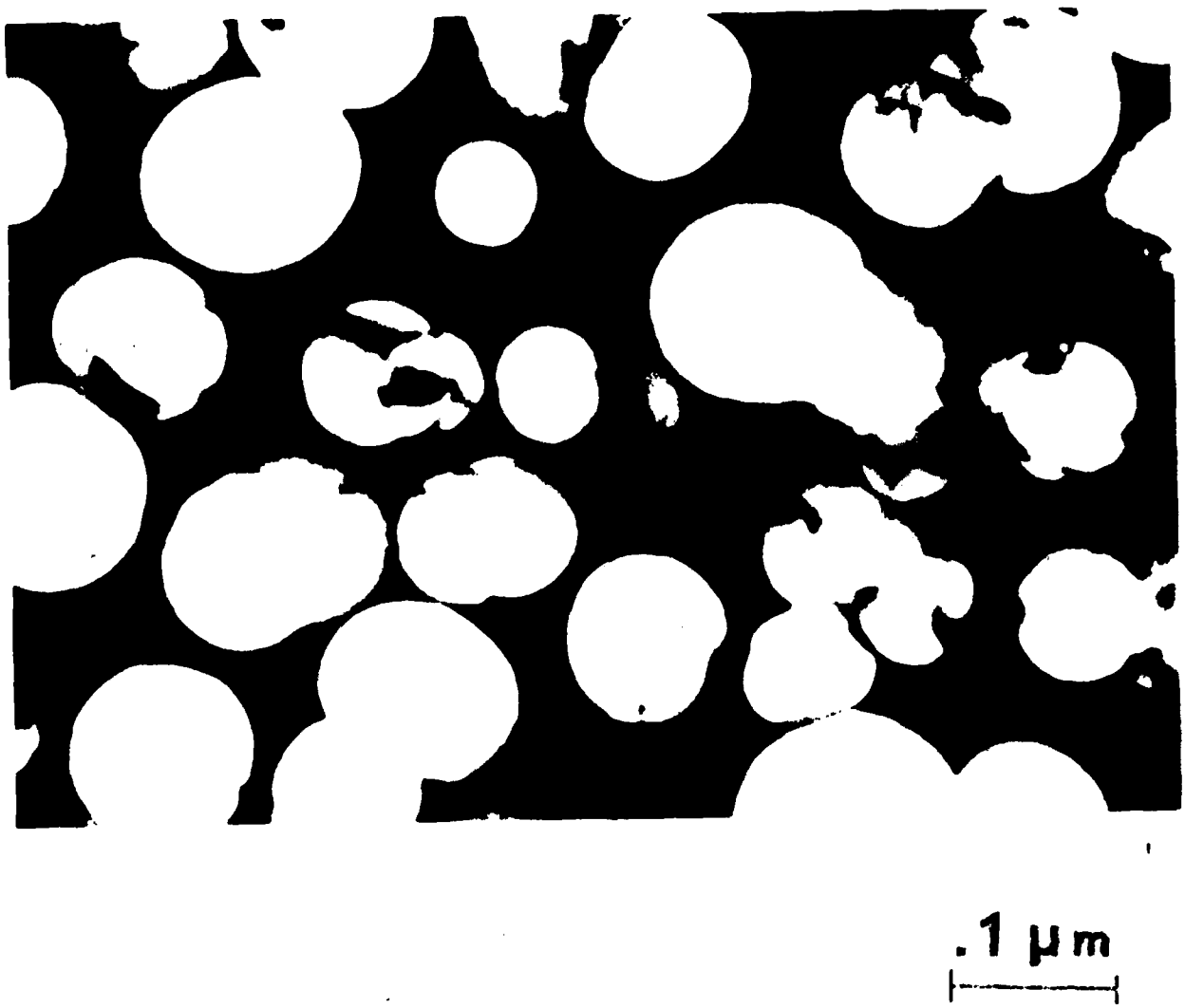

Figure 9. δ′ precipitates aged 8 weeks at 200°C.

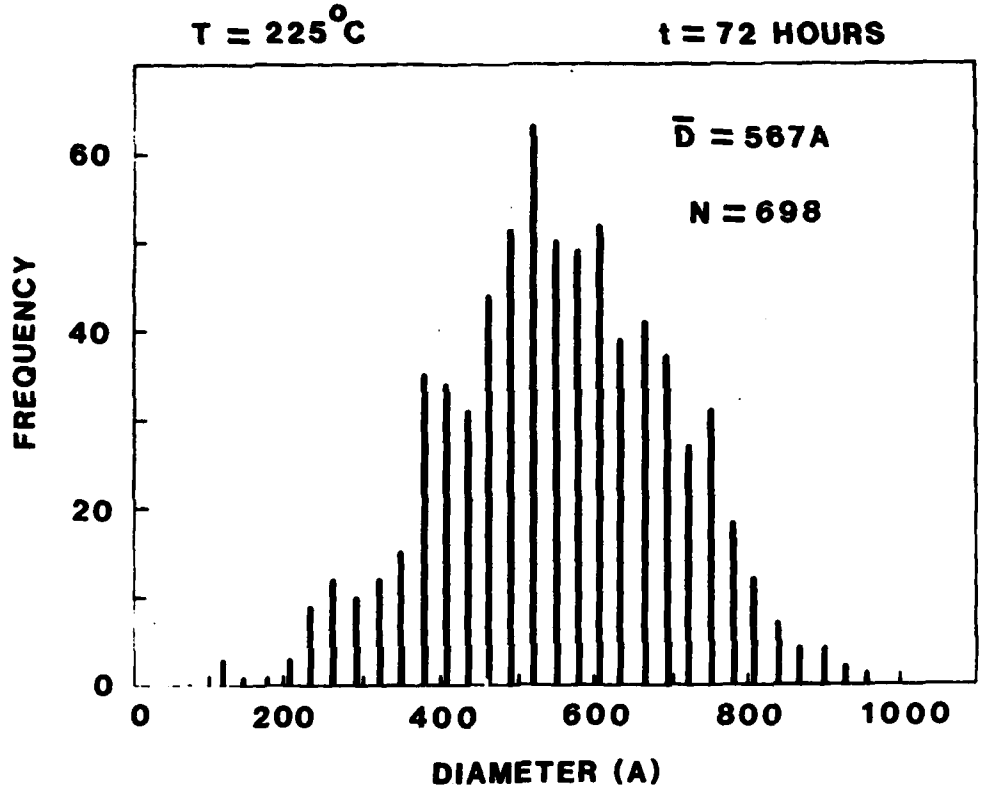

Figure 10. Particle size distribution function of δ′ precipitates.

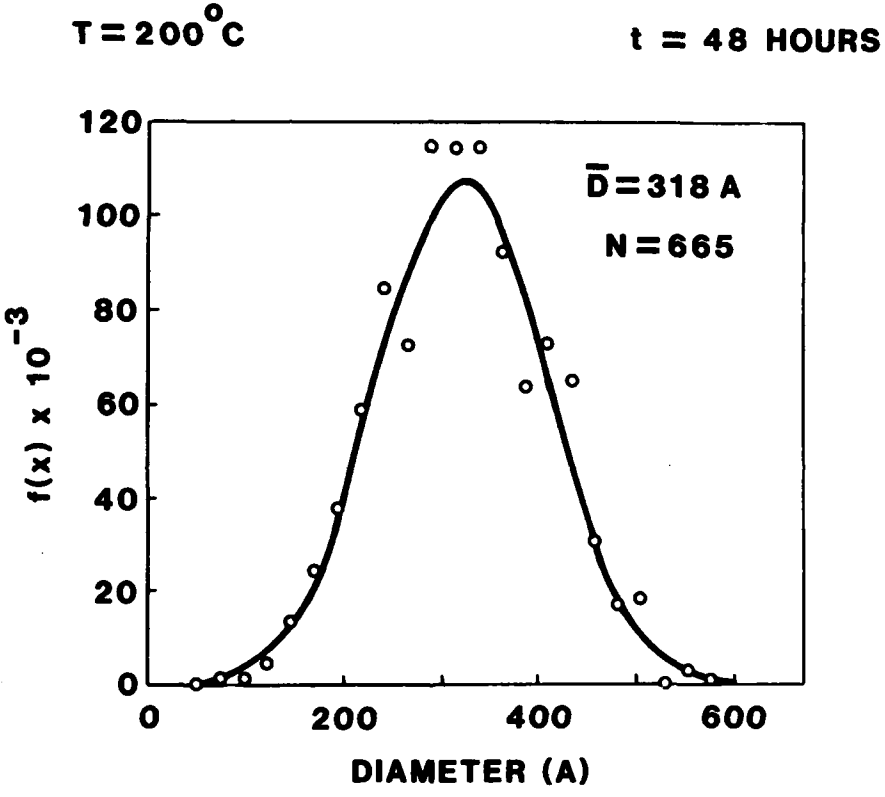

Figure 11. PSD with generated normal curve.

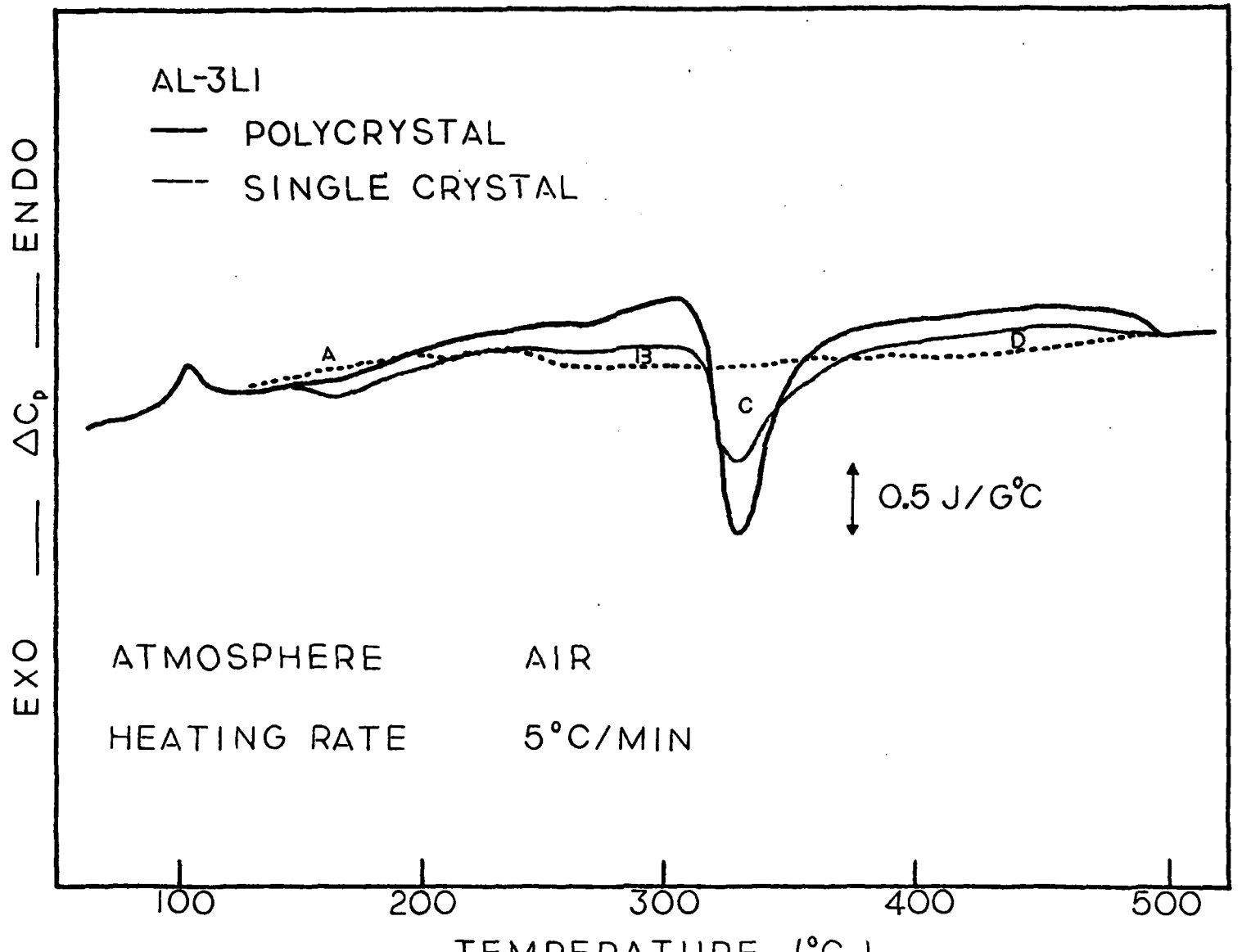

FIGURE 12. Specific heat versus temperature curves for the polycrystal and the single crystal of Al-3%Li.

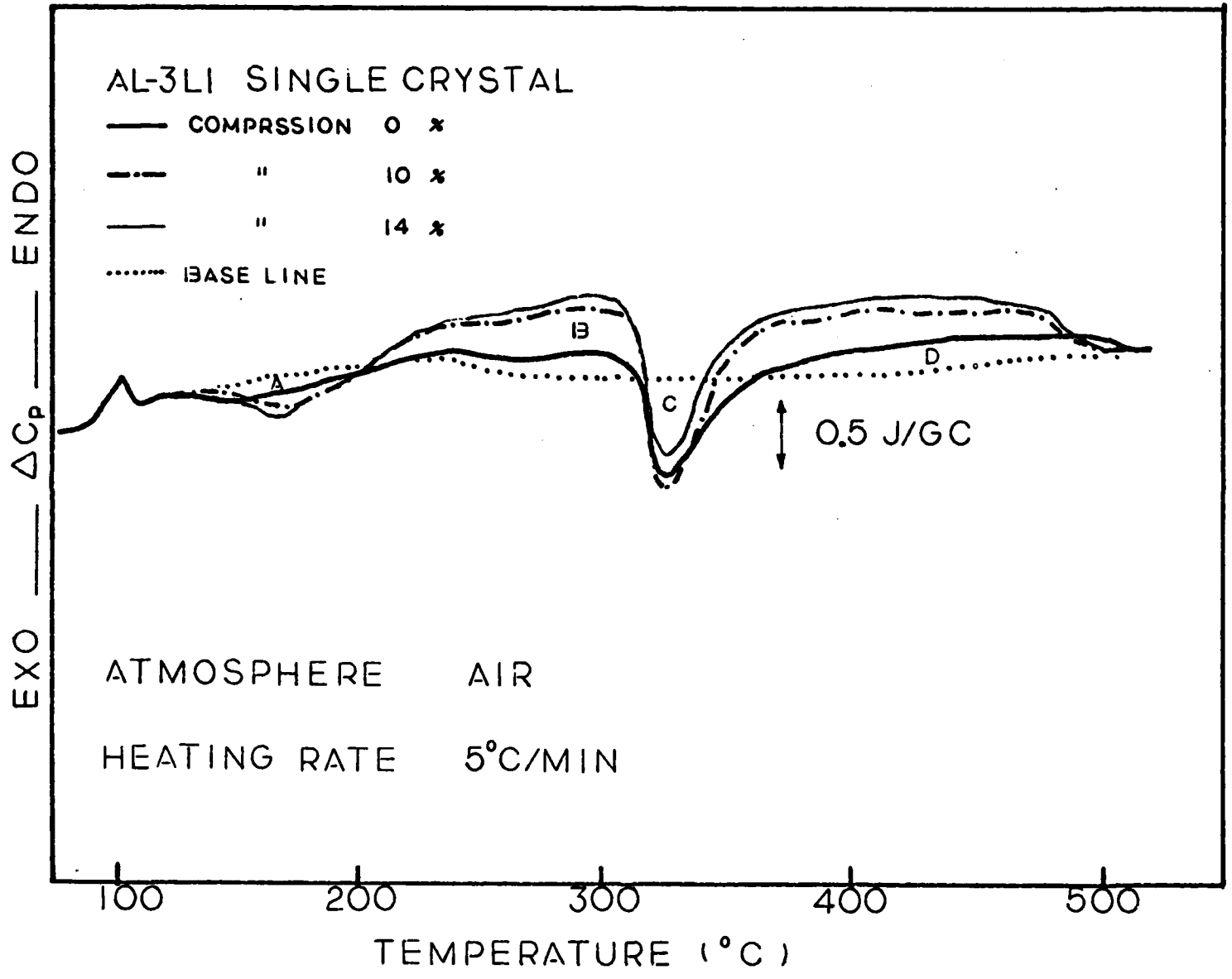

FIGURE 13. A series of specific heat versus temperature curves for the single crystals of Al-3%Li at the various amounts of compression.

AD-A134 836 PRECIPITATION MECHANISMS IN ALUMINUM-LITHIUM ALLOYS(U) 2/3
PURDUE UNIV LAFAYETTE IND DEPT OF MATERIALS ENGINEERING
T H SANDERS SEP 83 0303-53-1289 N00019-81-C-0471
UNCLASSIFIED F/G 11/6 NL

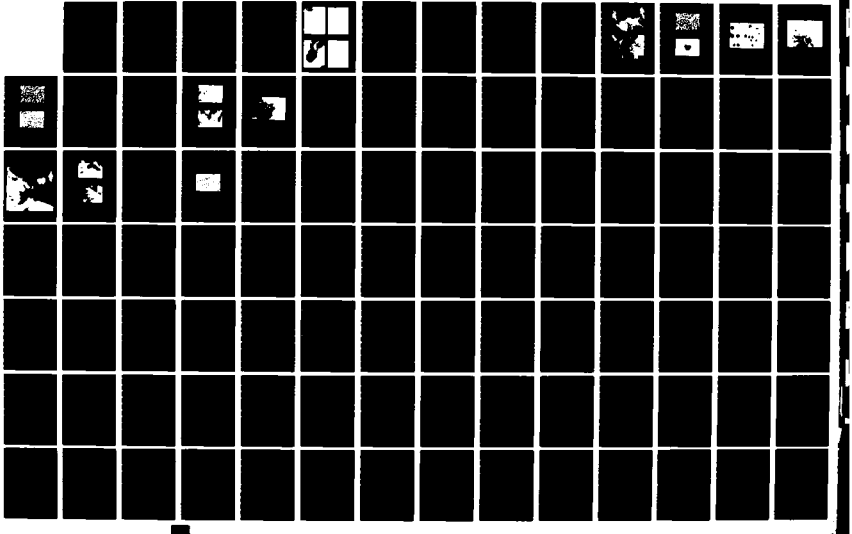

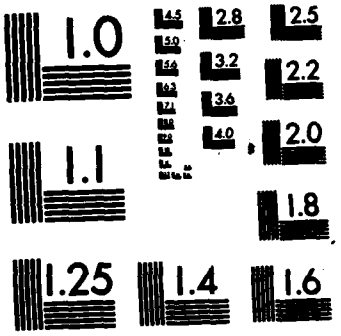

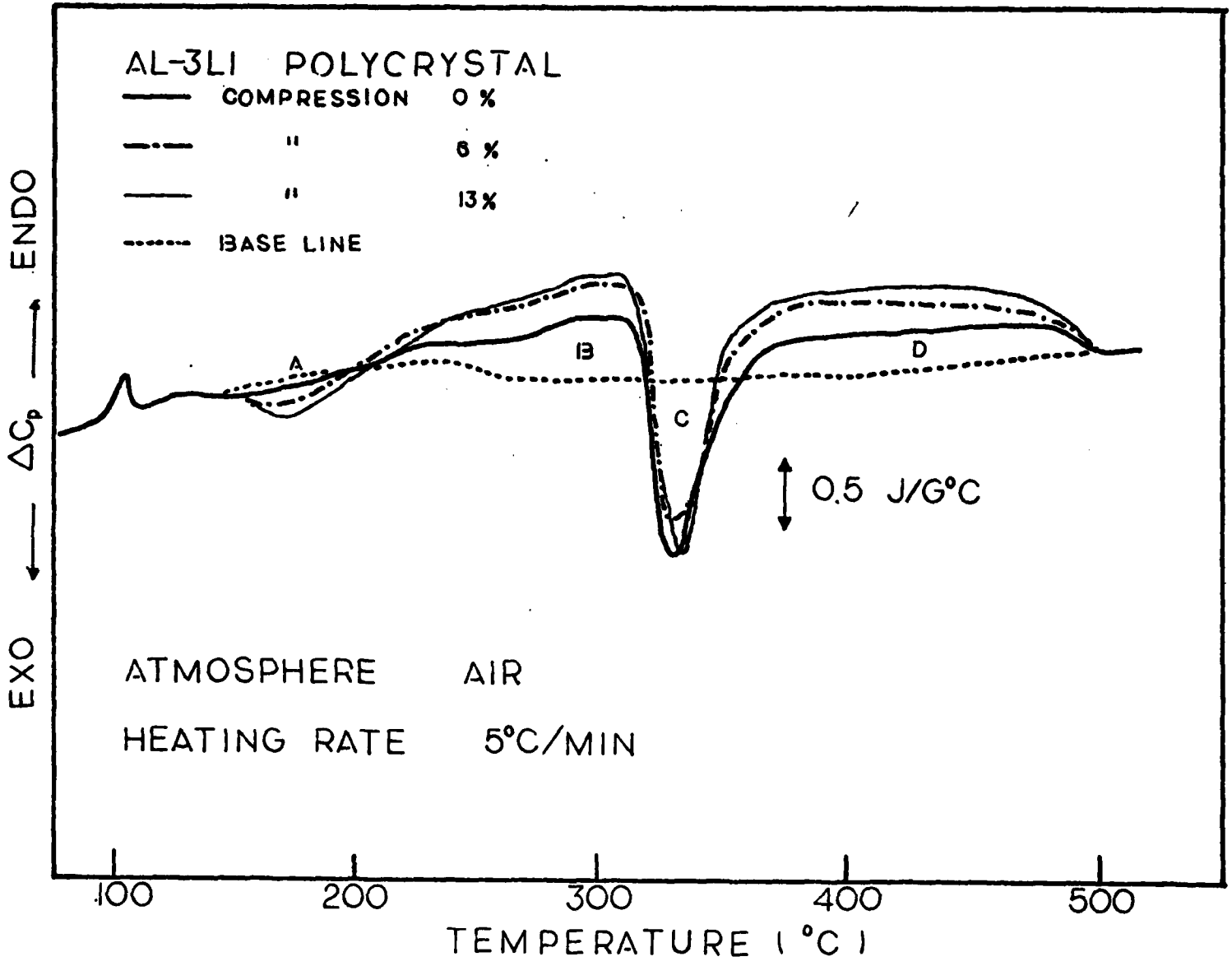

FIGURE 14. A series of specific heat versus temperature curves for the polycrystals of Al-3%Li at the various amounts of compression.

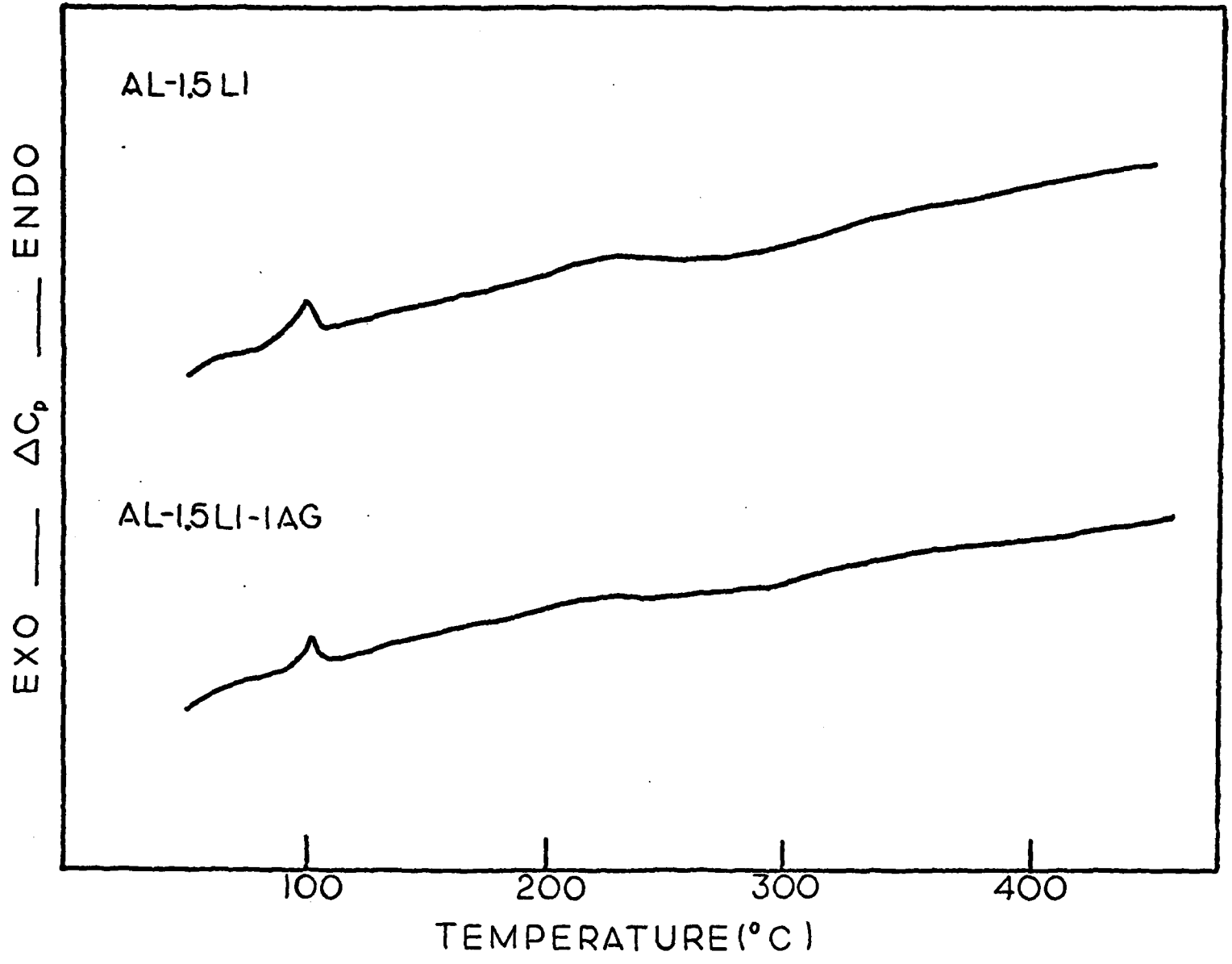

FIGURE 15. Specific heat versus temperature curves for the as-quenched alloys: (a) Al-1.5%Li, and (b) Al-1.5%Li-1%Ag.

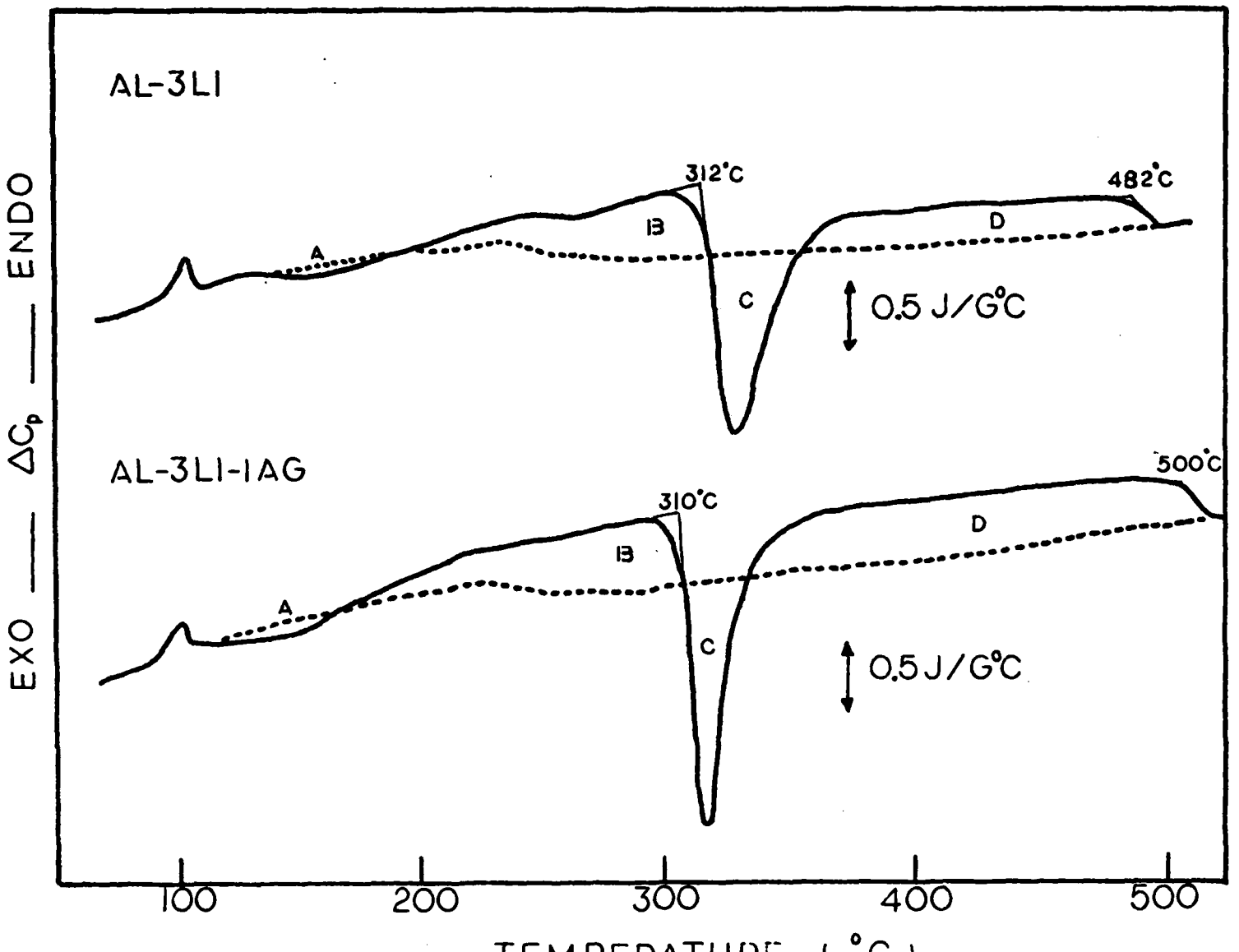

FIGURE 16. Specific heat versus temperature curves for the as-quenched alloys: (a) Al-3%Li, and (b) Al-3%Li-1%Ag.

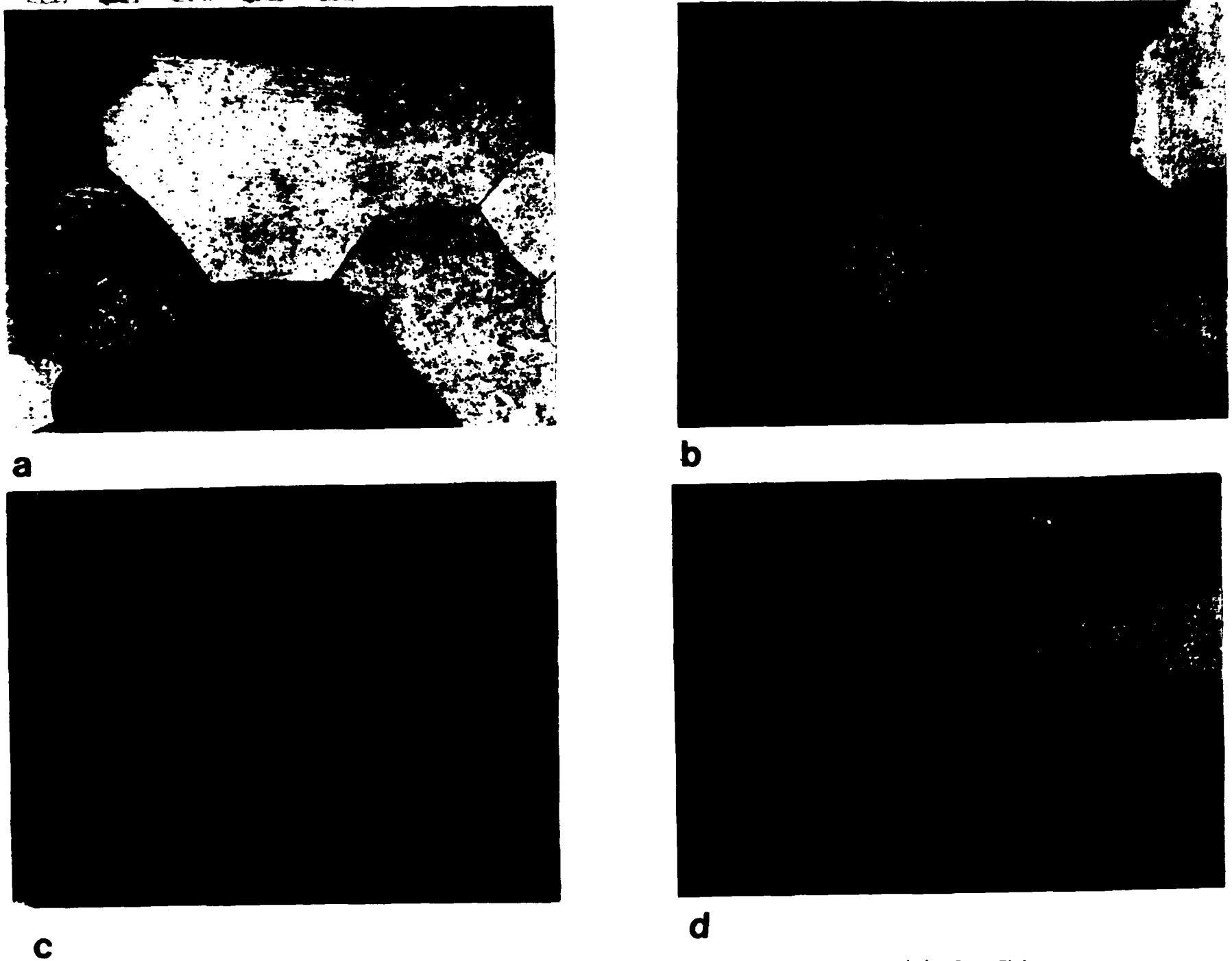

Figure 17. Longitudinal sections showing the coarse recrystallized grains in (a) Al-1.5Li, (b) Al-1.5Li-1.0Ag, (c) Al-3.0Li, and (d) Al-3.0Li-1.0Ag.

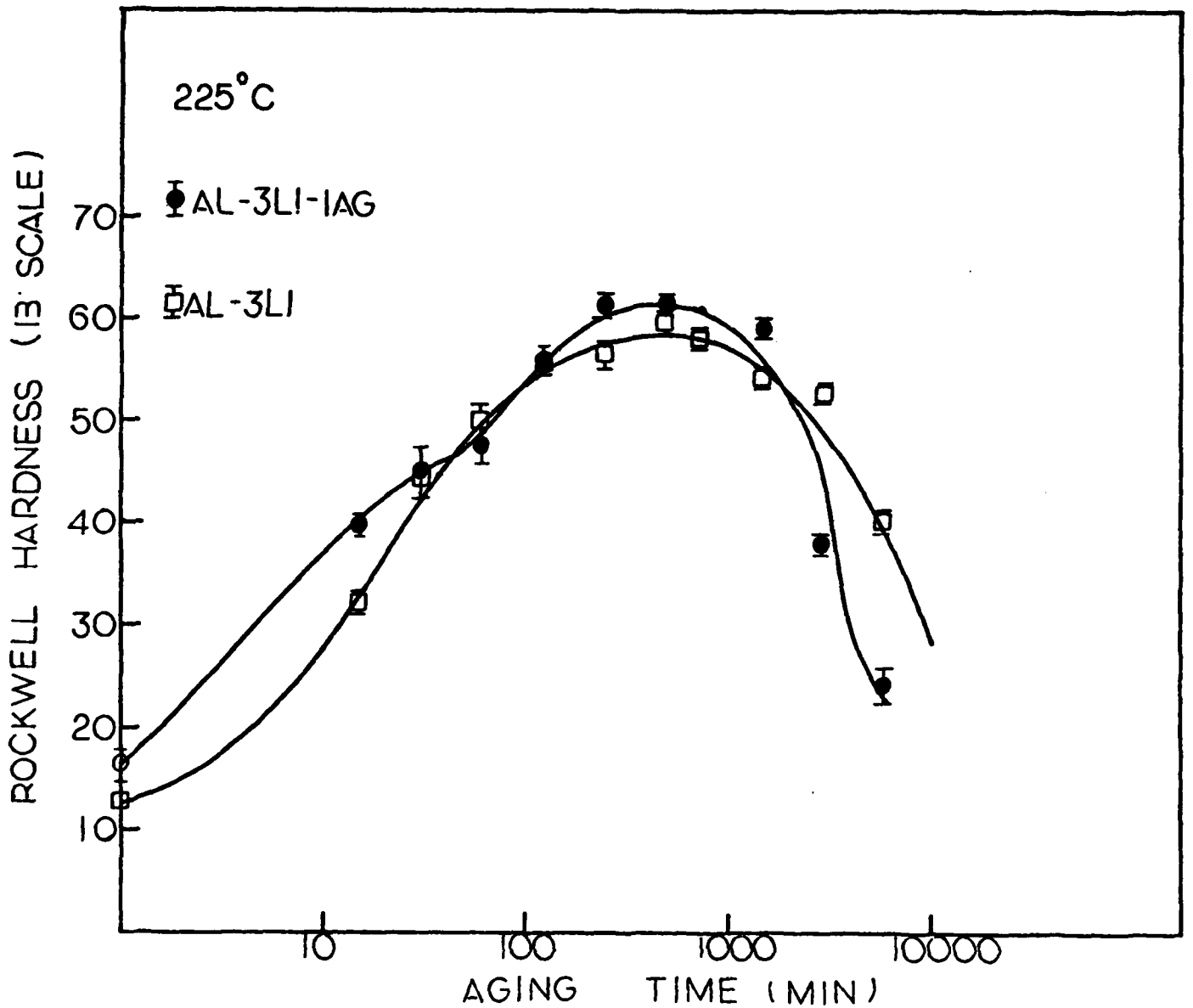

FIGURE 18. Hardness/aging-time curve for an Al-3%Li-1%Ag and an Al-3%Li, aged at 225°C.

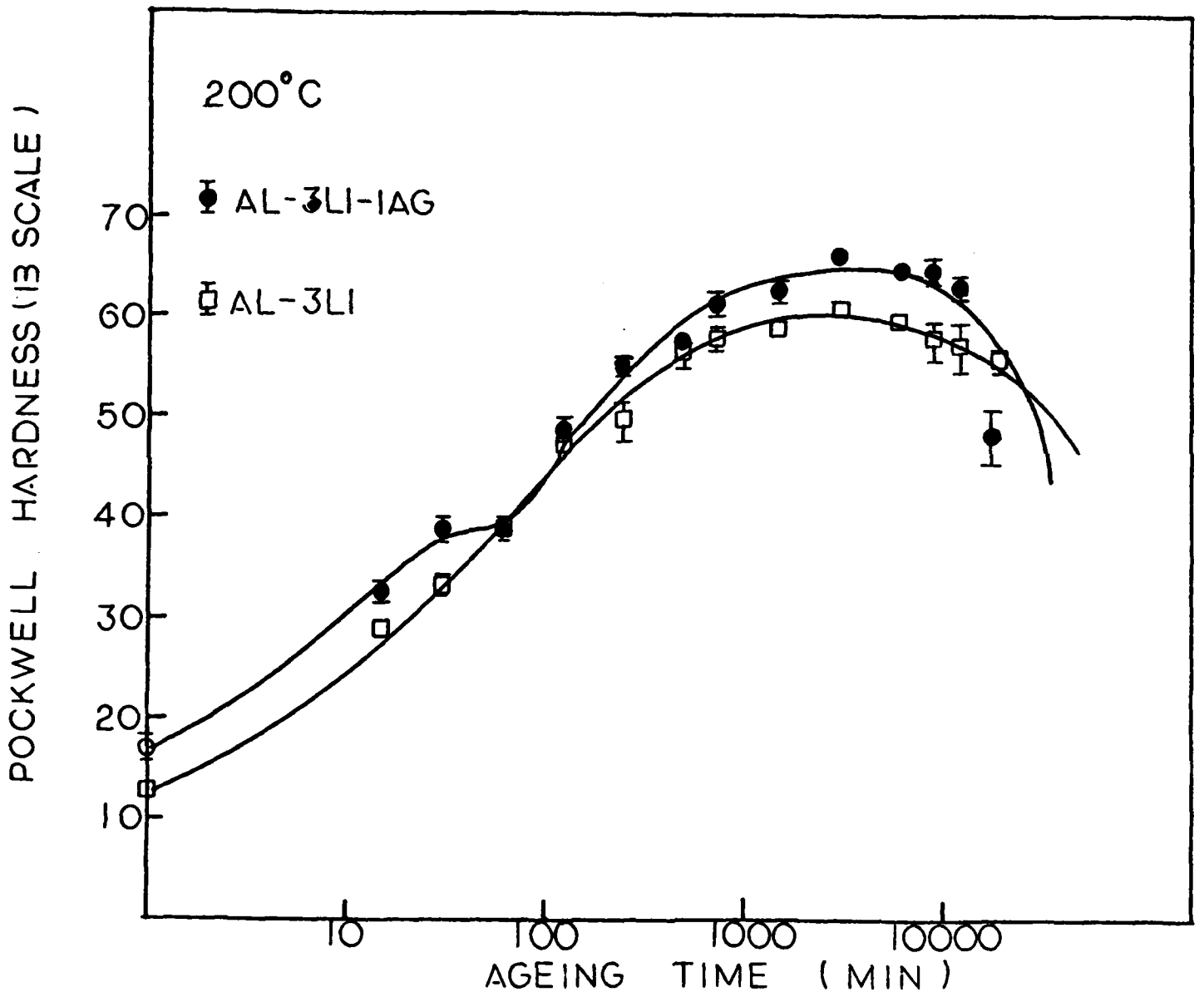

FIGURE 19. Hardness/aging-time curve for an Al-3%Li-1%Ag and an Al-3%Li, aged at 200°C.

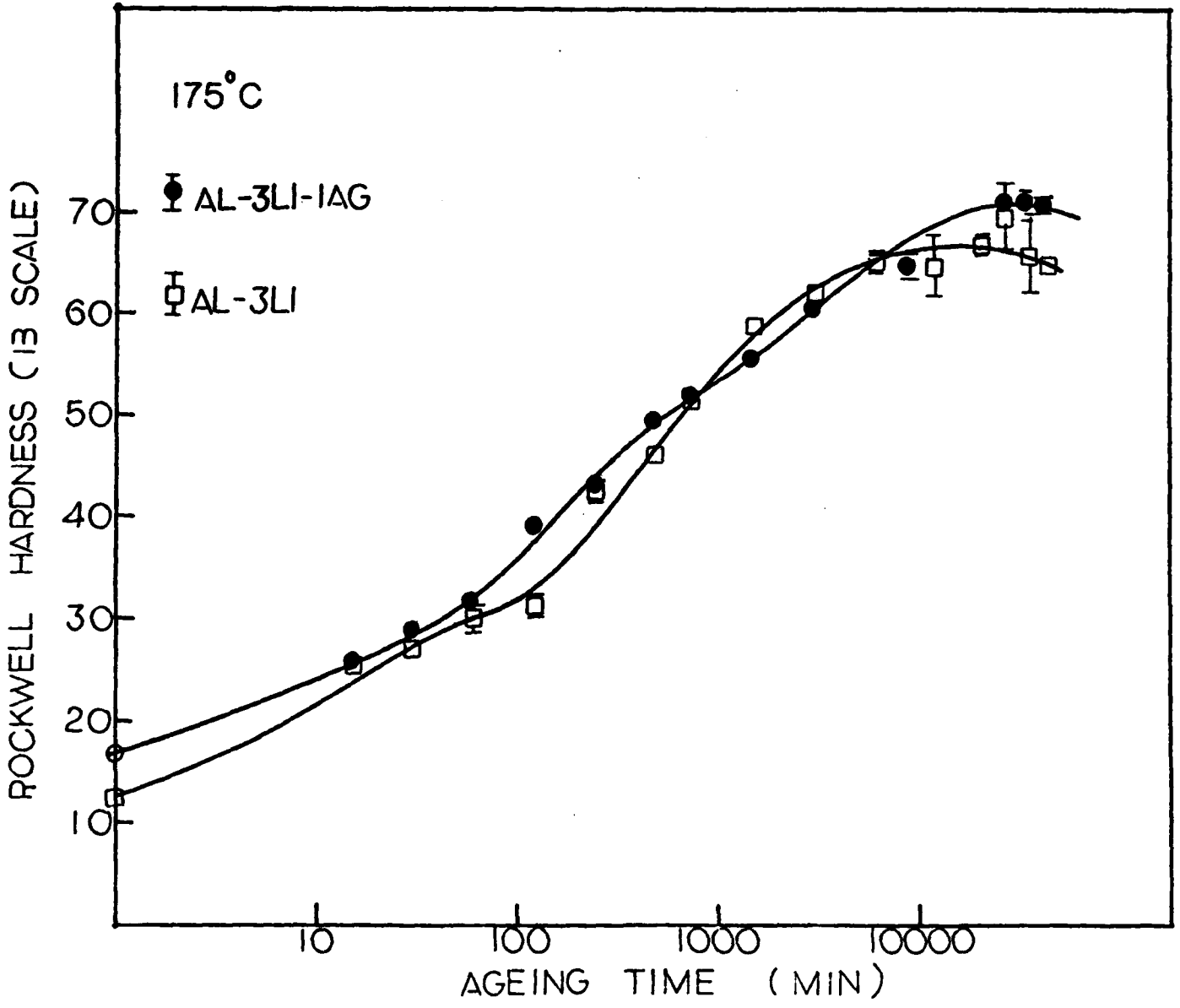

FIGURE 20. Hardness/aging-time curve for an Al-3%Li-1%Ag and on Al-3%Li, aged at 175°C.

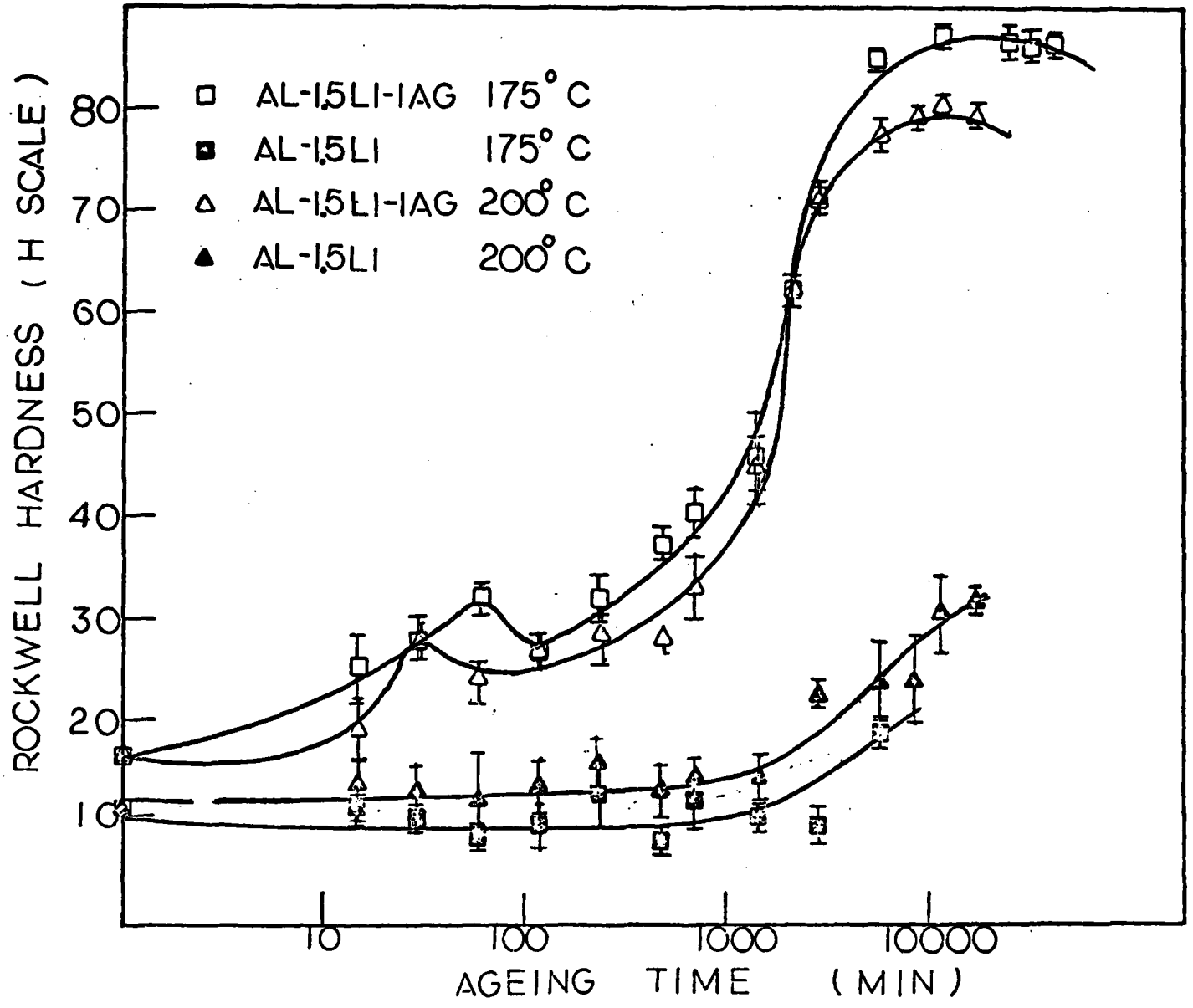

FIGURE 21. Hardness/aging-time curve for an Al-1.5%Li-1%Ag and an Al-1.5%Li, aged at 200°C and 175°C.

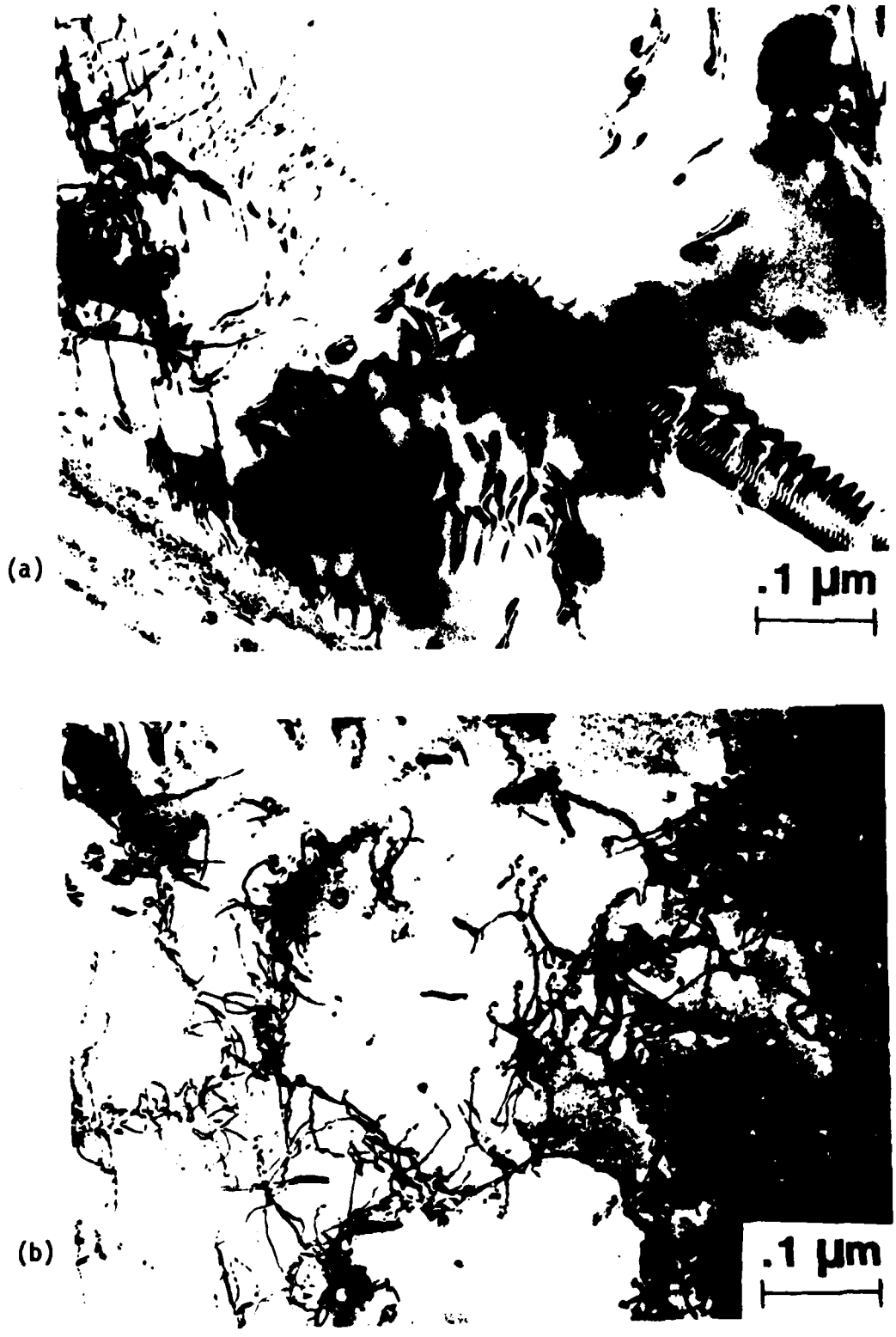

FIGURE 22. Microstructures of as-quenched samples: (a) Al-3%Li-1%Ag showing the presence of superdislocations, and (b) Al-1.5%Li-1%Ag showing the absence of superdislocations.

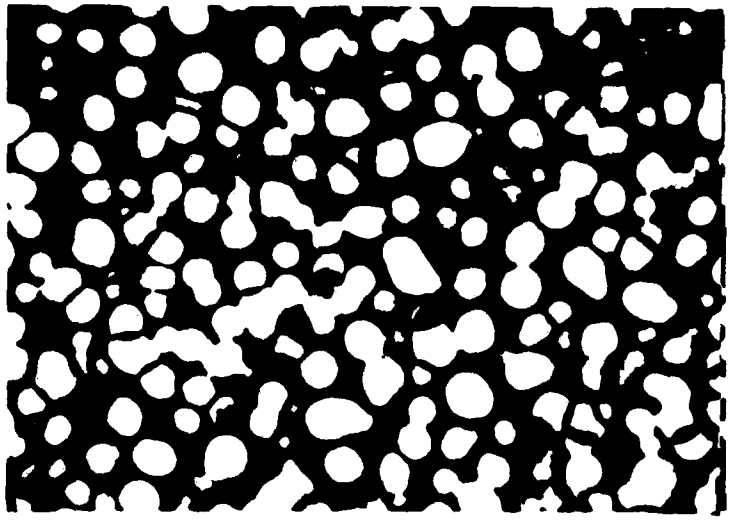

(a)

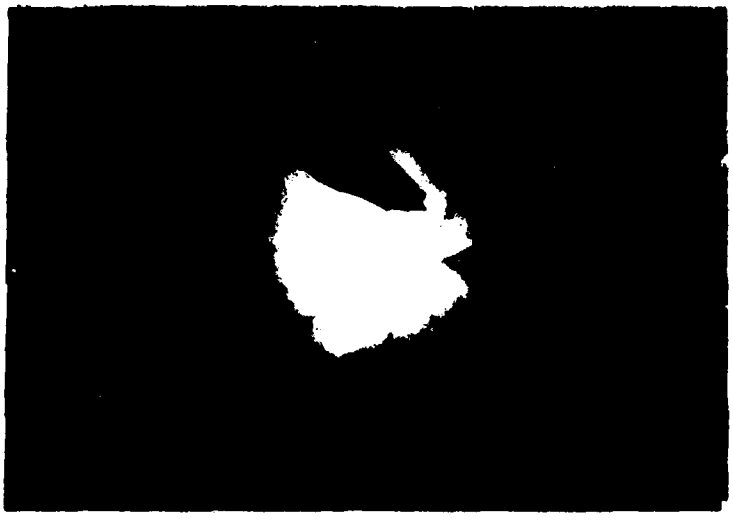

(b)

FIGURE 23. (a) Central Dark Field micrograph showing the spherical δ′ precipitates in the Al-3%Li-1%Ag aged 96 hours at 175°C, X150,000 (b) corresponding Selected Area Diffraction patterns center spot is a {110} δ′ superlattice reflection.

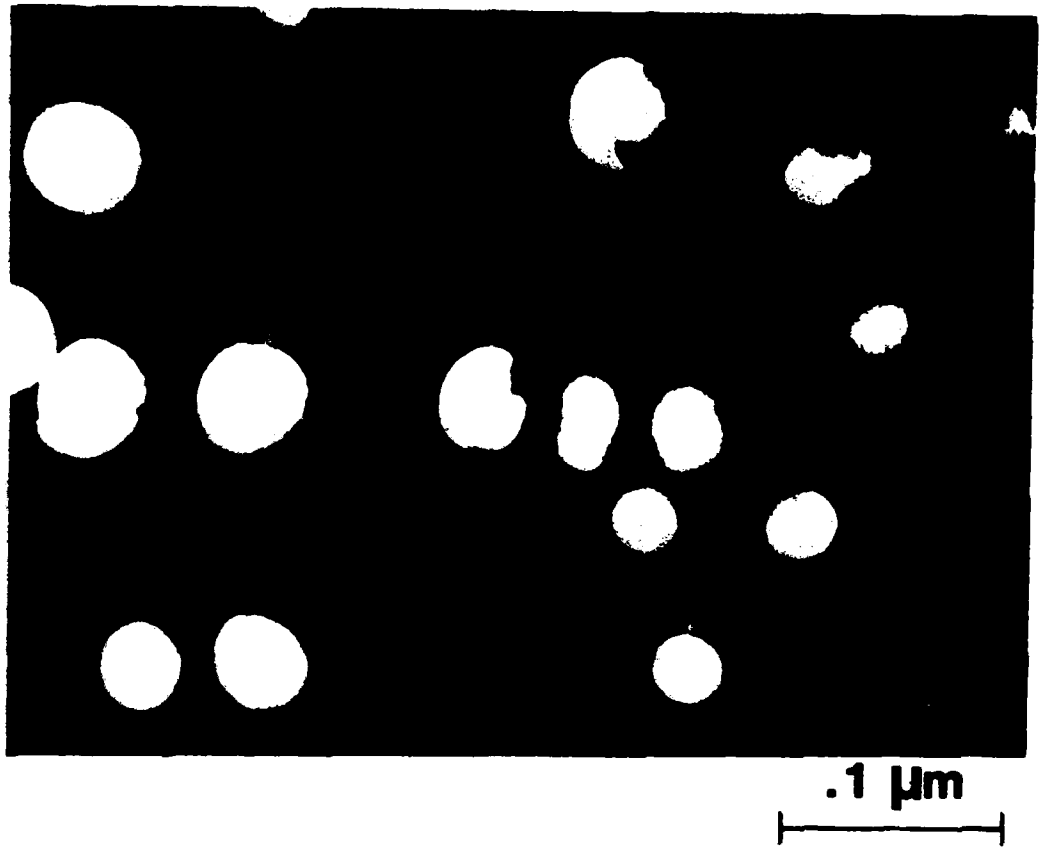

FIGURE 24. Central Dark Field micrograph showing the spherical δ′ precipitates in the Al-1.5%Li-1%Ag aged 96 hours at 175°C.

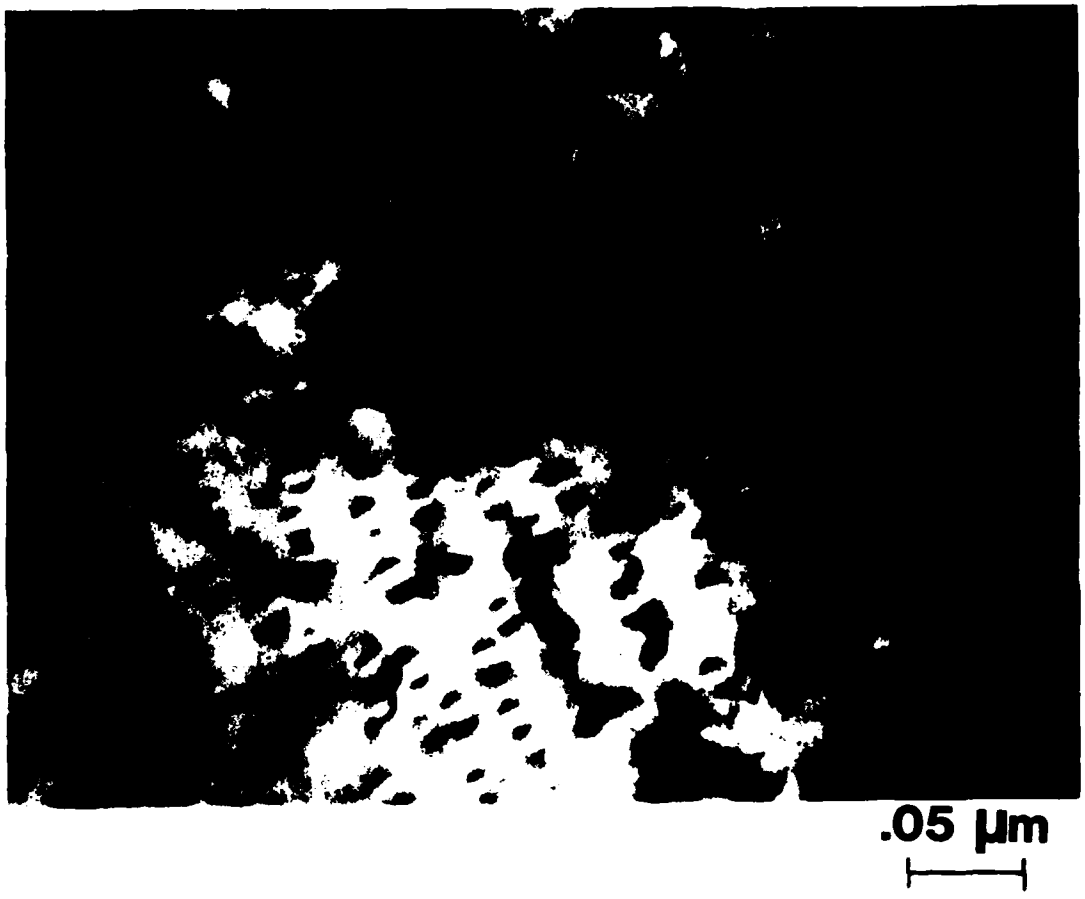

FIGURE 25. Ashby-Brown contrast (34) indicating the spherically symmetrical strain of δ´ precipitates.

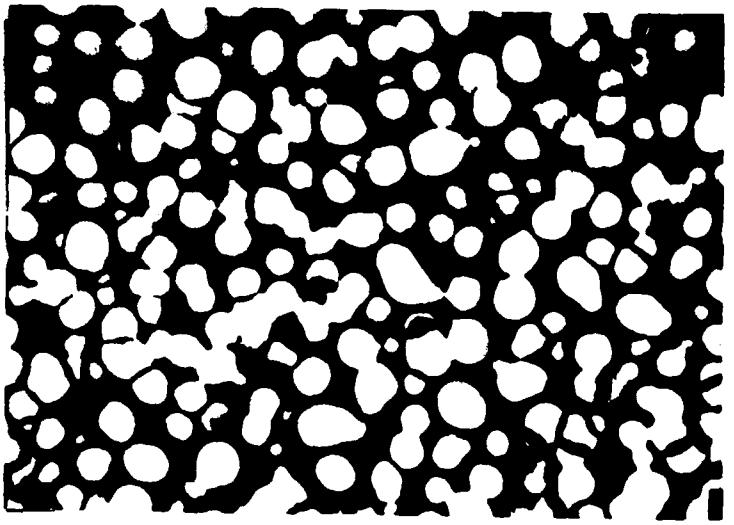

(a)

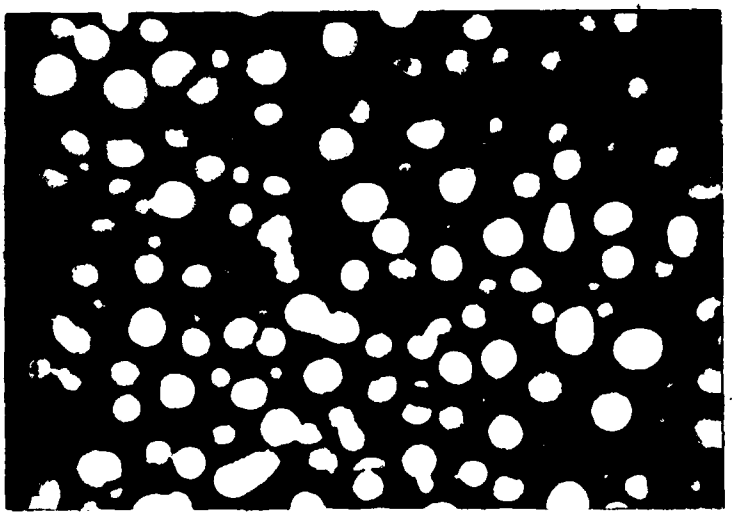

(b)

FIGURE 26. A comparison of the size distribution of δ′ after aged 96 hours at 175°C for (a) Al-3%Li-1%Ag, and (b) Al-3%Li.

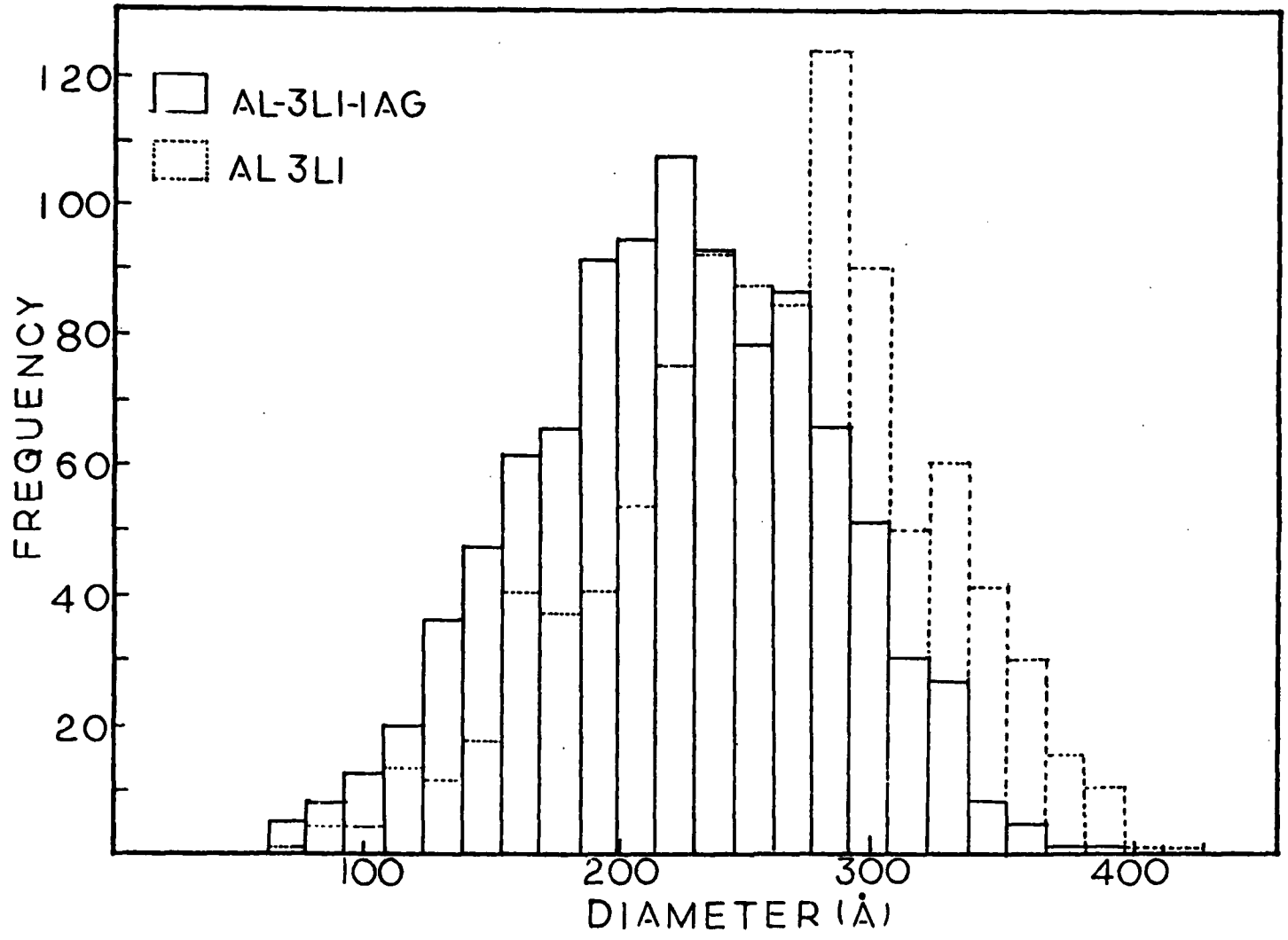

FIGURE 27. Size distribution of δ′ precipitates after aged 96 hours at 175°C. Mean particle size is 261A for Al-3%Li and 221A for Al-3%Li-1%Ag.

(a)

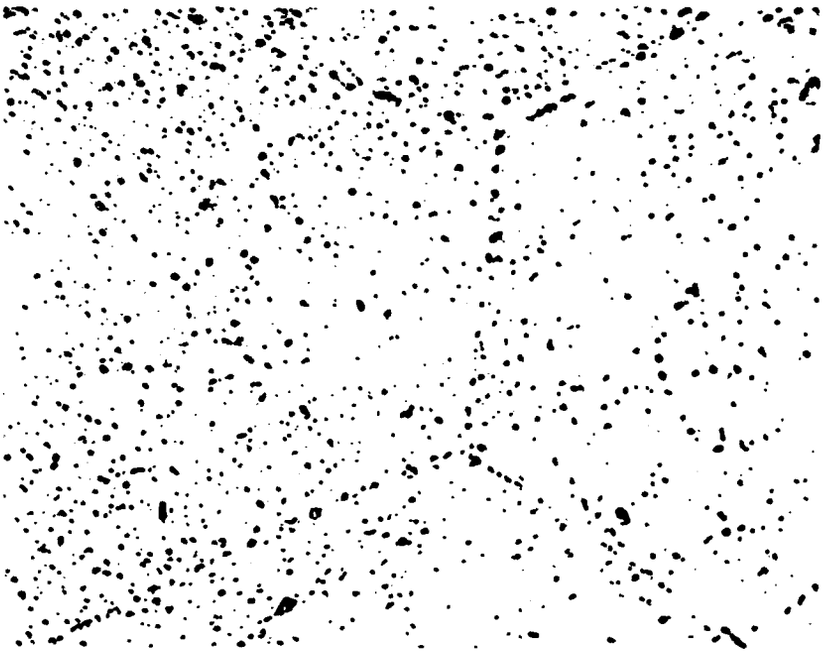

(b)

FIGURE 28. Optical micrographs showing the precipitates microstructure of overaged sample: (a) Al-3%Li-1%Ag, and (b) Al-3%Li after aging 322 hours at 200°C, X1000.

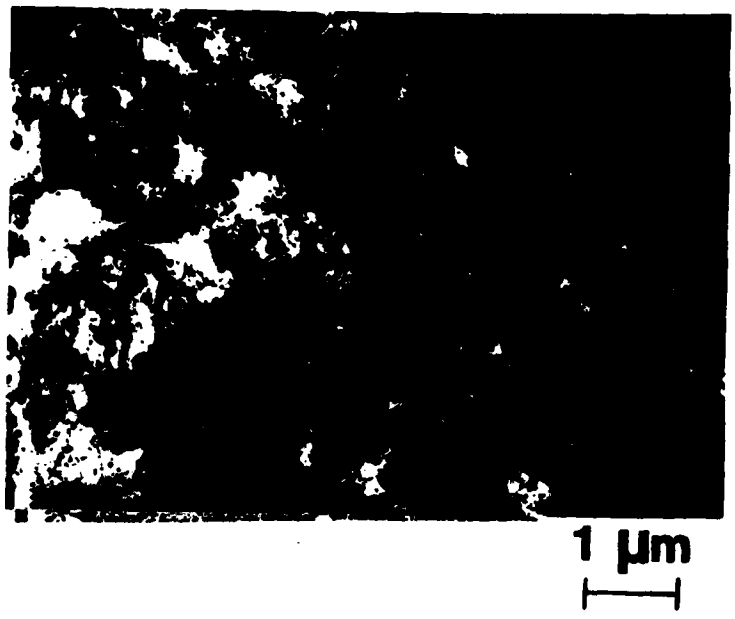

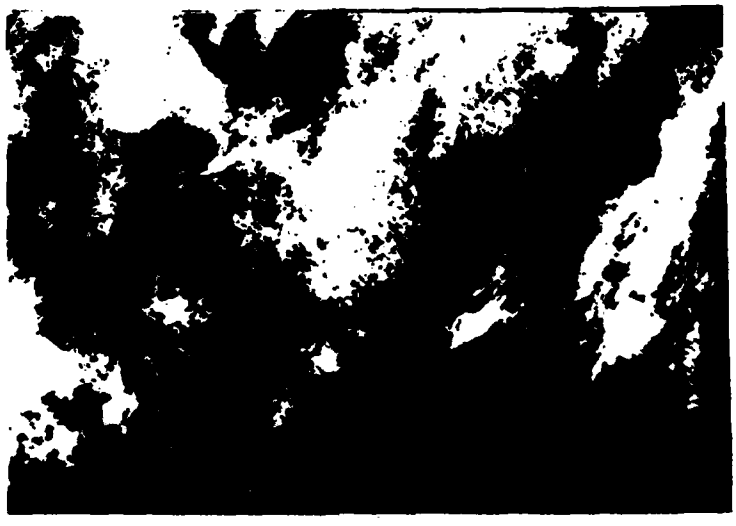

FIGURE 29. Electron micrograph showing the plate-like δ precipitates in Al-3%Li aged 2 hours at 300°C.

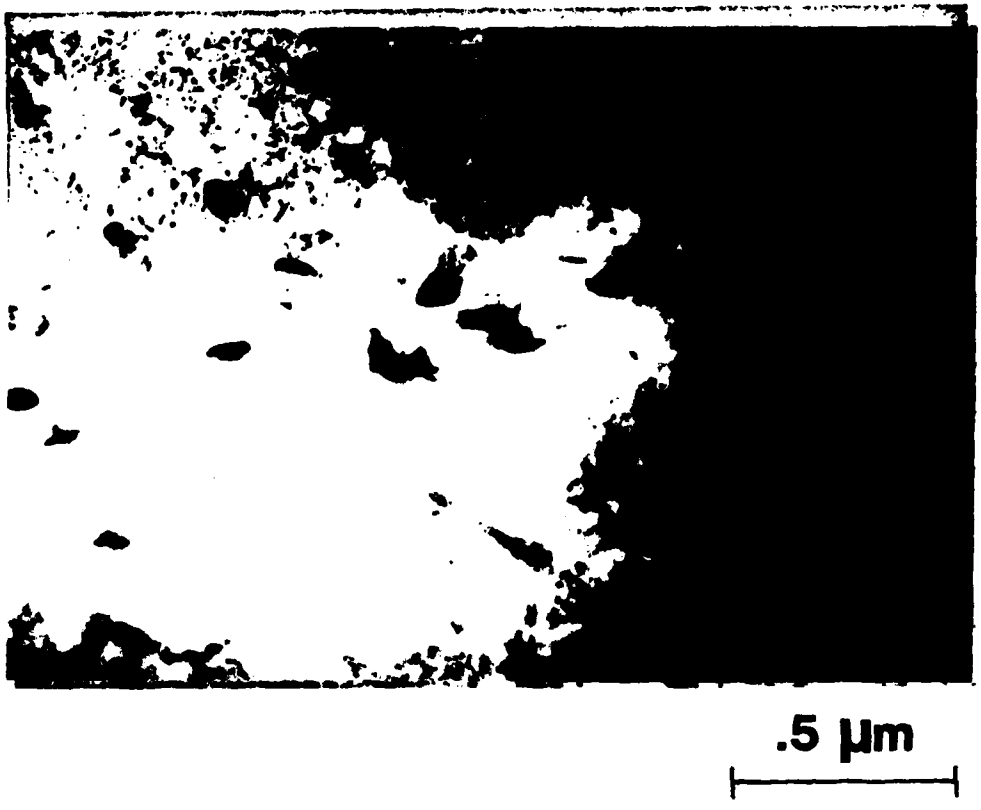

FIGURE 30. Electron micrograph showing the plate-like δ precipitates in the Al-1.5%Li-1%Ag after slightly deformed and aged 1 week at 175°C, X60,000.

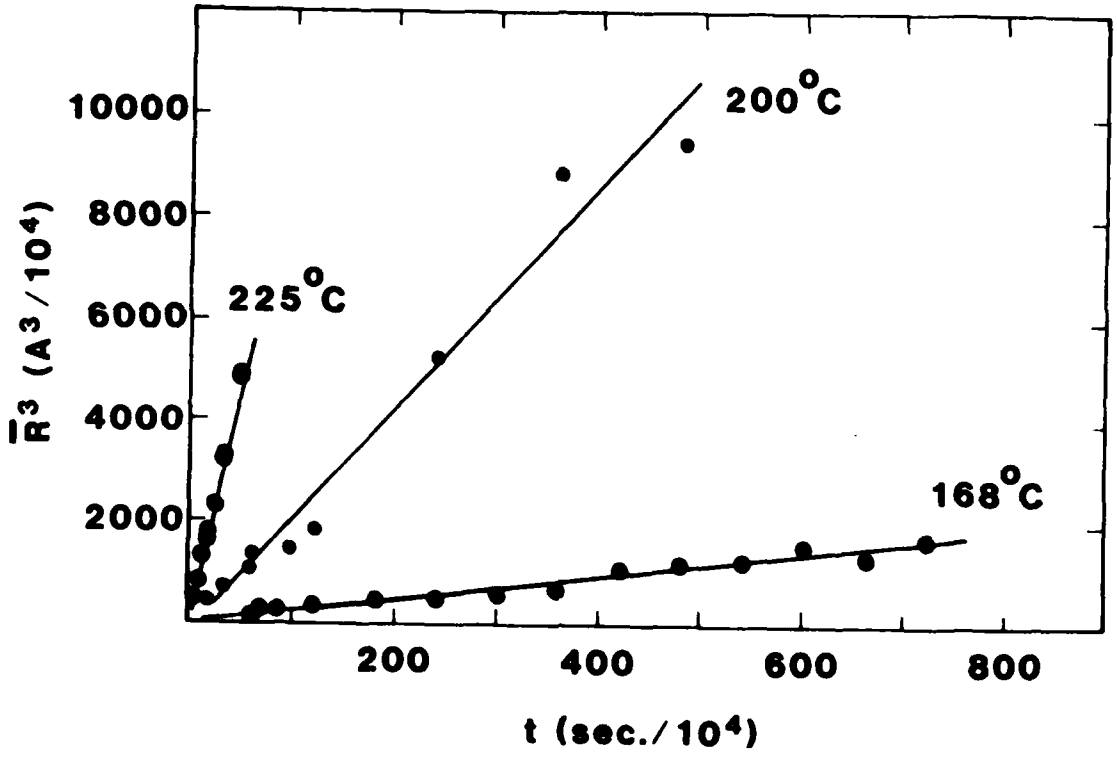

FIGURE 31. Plot of $\bar{R}^3$ versus time based on experimental results, as noted in Equation 22.

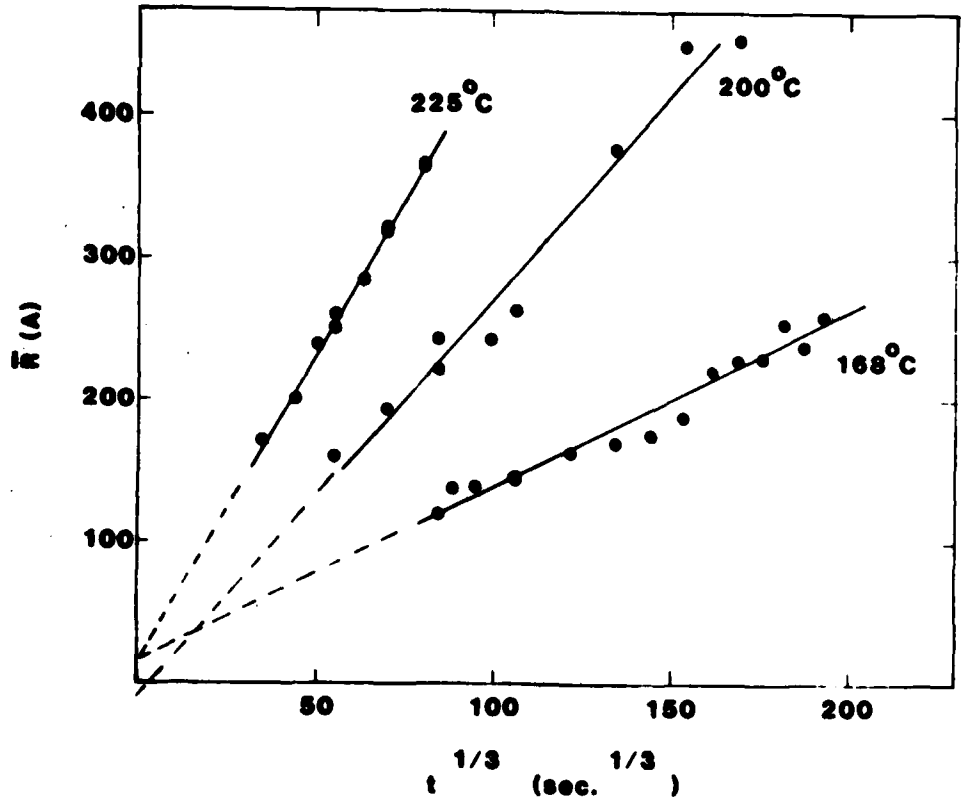

FIGURE 32. Plot of $\bar{R}$ versus time$^{1/3}$

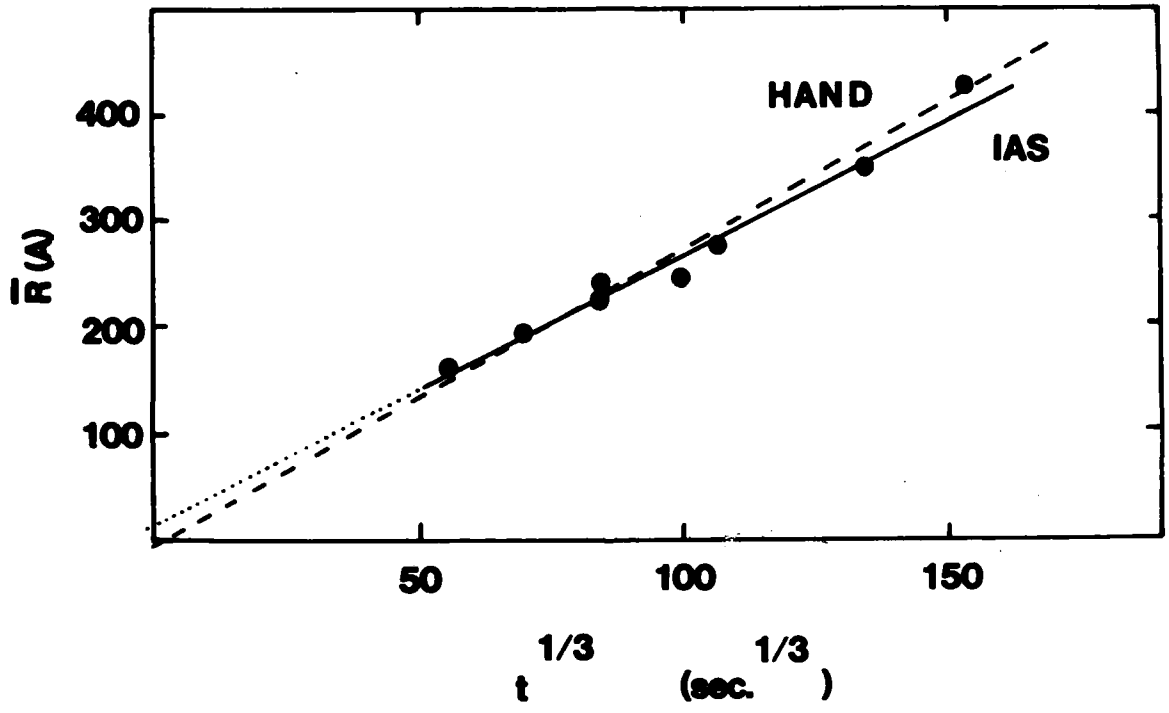

Figure 33. Plot of $\overline{R}$ versus $(\text{time})^{1/3}$ for both hand measured and IAS measured results at 200°C.

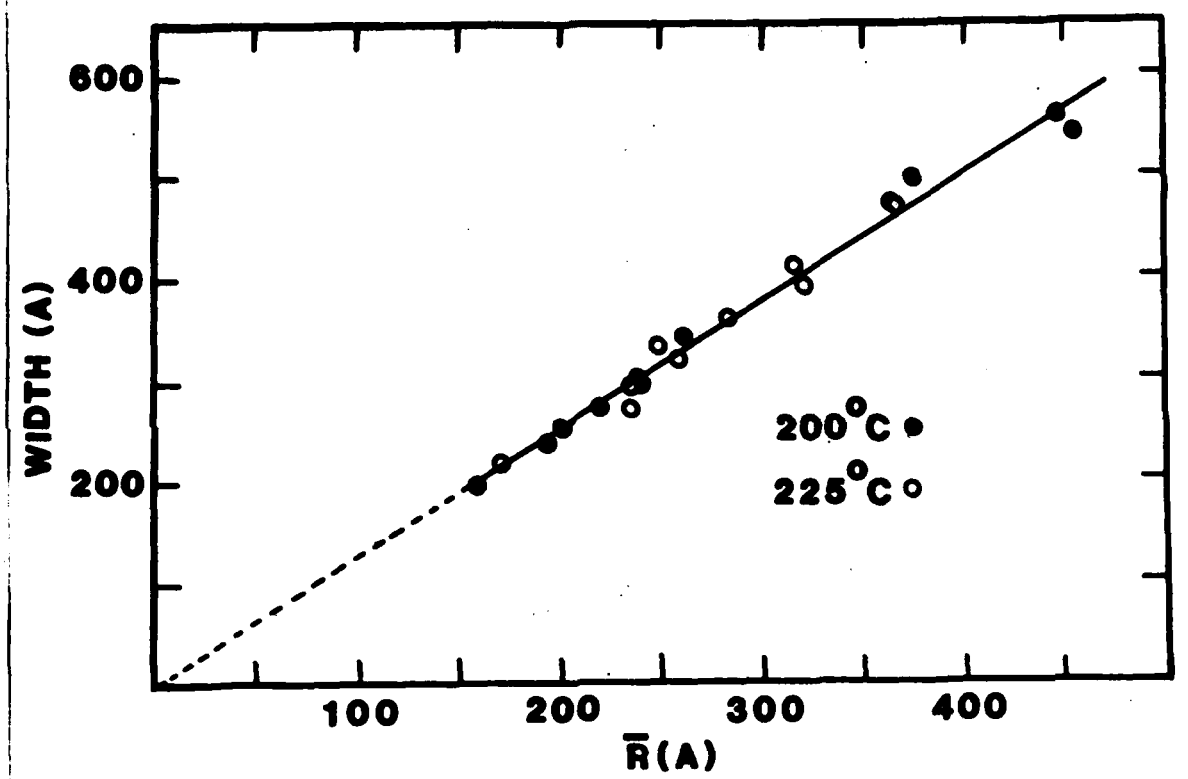

Figure 34. Plot of peak width at half height versus $\bar{R}$ based on experimental and calculated results.

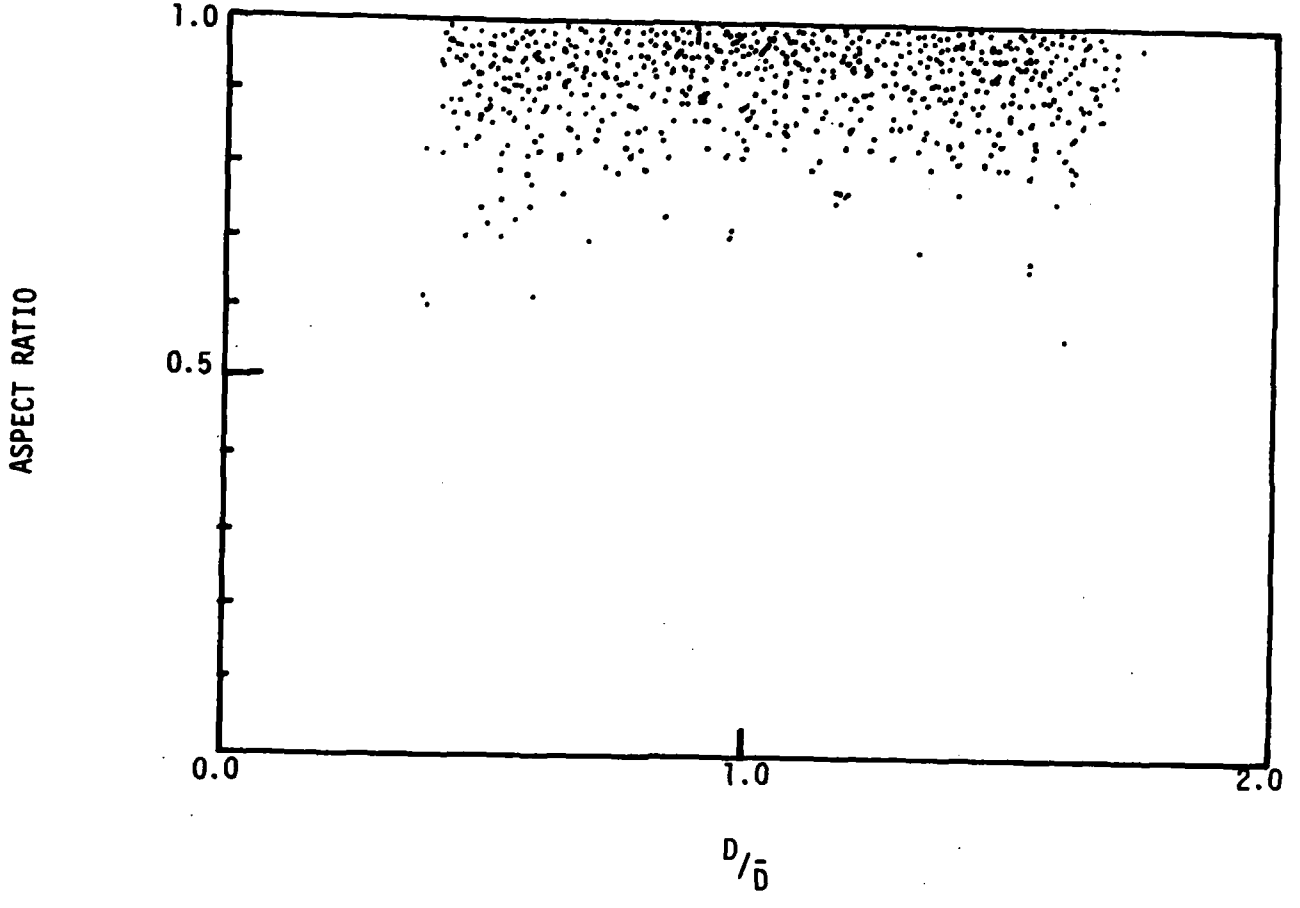

Figure 35. Aspect ratio versus $D/\bar{D}$

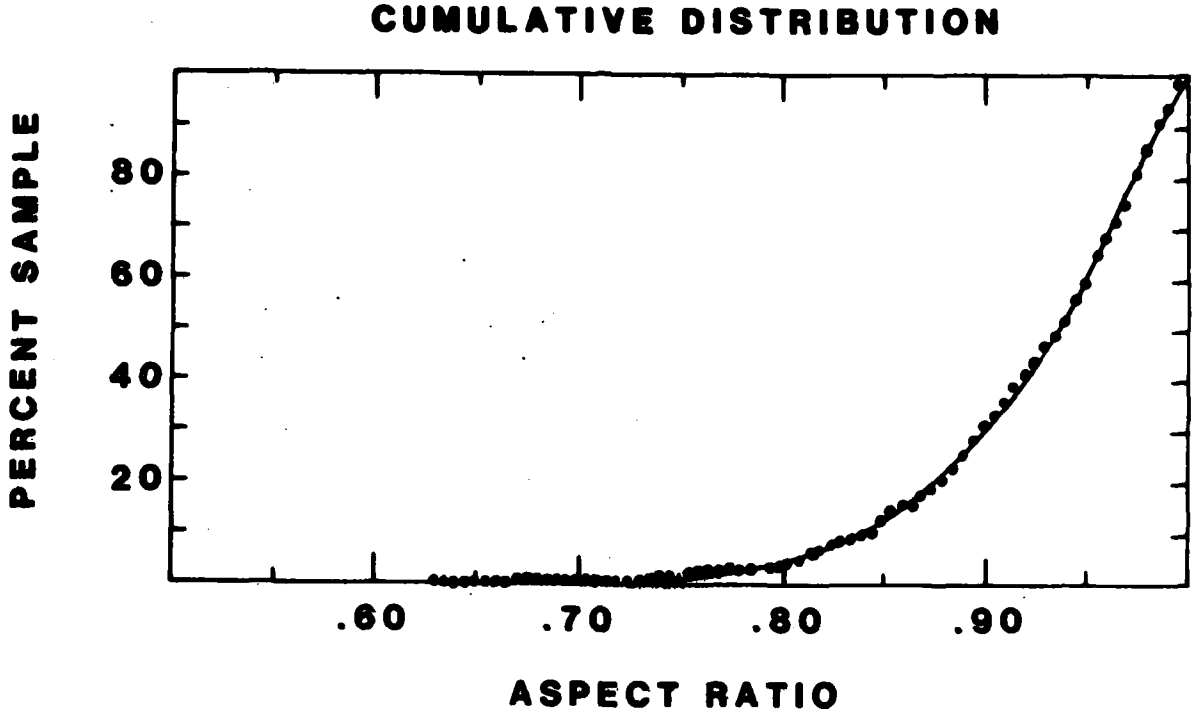

FIGURE 36. Cumulative plot of aspect ratios for δ′ precipitates.

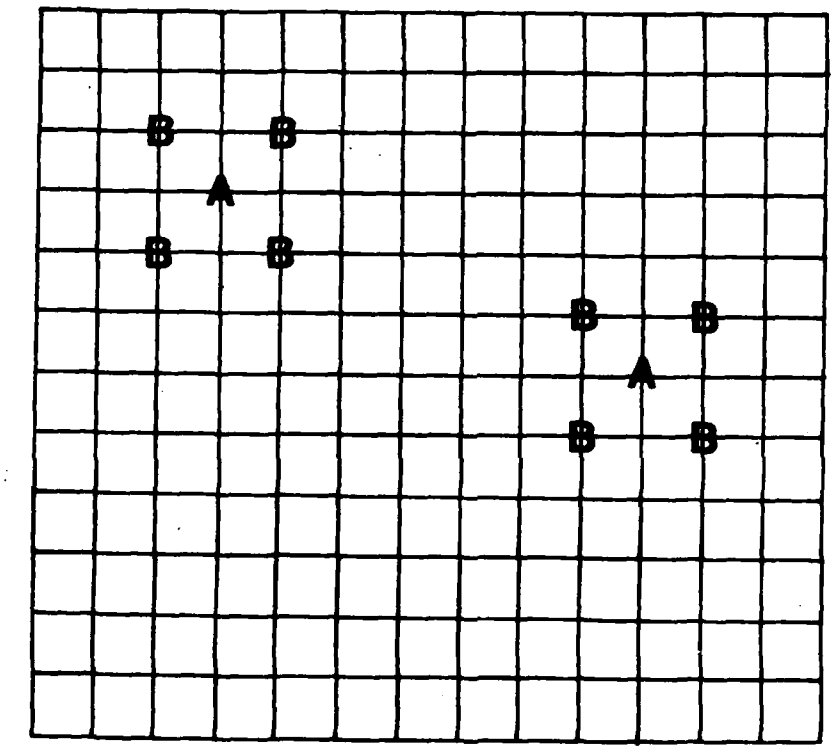

Figure 37. Illustration of two δ′ precipitates located on the theoretical lattice sites.

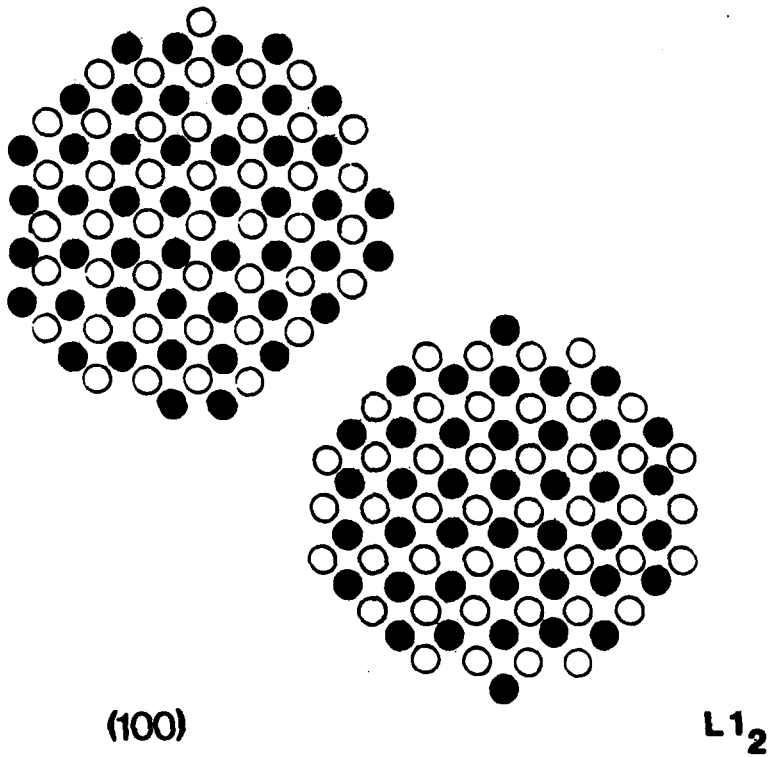

Figure 38. Illustration of two growing δ' precipitates.

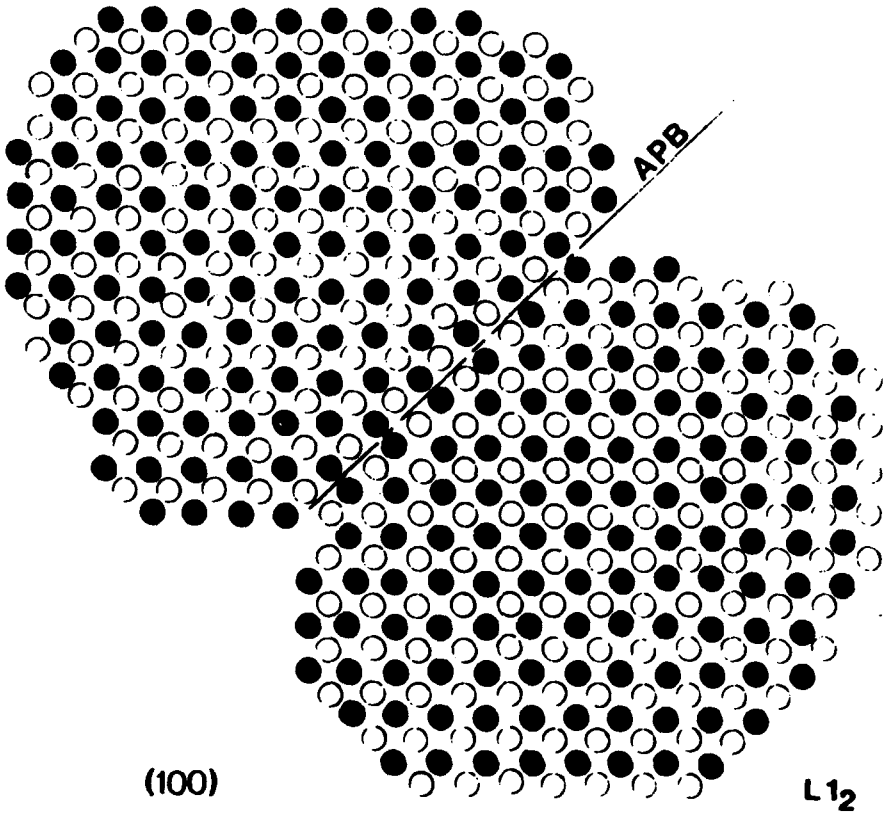

Figure 39. Illustration of a precipitate formed by the encounter of two precipitates, forming an antiphase domain boundary (APB).

Figure 40. Lattice image of one δ′ precipitate showing the 4.04A repeat distance. The alloy was aged for 8 weeks at 200°C.

(a) .1 μm

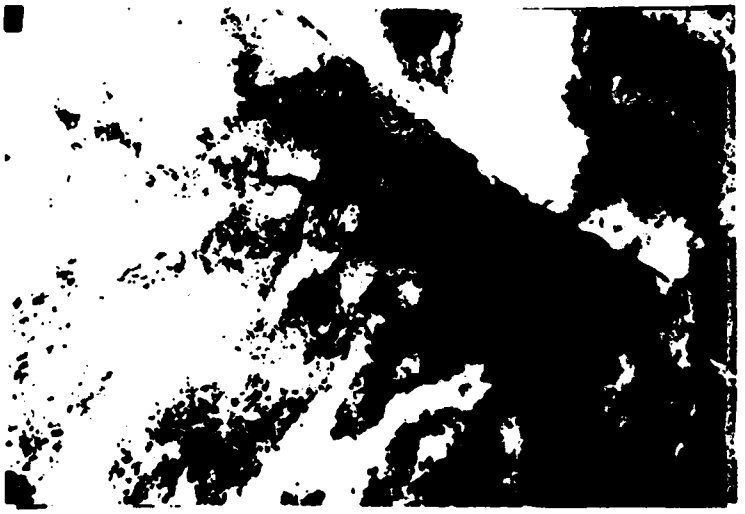

(b)

FIGURE 41. Microstructure of Al-3%Li heated up to 275°C in DSC cell, showing the δ precipitates: (a) in the matrix, and (b) at the grain boundary, X90,000.

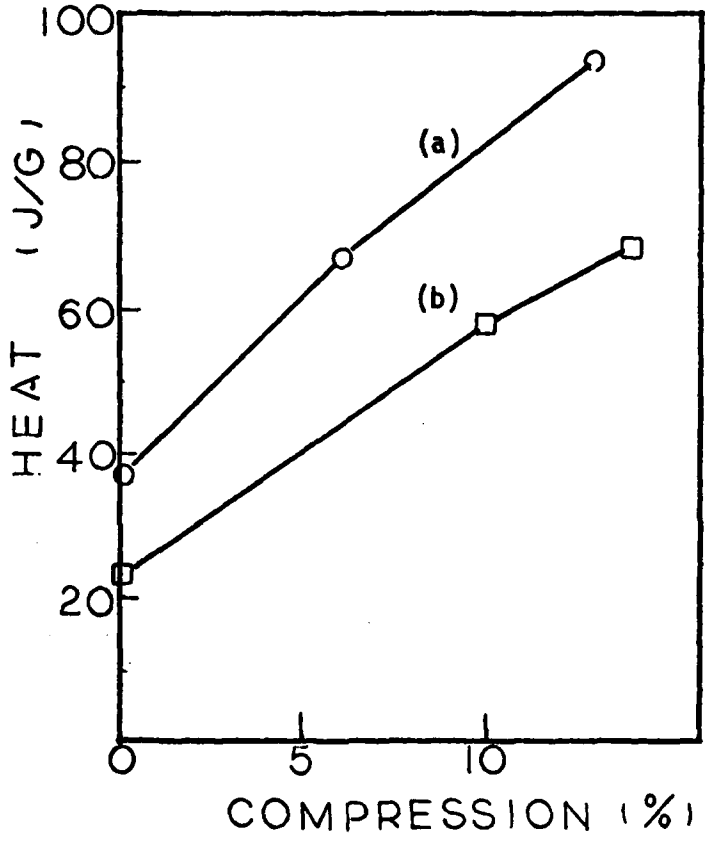

FIGURE 42. Heat of reaction for the dissolution of δ phase against the amount of compression: (a) polycrystal of Al-3%Li, and (b) single crystal of Al-3%Li.

FIGURE 43. Electron micrograph showing the δ′ precipitates at a dislocation in the Al-1.5%Li after slightly deformed and aged 1 week at 175°C.

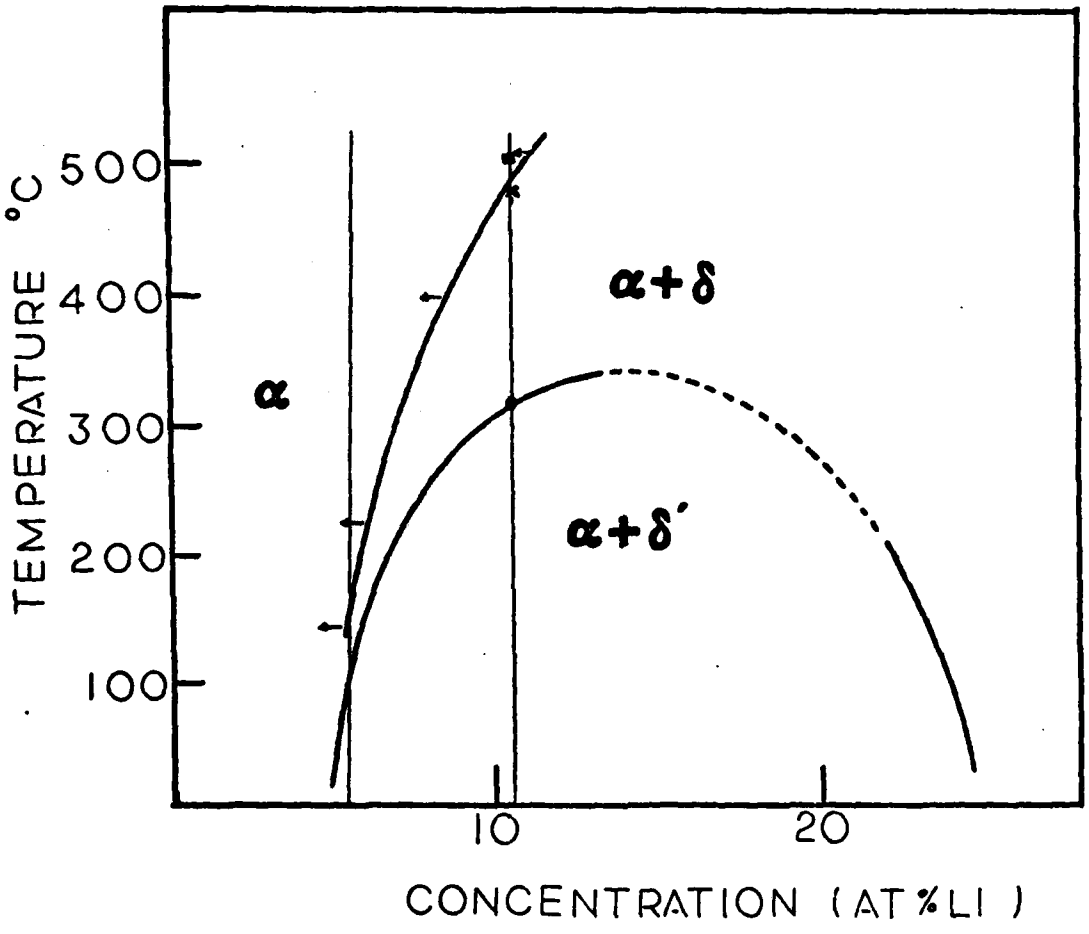

FIGURE 44. The Al-Li Phase diagram showing metastable miscibility gap gap for δ' after Williams(38), compared with present DSC work: ■ peak of 'D' for Al-3%Li-1%Ag; x peak of 'D' for Al-3%Li; ● peak of 'B' for Al-3%Li and Al-3%Li-1%Ag. The vertical lines indicate the position of the Li contents of the alloys investigated.

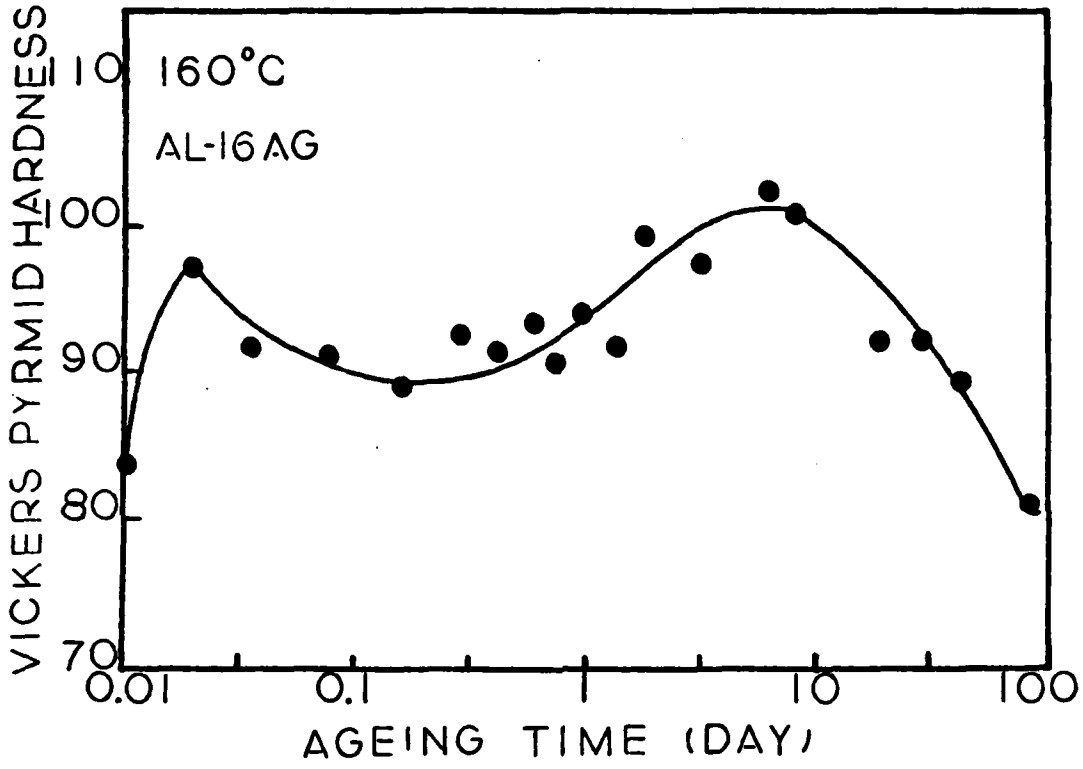

FIGURE 45. Hardness/aging-time curve for an Al-16%Ag alloy aged at 160°C, from Nicholson et al. (4).

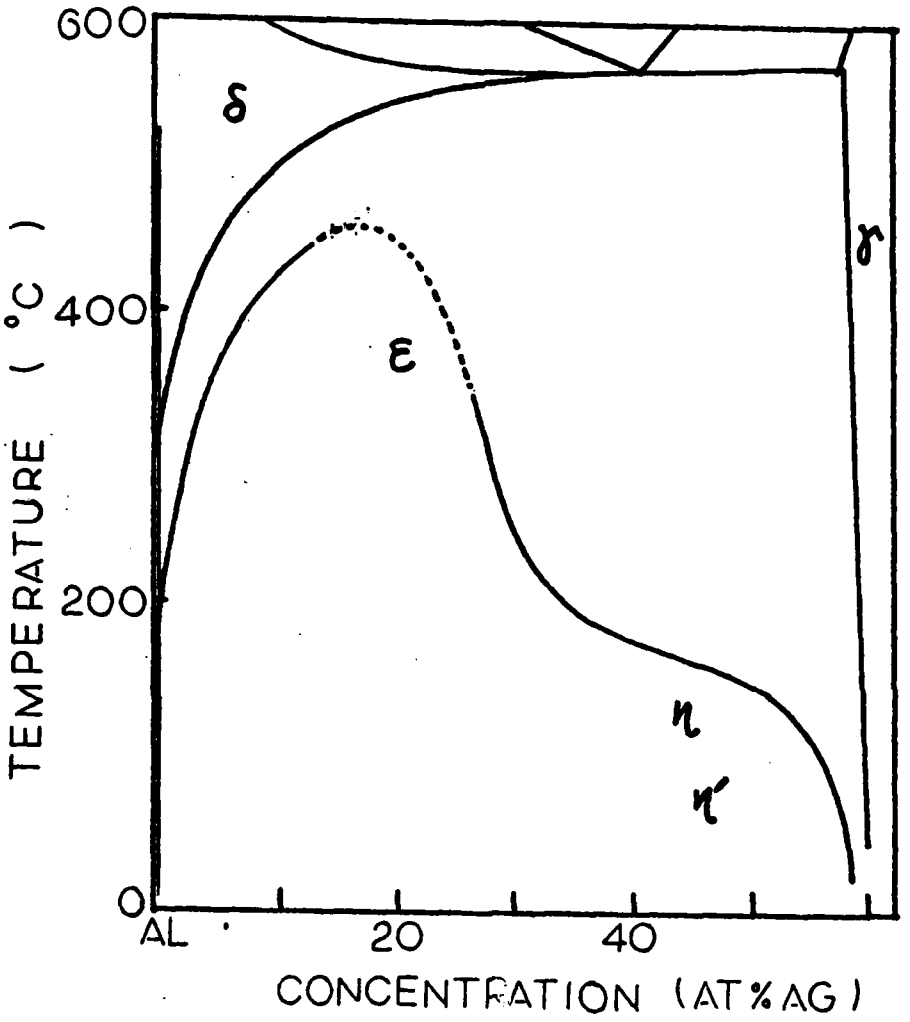

FIGURE 46. The Al-Ag phase diagram with metastable miscibility gap for G. P. Zone, after Baur et al. (43).

APPENDICES

Appendix A

PSD Functions

The Particle Size Distribution (PSD) functions were constructed from the accummulated measurements at a particular aging condition. The particle diameters were measured to the nearest 1mm when viewed through a photographic enlarger. To be consistent a magnificaton factor of approximately 2.75X was used for each film. The data were analyzed using a computer program found in Appendix E. Actual diameters in Angstrom units were calculated using appropriate magnification factors. For these initial results, a sample population of approximately 600 particles was assumed to be statistically significant.

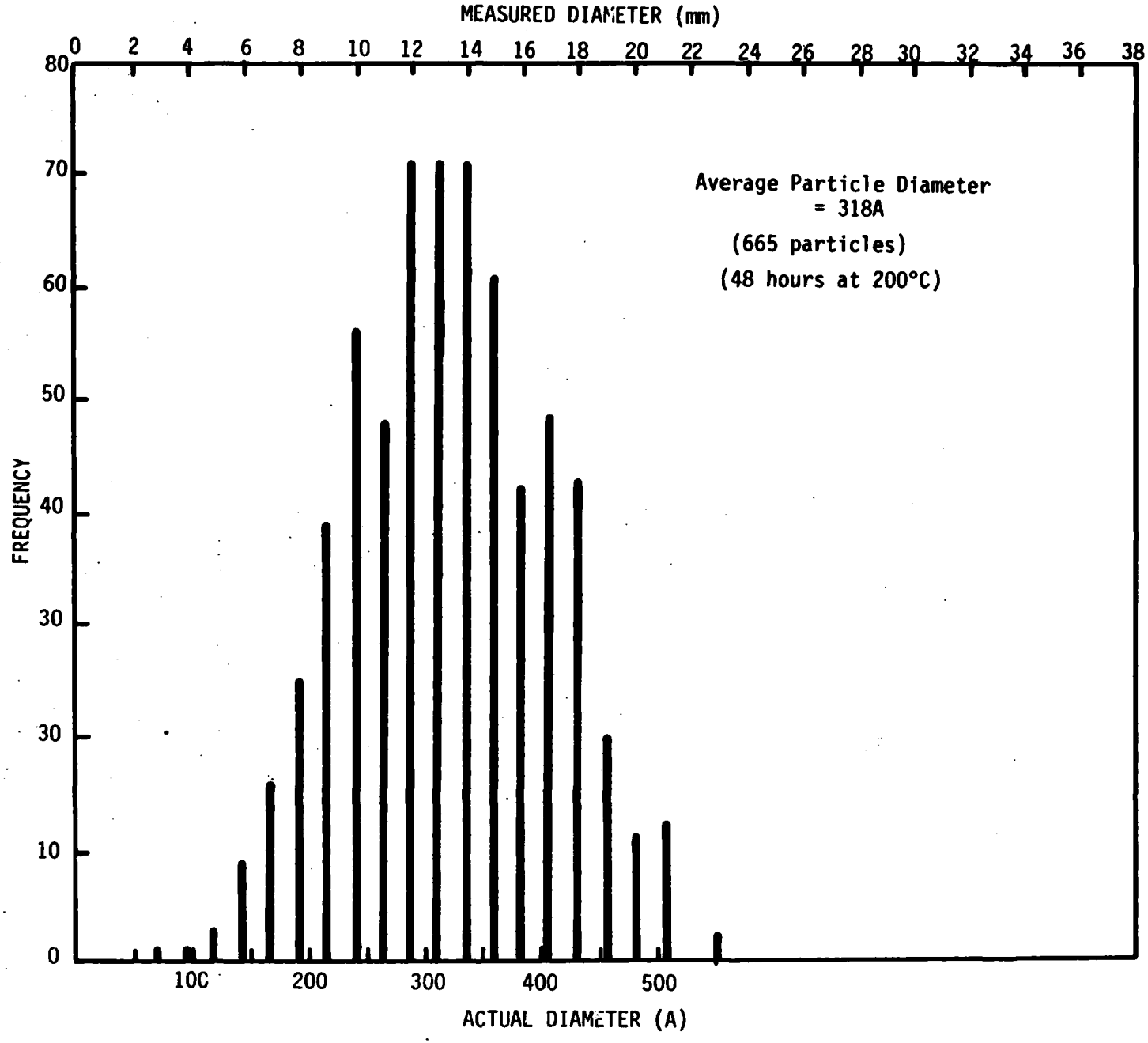

Figure A1. Particle size distribution function of δ' precipitates.

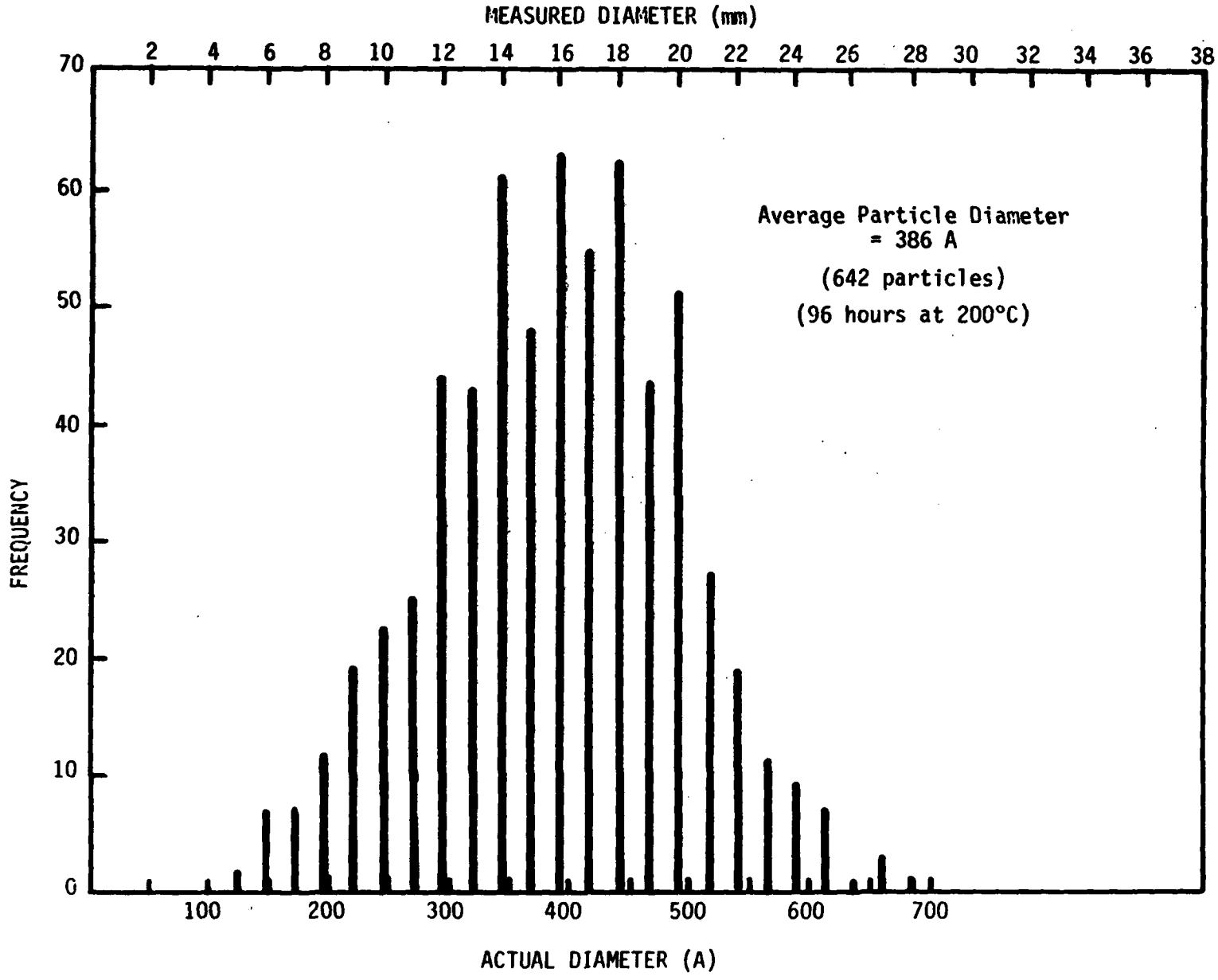

Figure A2. Particle size distribution function of δ' precipitates.

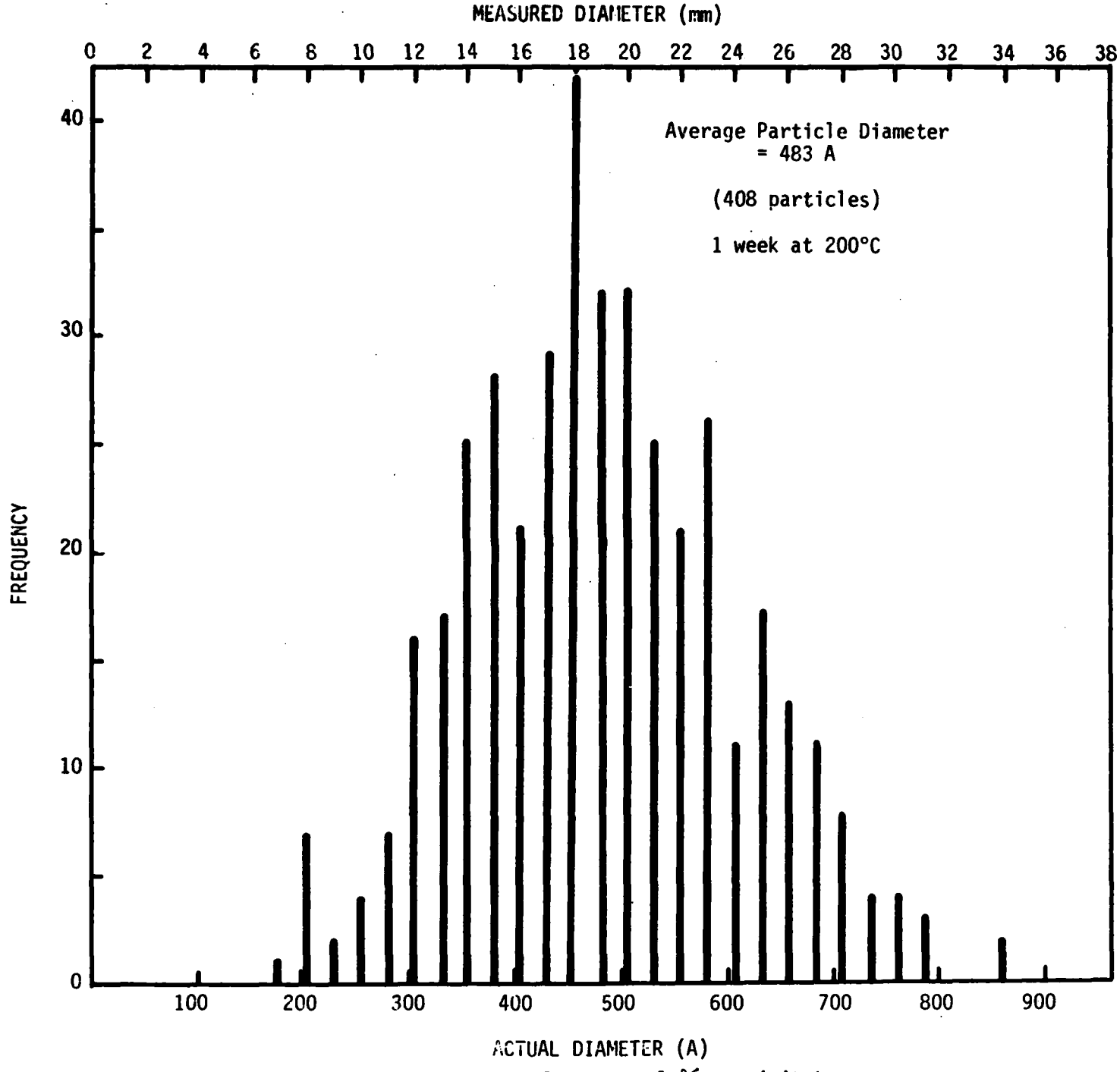

Figure A3. Particle size distribution function of δ' precipitates.

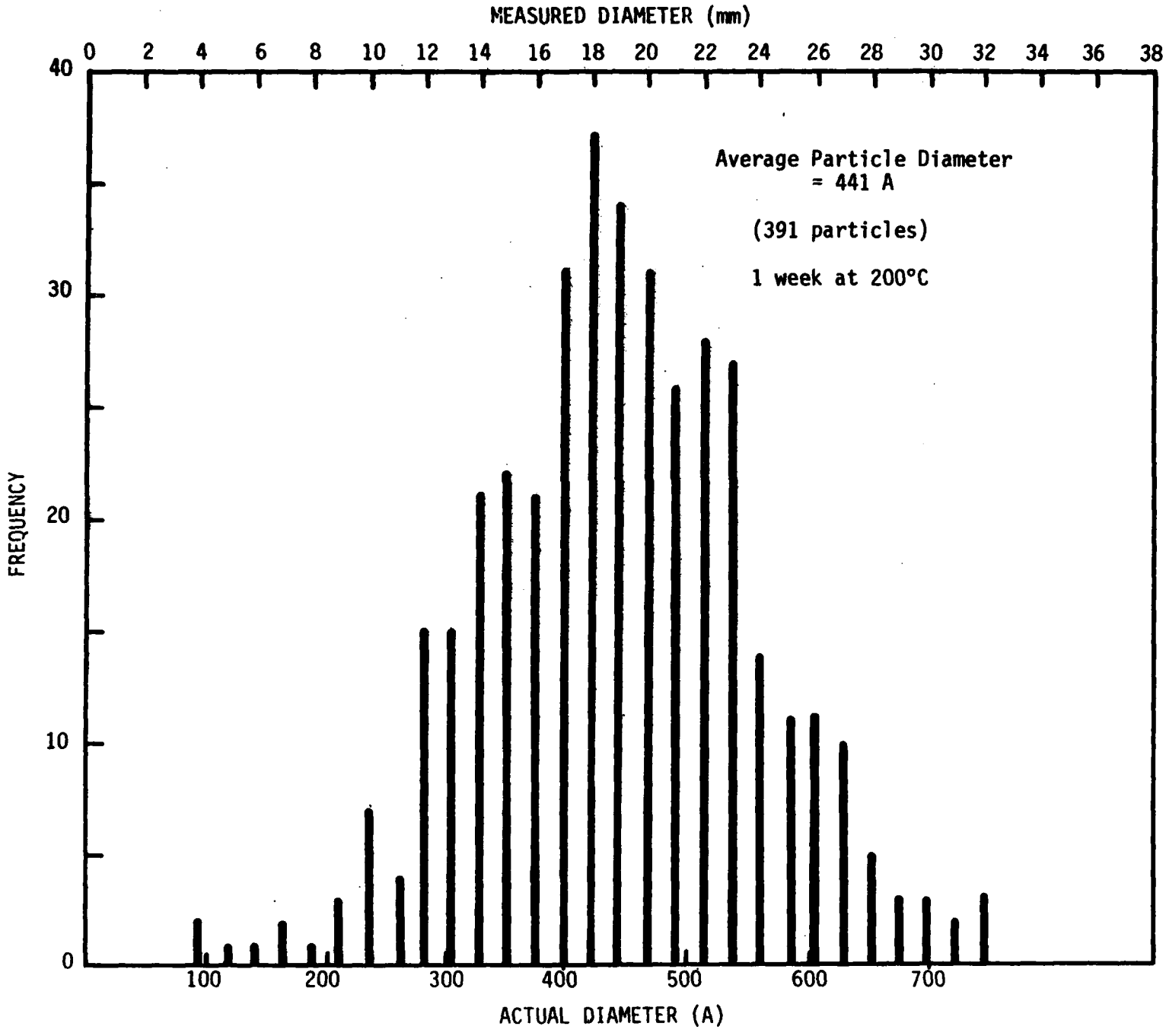

Figure A4. Particle size distribution function of δ' precipitates.

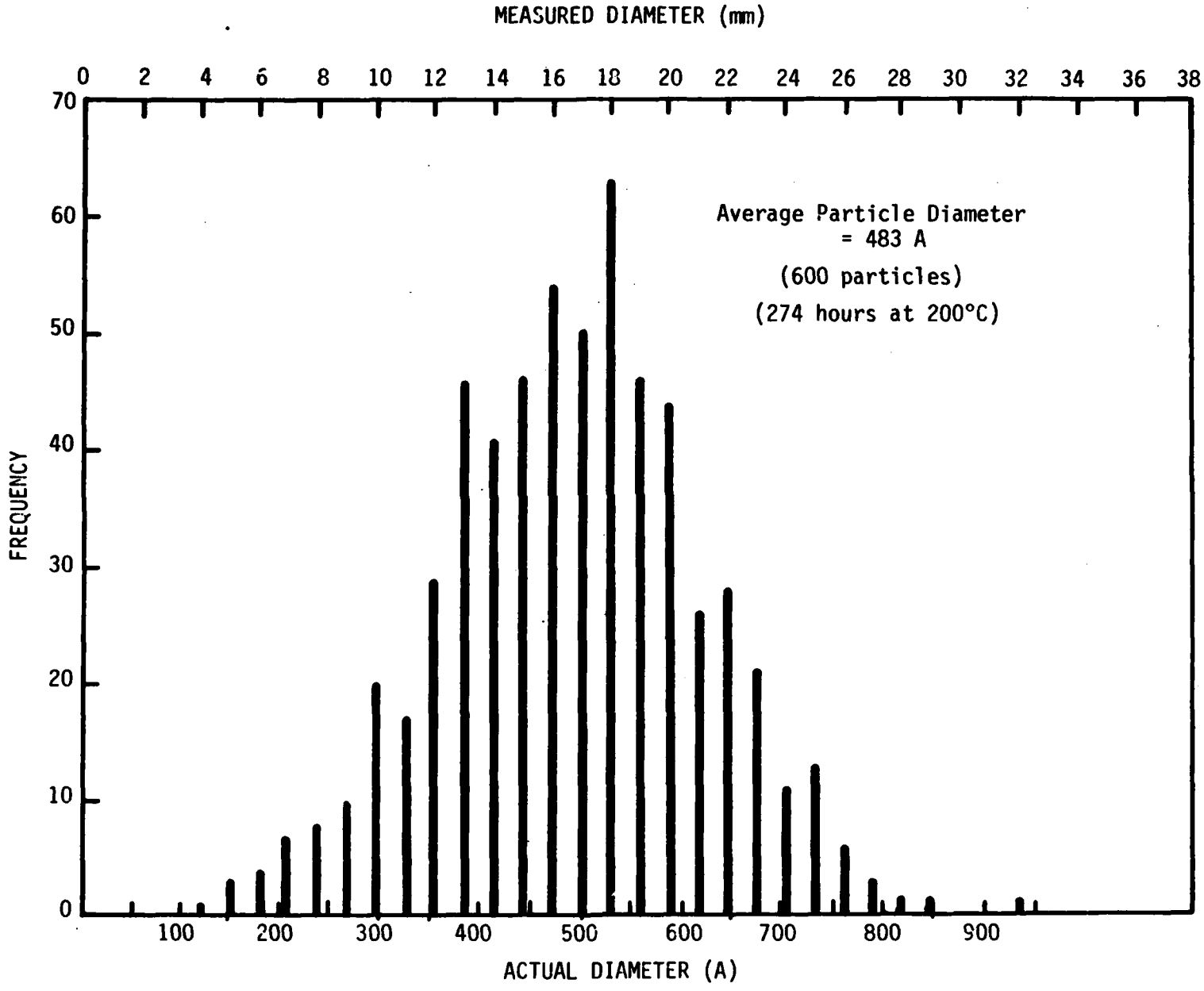

Figure A5. Particle size distribution function of δ' precipitates.

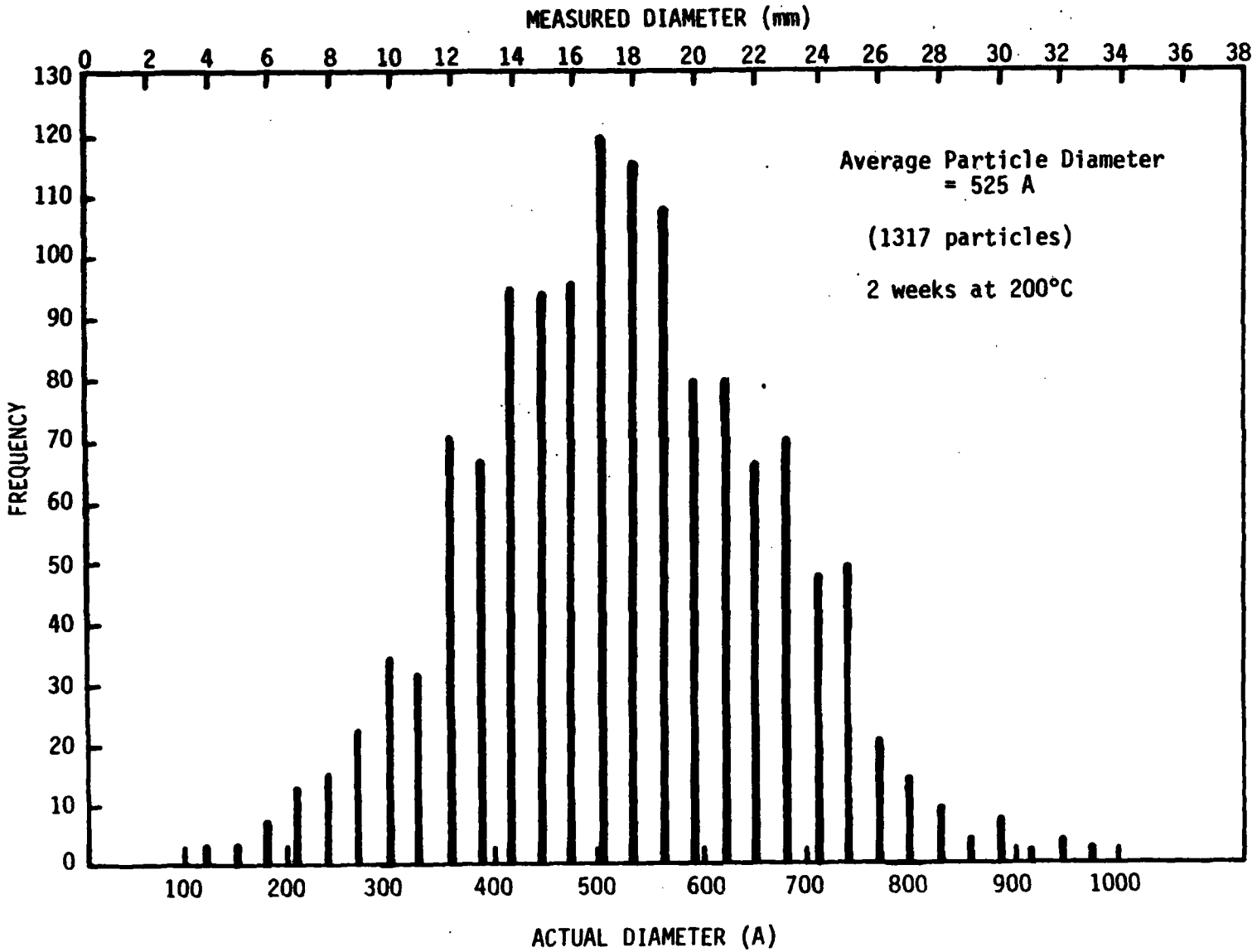

Figure A6. Particle size distribution function of δ′ precipitates.

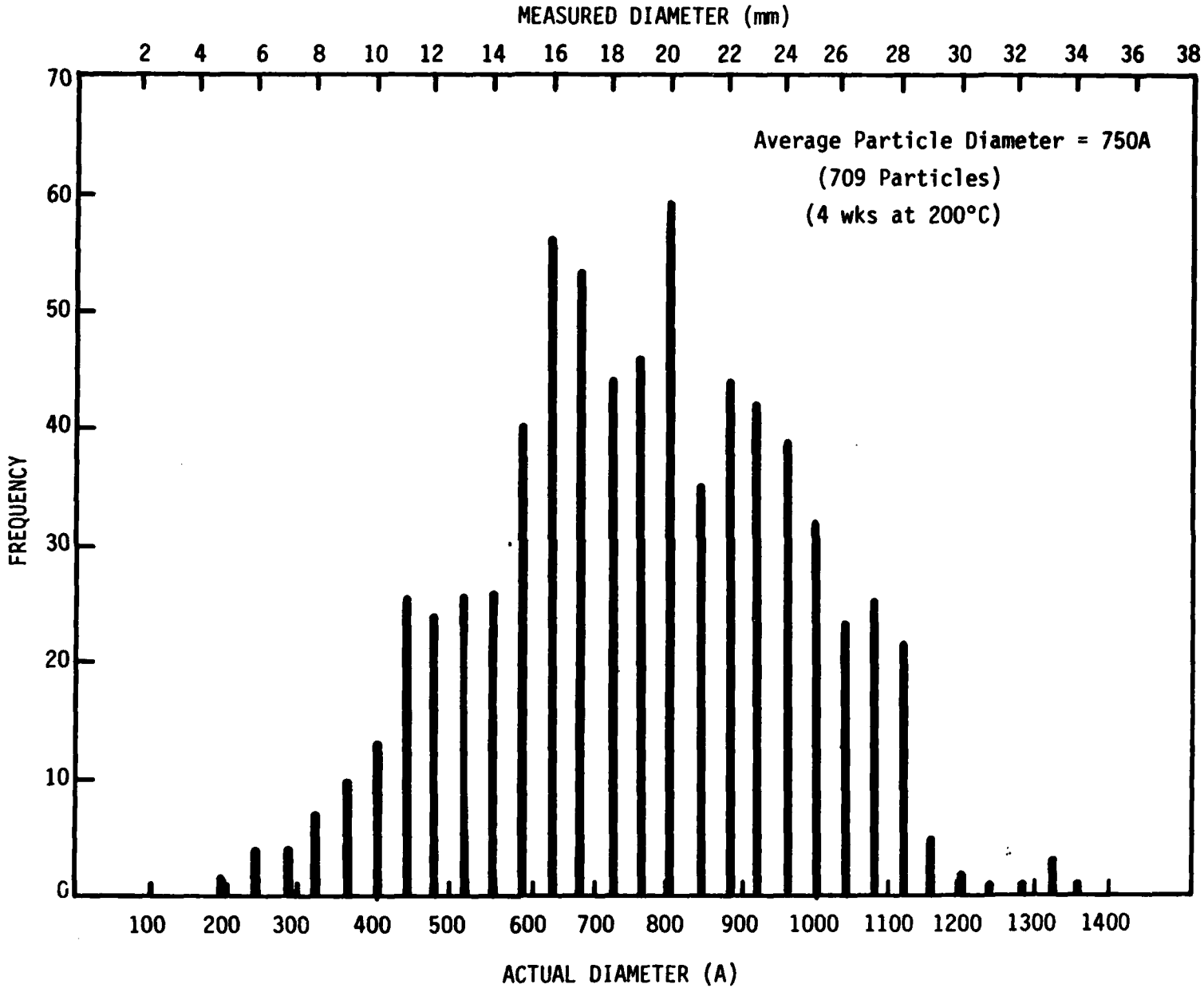

Figure A7. Particle size distribution function of δ' precipitates.

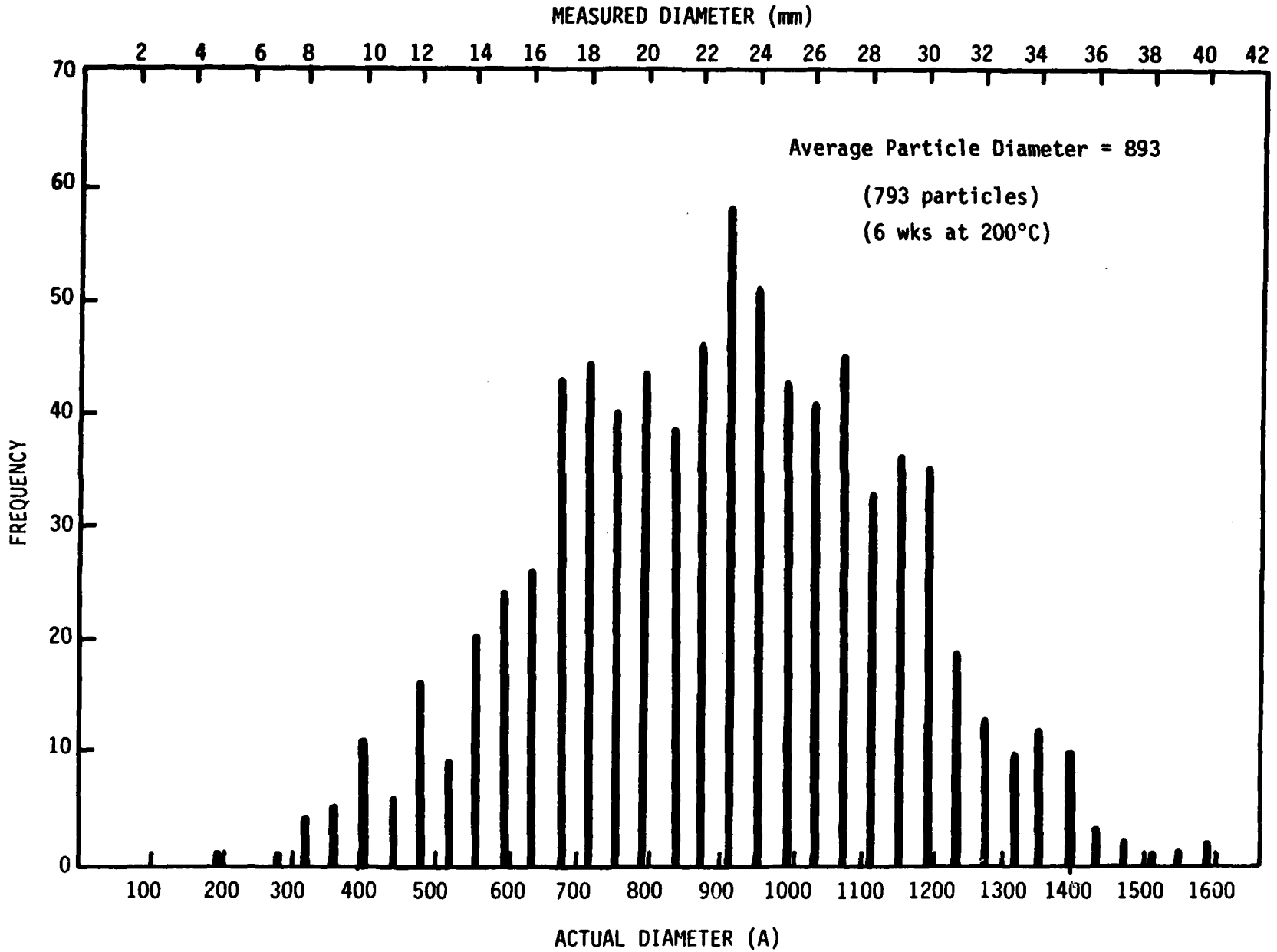

Figure A8. Particle size distribution function of δ' precipitates.

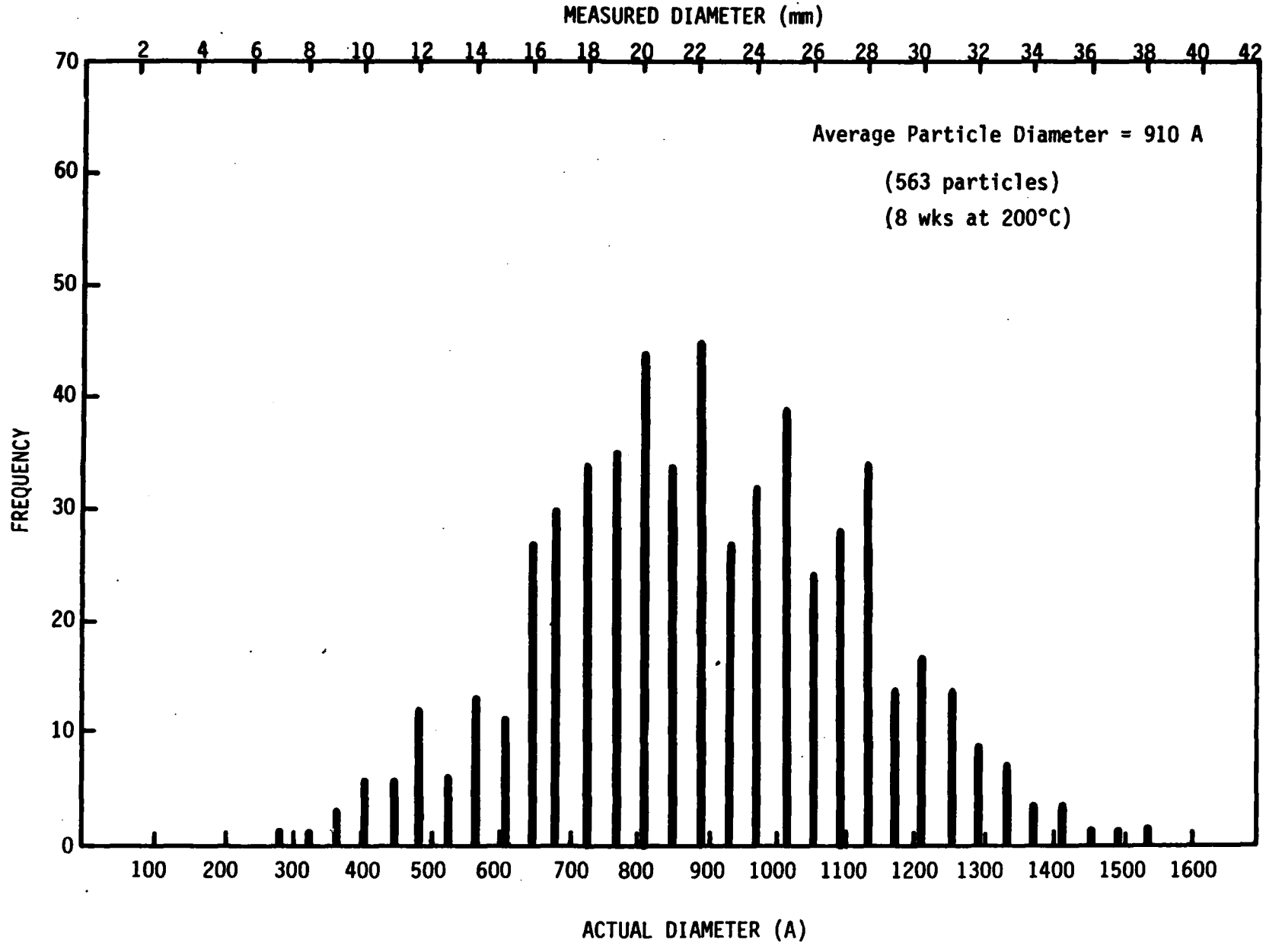

Figure A9. Particle size distribution function of δ' precipitates.

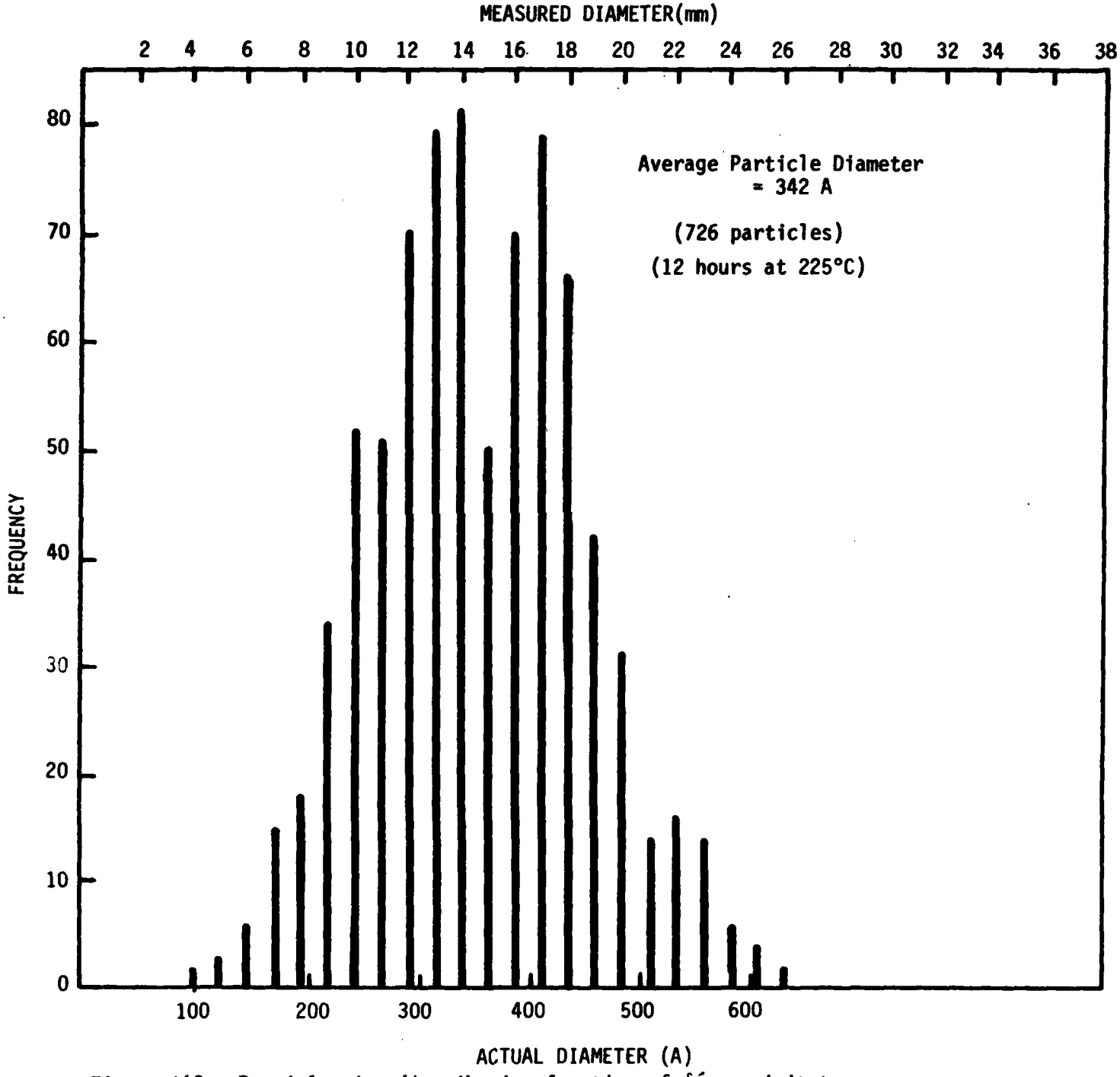

Figure A10. Particle size distribution function of δ' precipitates.

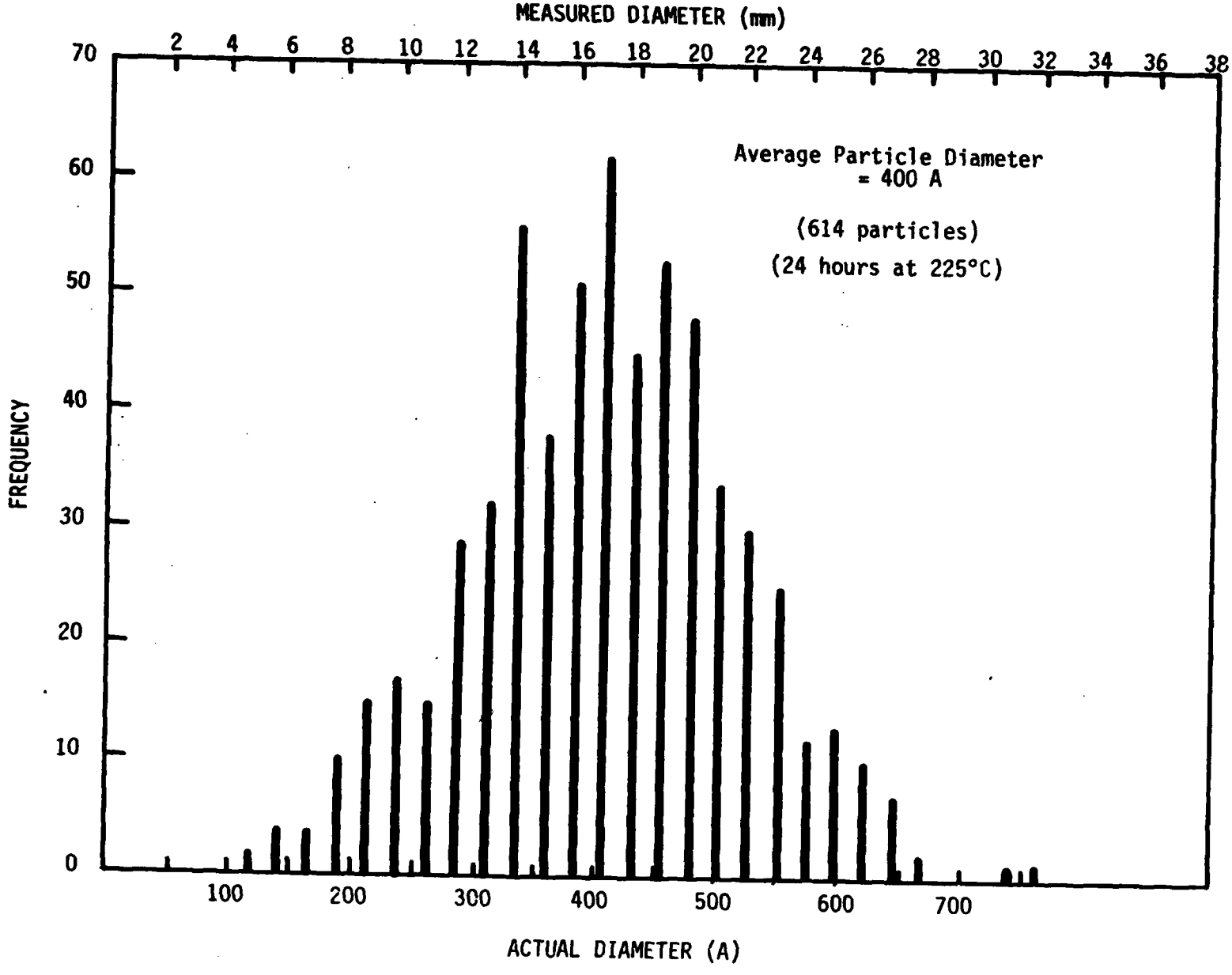

Figure A11. Particle size distribution function of δ' precipitates.

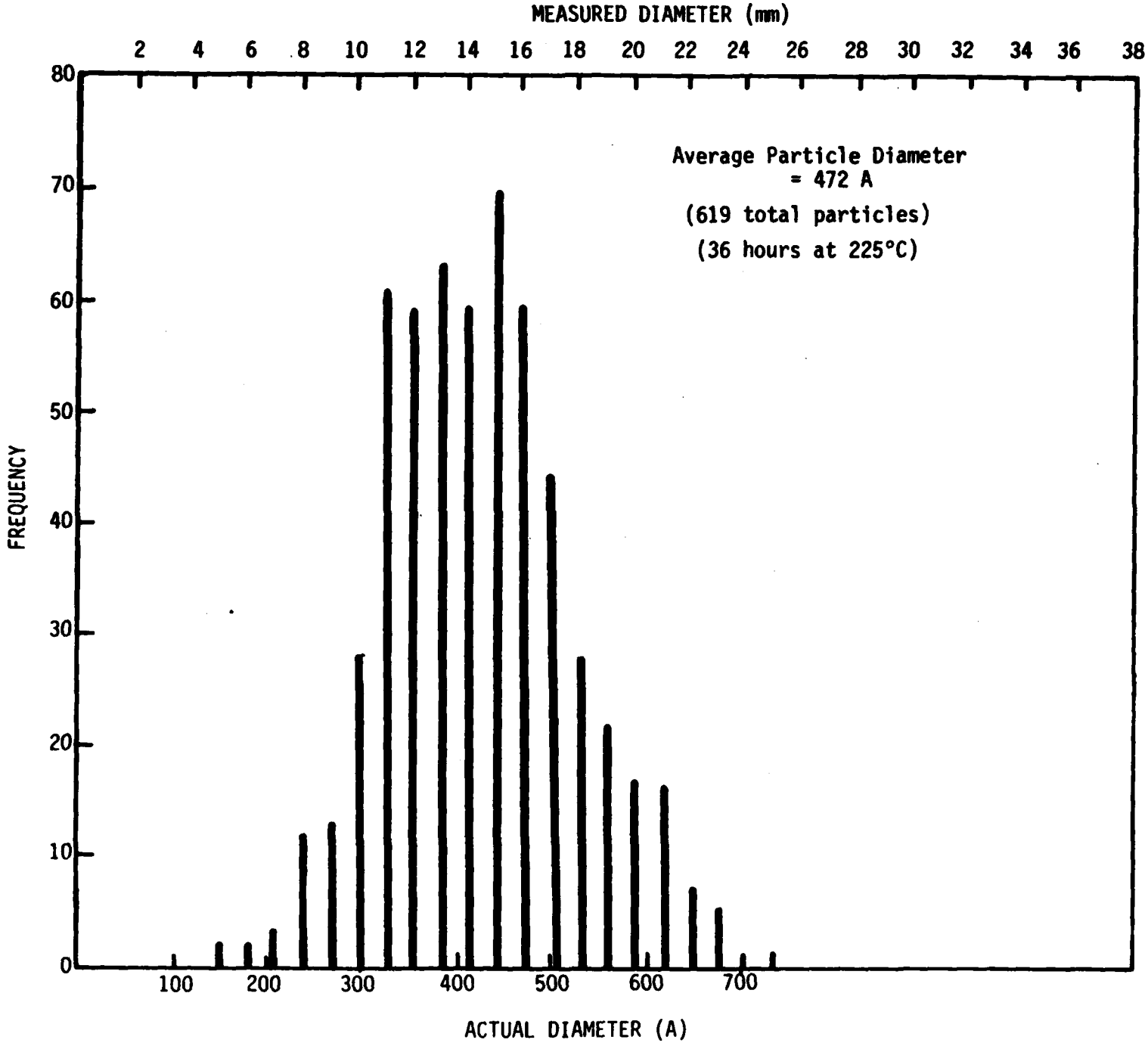

Figure A12. Particle size distribution function of δ' precipitates.

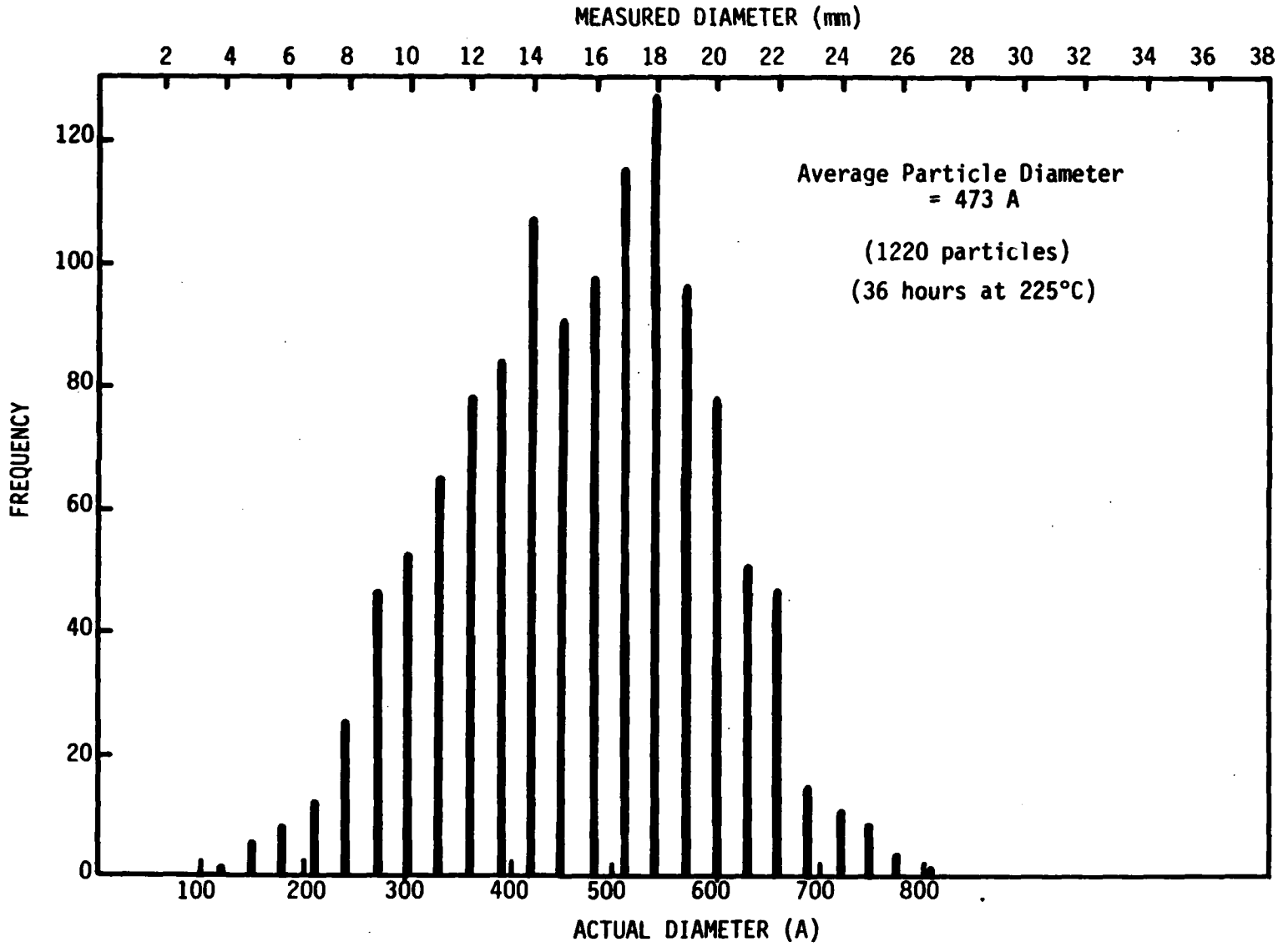

Figure A13. Particle size distribution function of δ' precipitates.

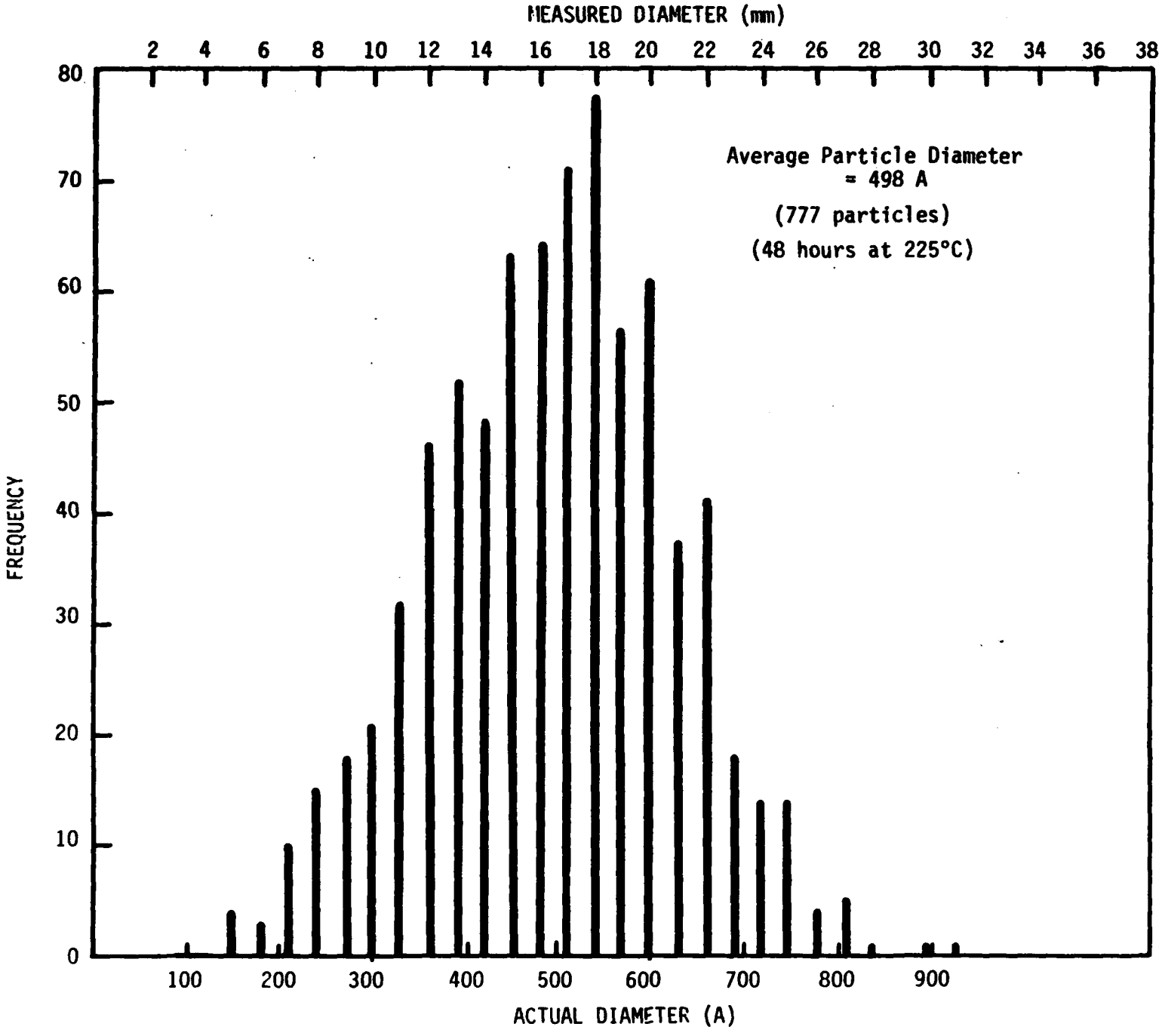

Figure A14. Particle size distribution function of δ' precipitates.

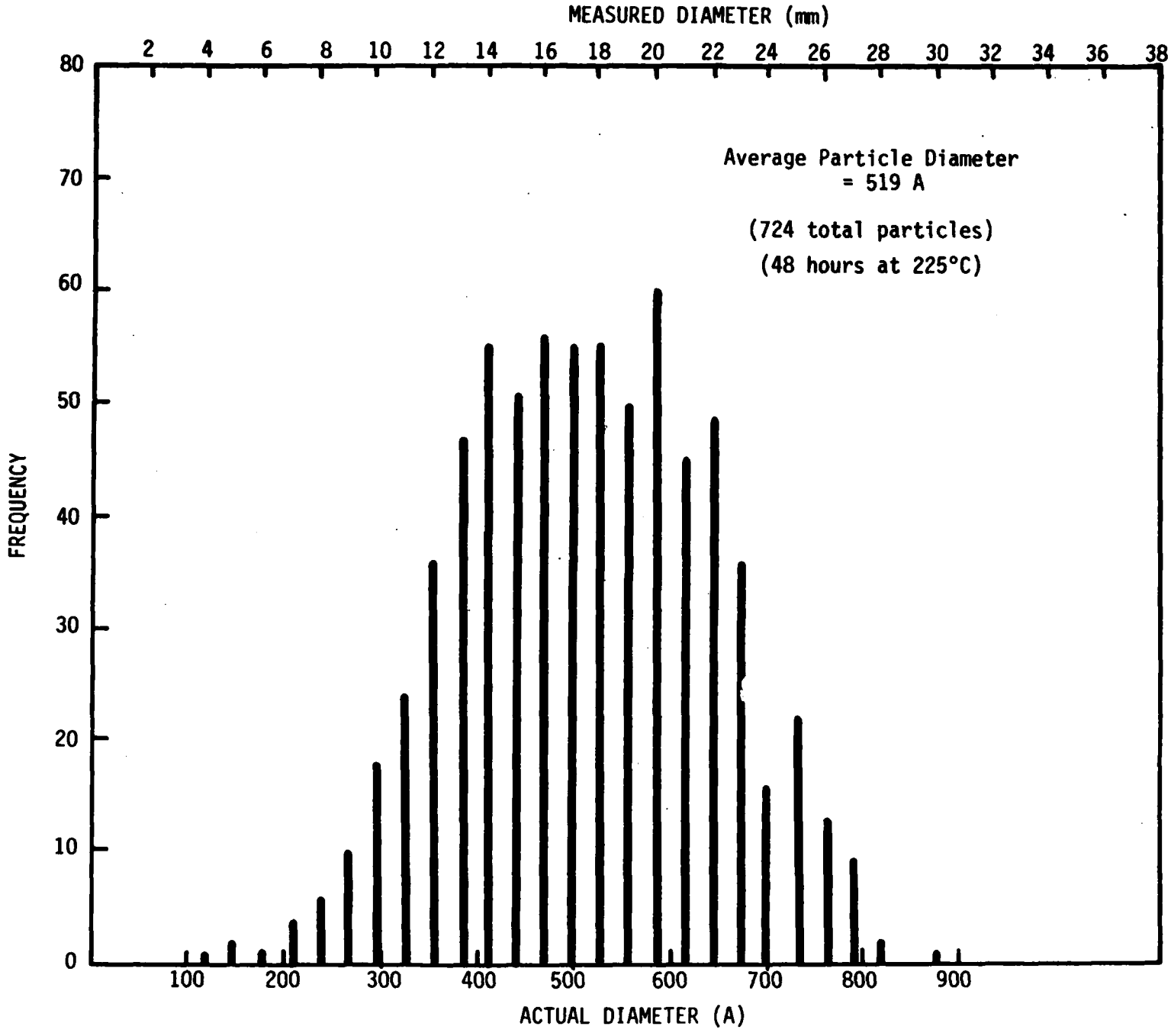

Figure A15. Particle size distribution function of δ' precipitates.

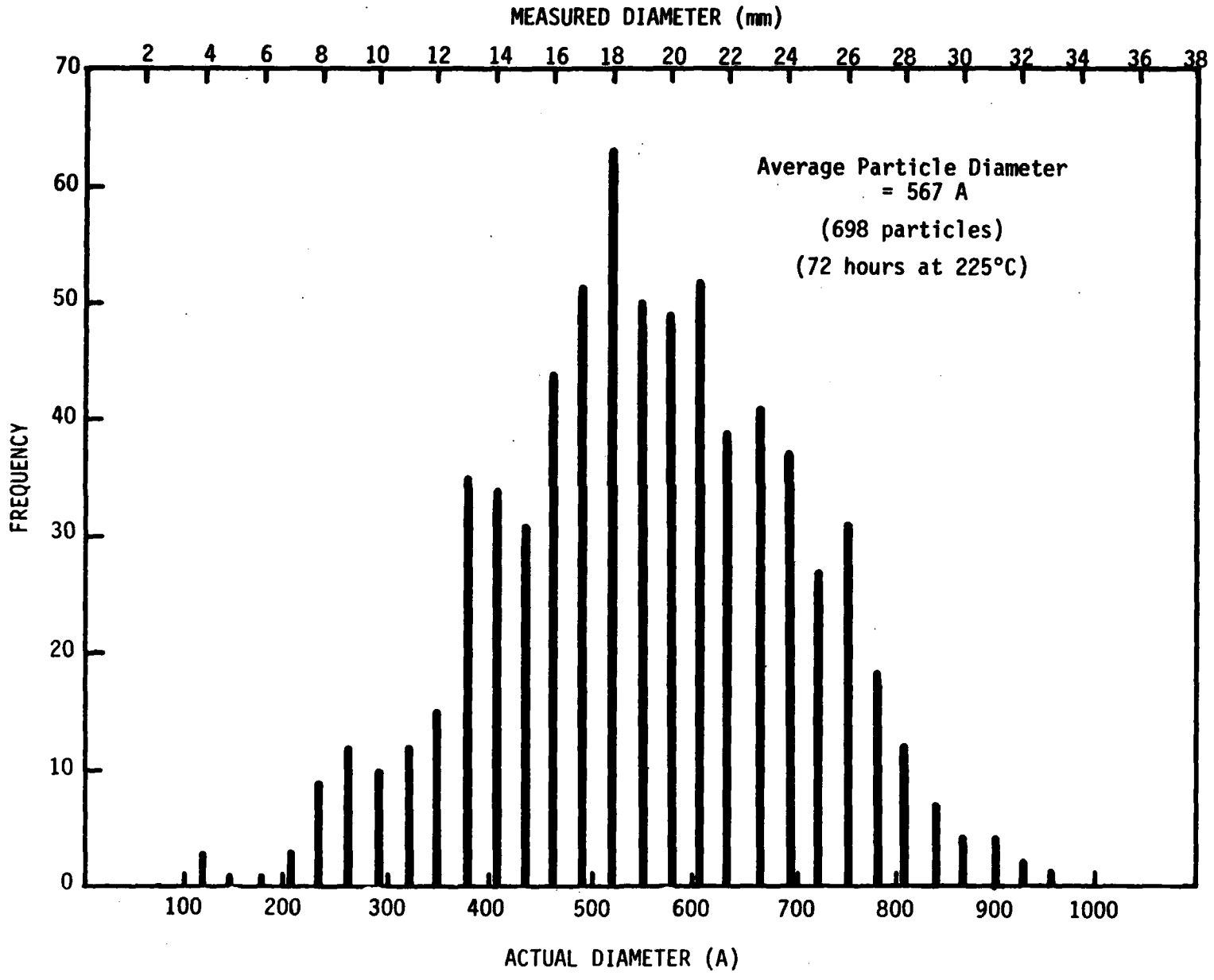

Figure A16. Particle size distribution function of δ′ precipitates.

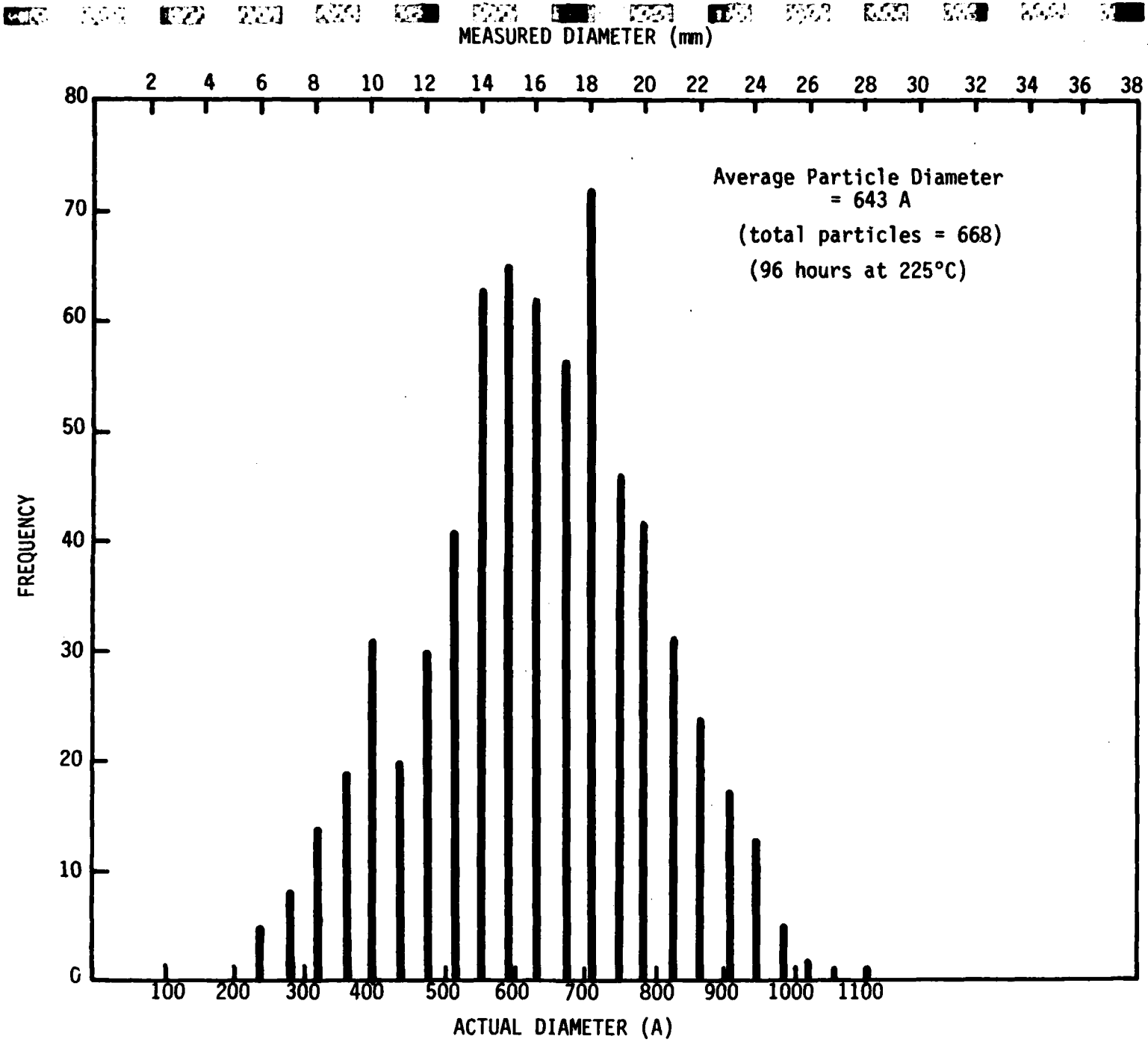

Figure A17. Particle size distribution function of δ' precipitates.

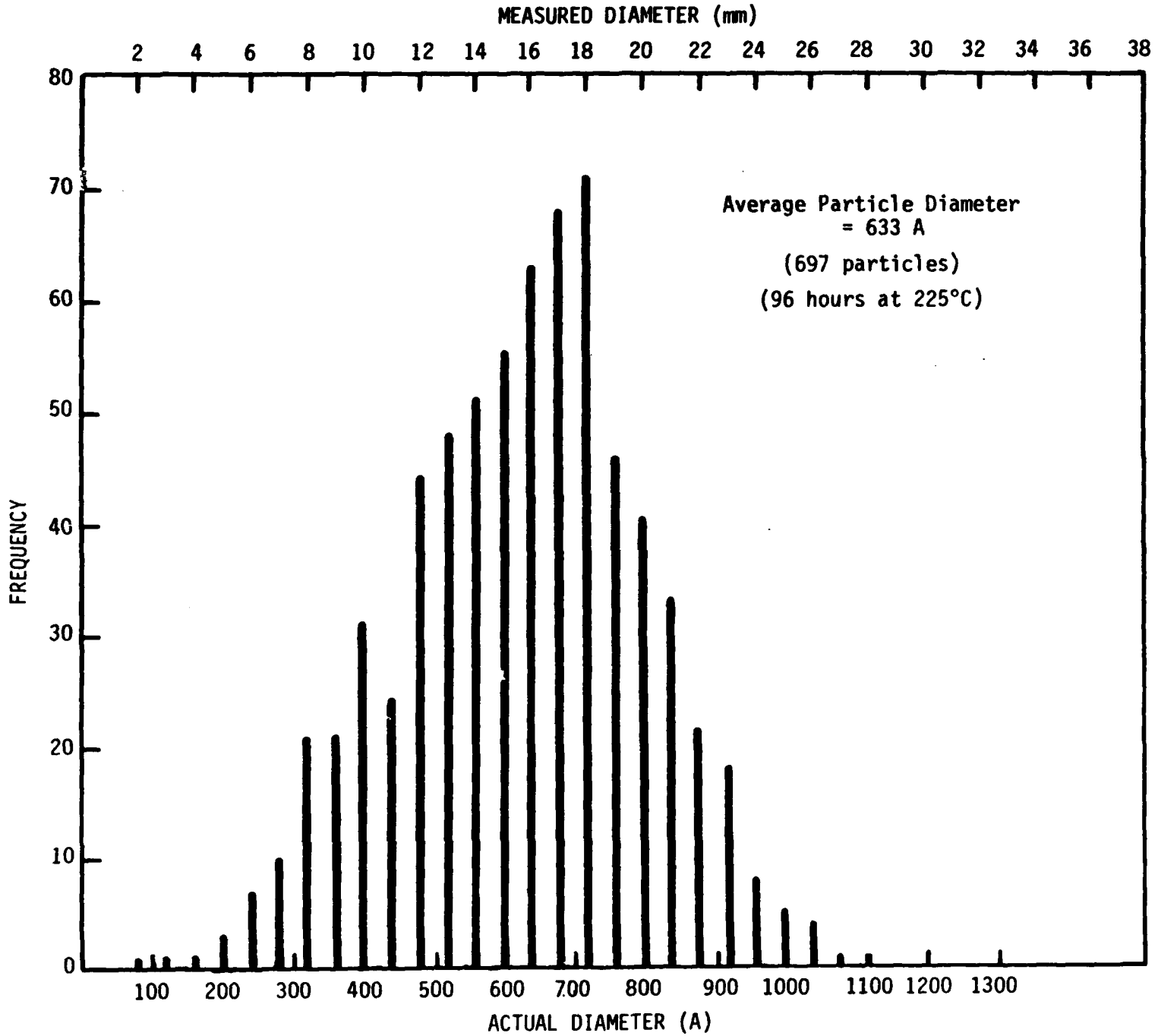

Figure A18. Particle size distribution function of δ' precipitates.

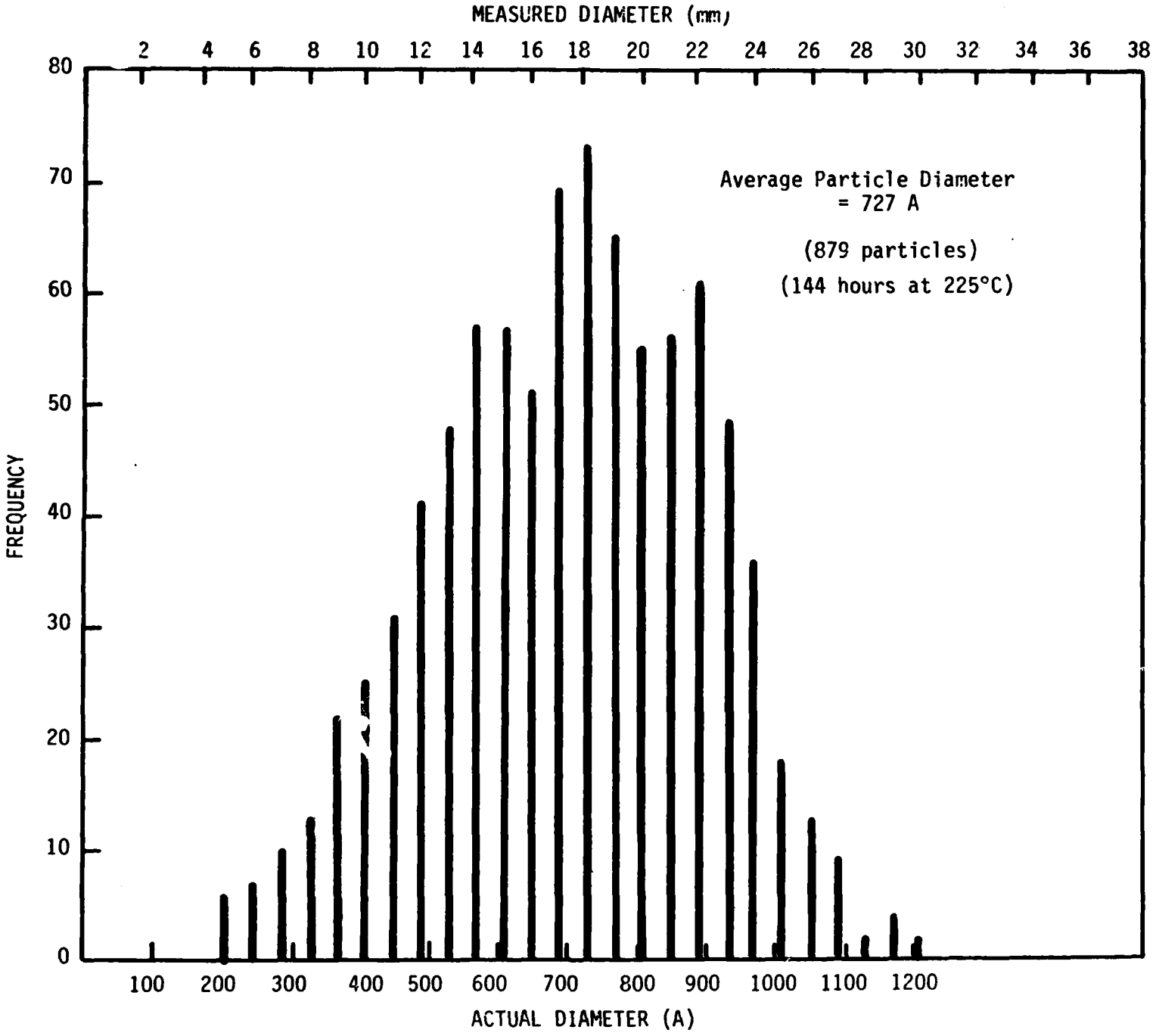

Figures A19. Particle size distribution function of δ′ precipitates.

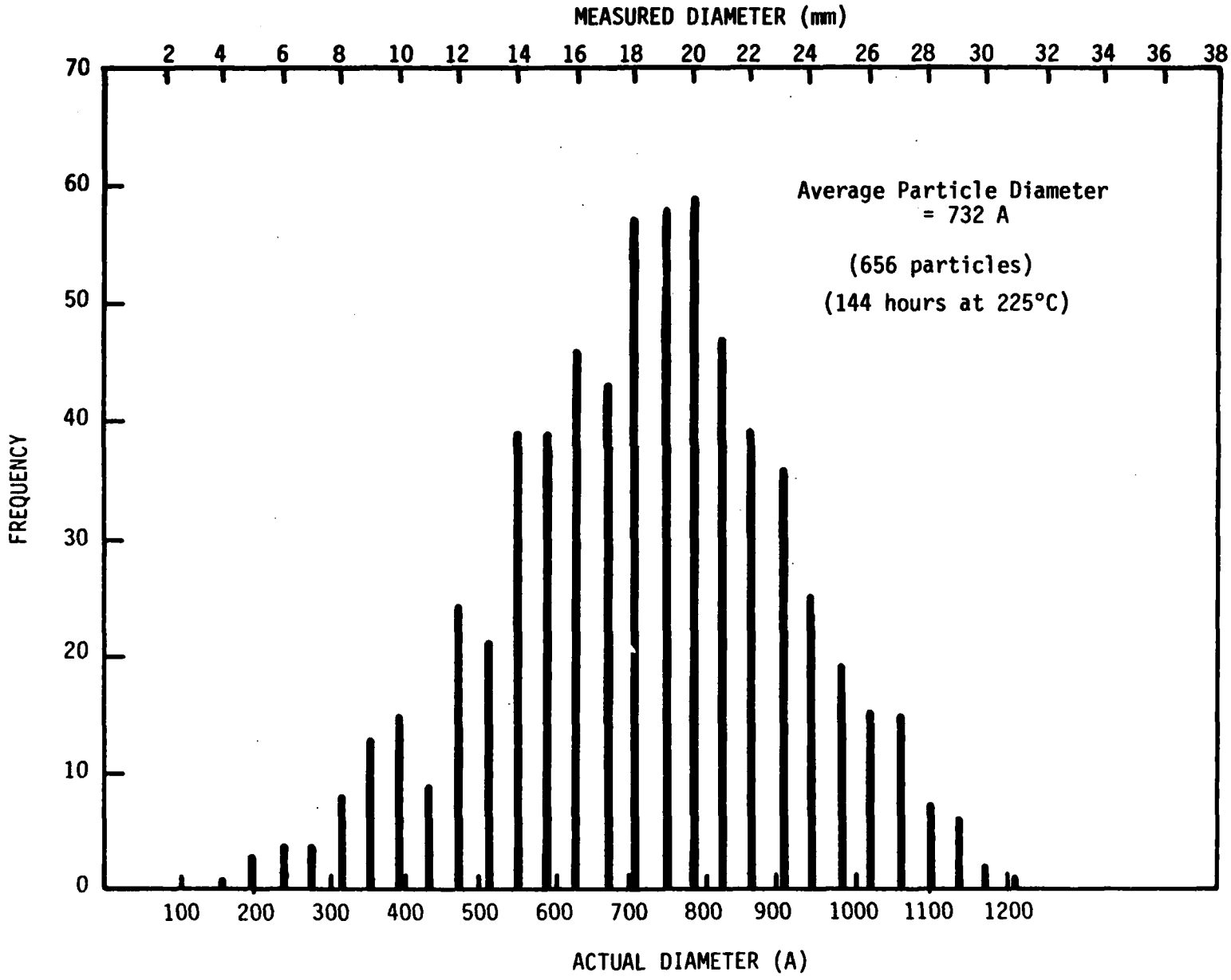

Figure A20. Particle size distribution function of δ´ precipitates.

Appendix B

Use of the Image Analyzing System (IAS)

The measurement of the size of precipitates using a photgraphic enlarger requires a great deal of time. To quicken the process a computer program was written to acquire and analyze the measurements obtained from an image analyzer. This program requires the entry of a specimen number, the magnification factor of the negatives (the magnification must be entered as a real number), the size of the standard line in cm, and the calibration of this standard line. The data consist of two sets of two measurements per particle, to account for the overall shape of the precipitate. The results are computed and stored in a data file which must be called to produce the results.

Using an aging condition of 2 weeks at 200°C as a test, the semi-automatic image analyzing system (IAS) produced a nearly identical value of $\bar{R}$ as compared to that done by hand. The intervals were much smaller, producing curves which were not as sharp. As a second test, a population consisting of 400 particles was measured for all aging times at 200°C, with results for $\bar{R}$ nearly the same as for the hand measured PSD's. The overall shape of the curves were again not as smooth as expected. This discontinuity is due to the size of the class intervals for the measurement. Too small of class intervals will produce a PSD with no readily identifiable shape. There will not be enough

values at a particlur measurement to generate an identifiable PSD. This will place doubt upon the form of the PSD, even it larger numbers of particles are measured.

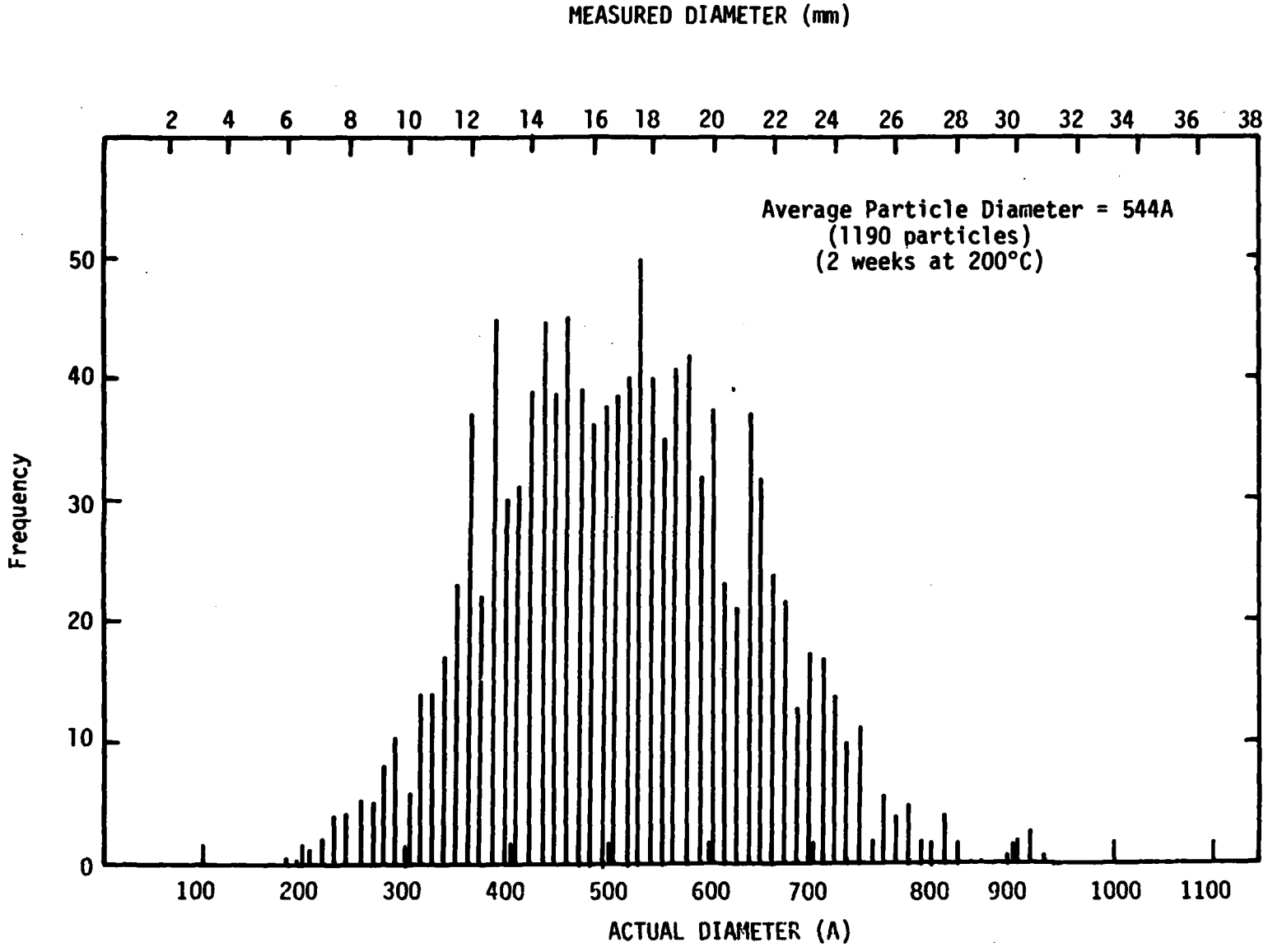

Figure B1. Particle size distribution function measured by image analyzer.

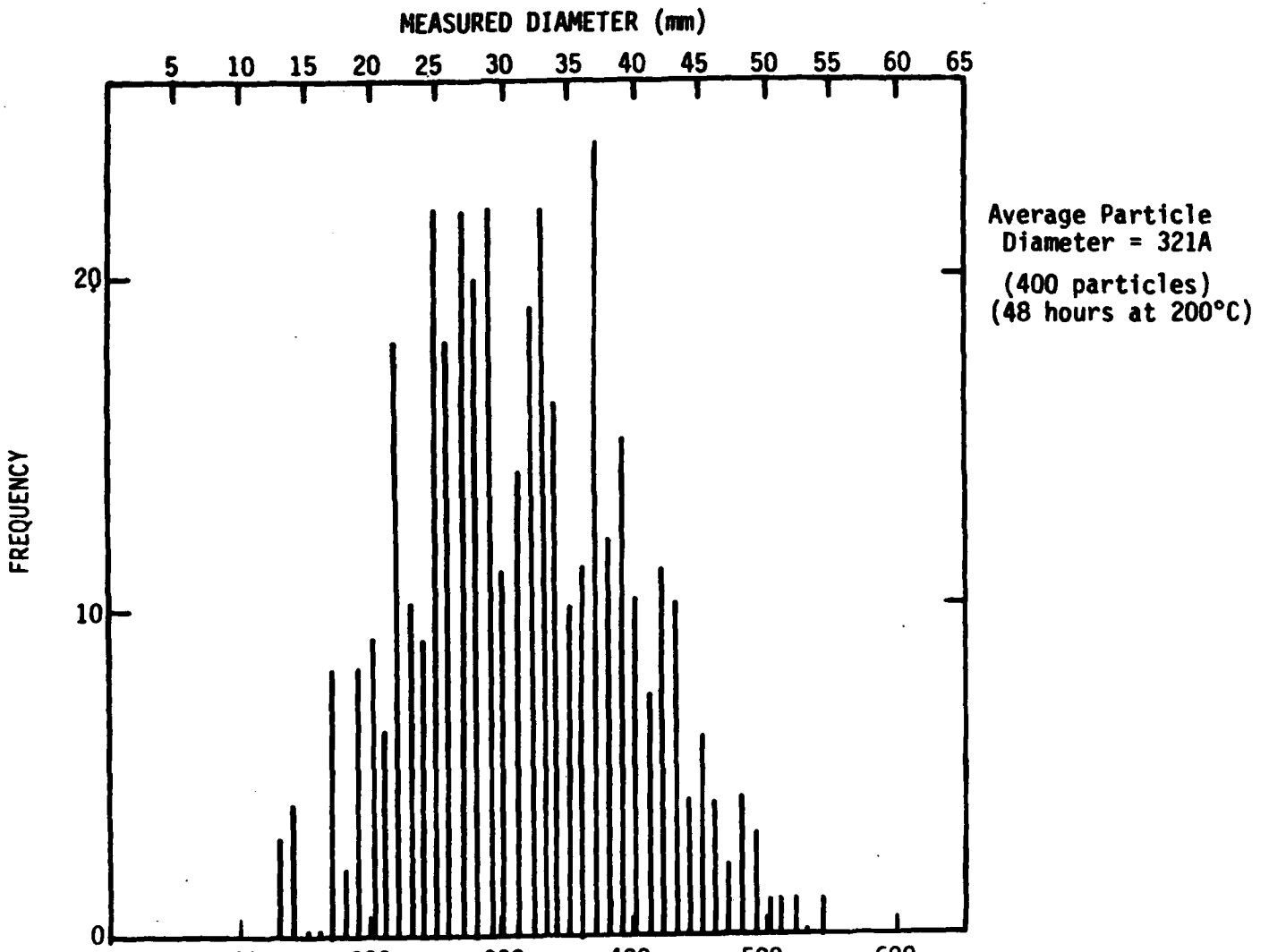

Figure B2. Particle size distribution function measured by image analyzer using 400 particle standard.

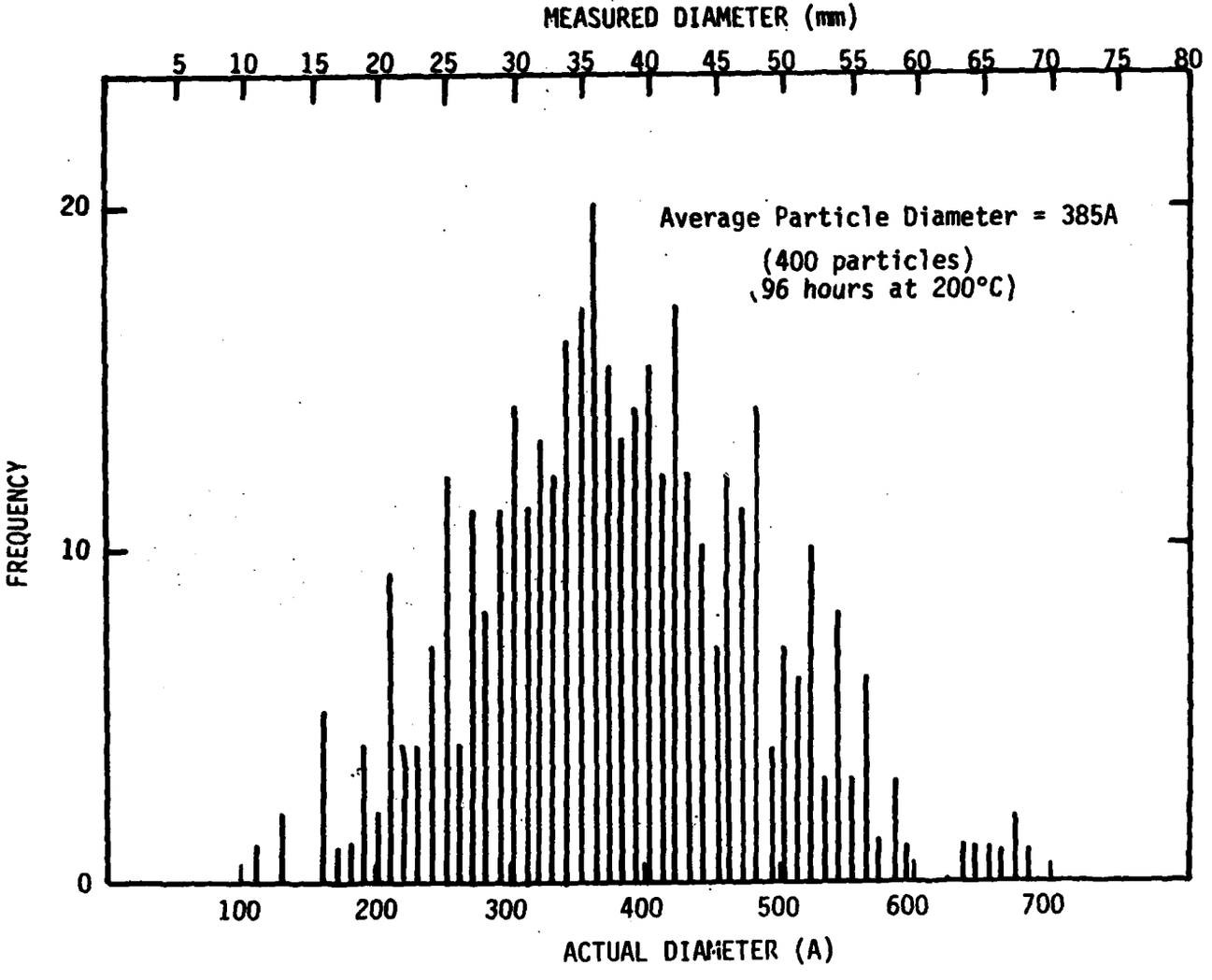

Figure B3. Particle size distribution function measured by image analyzer using 400 particle standard.

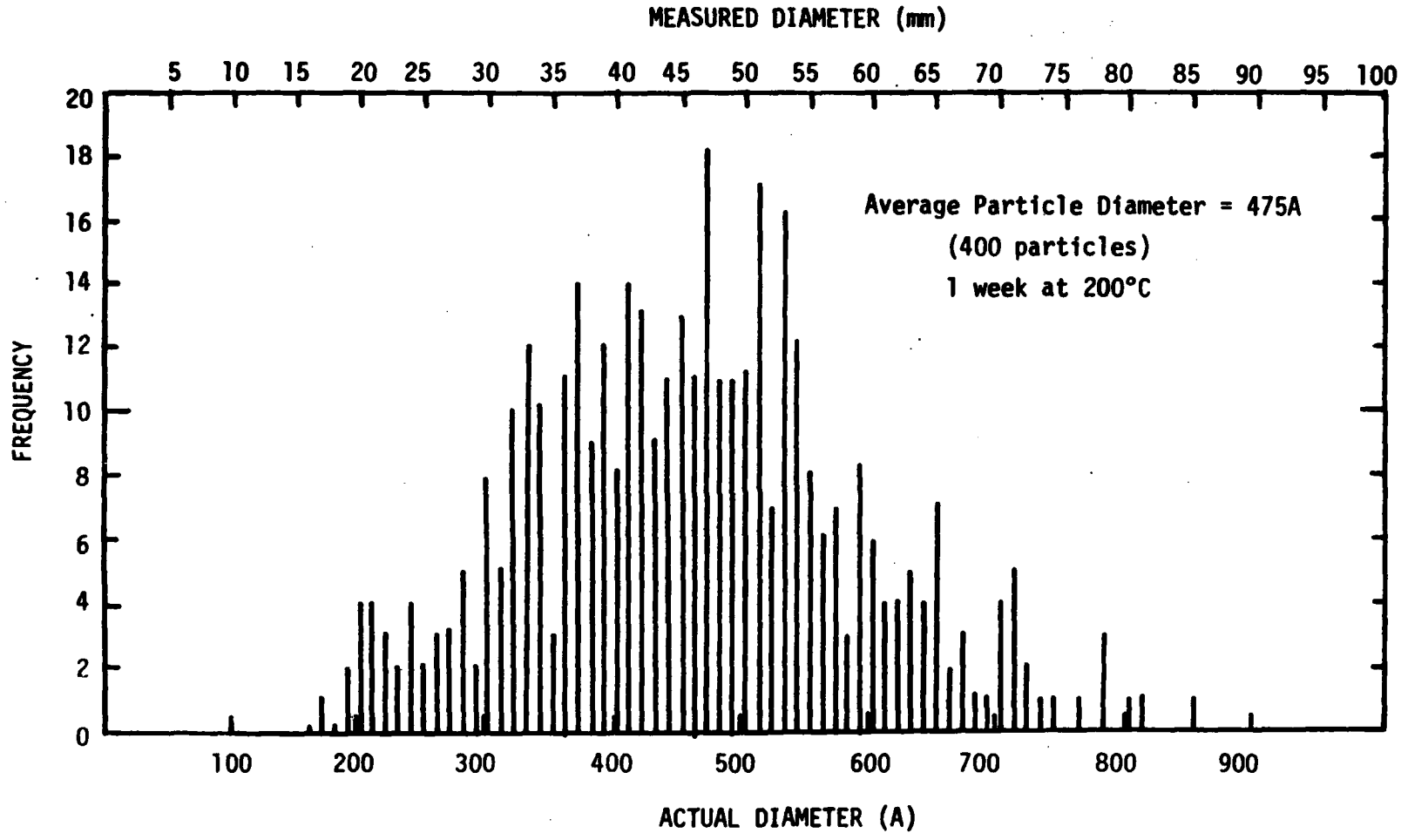

Figure B4. Particle size distribution function measured by image analyzer using 400 particle standard.

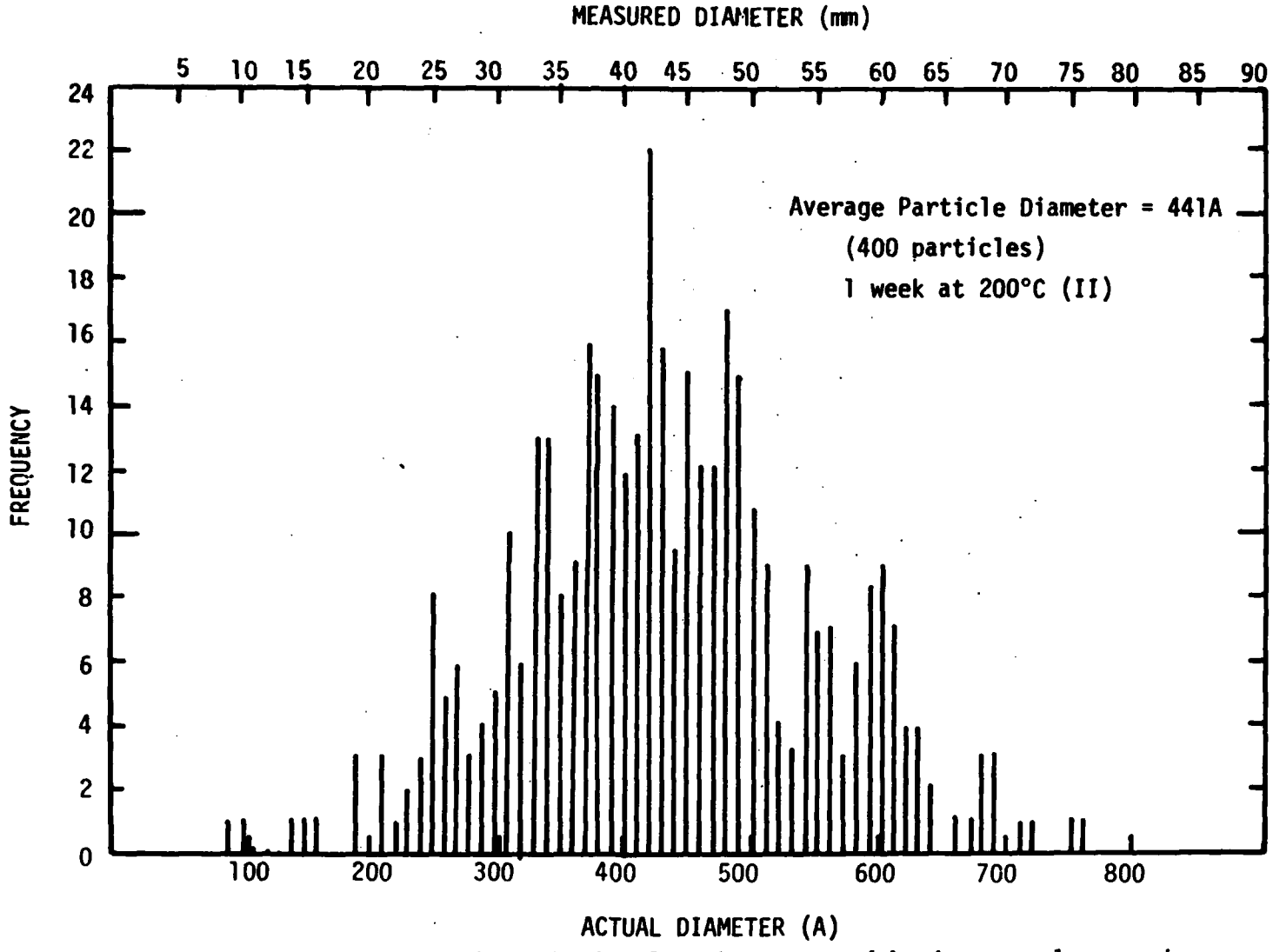

Figure B5. Particle size distribution function measured by image analyzer using 400 particle standard.

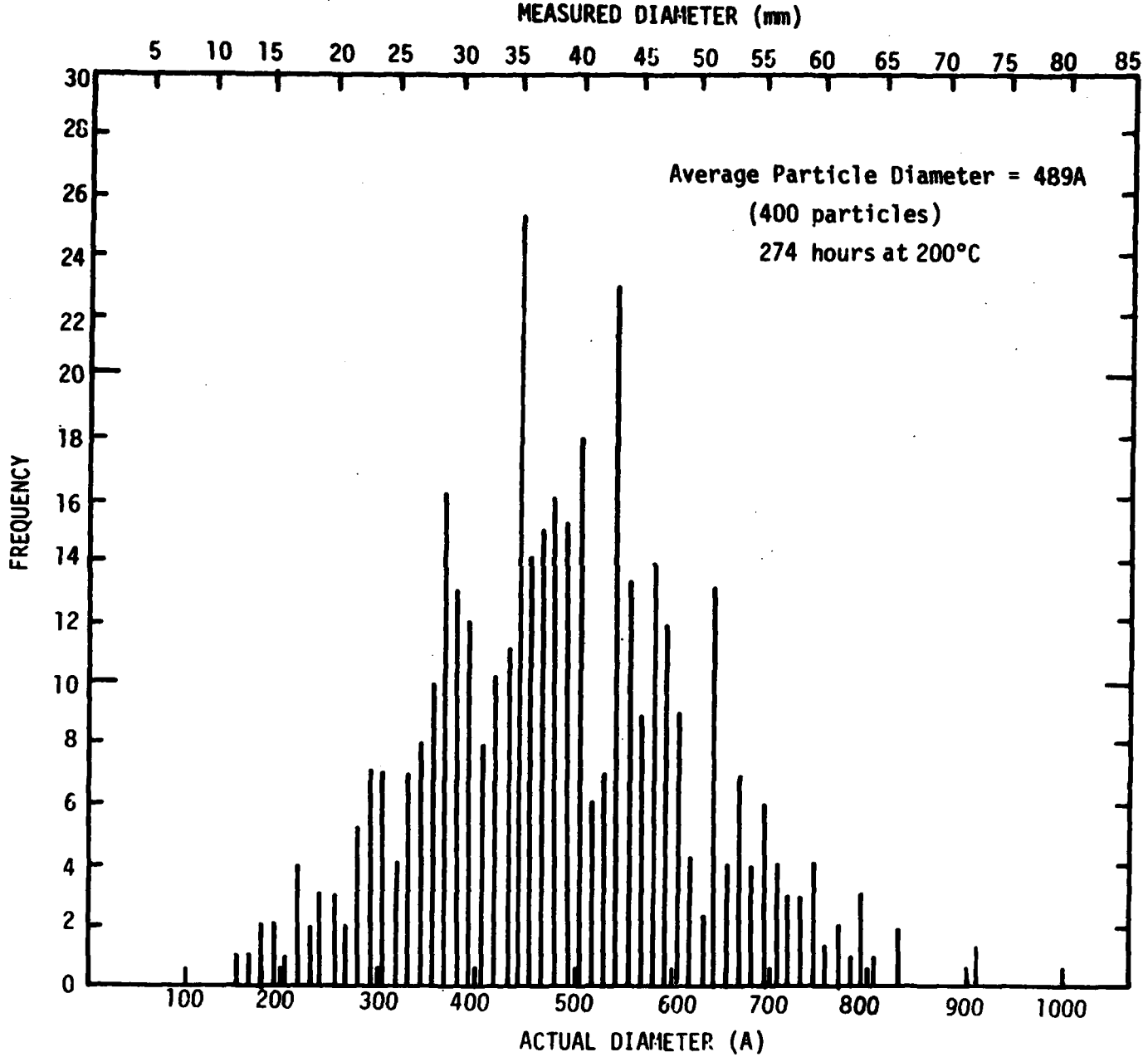

Figure B6. Particle size distribution function measured by image analyzer using 400 particle standard.

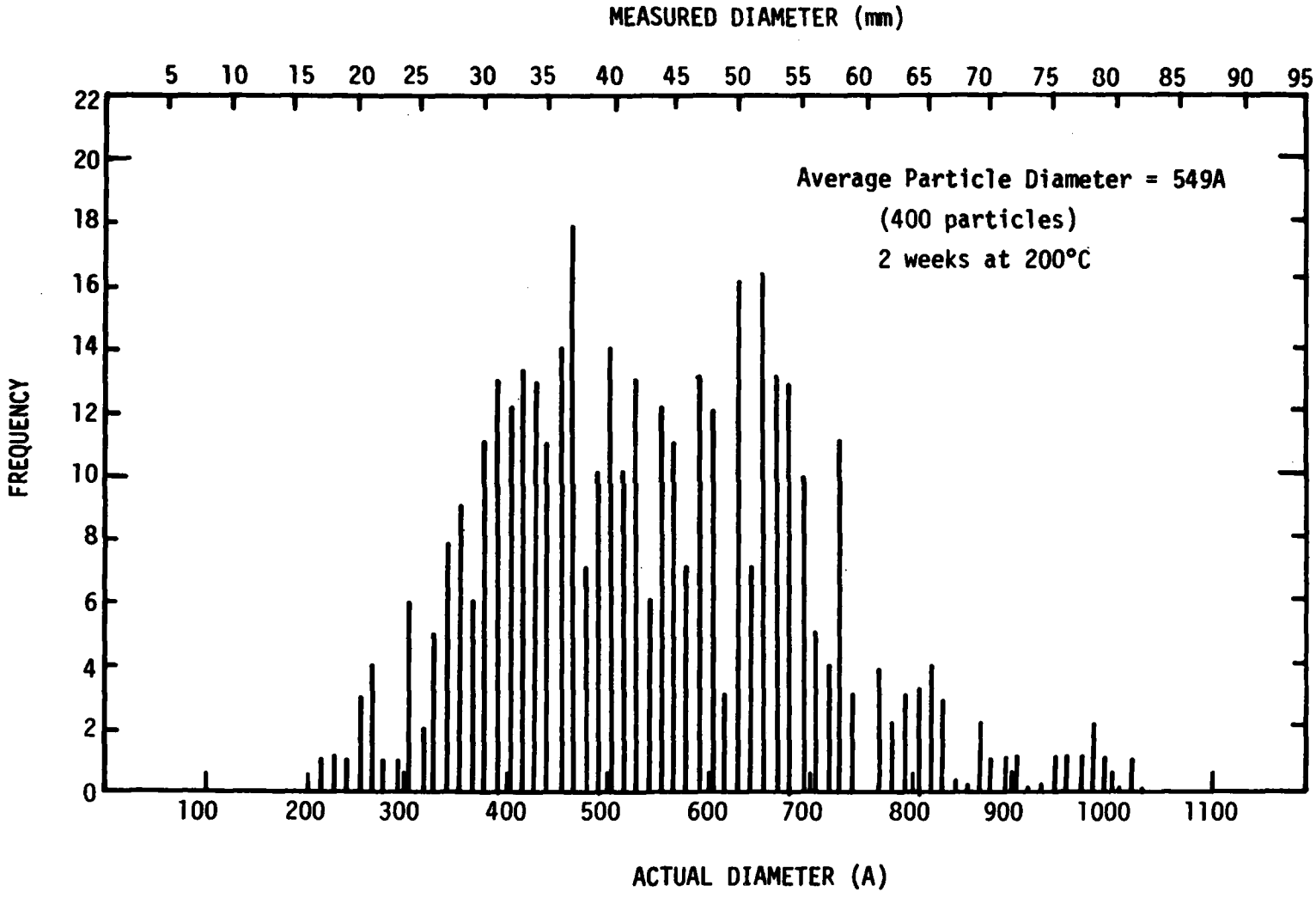

Figure B7. Particle size distribution function measured by image analyzer using 400 particle standard.

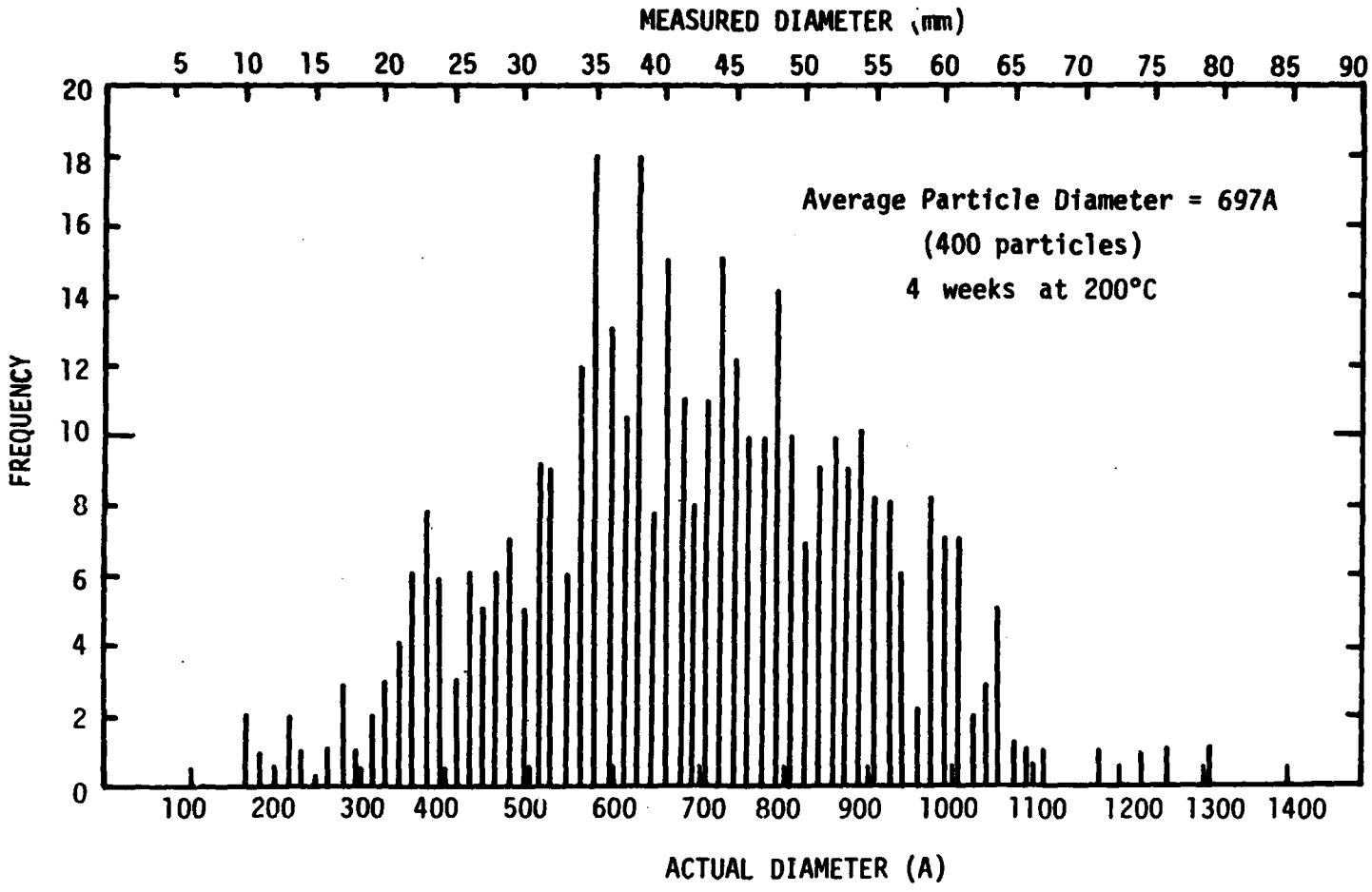

Figure B8. Particle size distribution function measured by image analyzer using 400 particle standard.

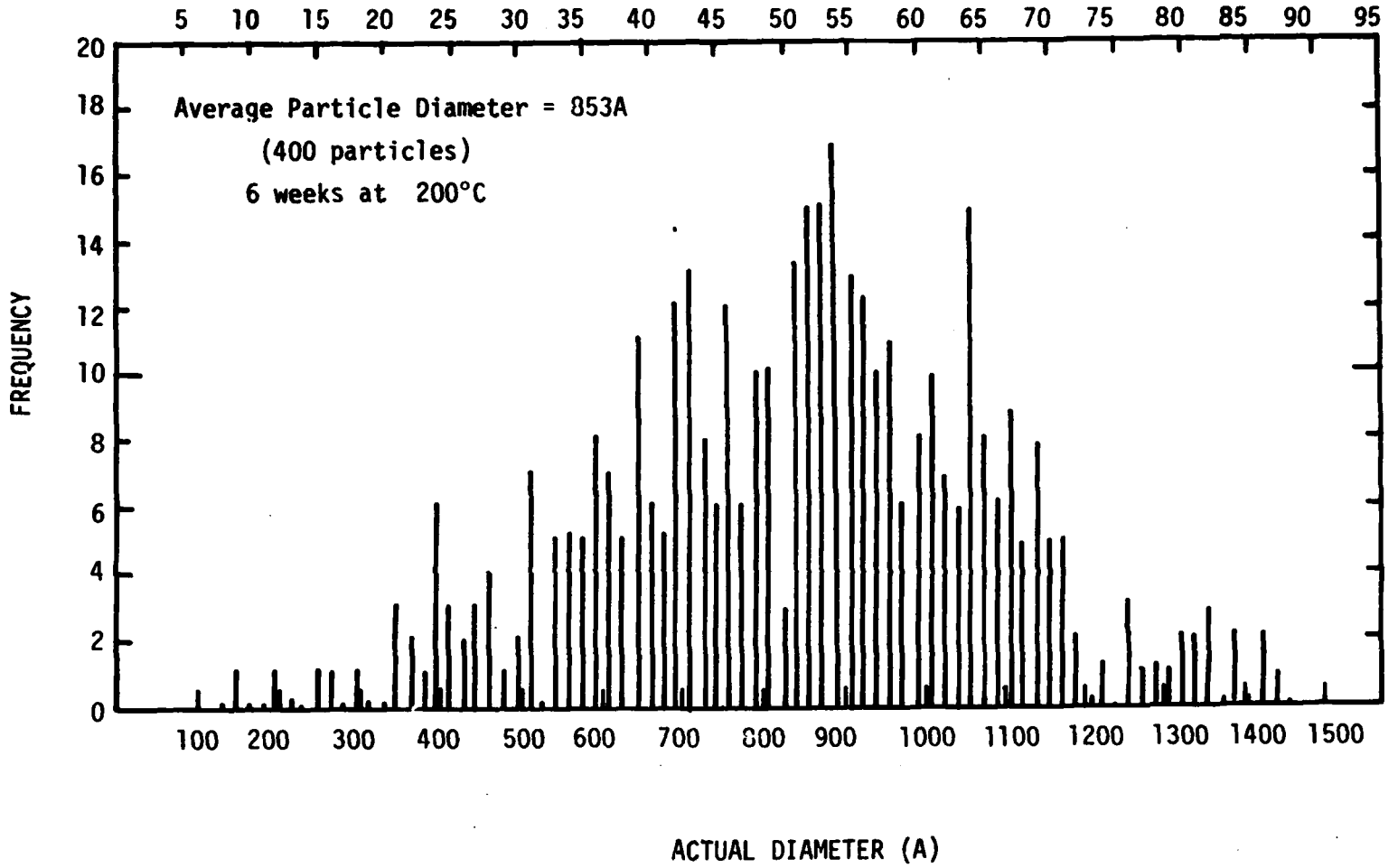

Figure B9. Particle size distribution function measured by image analyzer using 400 particle standard.

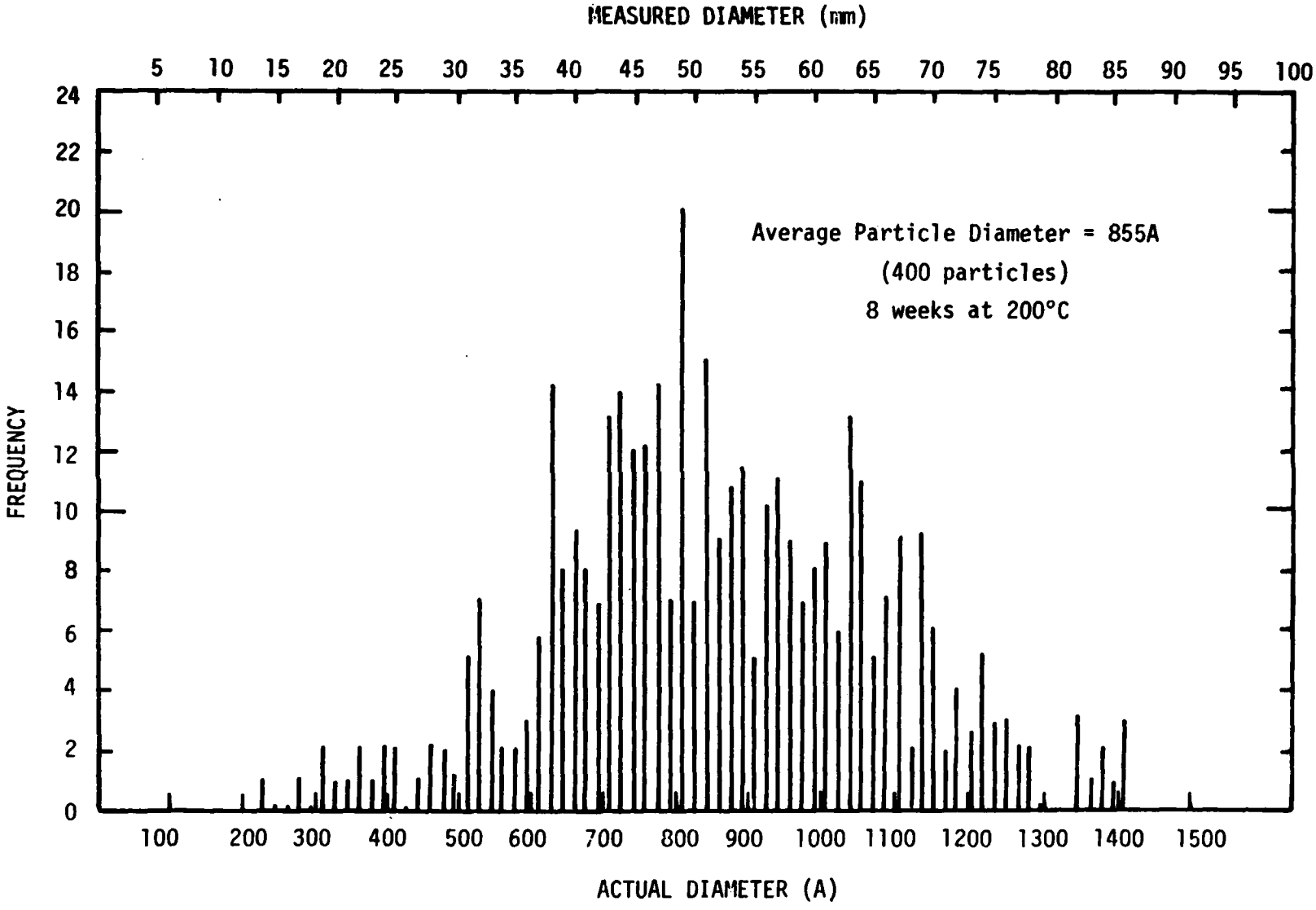

Figure B10. Particle size distribution function measured by image analyzer using 400 particle standard.

Appendix C

Computer Program for Image Analyzer

The following is the computer program used to measure and compile data read from the image analyzer. This program contains the instructions to make the measurements, store the raw data in a two dimensional array and analyzes the raw data. The output contains the final size distribution along with calculated values of $\overline{R}$ in Angstrom units and the total number of precipitate particles.

Appendix D

Effect of Interval Size Upon PSD Measurements

The measured interval size was varied to determine the effect of measuring interval size on the experimental PSD's. The two aging conditions which had the most data points were used for the analysis - 2 weeks at 200°C and 36 hours at 225°C. The measurements were taken to the nearest 1mm as described in Appendix A. The new class interval sizes were formed by the combination of the results from the initial 1mm wide intervals into larger 2, 3, and 4mm wide intervals. These new intervals in the figures are identified by the numerically greatest measurement within the newly defined class interval. As an example, the value 16 mm for the 4 mm interval will include the 1 mm measurements of 13, 14, 15, and 16 mm.

The increase in interval size did not dramatically change the overall shape of the PSD's, but the mean value, $\bar{R}$, was consistently increased at both aging conditions examined. This increase in $\bar{R}$ may be due to the round-up which occured when the new intervals were constructed from the 1 mm measurements.

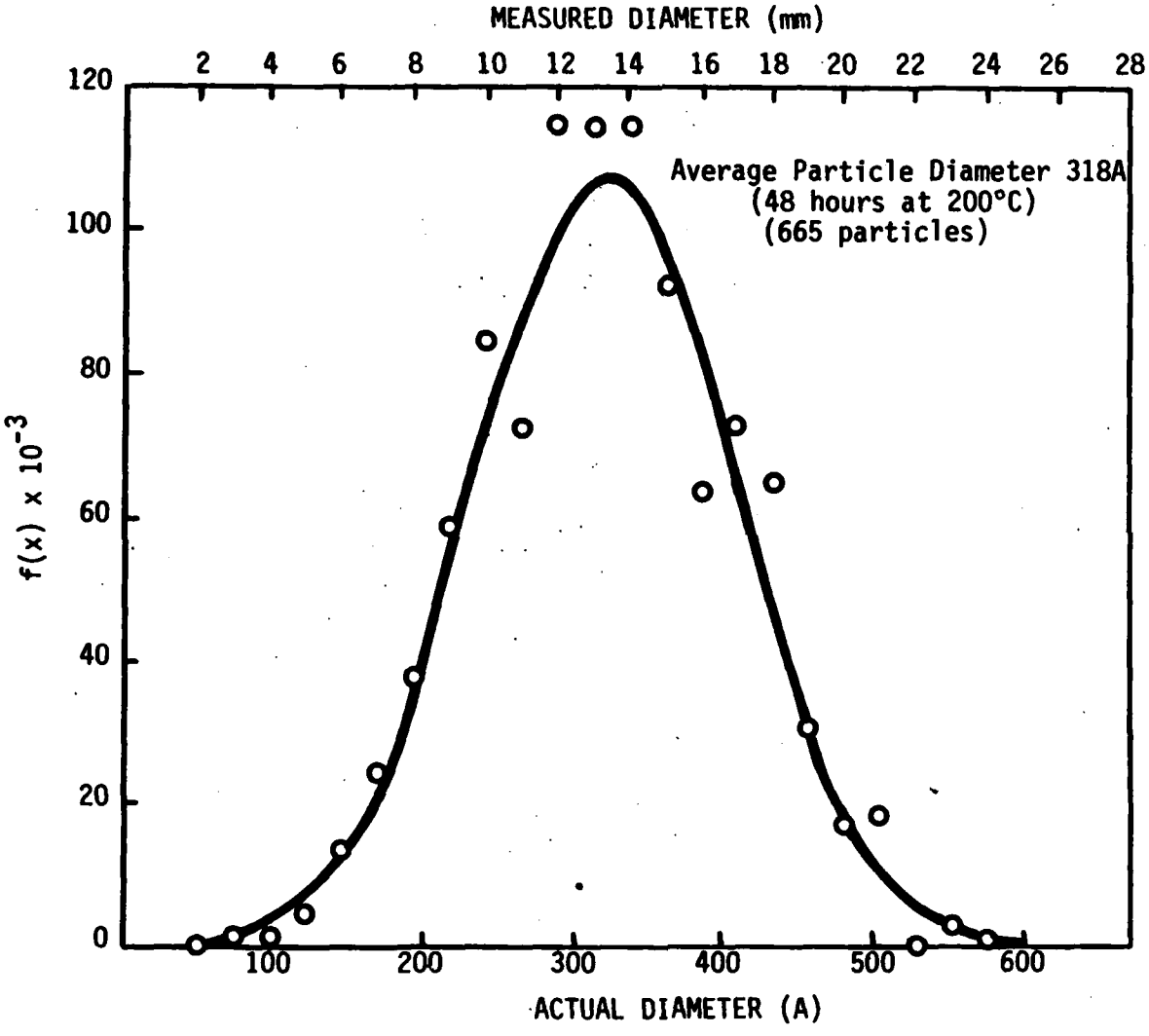

Figure D1. PSD with generated normal curve.

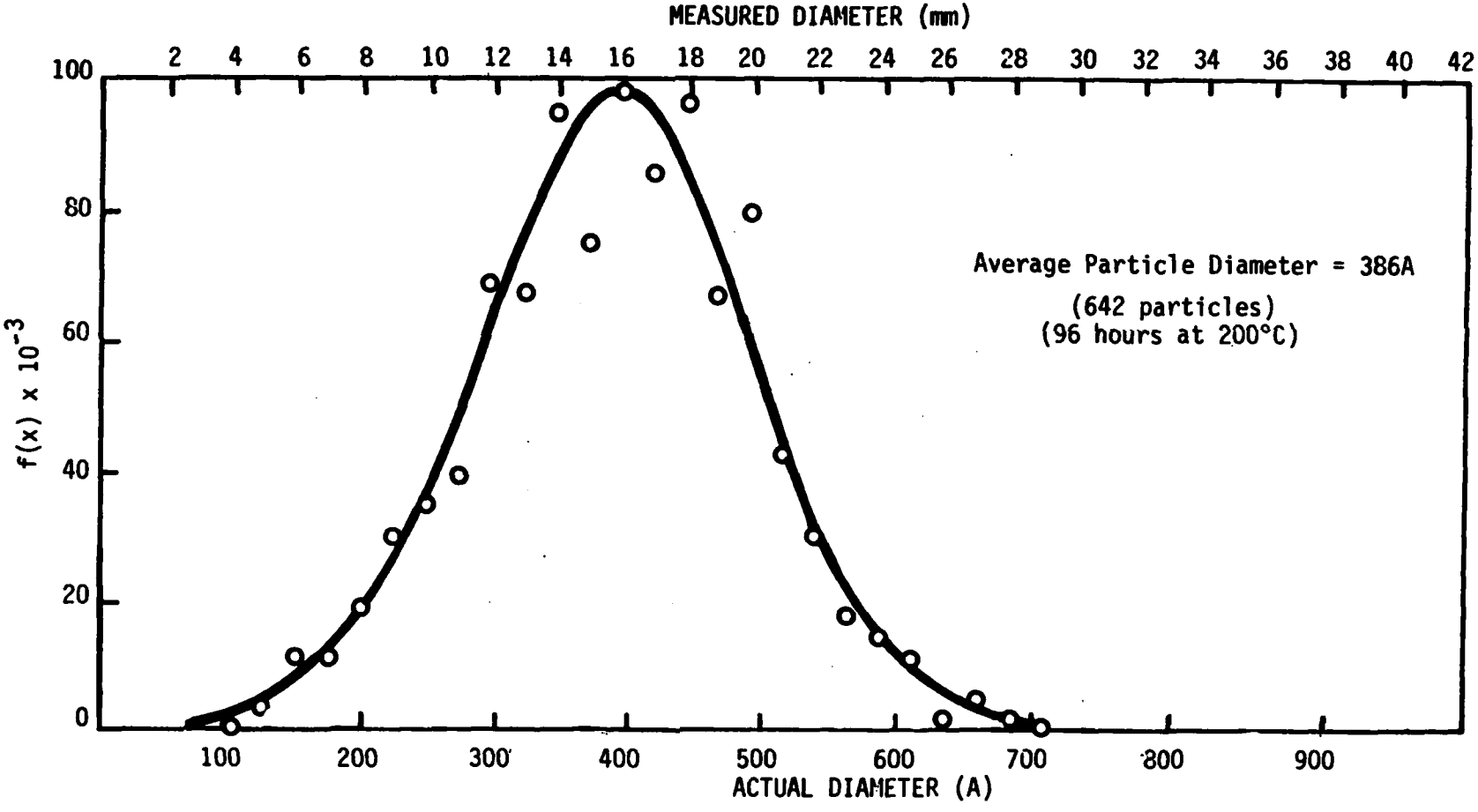

Figure D2. PSD with generated normal curve.

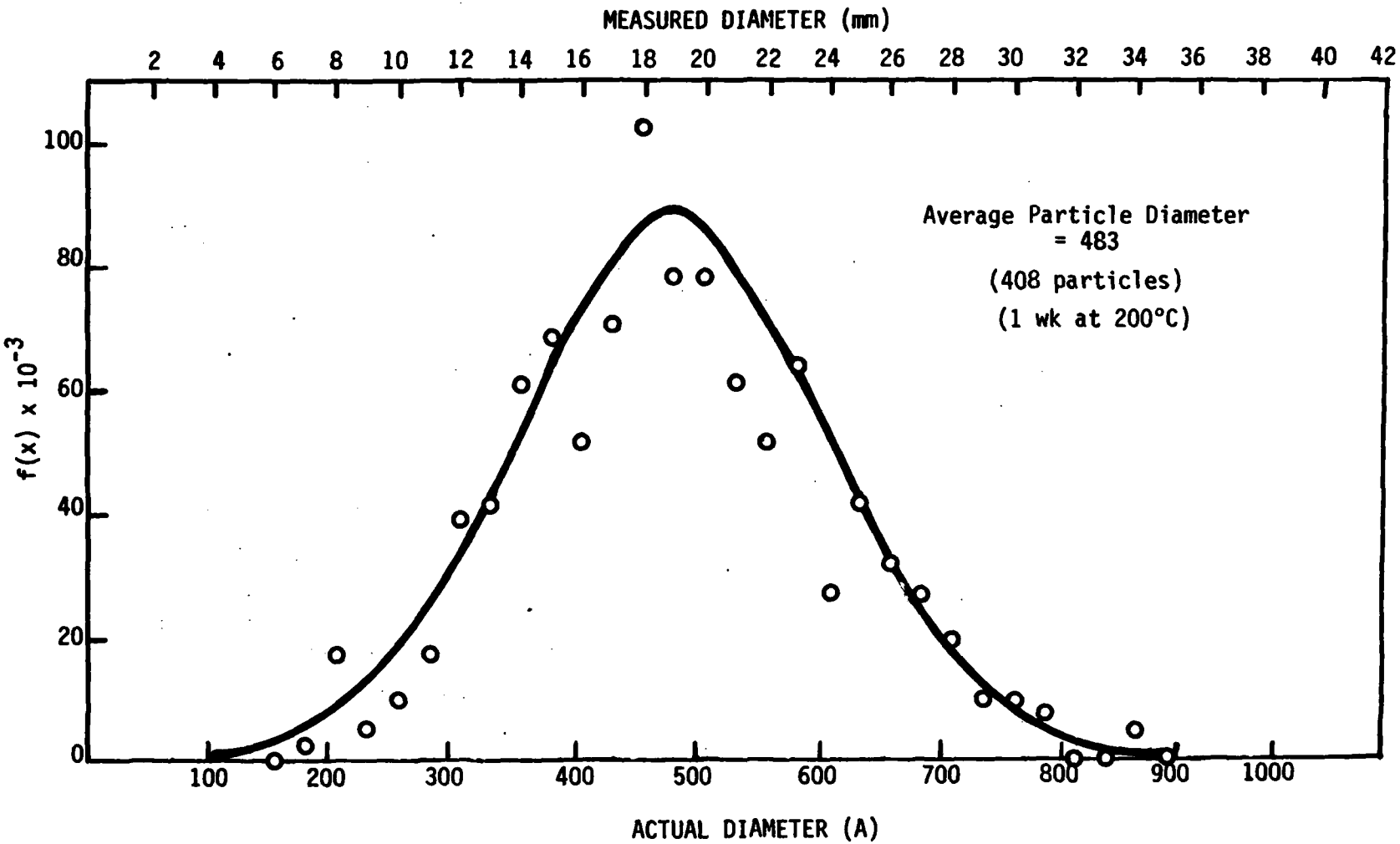

Figure D3. PSD with generated normal curve.

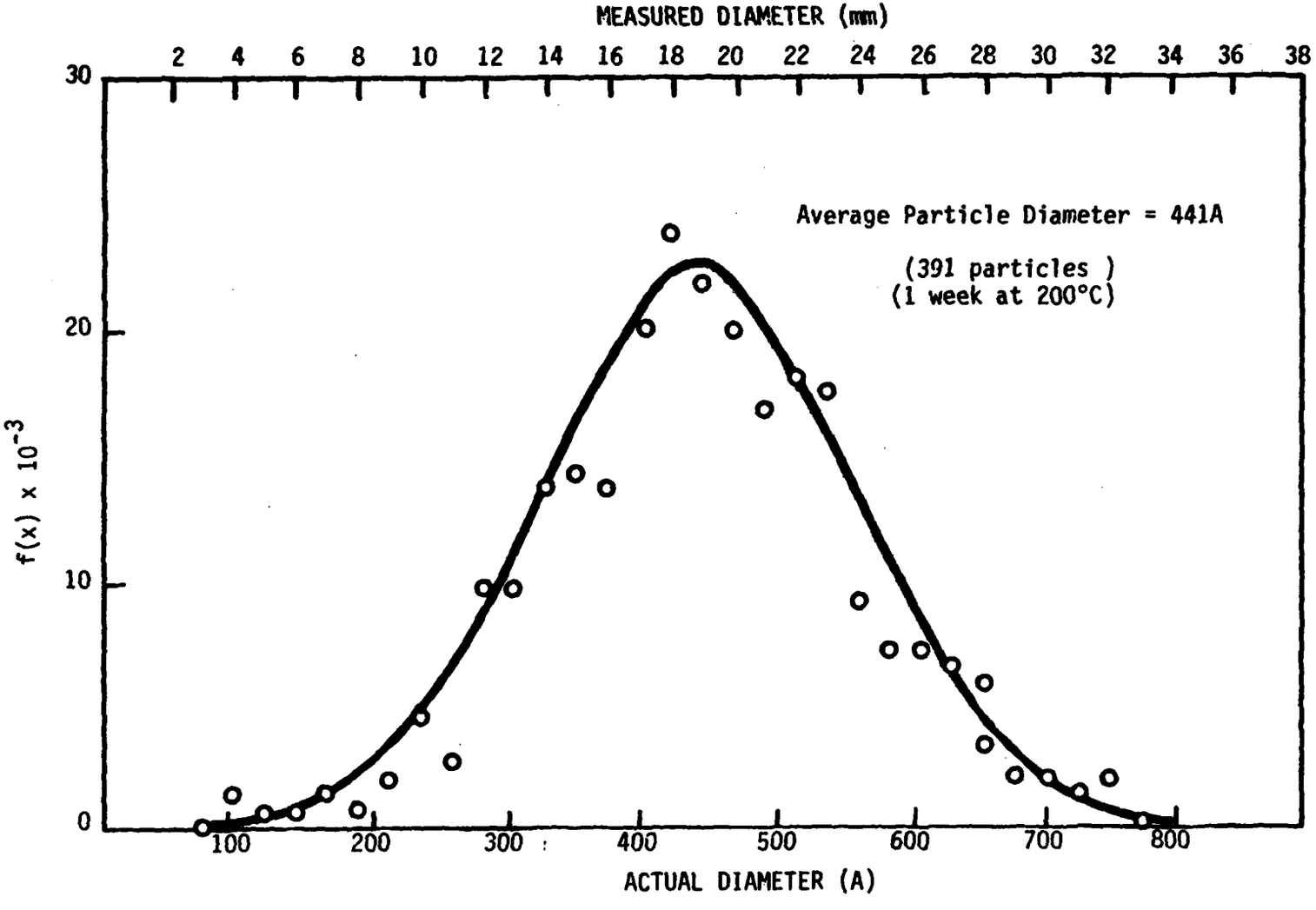

Figure D4. PSD with generated normal curve.

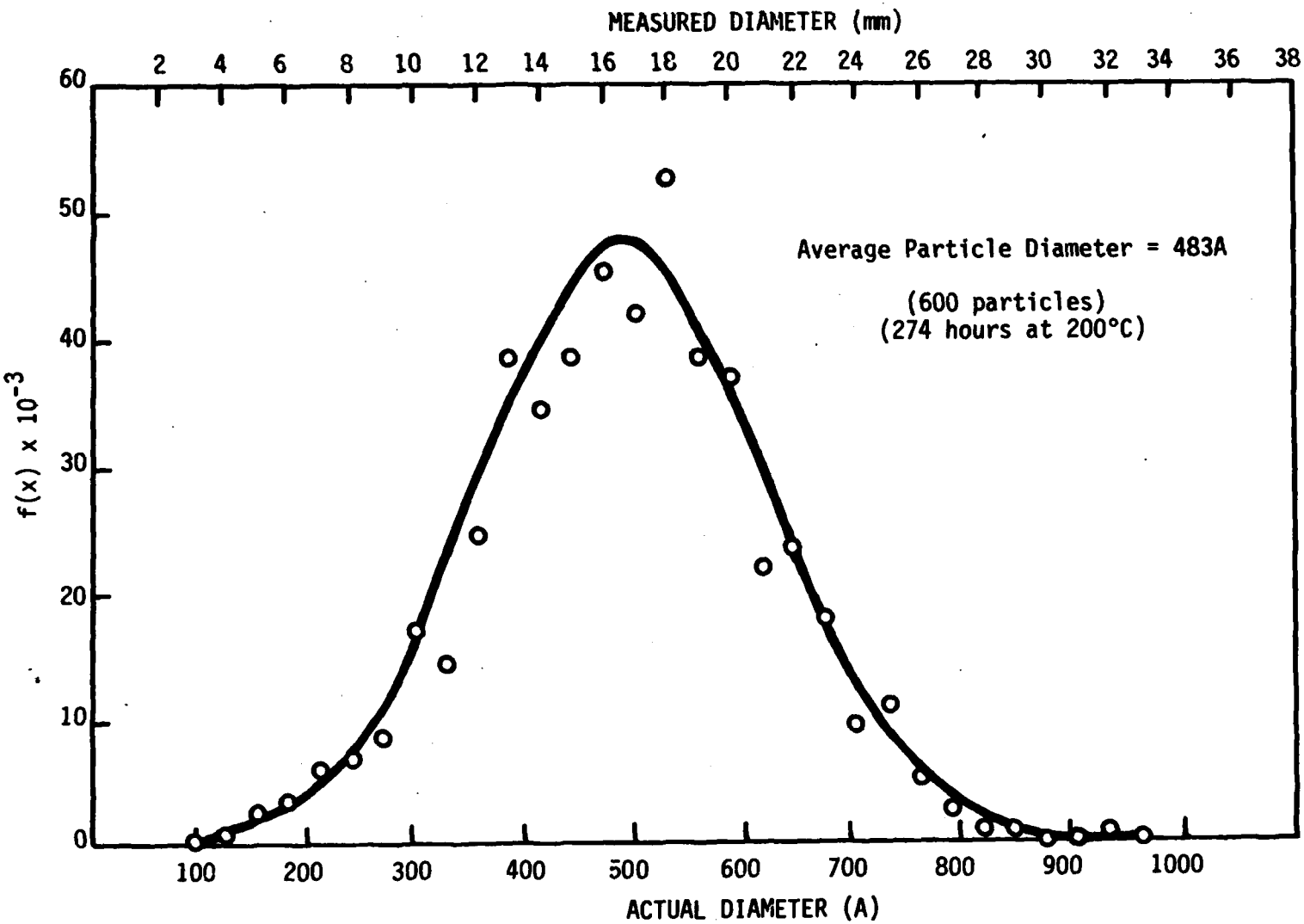

Figure D5. PSD with generated normal curve.

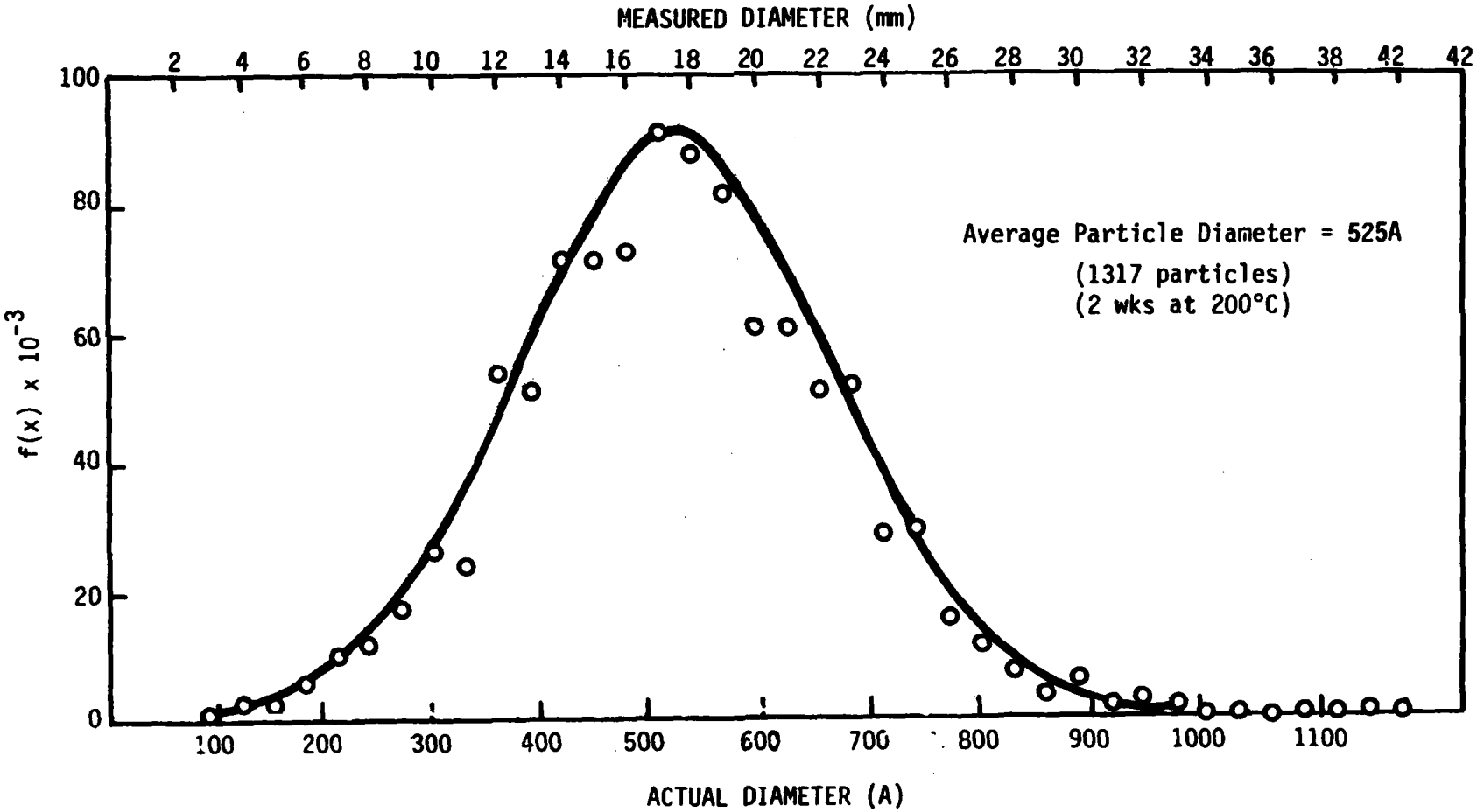

Figure D6. PSD with generated normal curve.

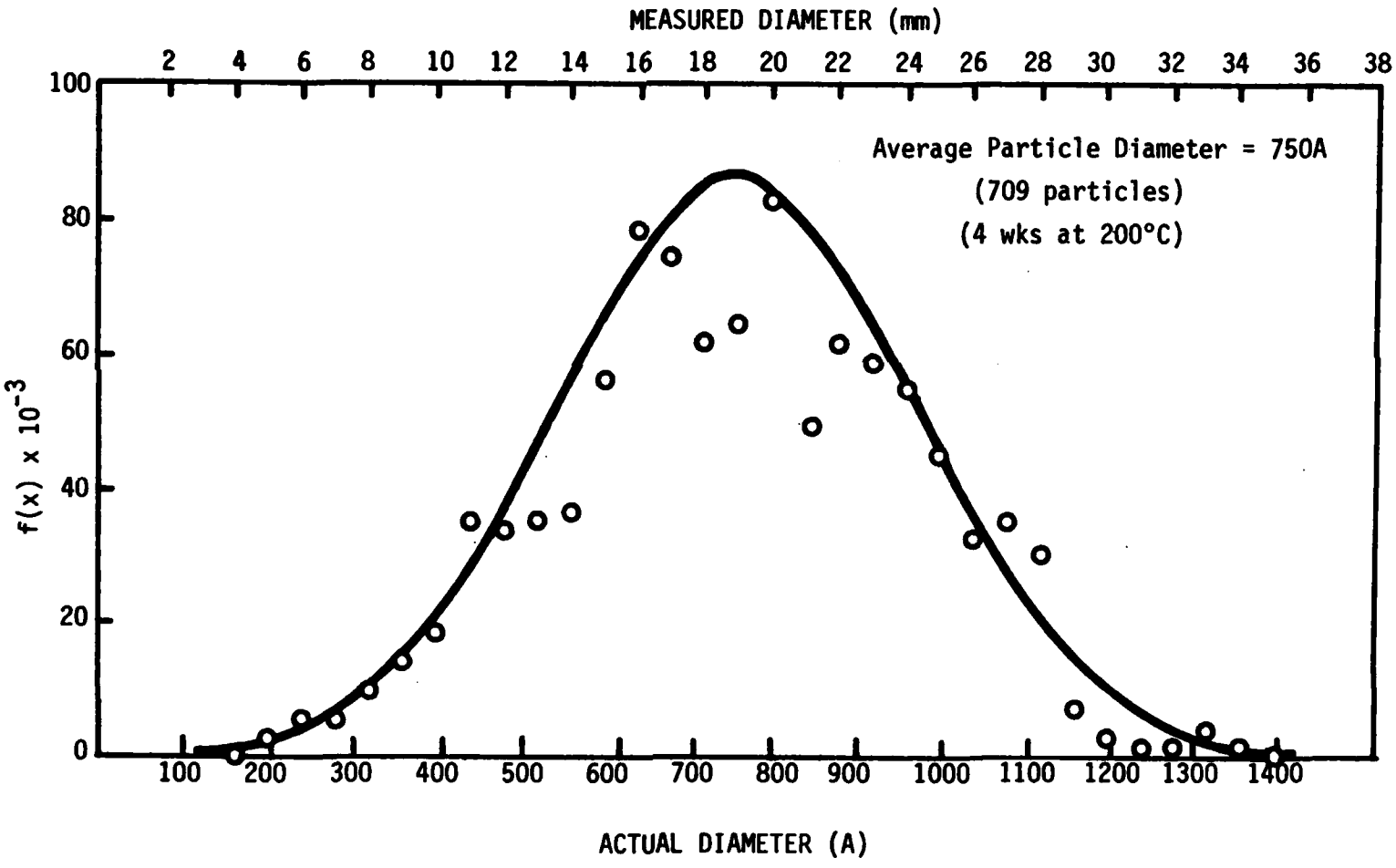

Figure D7. PSD with generated normal curve.

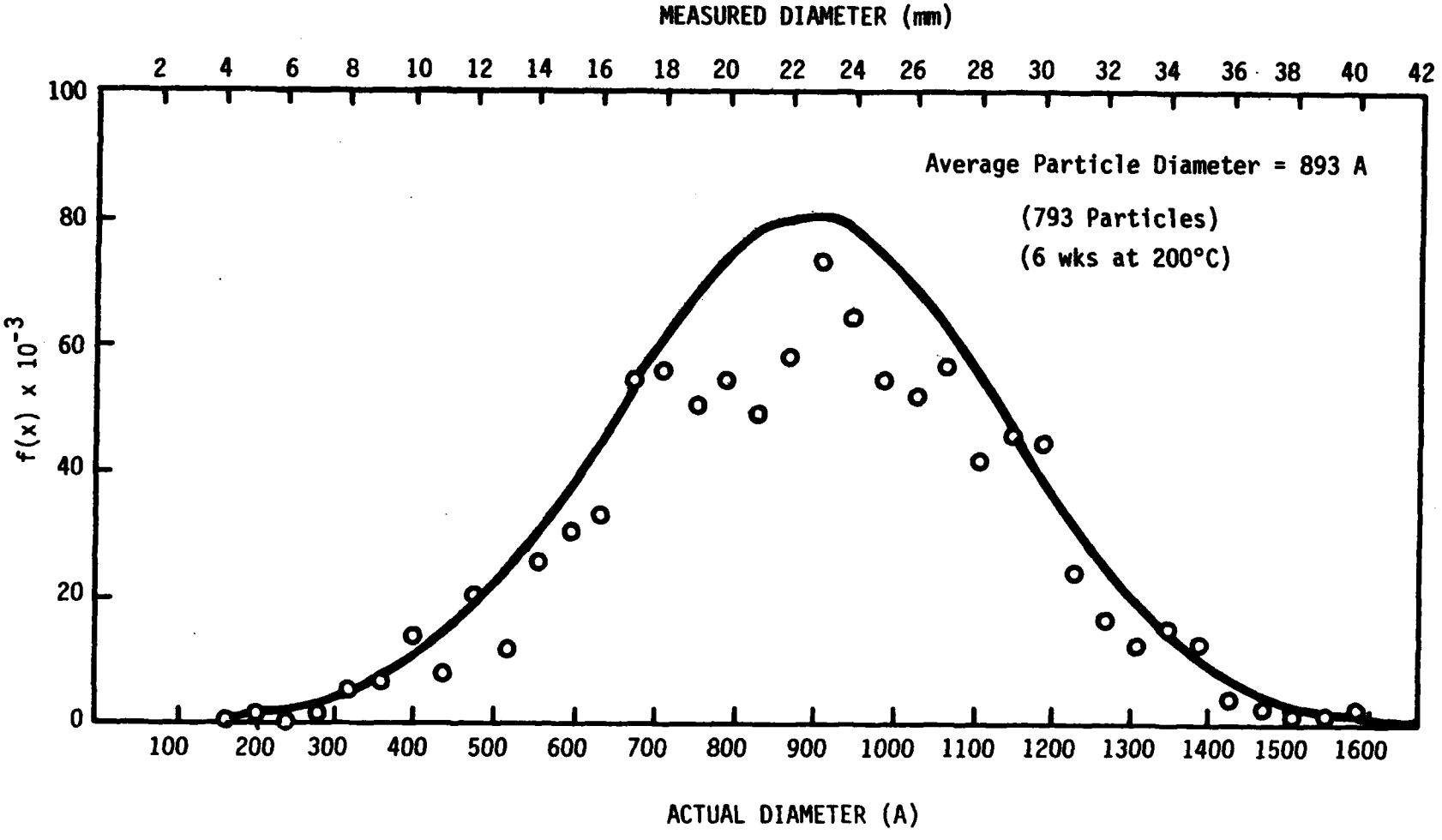

Figure D8. [illegible] with generated normal curve.

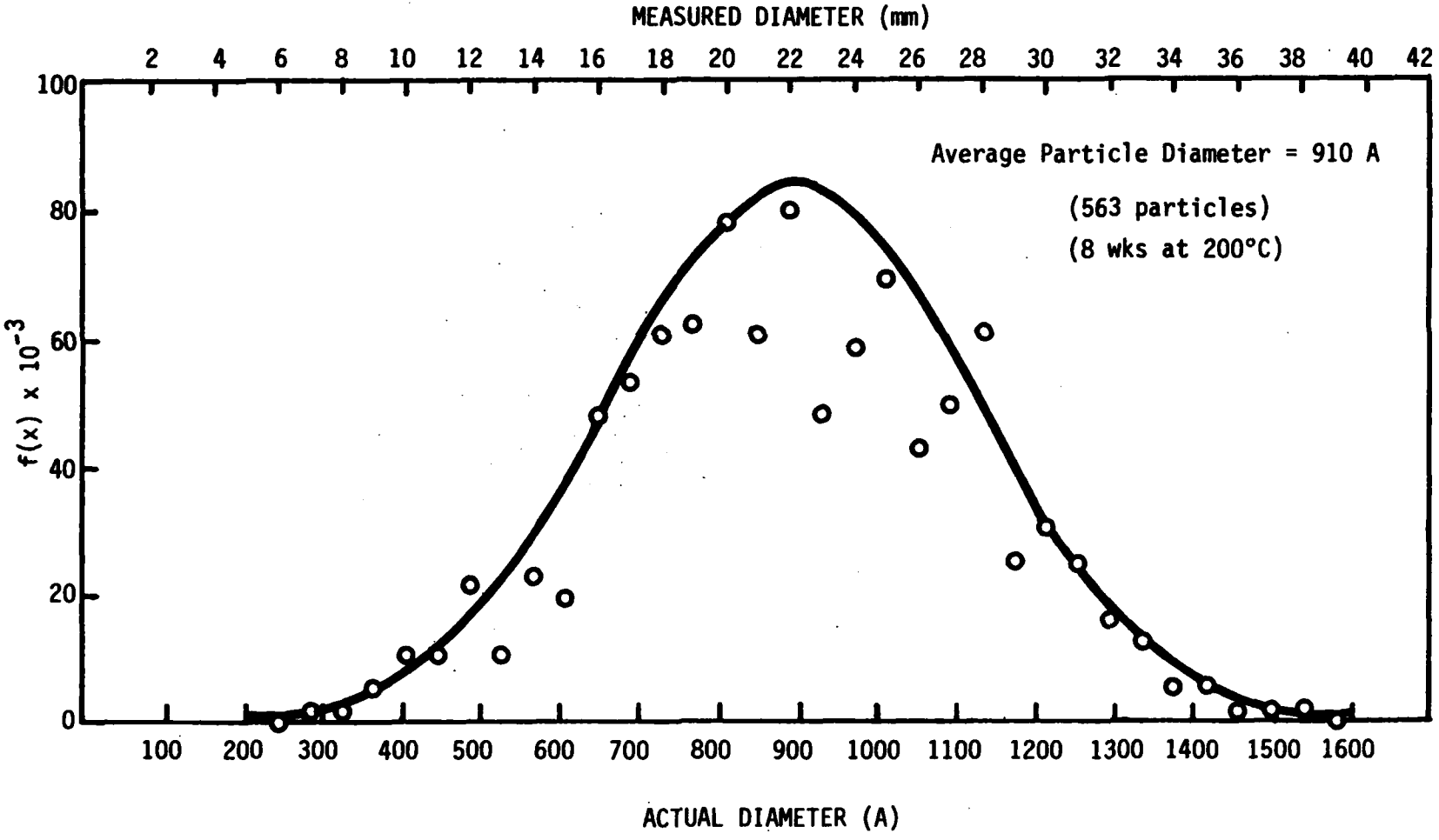

Figure D9. PSD with generated normal curve.

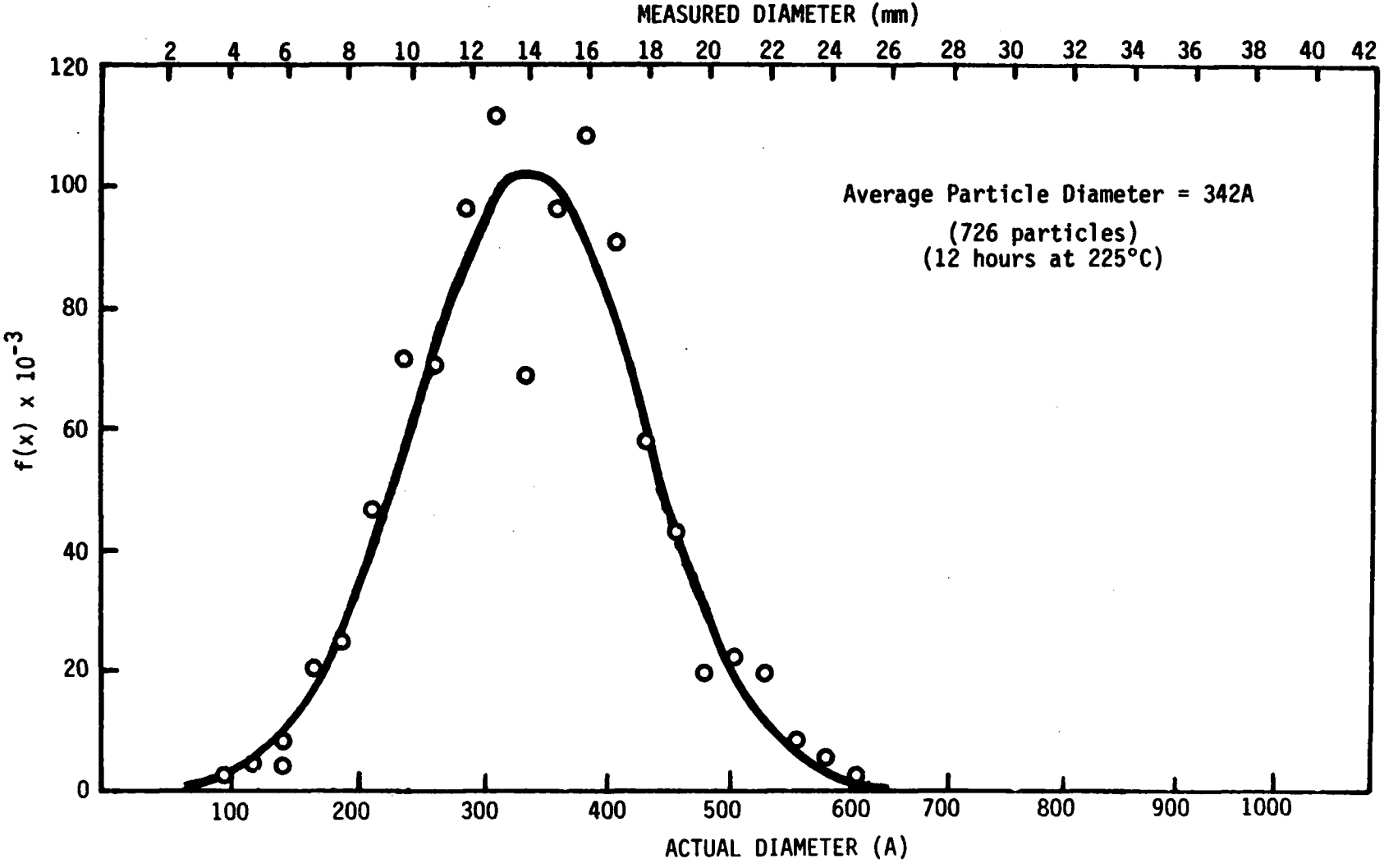

Figure D10. PSD with generated normal curve.

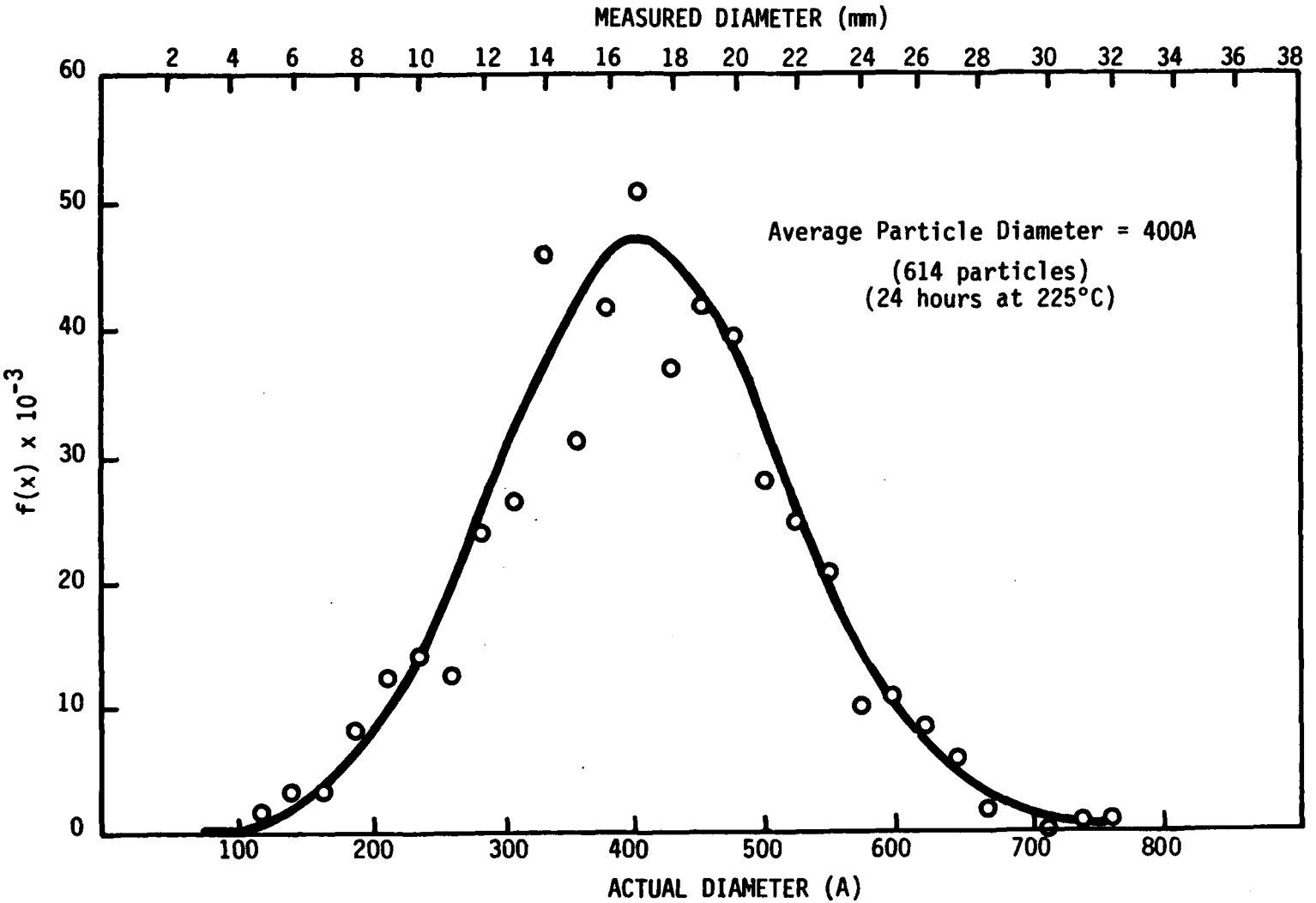

Figure D11. PSD with generated normal curve.

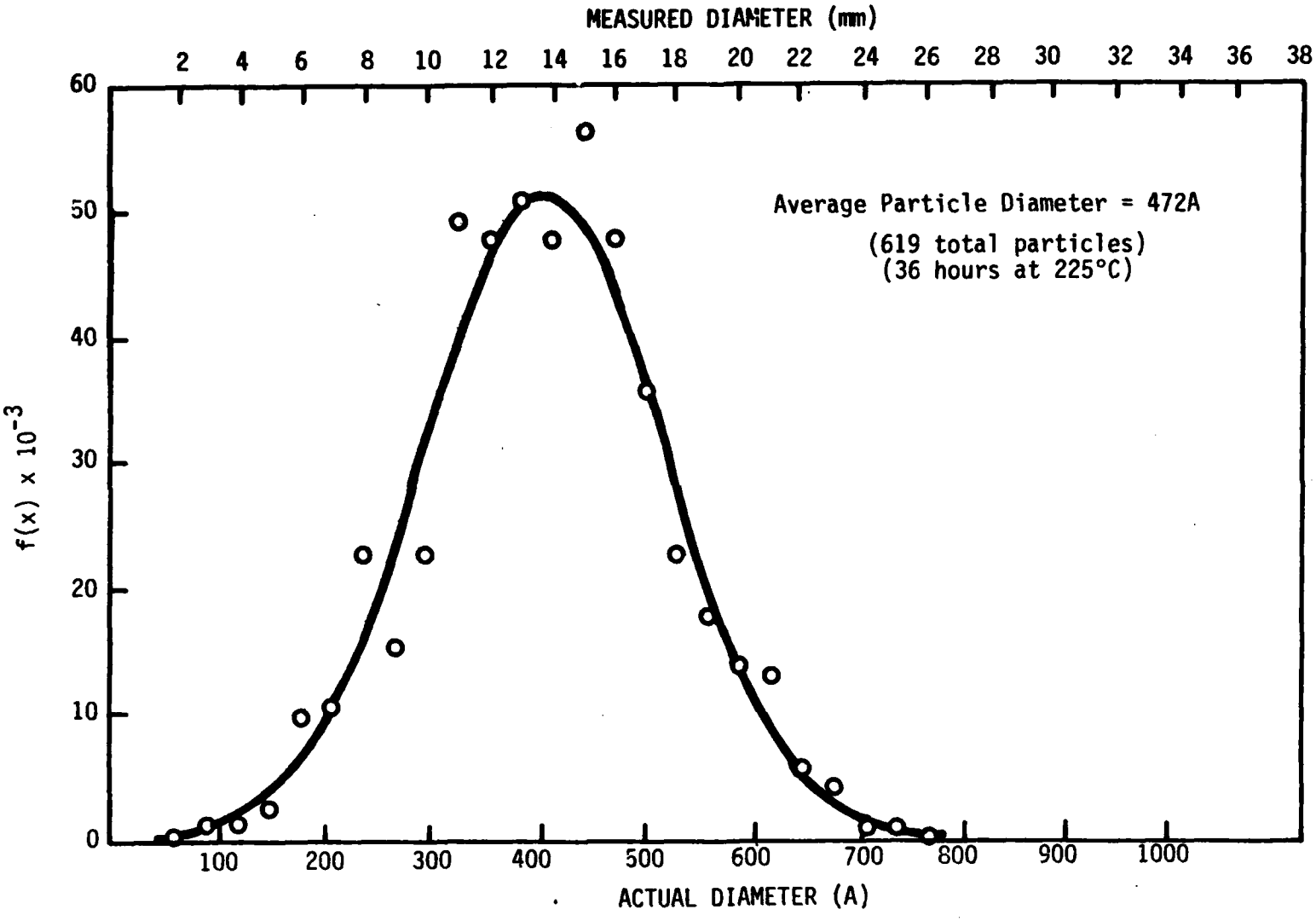

Figure D12. PSD with generated normal curve.

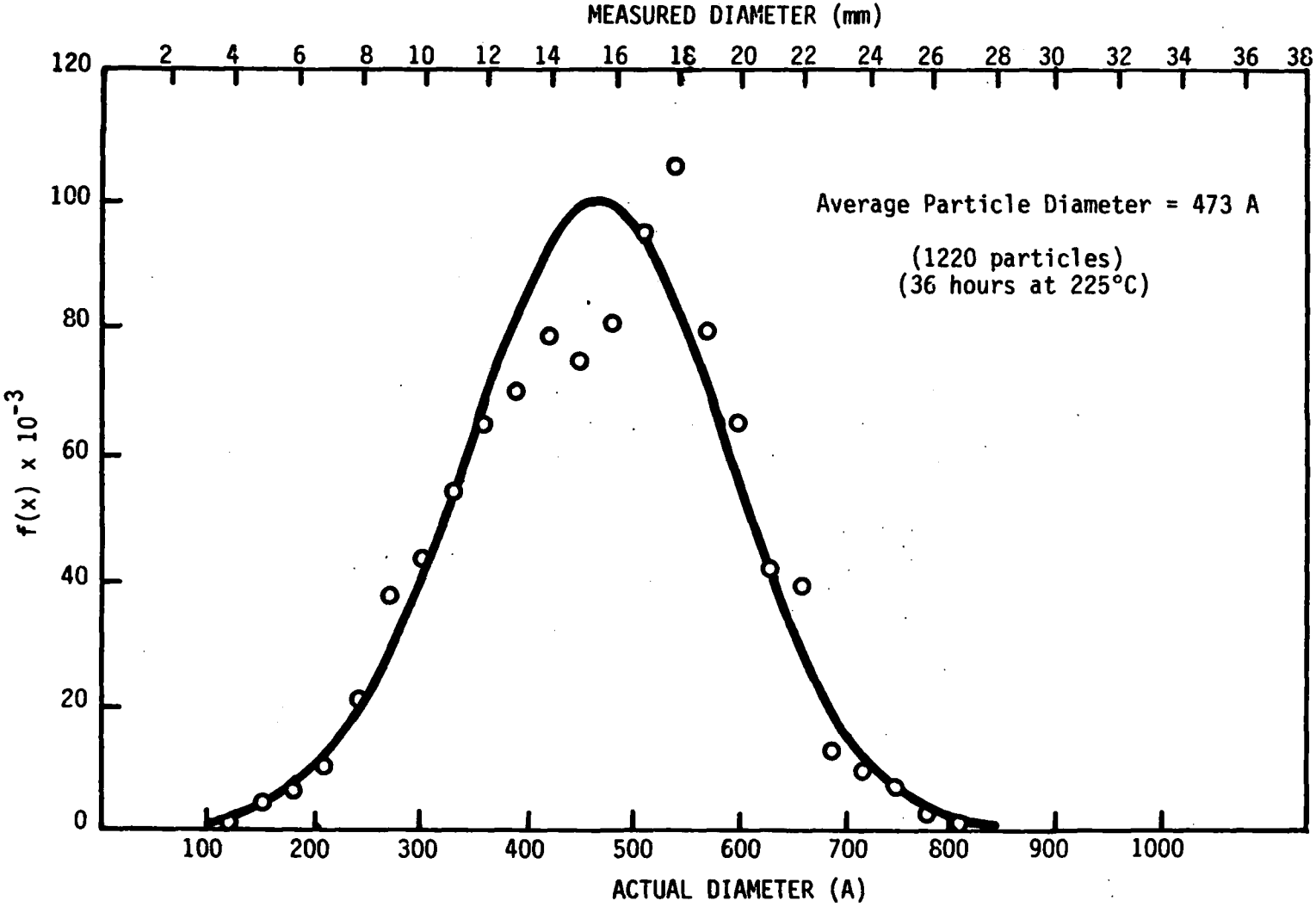

Figure D13. PSD with generated normal curve.

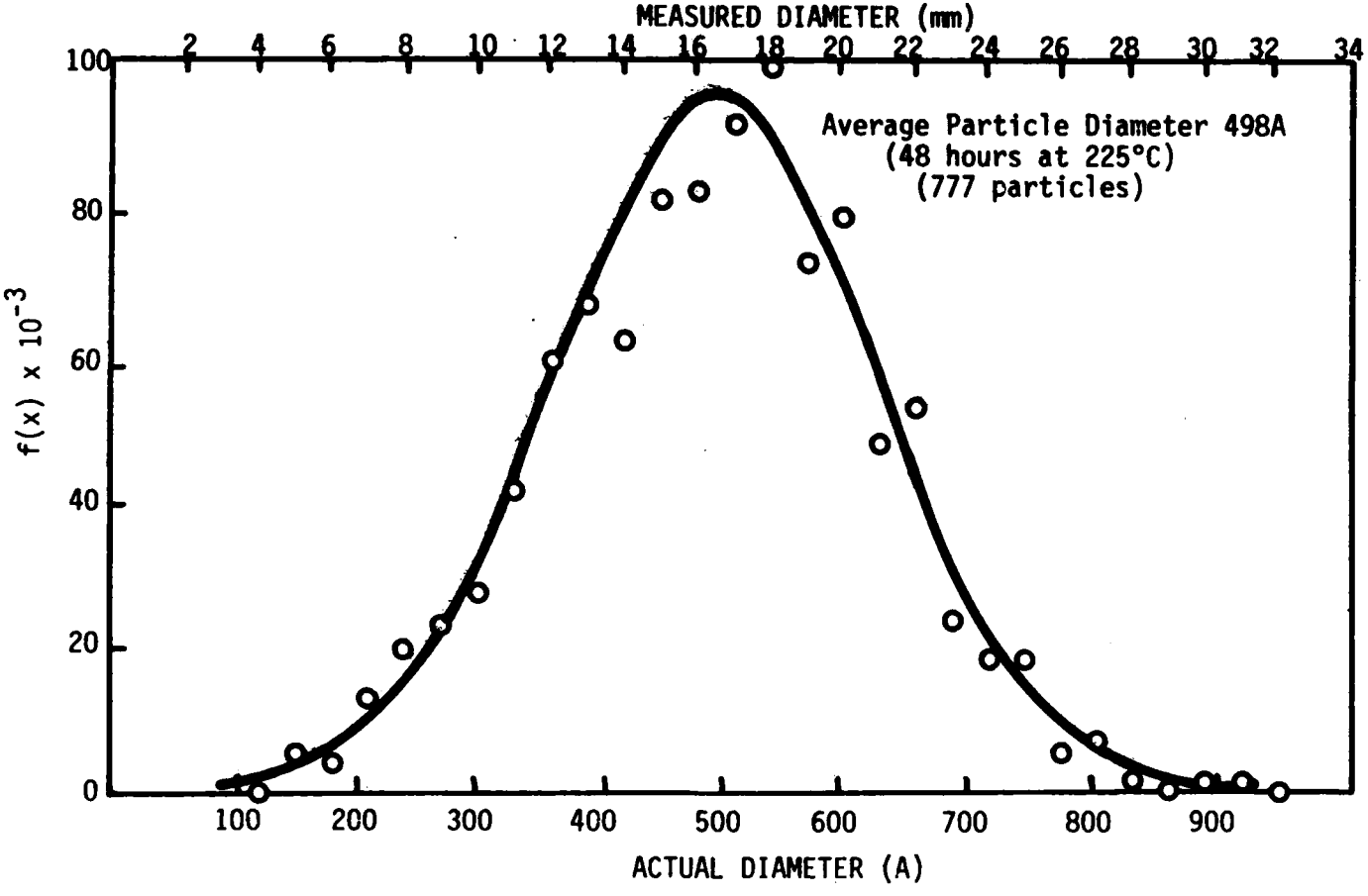

Figure D14. PSD with generated normal curve.

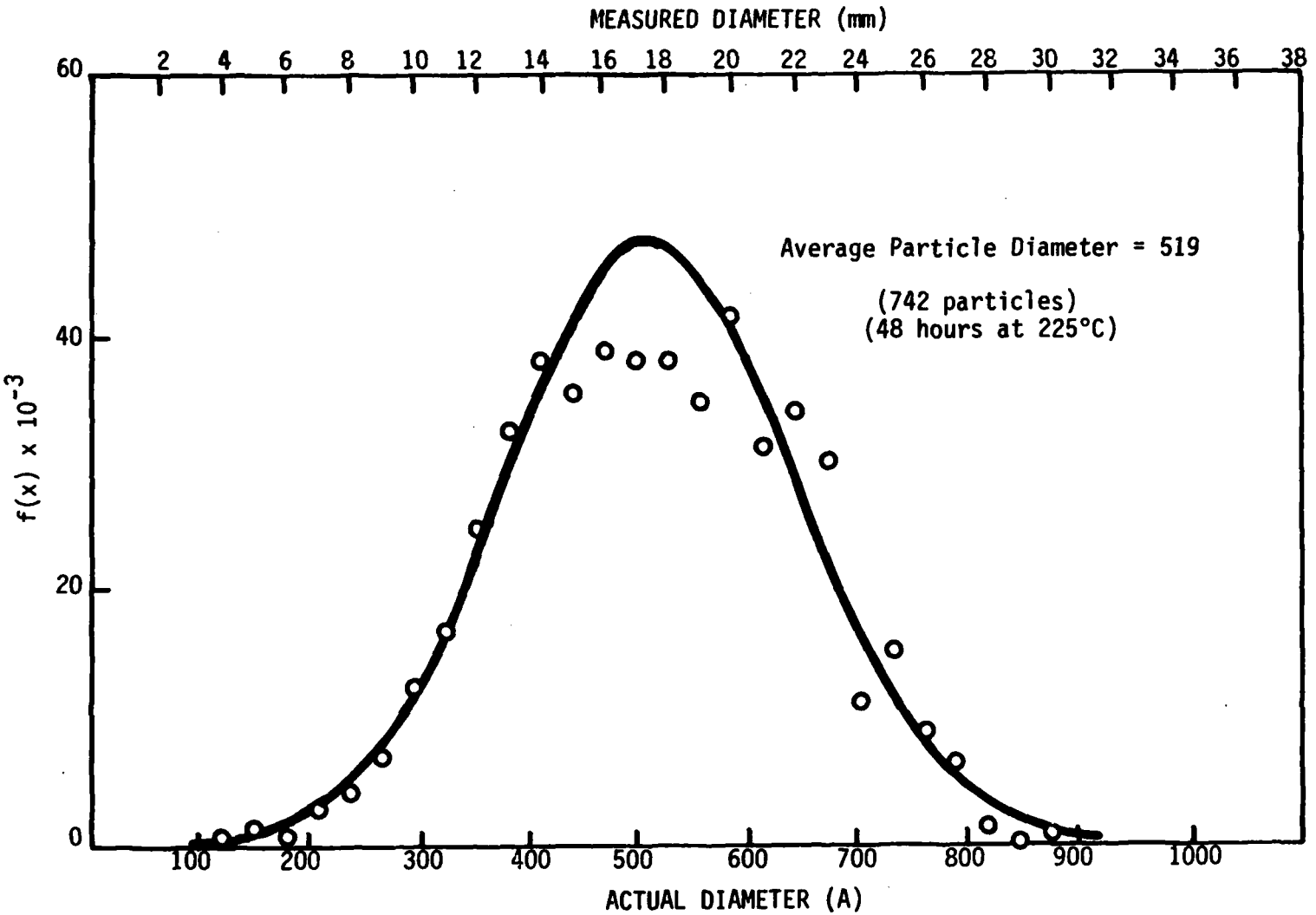

Figure D15. PSD with generated normal curve.

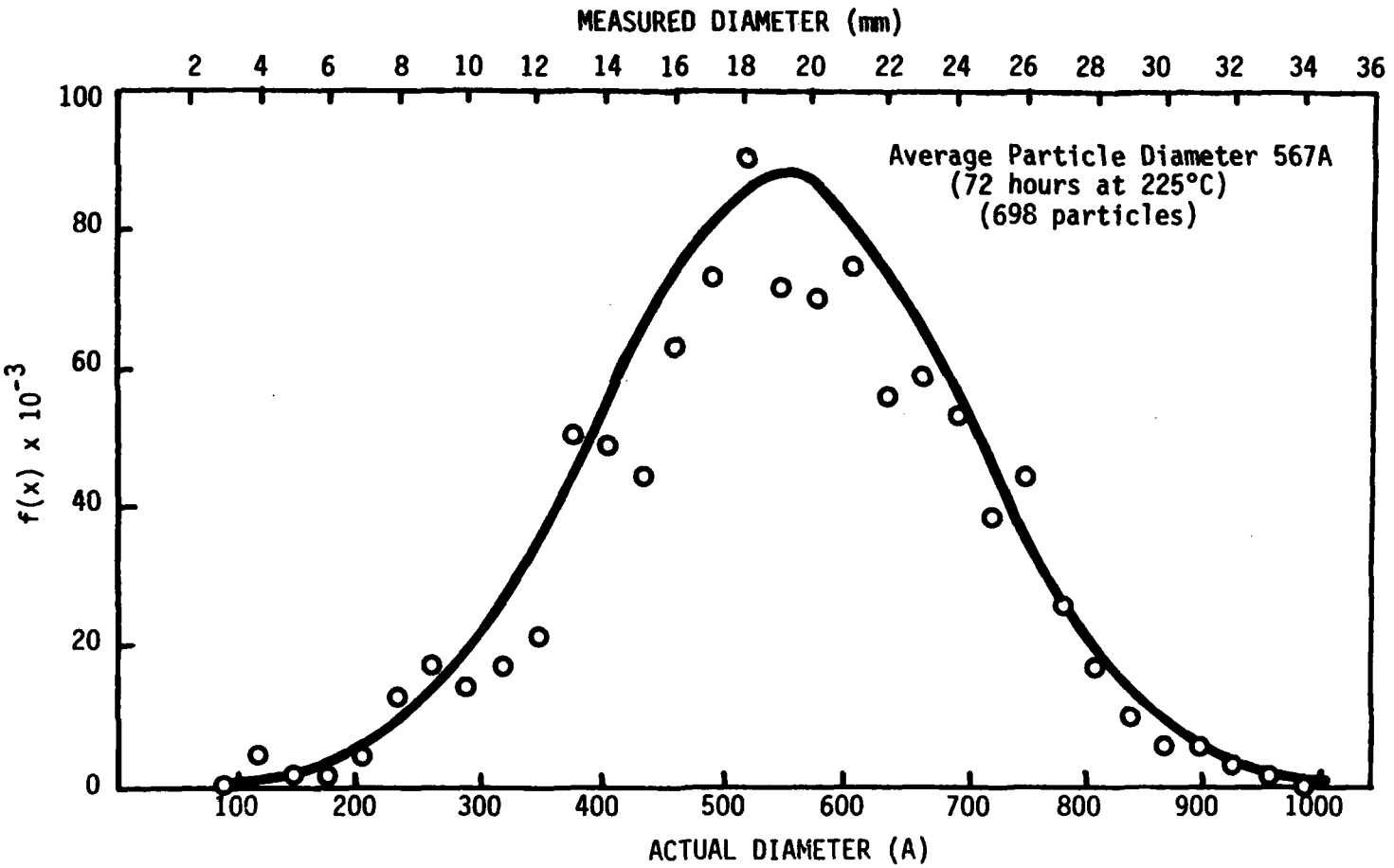

Figure D16. PSD with generated normal curve.

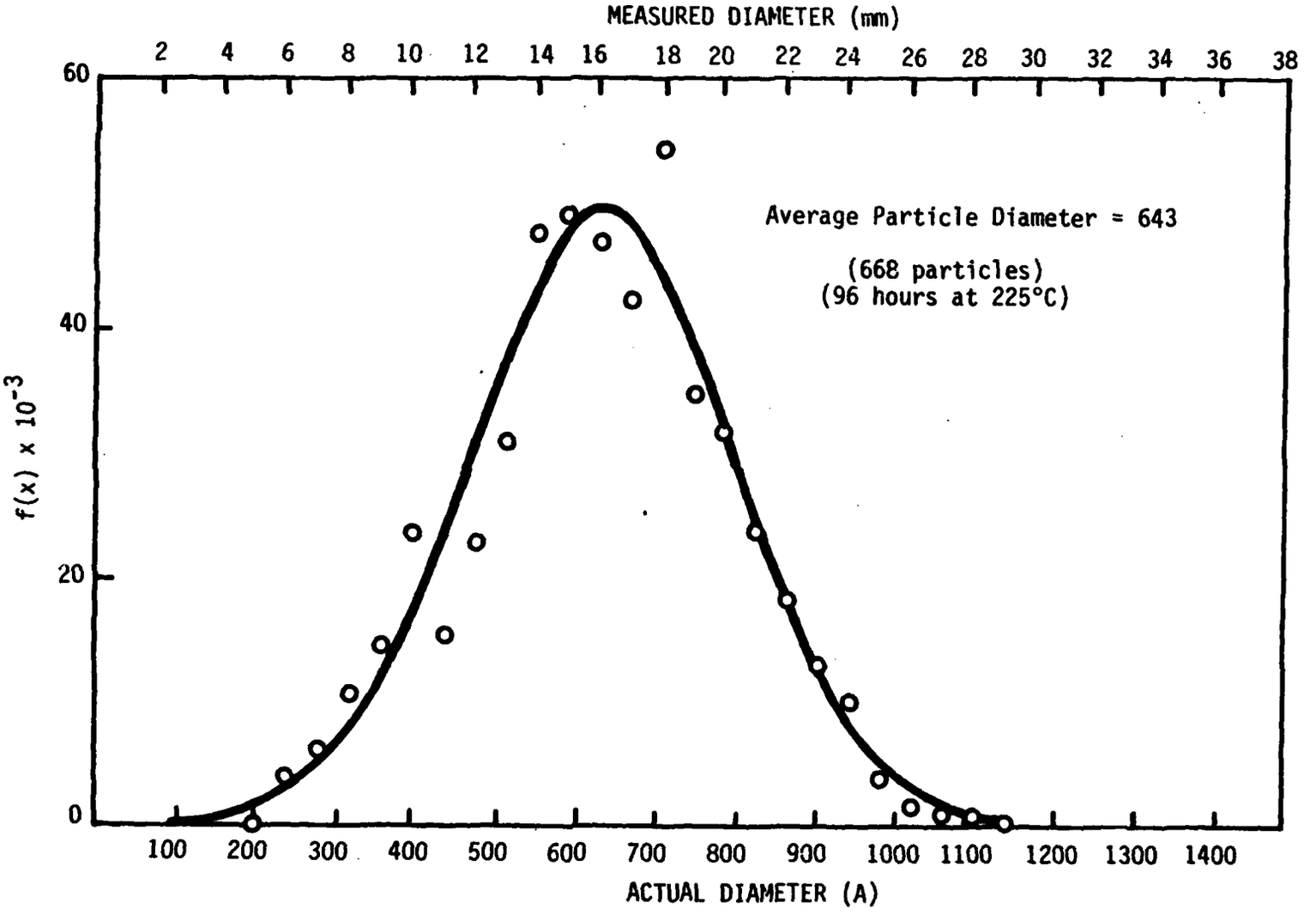

Figure D17. PSD with generated normal curve.

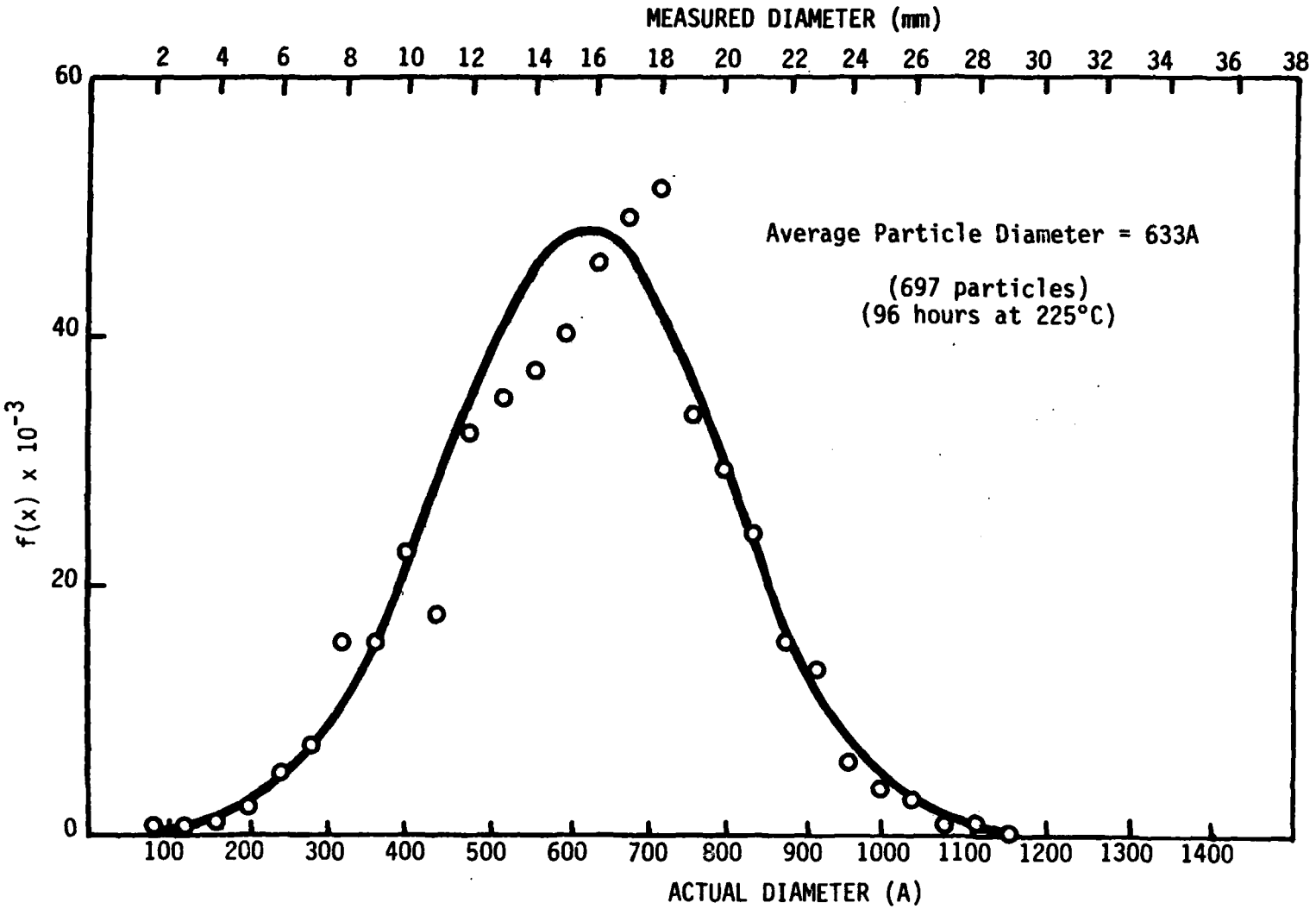

Figure D18. PSD with generated normal curve.

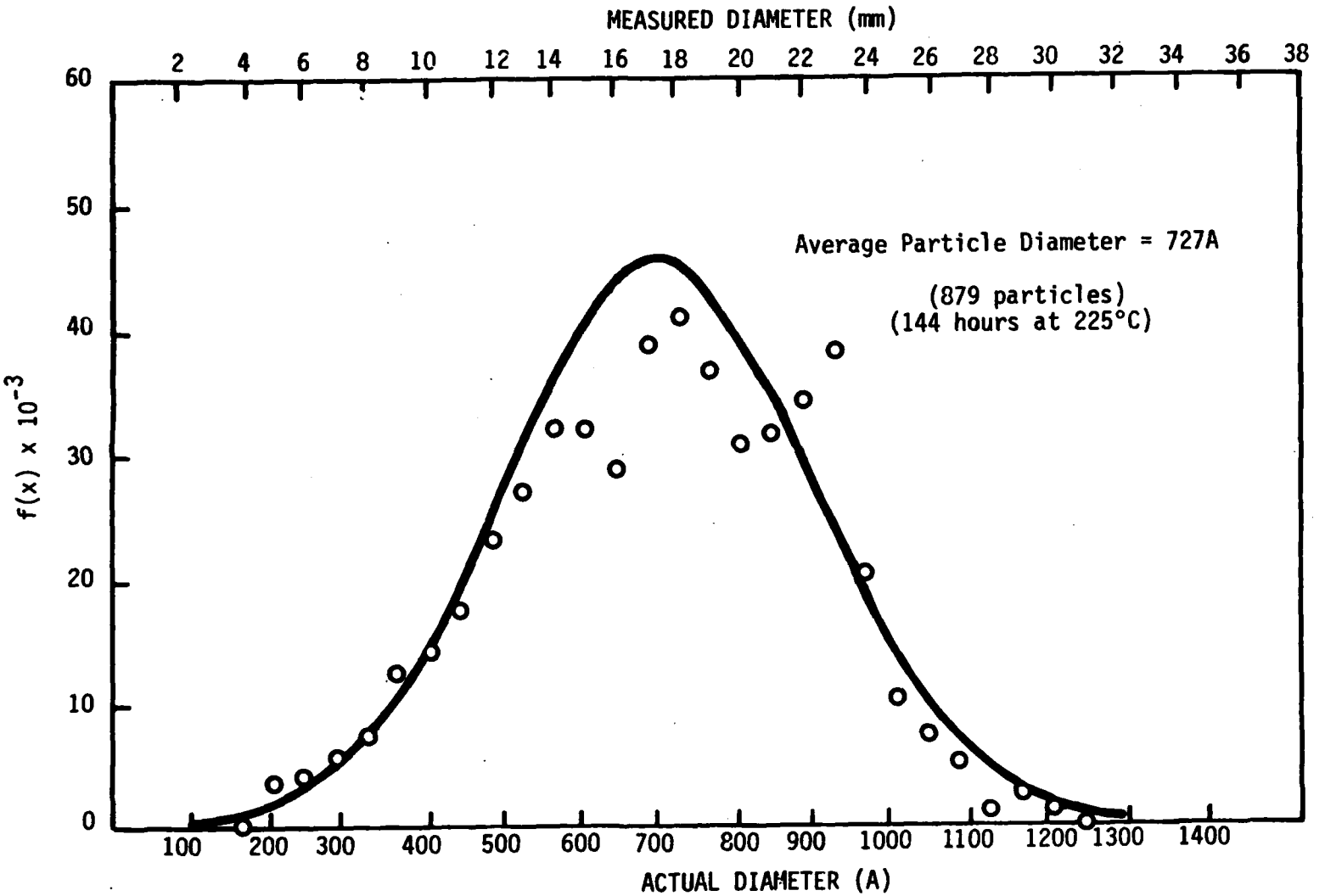

Figure D19. PSD with generated normal curve.

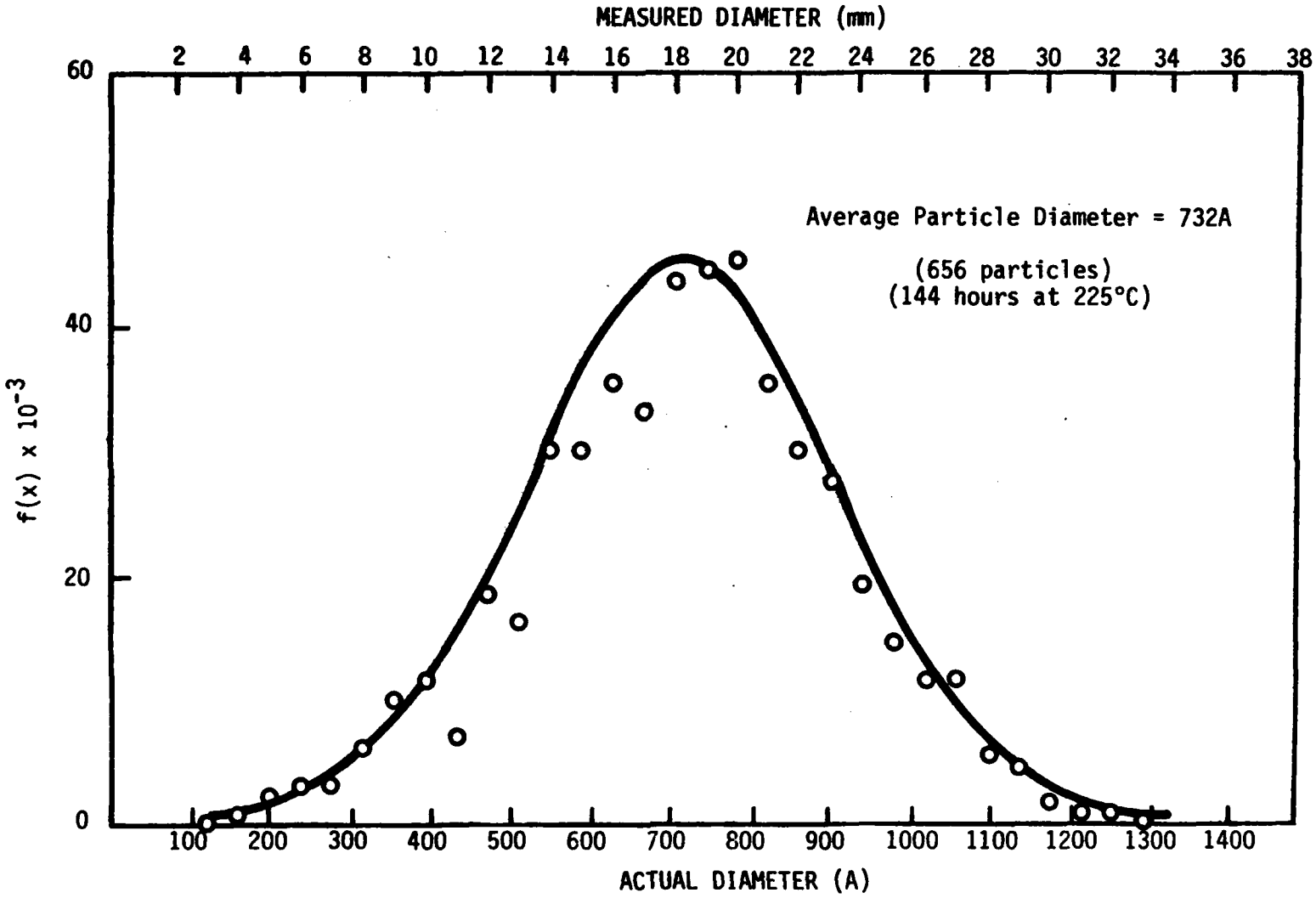

Figure D20. PSD with generated normal curve.

Appendix E

Fitting of Normal Curves to Experimental PSD Functions

The normal curve appeared to be a reasonable approximation for the overall shape of the experimental PSD's. Based on this assumption a computer program was written to determine a normal curve based on the parameters (mean and standard derivation) calculated from the experimental data. The program requires only the class intervals and the number of particles at each class interval as input. Also included in the Appendix are the calculated normal curves superimposed upon the experimental data for comparison.

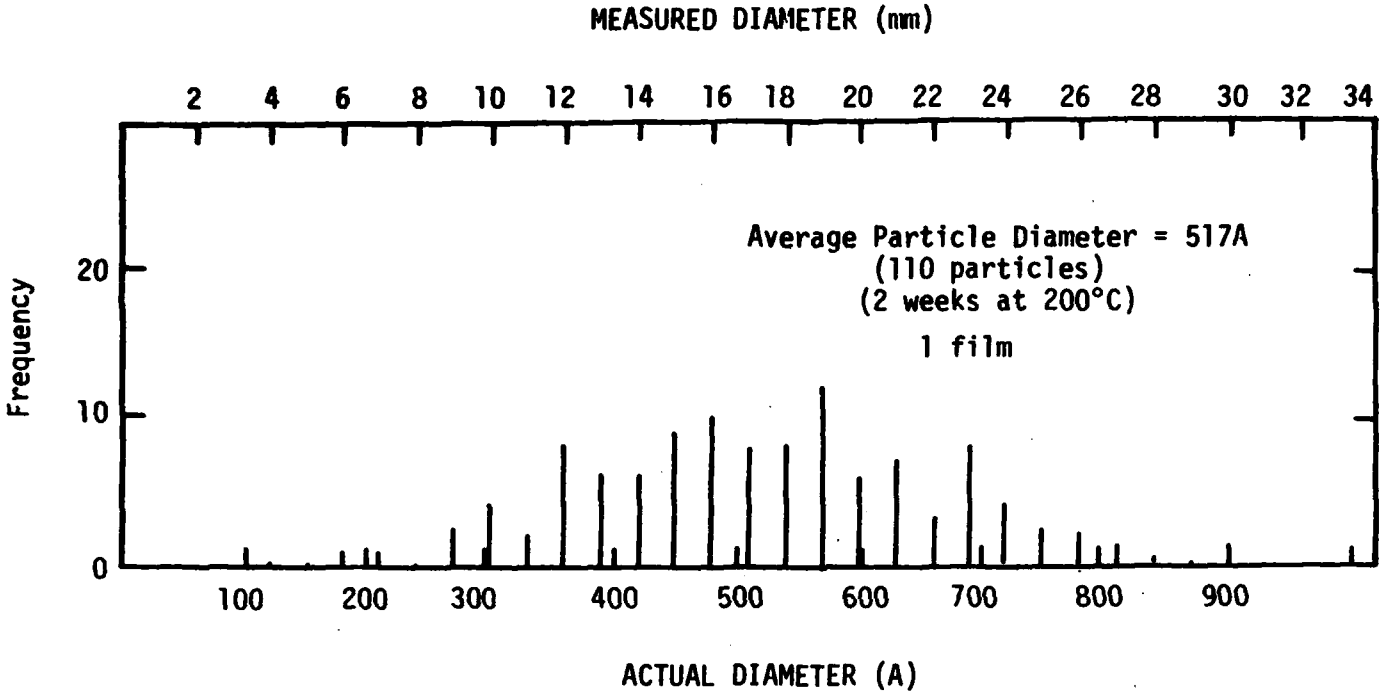

Figure E1. Particle size distribution function of 1 TEM negative.

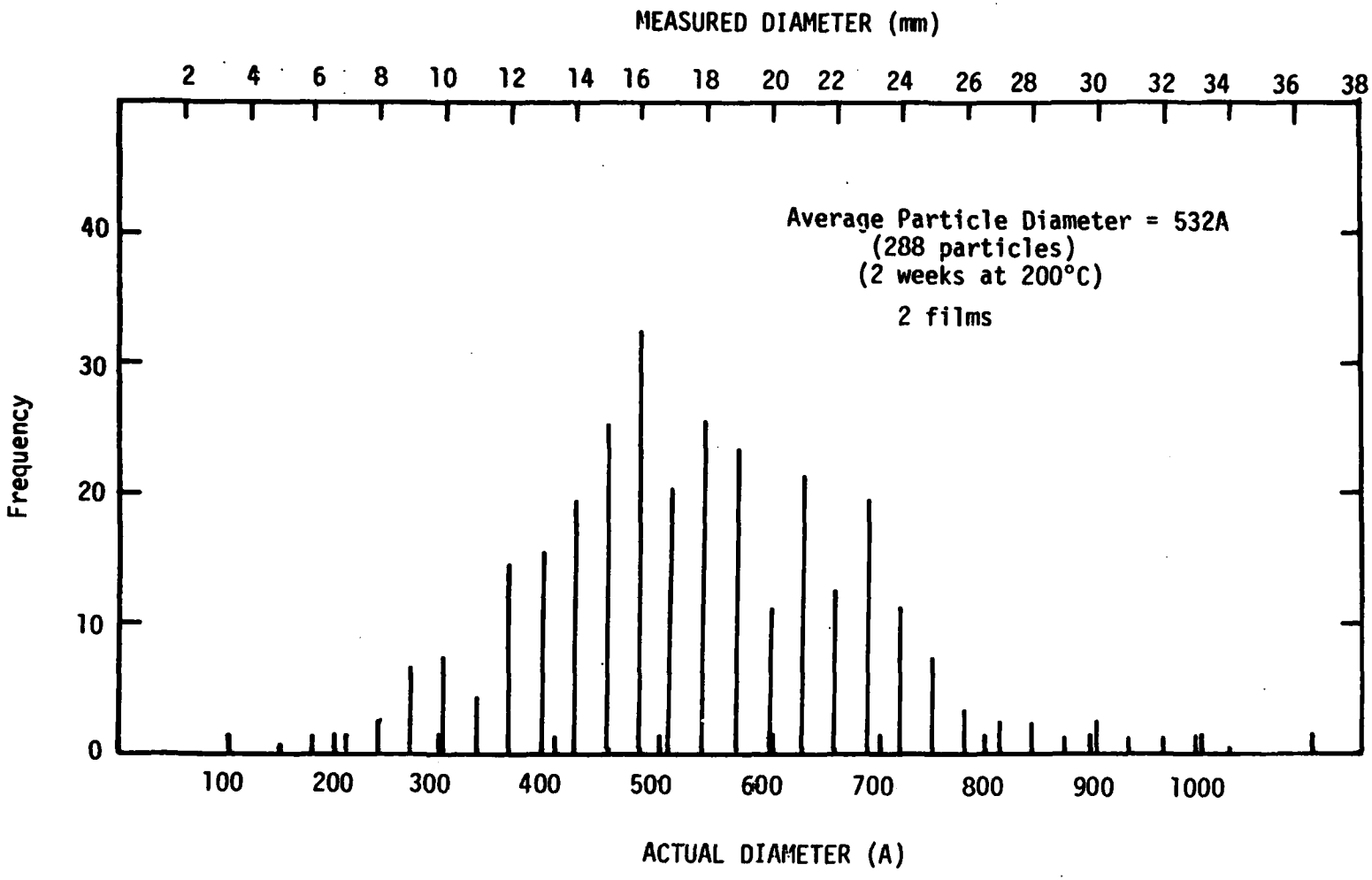

Figure E2. Particle size distribution function of 2 TEM negatives.

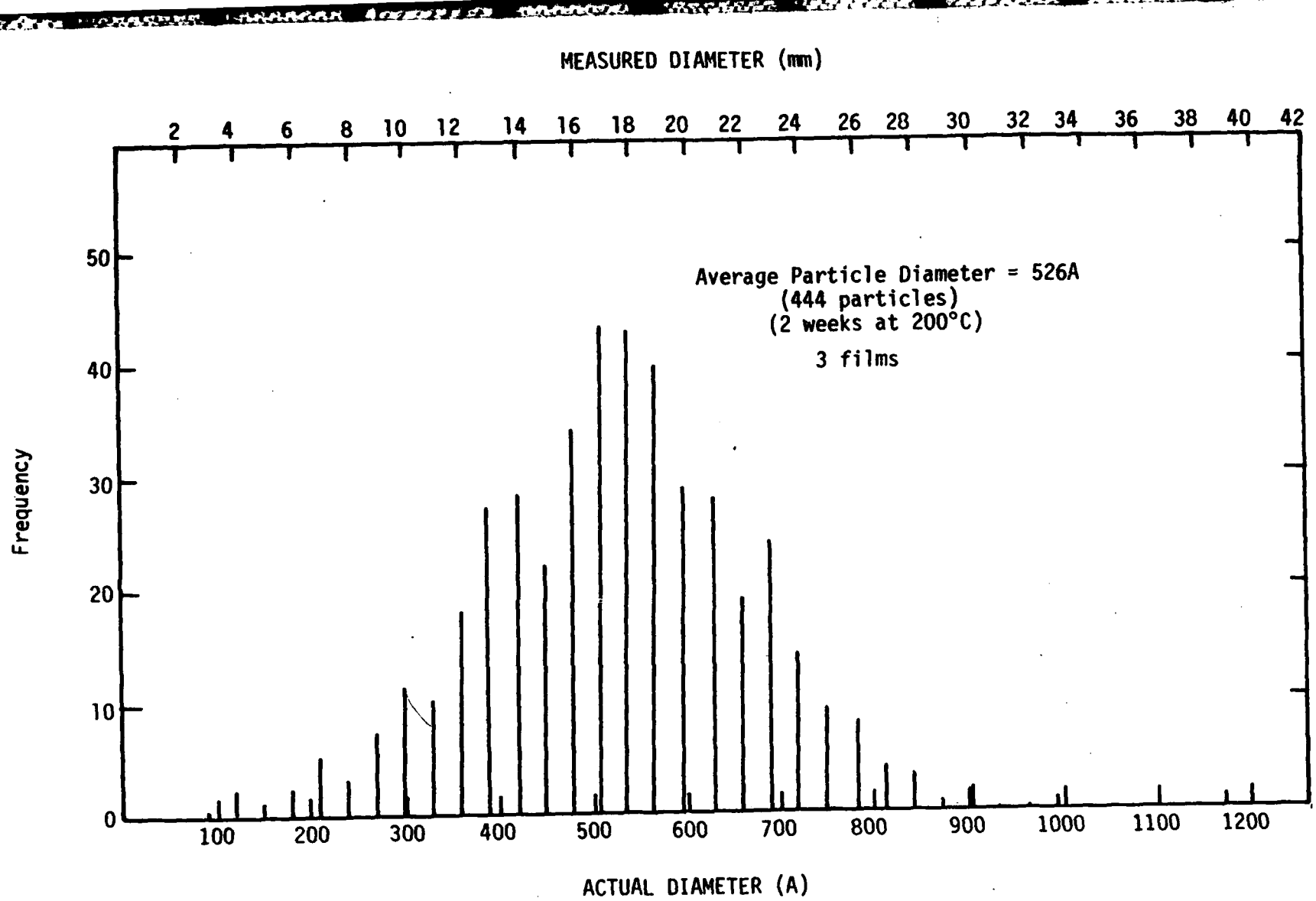

Figure E3. Particle size distribution function of 3 TEM negatives.

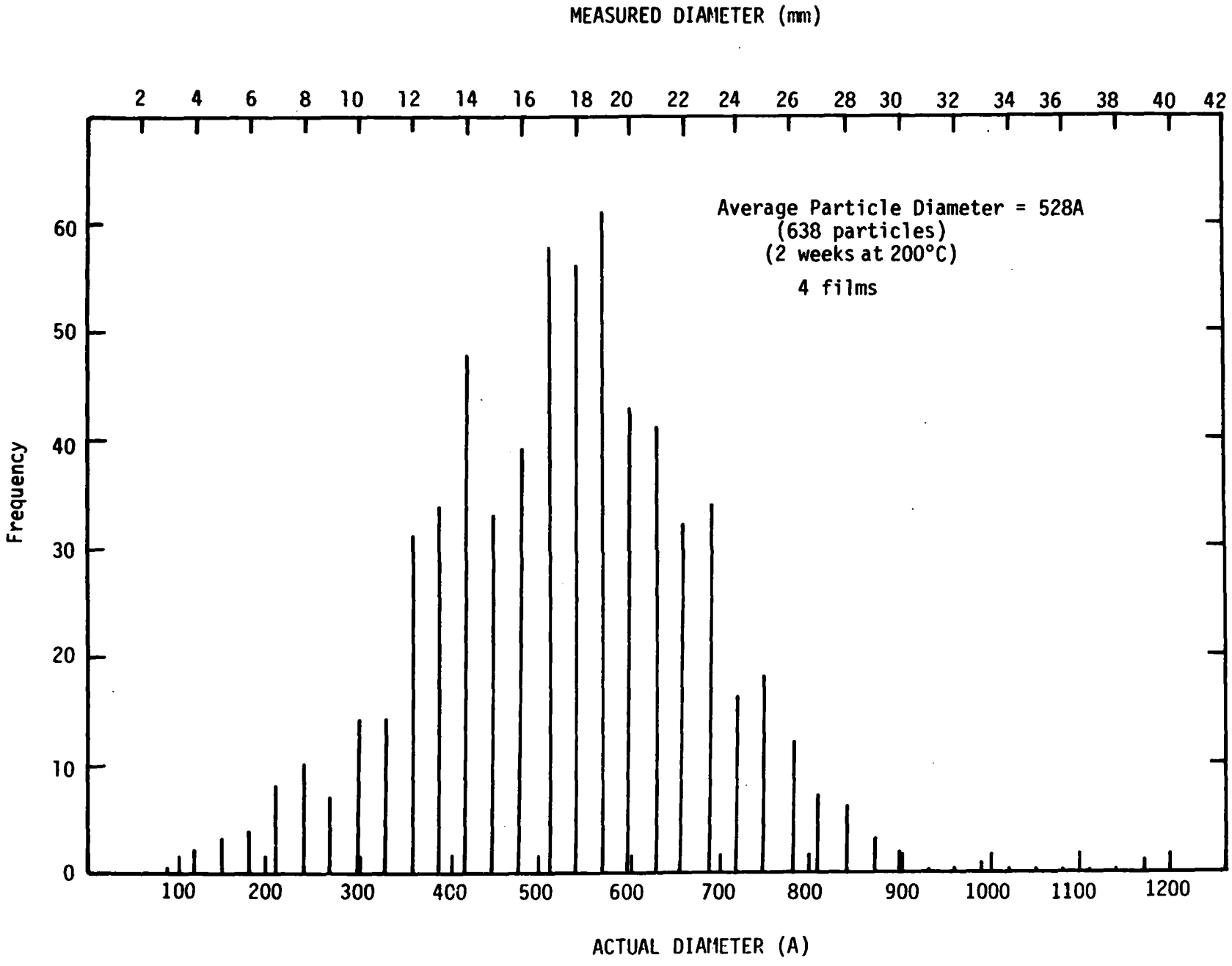

Figure E4. Particle size distribution function of 4 TEM negatives.

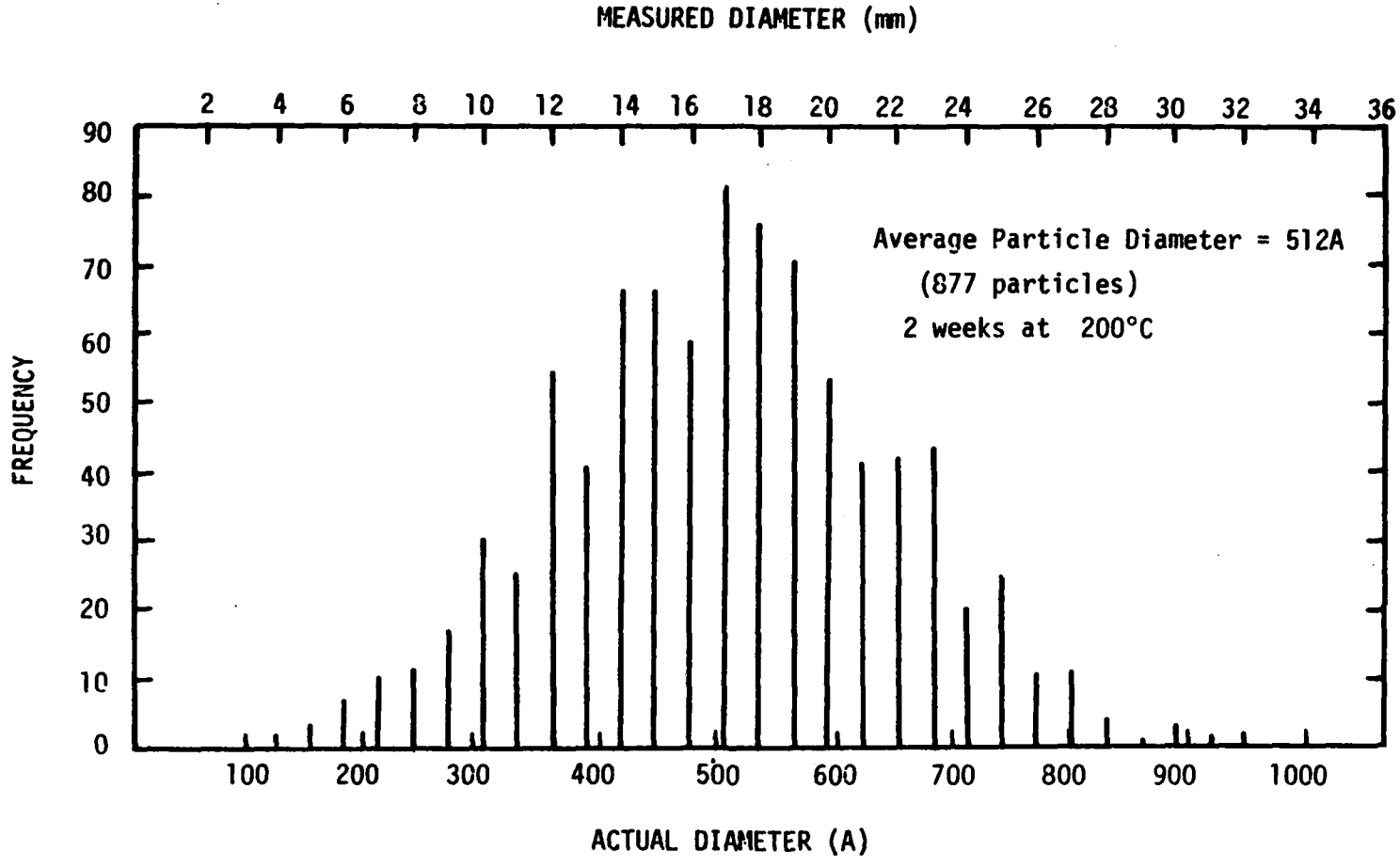

Figure E5. Particle size distribution function of 5 TEM negatives.

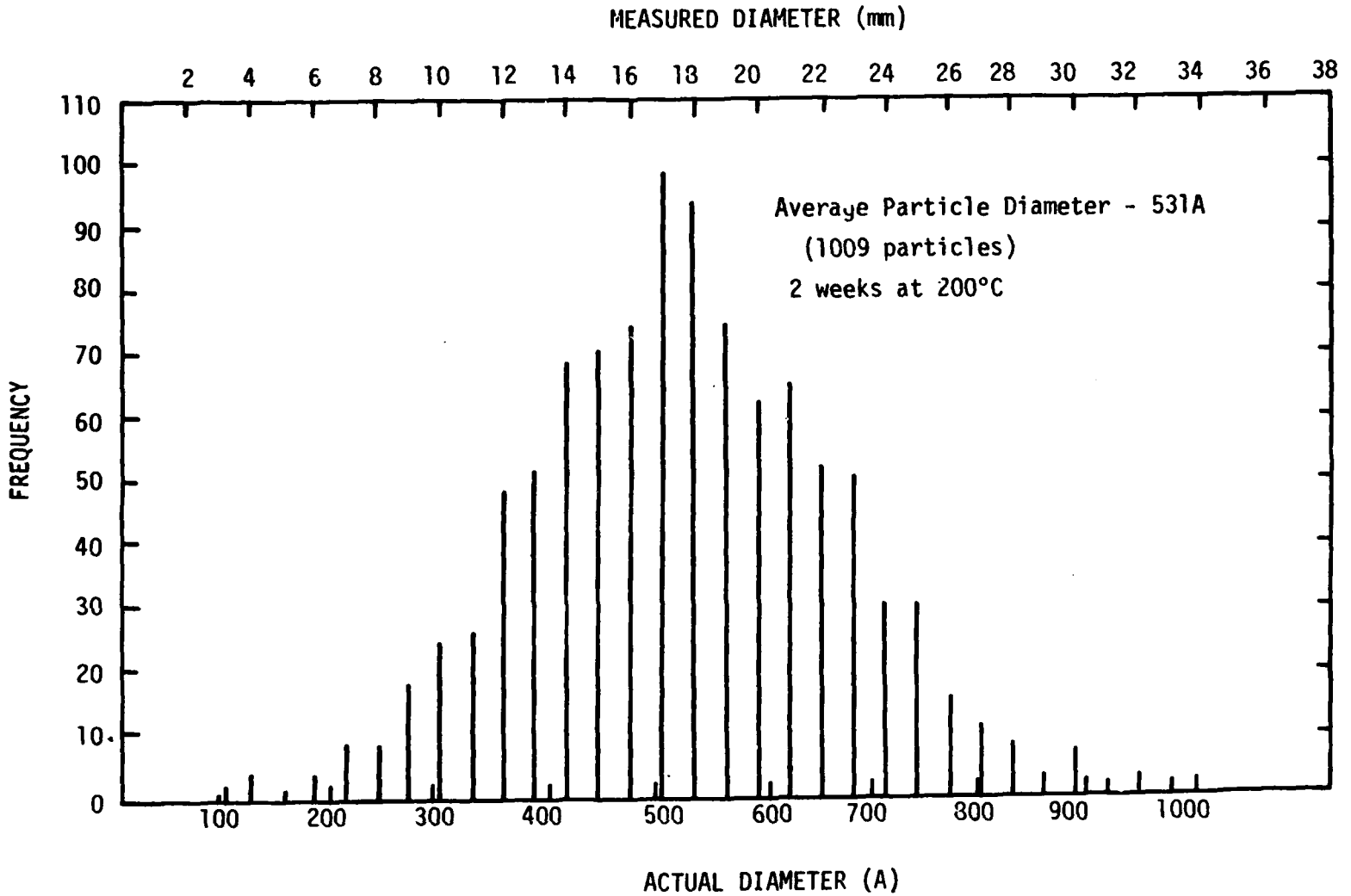

Figure E6. Particle size distribution function of 6 TEM negatives.

AD-A134 836 PRECIPITATION MECHANISMS IN ALUMINUM-LITHIUM ALLOYS(U) 3/3
PURDUE UNIV LAFAYETTE IND DEPT OF MATERIALS ENGINEERING
T H SANDERS SEP 83 0303-53-1289 N00019-81-C-0471
UNCLASSIFIED F/G 11/6 NL

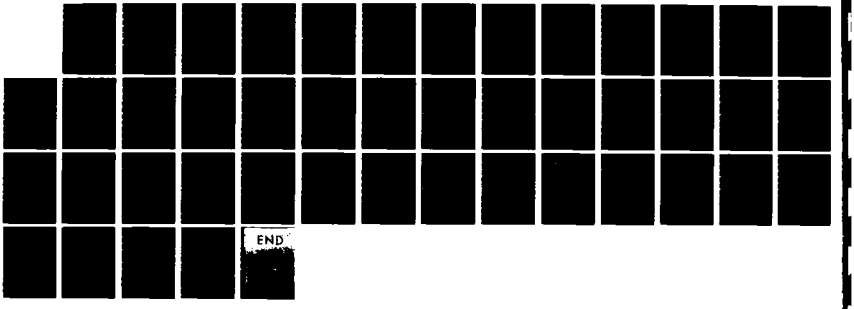

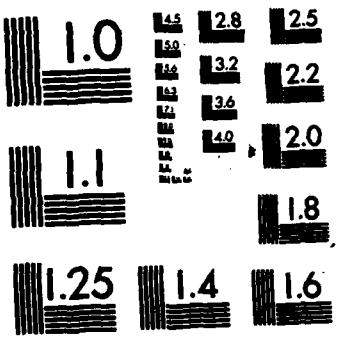

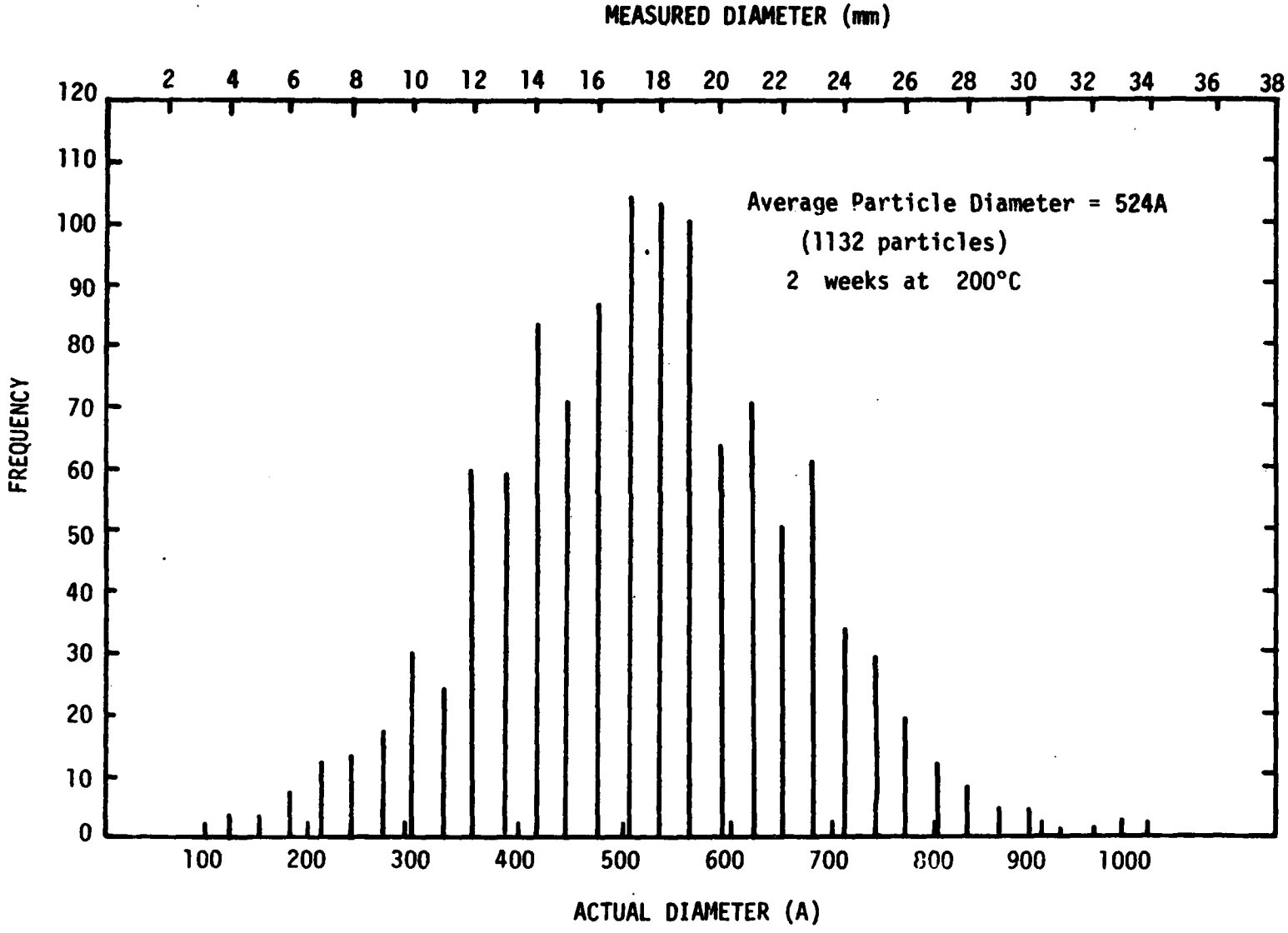

Figure E7. Particle size distribution function of 7 TEM negatives.

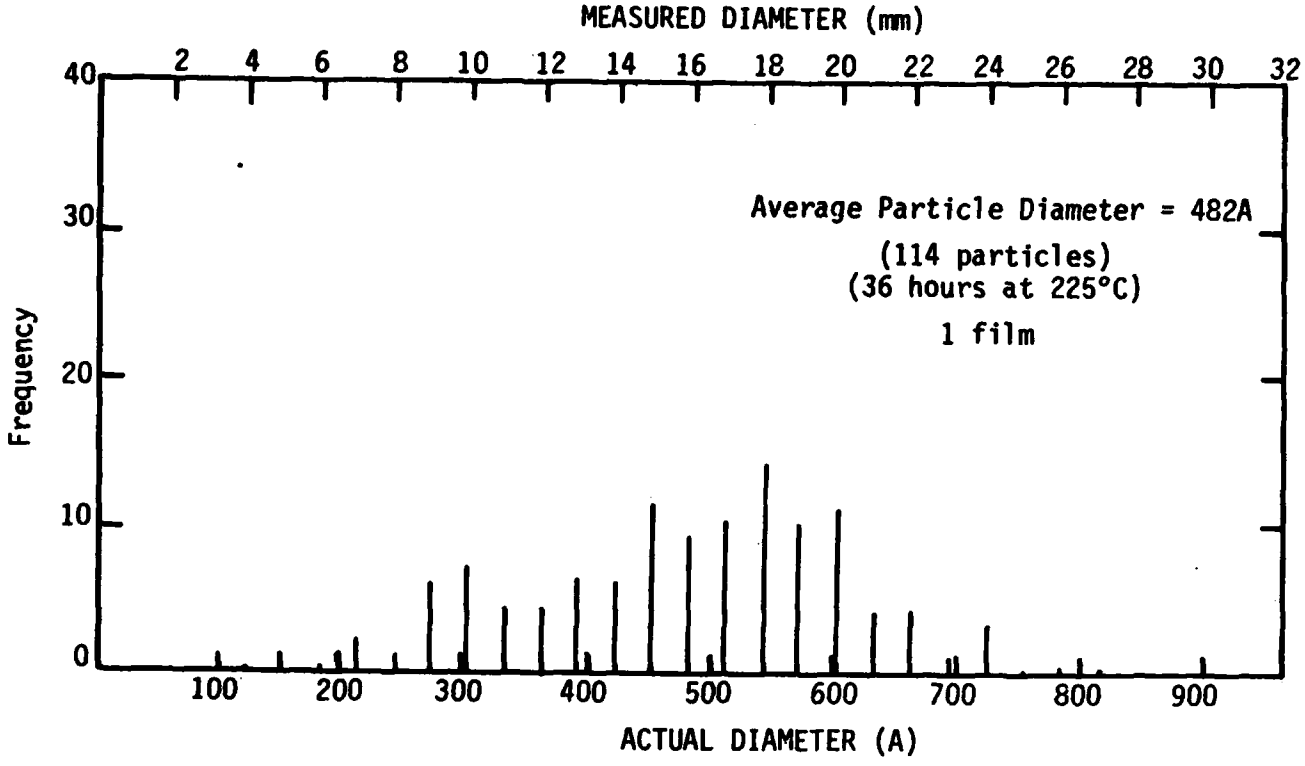

Figure E8. Particle size distribution function of 1 TEM negative.

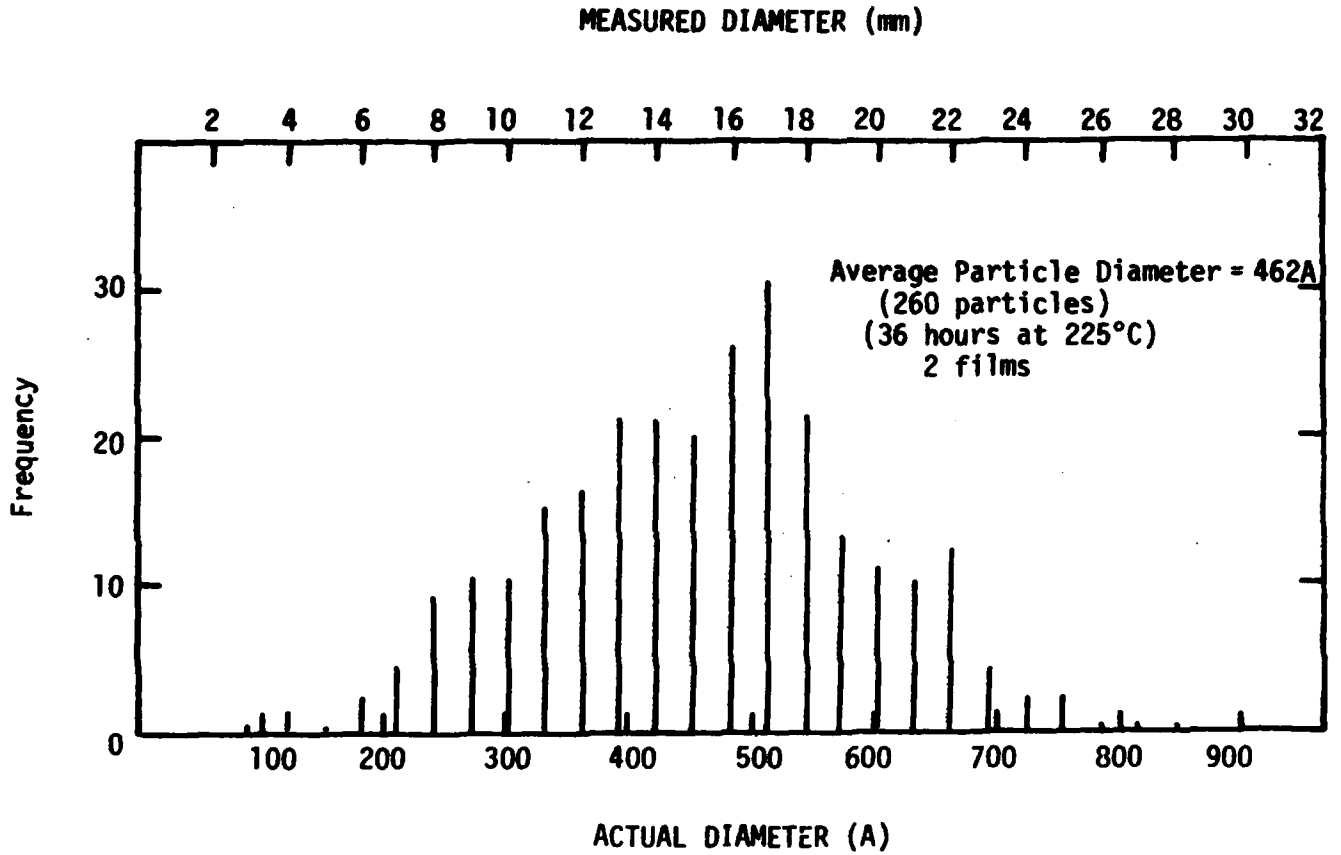

Figure E9. Particle size distribution function of 2 TEM negatives.

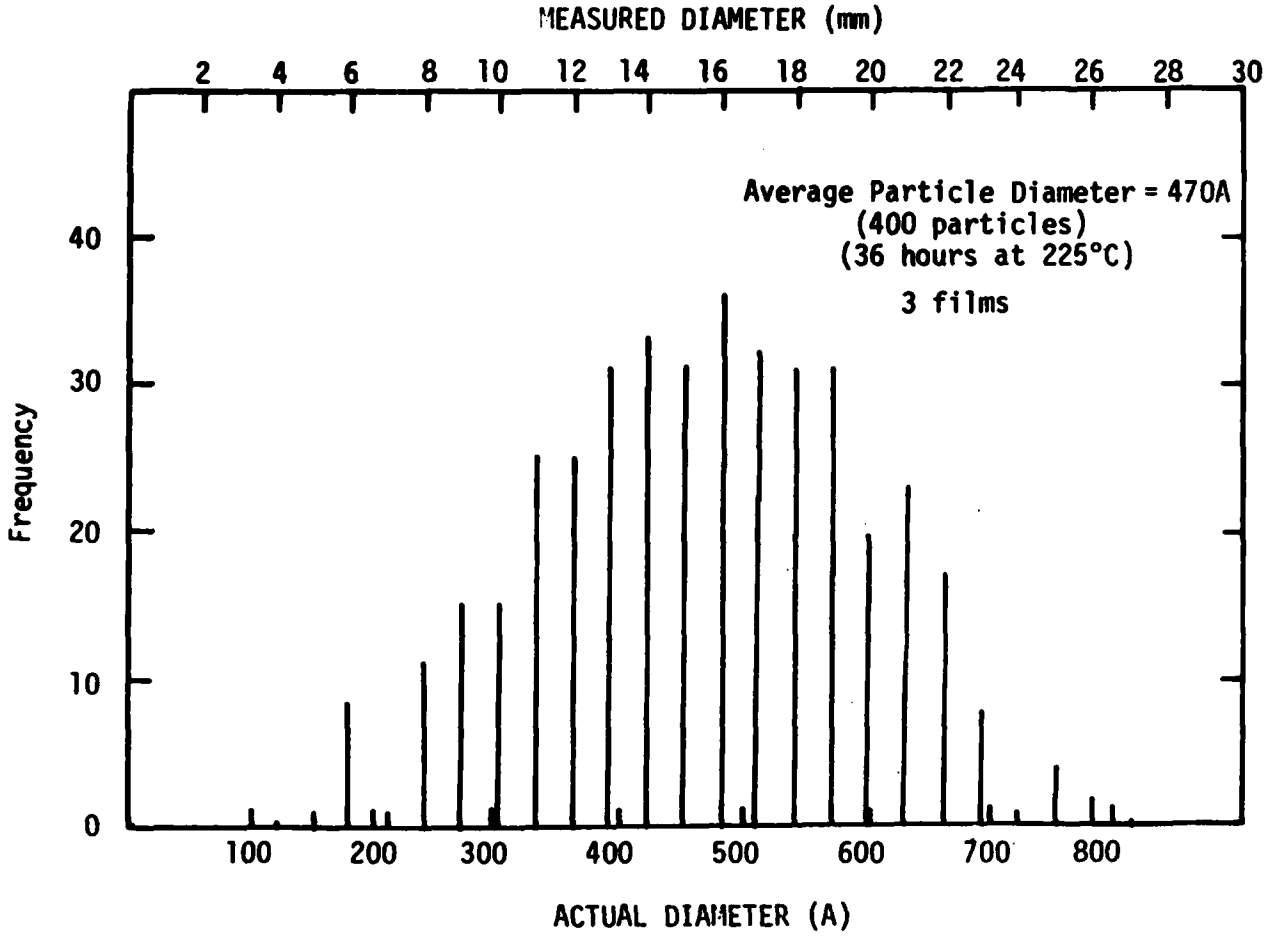

Figure E10. Particle size distribution function of 3 TEM negatives.

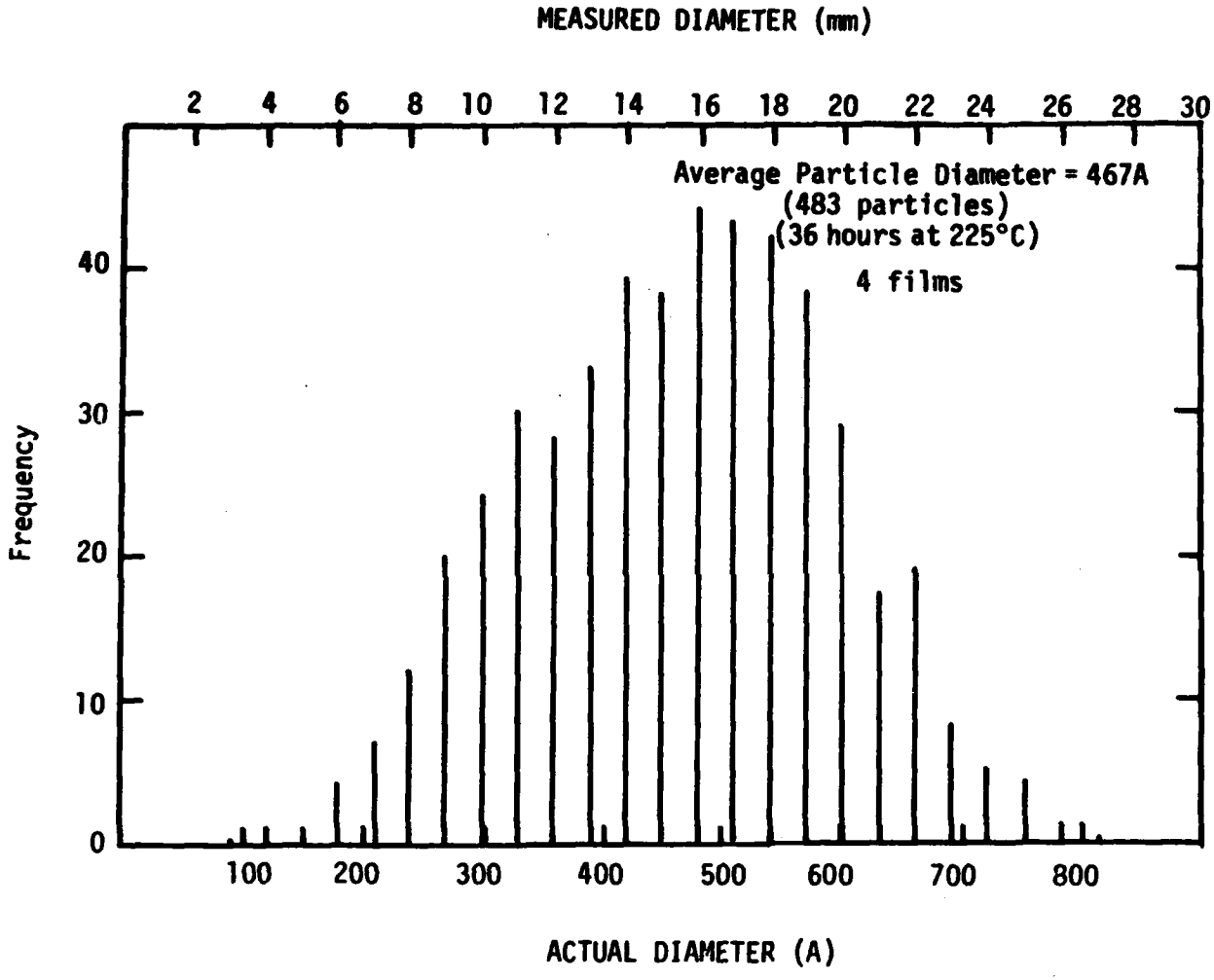

Figure E11. Particle size distribution function of 4 TEM negatives.

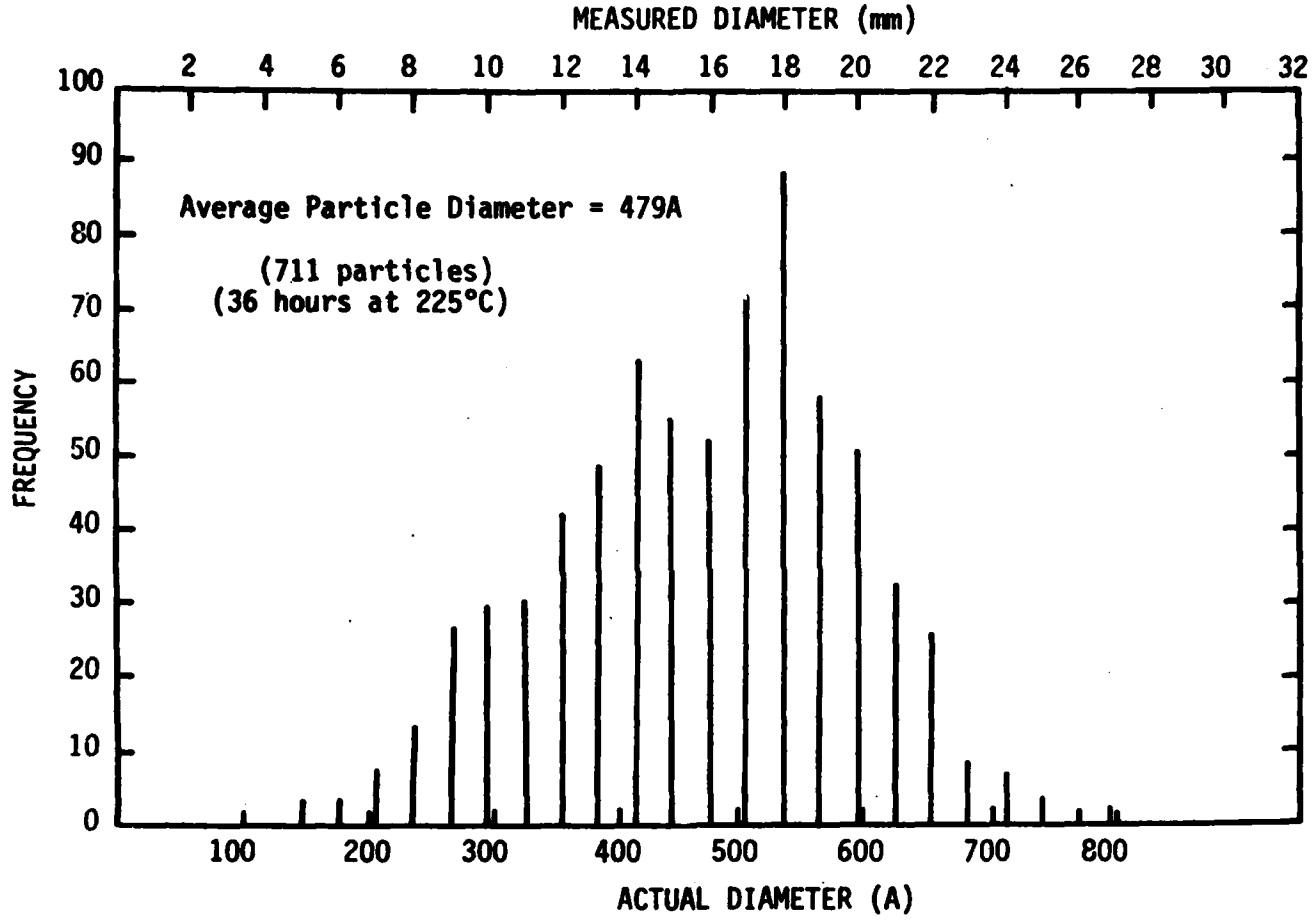

Figure E12. Particle size distribution function of 5 TEM negatives.

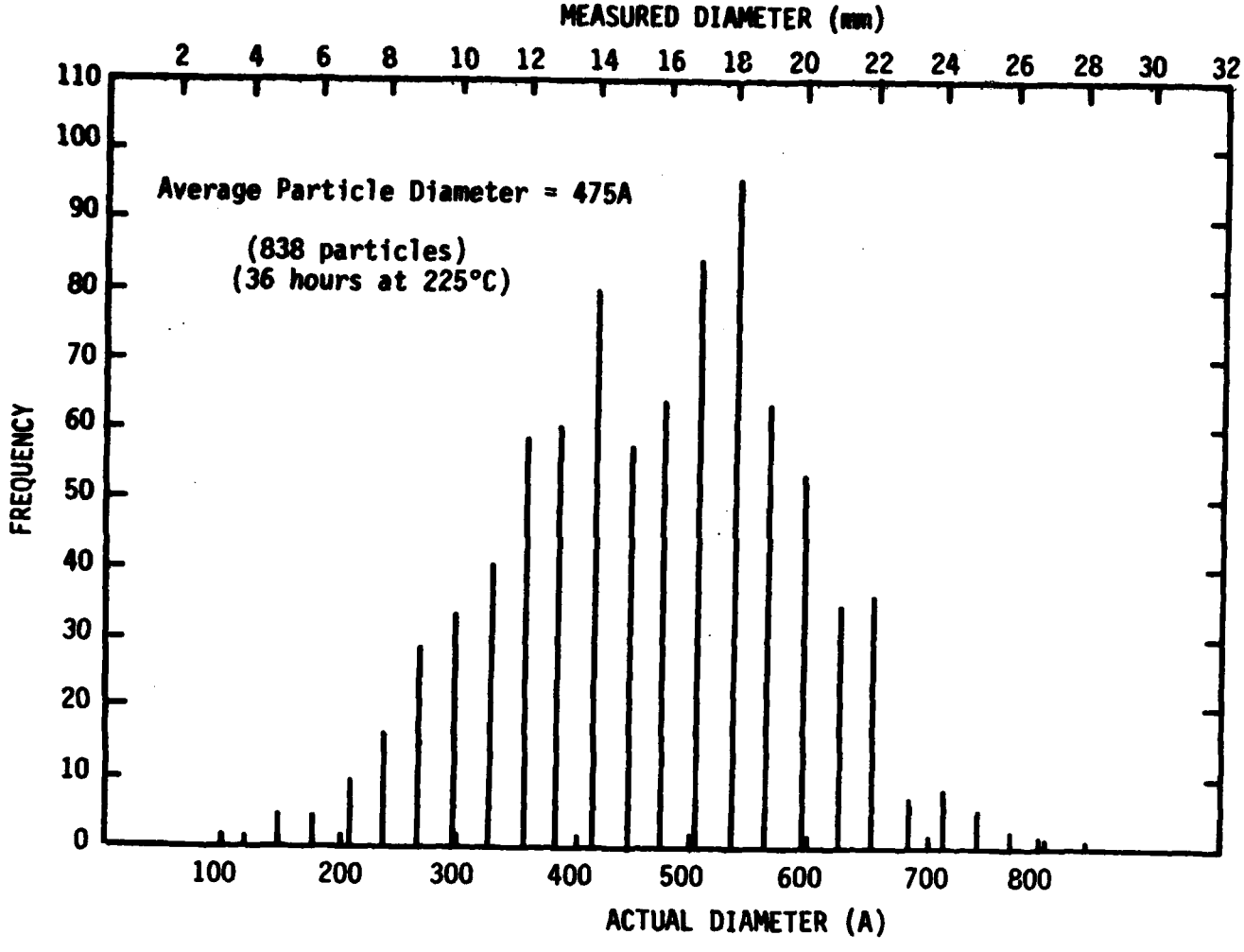

Figure E13. Particle size distribution function of 6 TEM negatives.

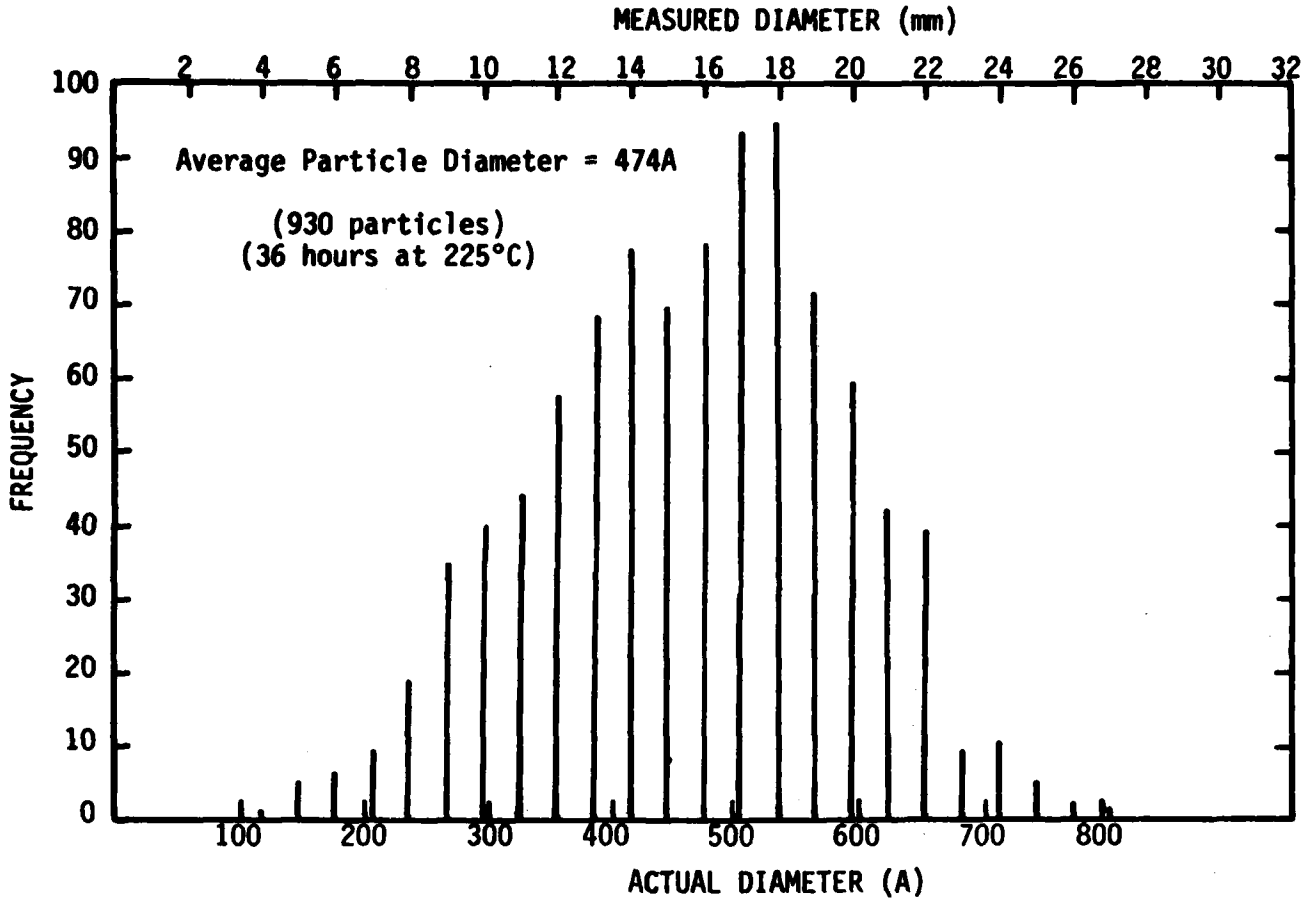

Figure E14. Particle size distribution function of 7 TEM negatives.

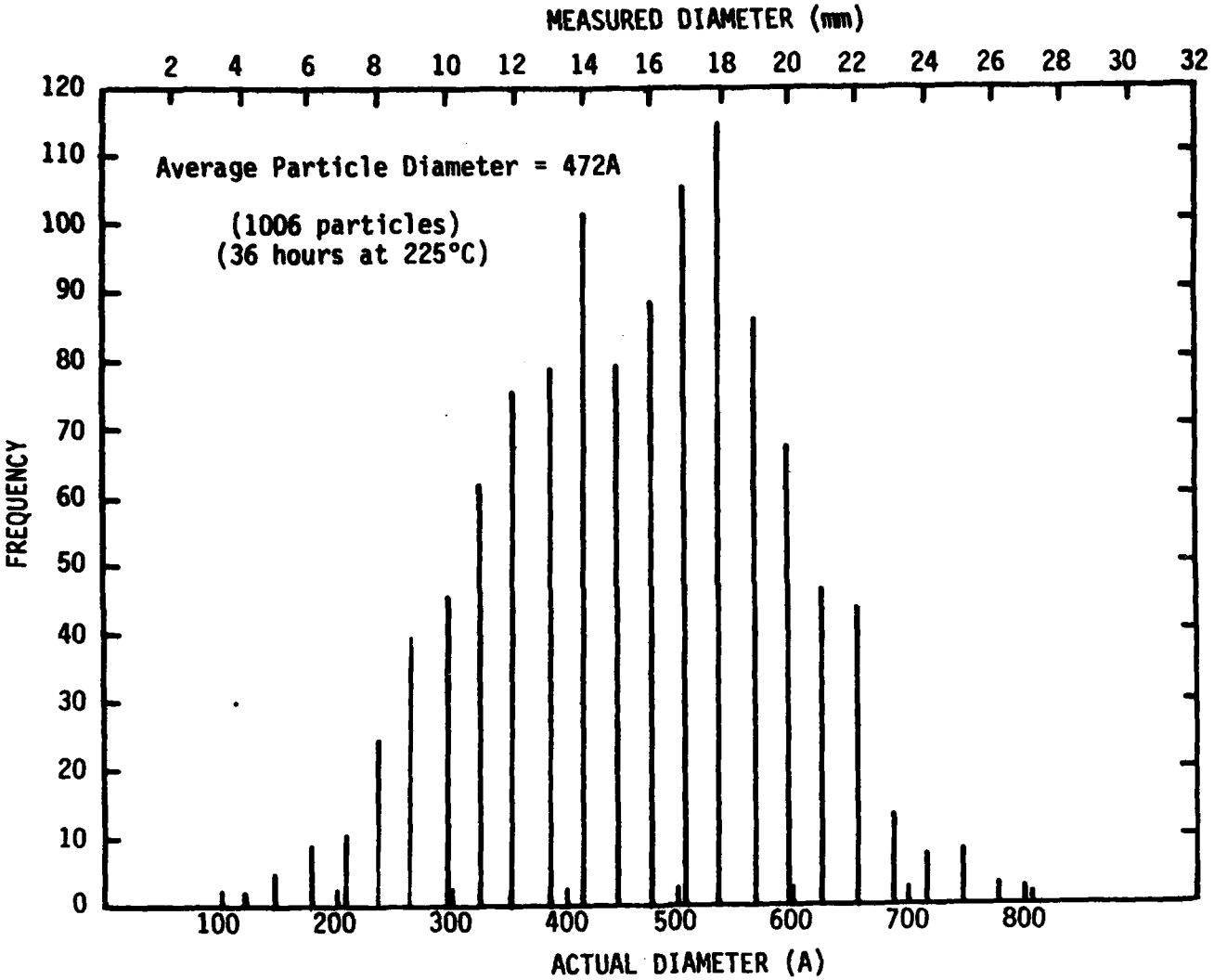

Figure E15. Particle size distribution function of 8 TEM negatives.

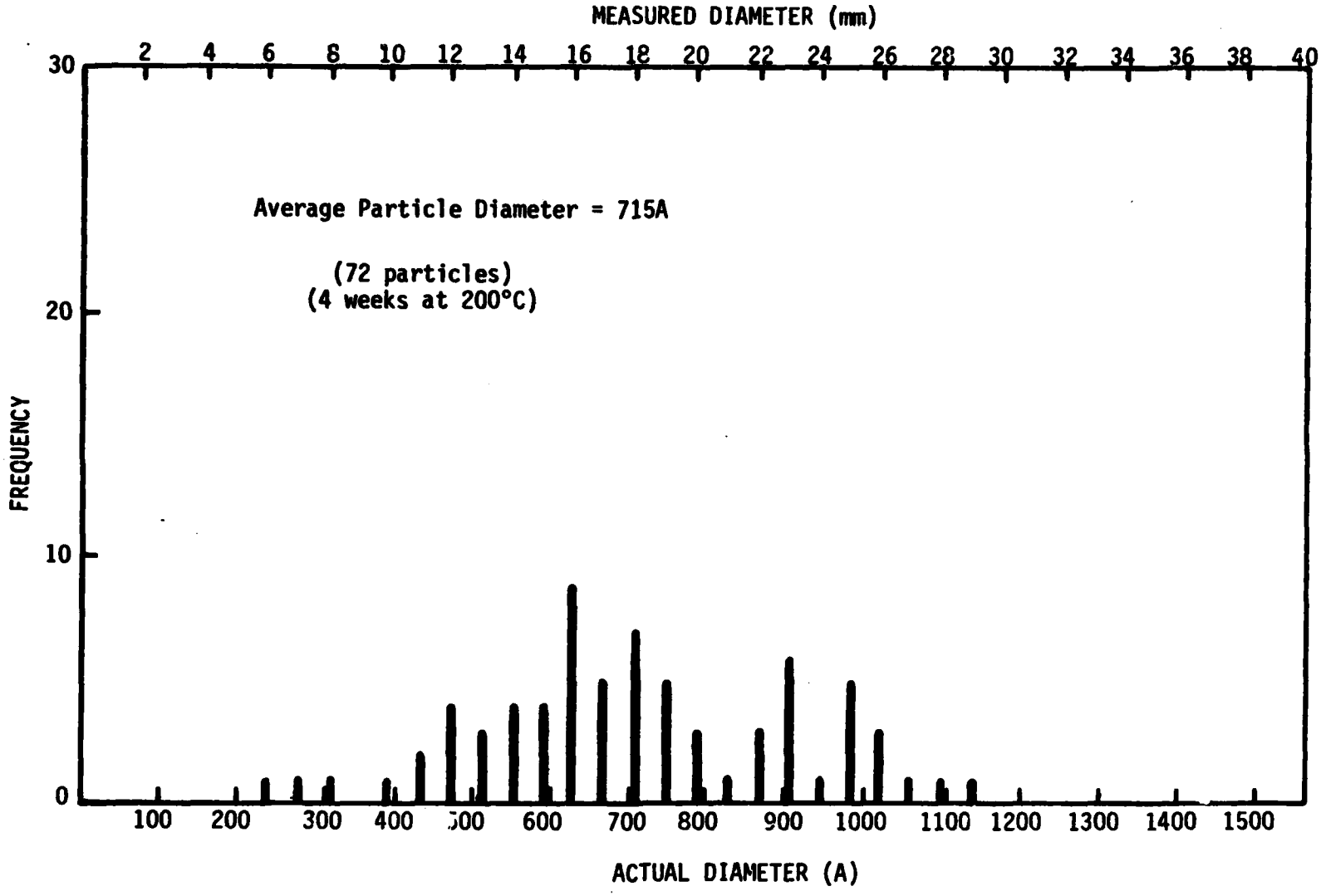

Figure E16. Particle size distribution function of 1 TEM negative.

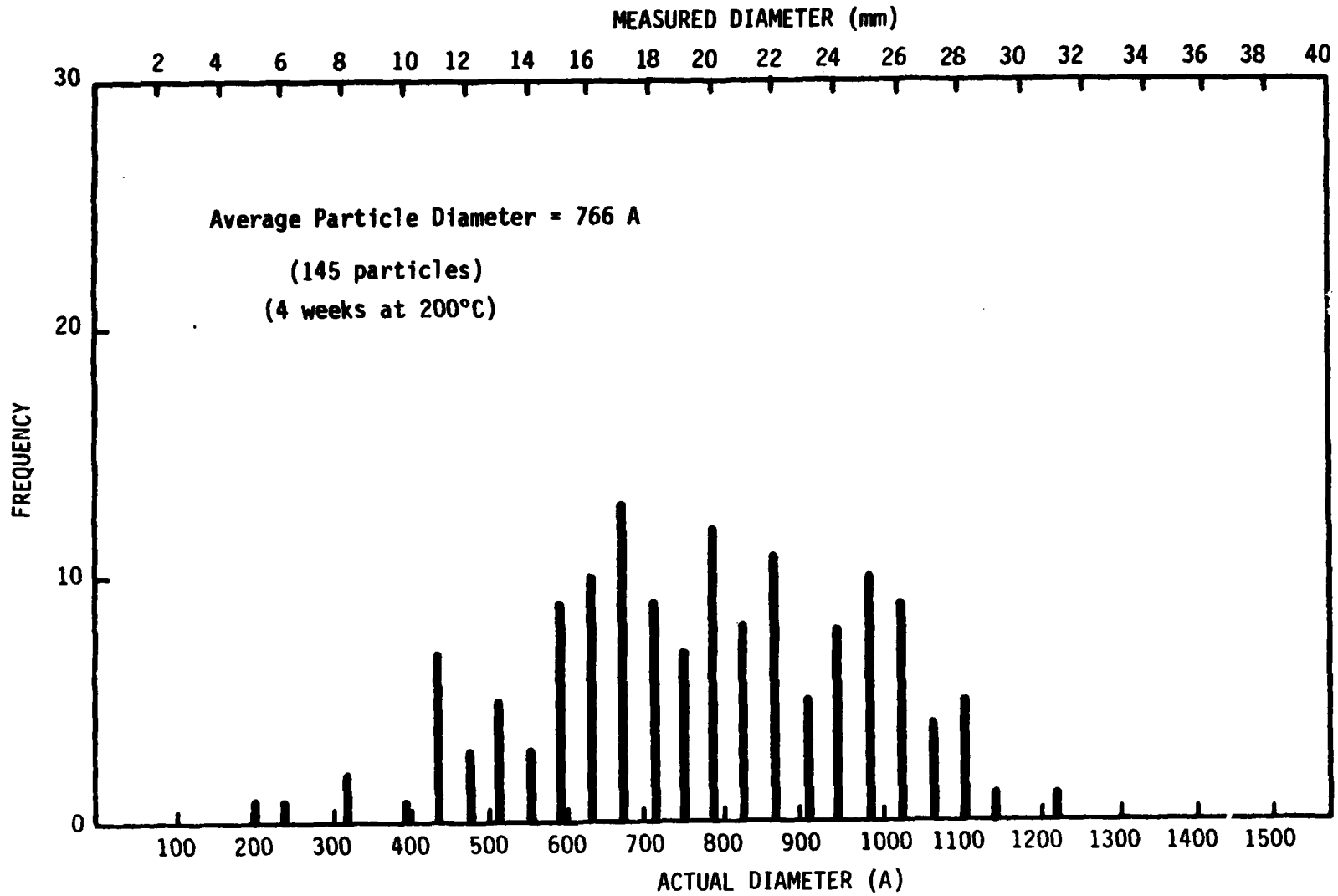

Figure E17. Particle size distribution function of 2 TEM negatives.

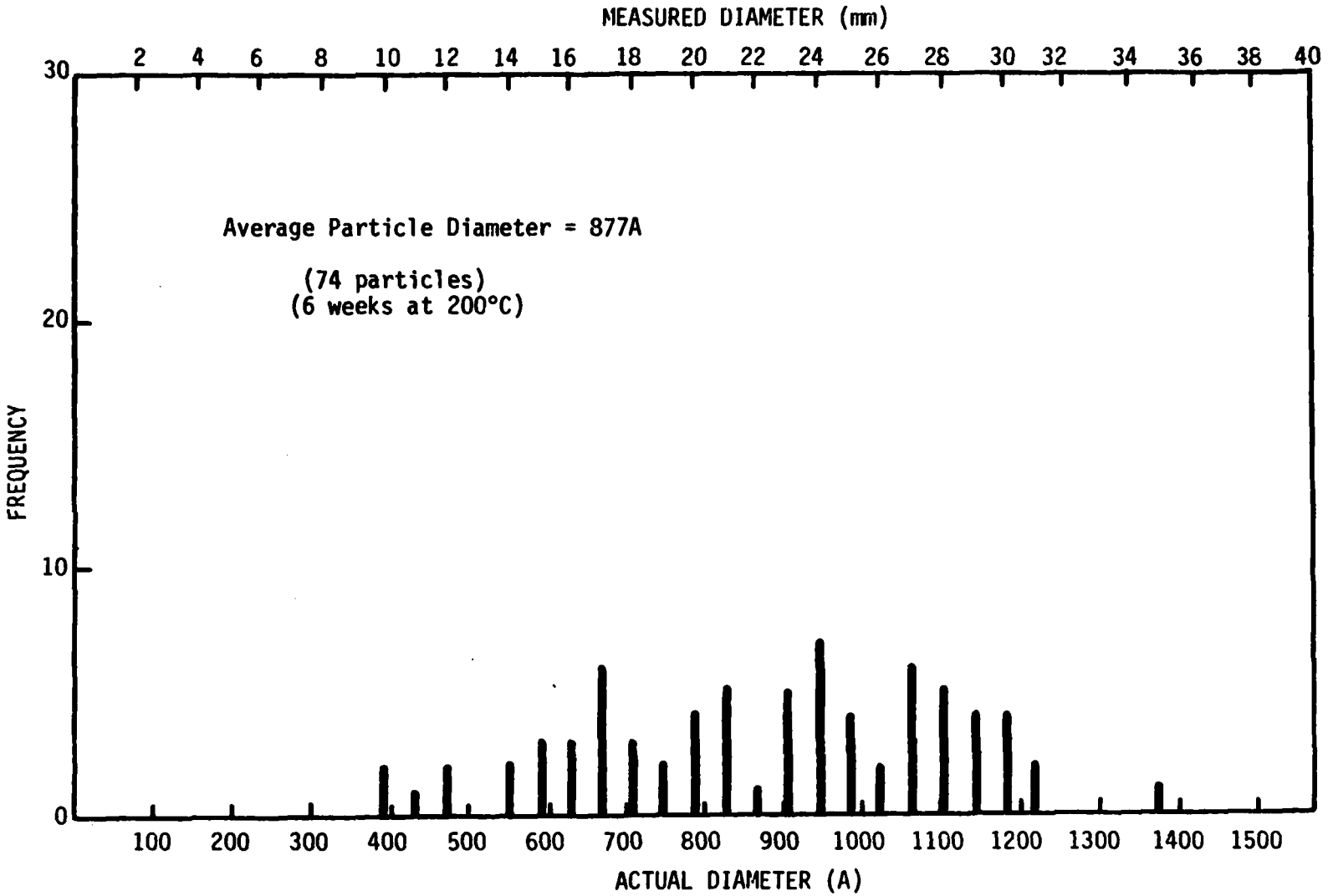

Figure E18. Particle size distribution function of 1 TEM negative.

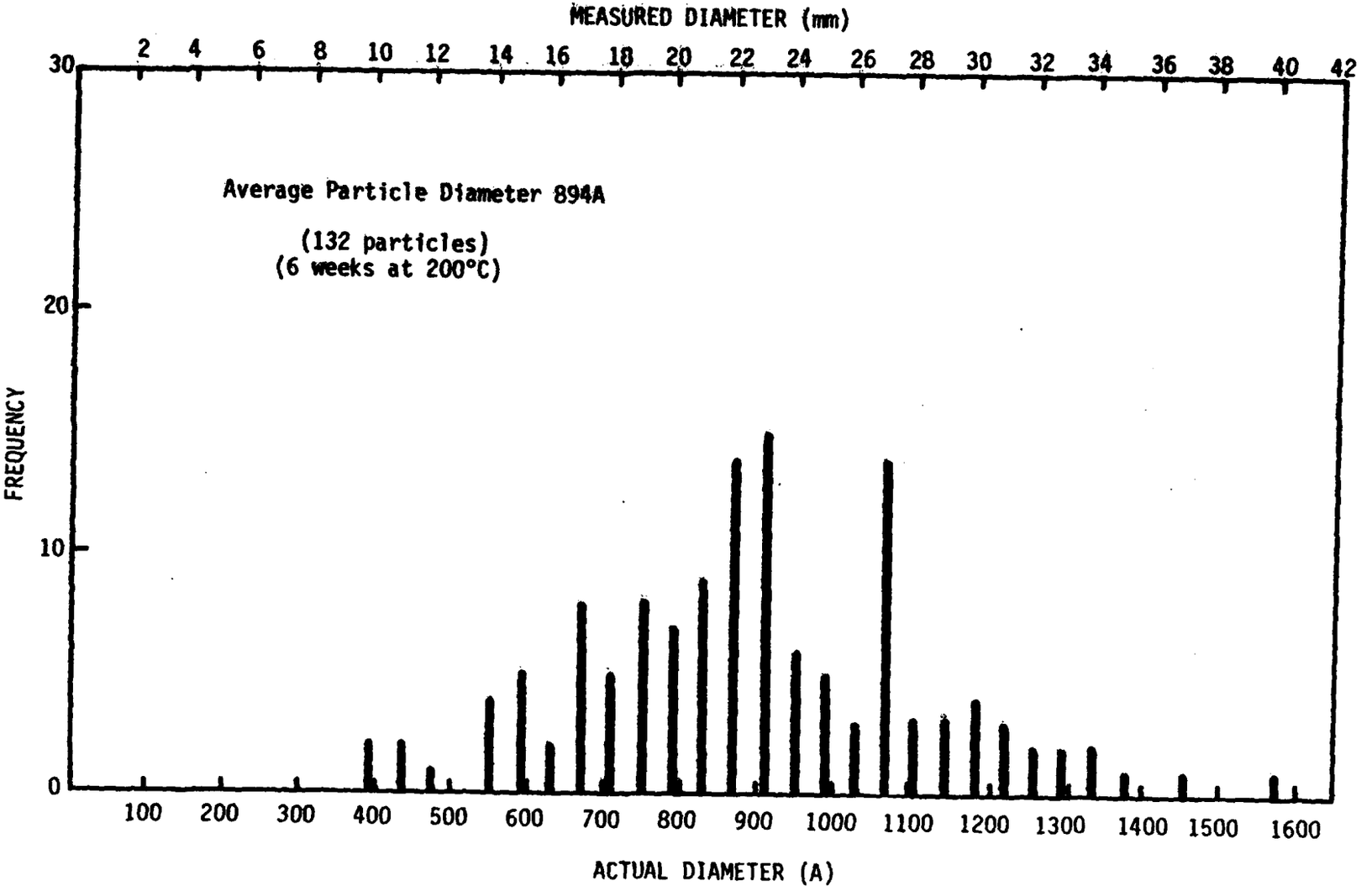

Figure E19. Particle size distribution function of 2 TEM negatives.

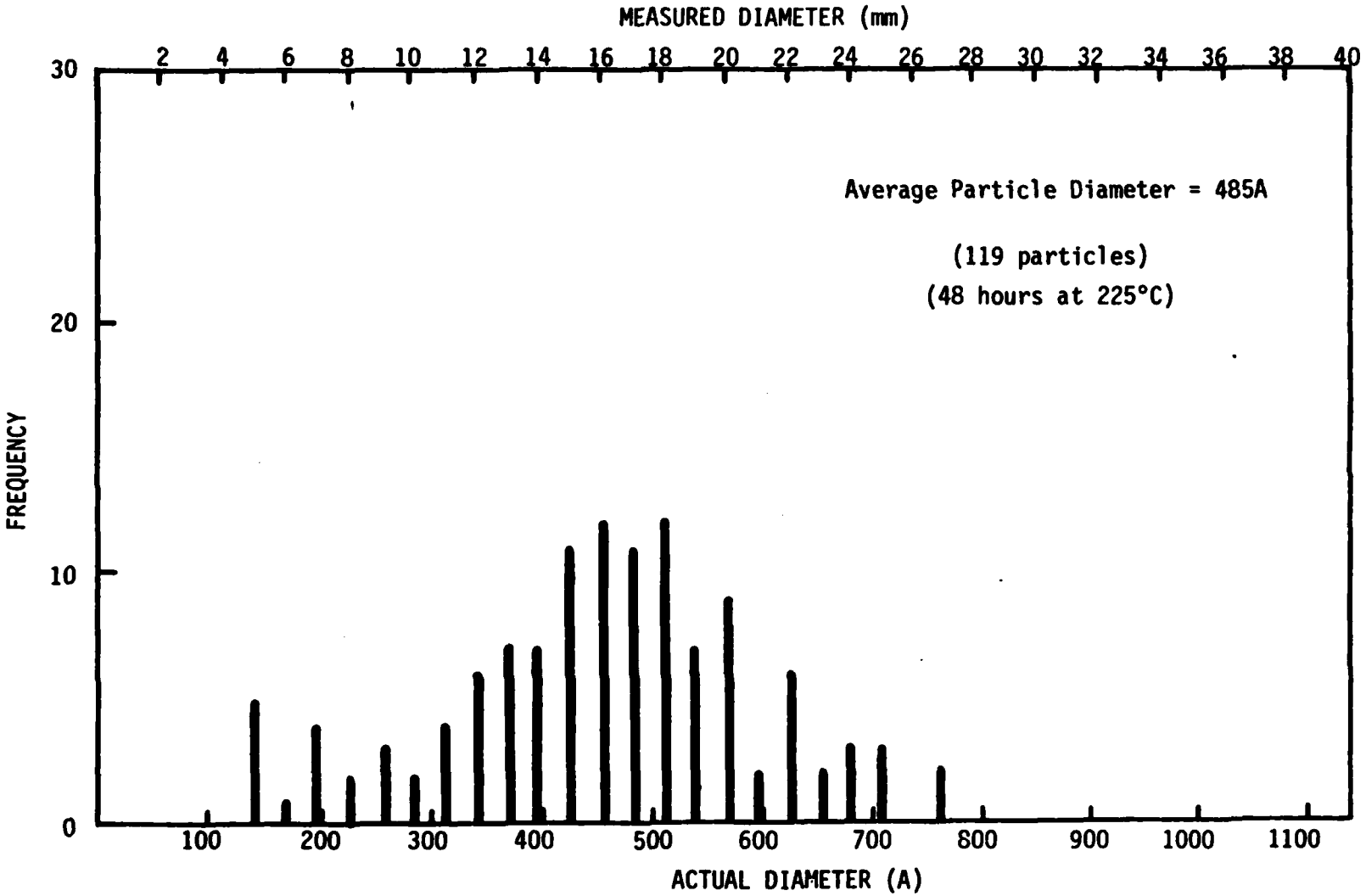

Figure E20. Particle size distribution function of 1 TEM negative.

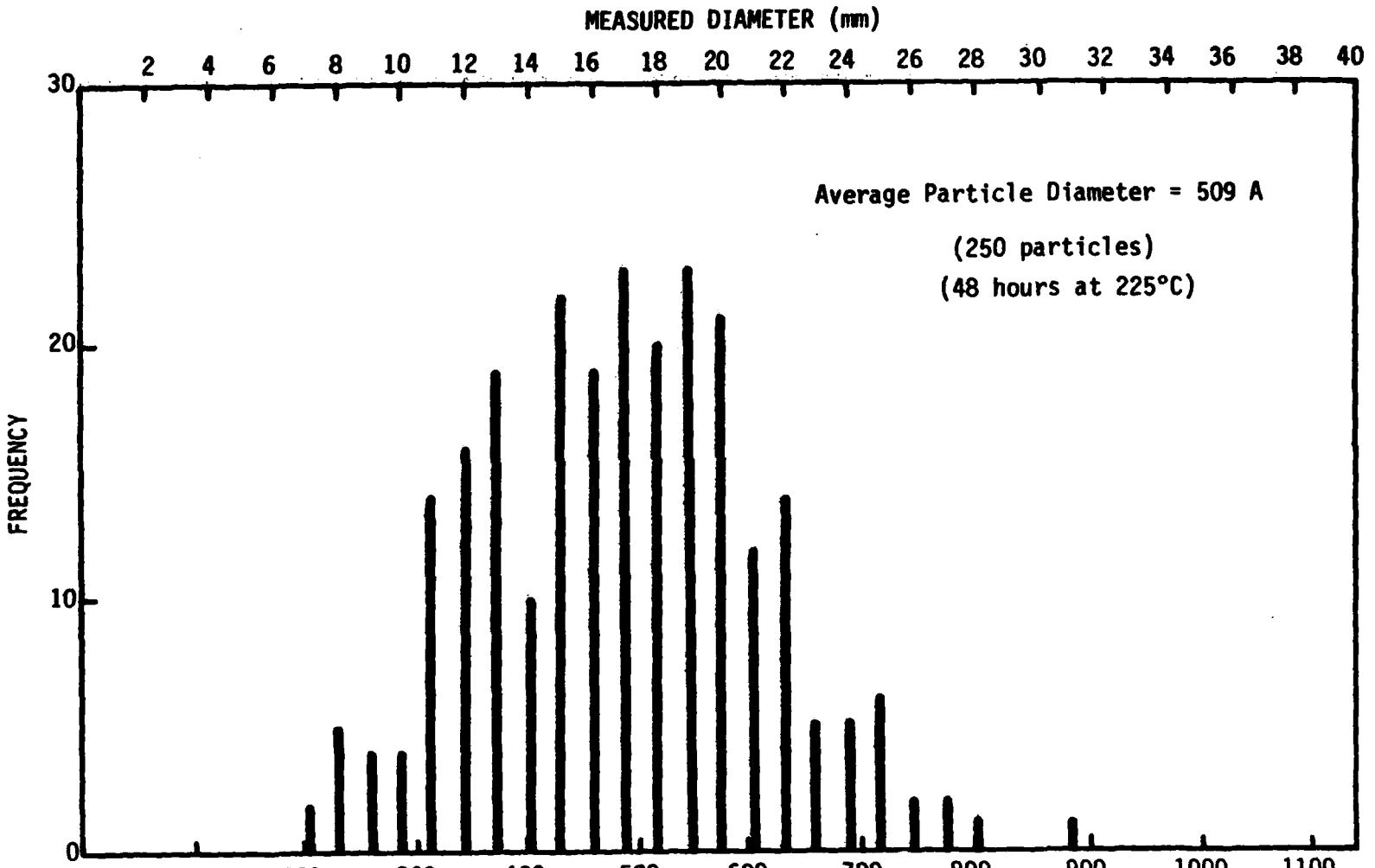

Figure E21. Particle size distribution function of 2 TEM negatives.

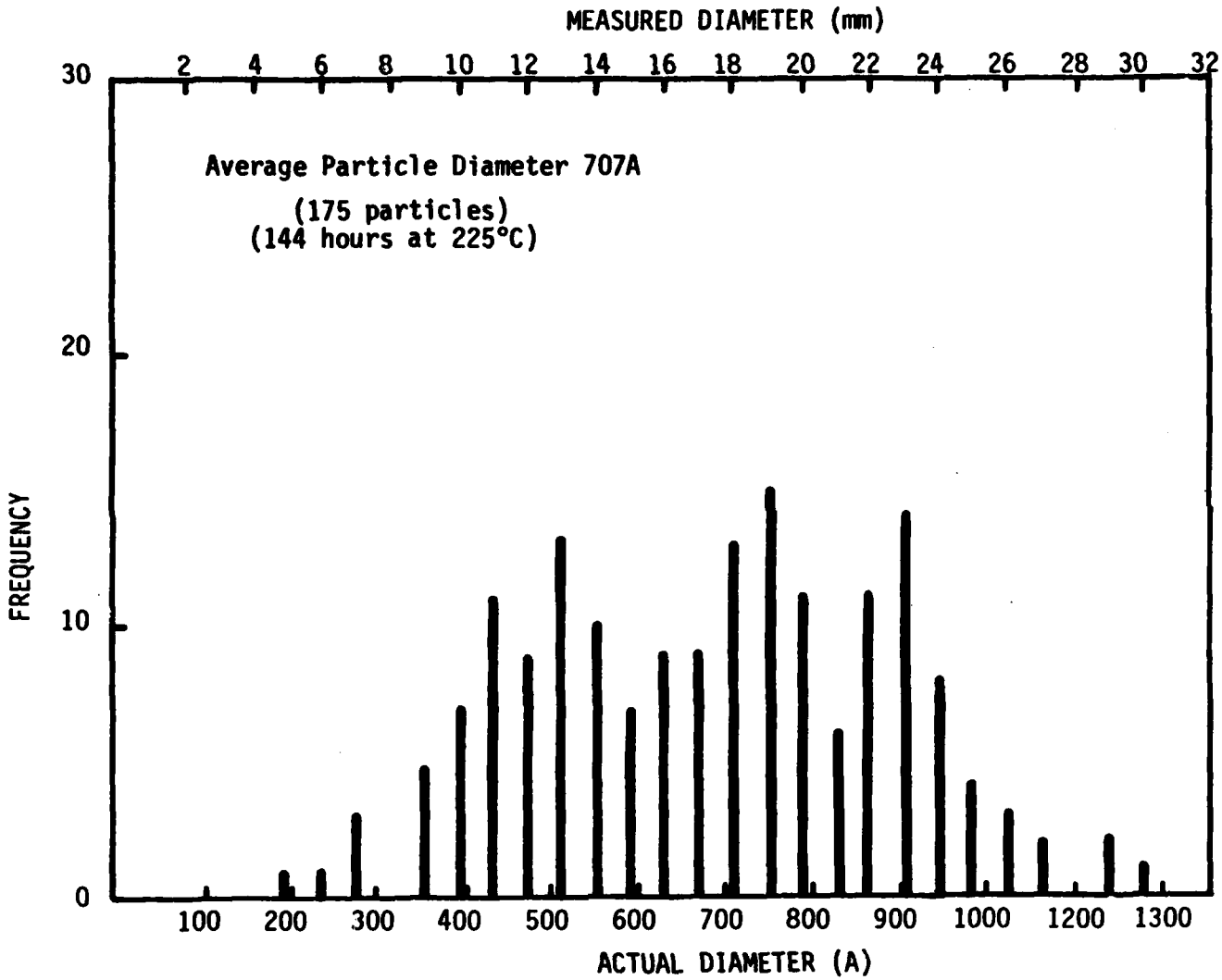

Figure E22. Particle size distribution function of 1 TEM negative.

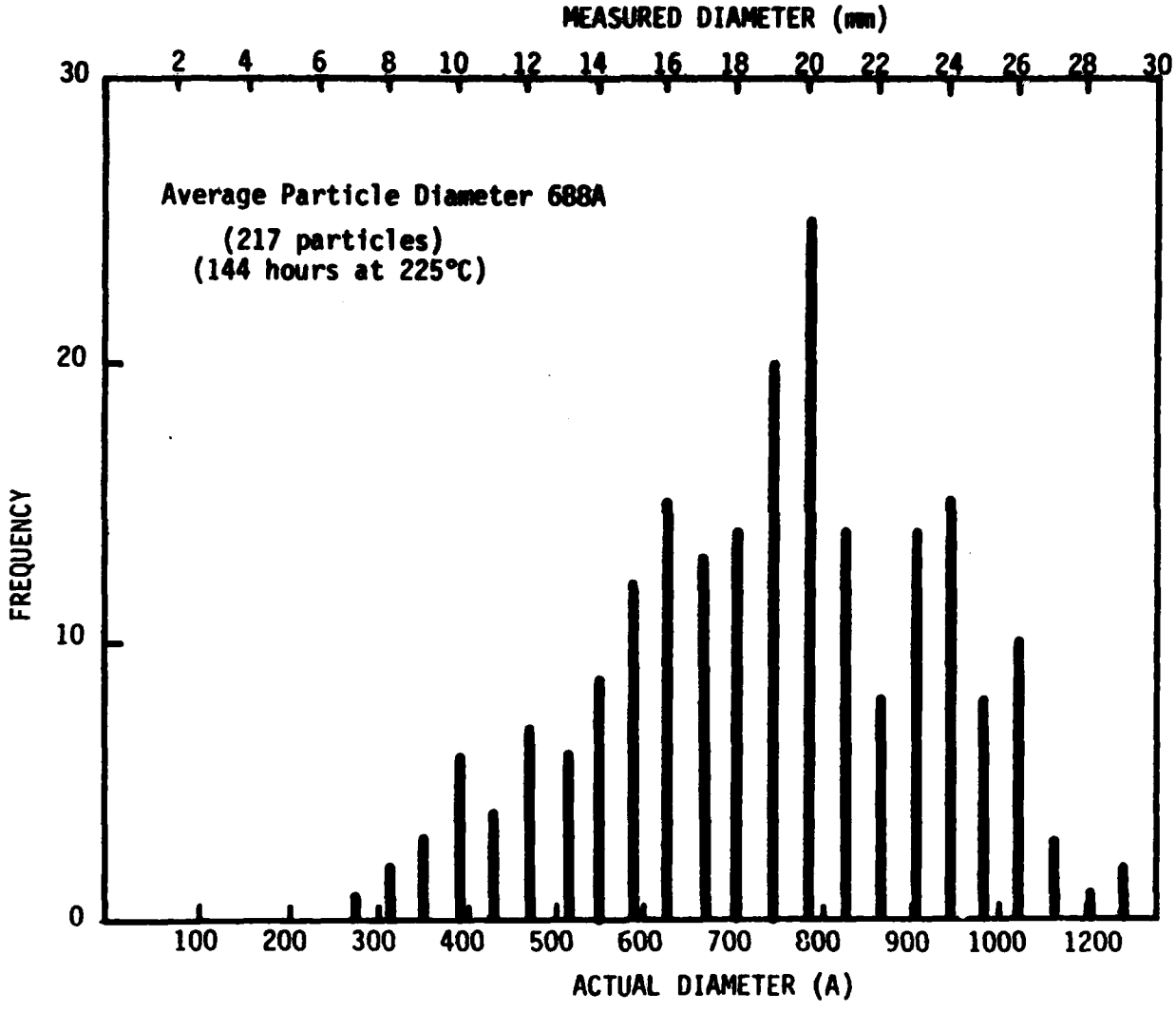

Figure E23. Particle size distribution function of 2 TEM negatives.

Appendix F

Number of Measurements Necessary to Determine $\bar{R}$

An important parameter for the accuracy of $\bar{R}$ is the particle population size. To determine what effect the total number of particles had on $\bar{R}$, at two differing aging conditions the population size was varied. These variations were based on the number of individual TEM negatives used in the measurements. The measurements of 1 film, 2 films, etc. were compiled and $\bar{R}$ and standard deviations were calculated for each population size. In order to check our results, results for 1 and 2 films were found for other aging conditions.

It was found that even as few as 100 precipitate particles will produce a reasonably accurate determination of $\bar{R}$. The variation in $\bar{R}$ for differing population sizes was not great, varying by only a few Angstrom units. This desired accuracy can thus be achieved through the quick measurement of only a small number of particles for a desired system.

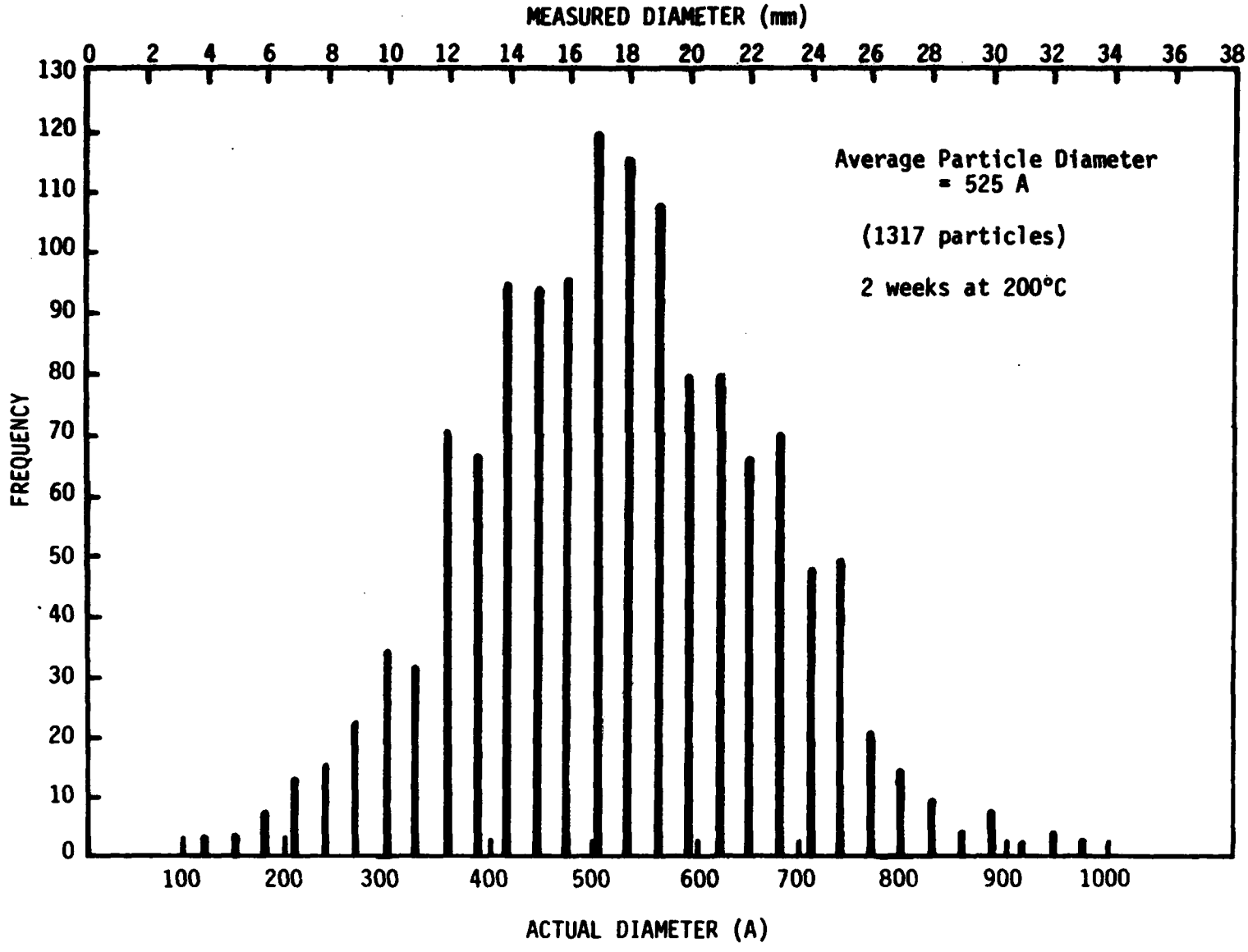

Figure F1. Particle size distribution function with 1mm measurement intervals.

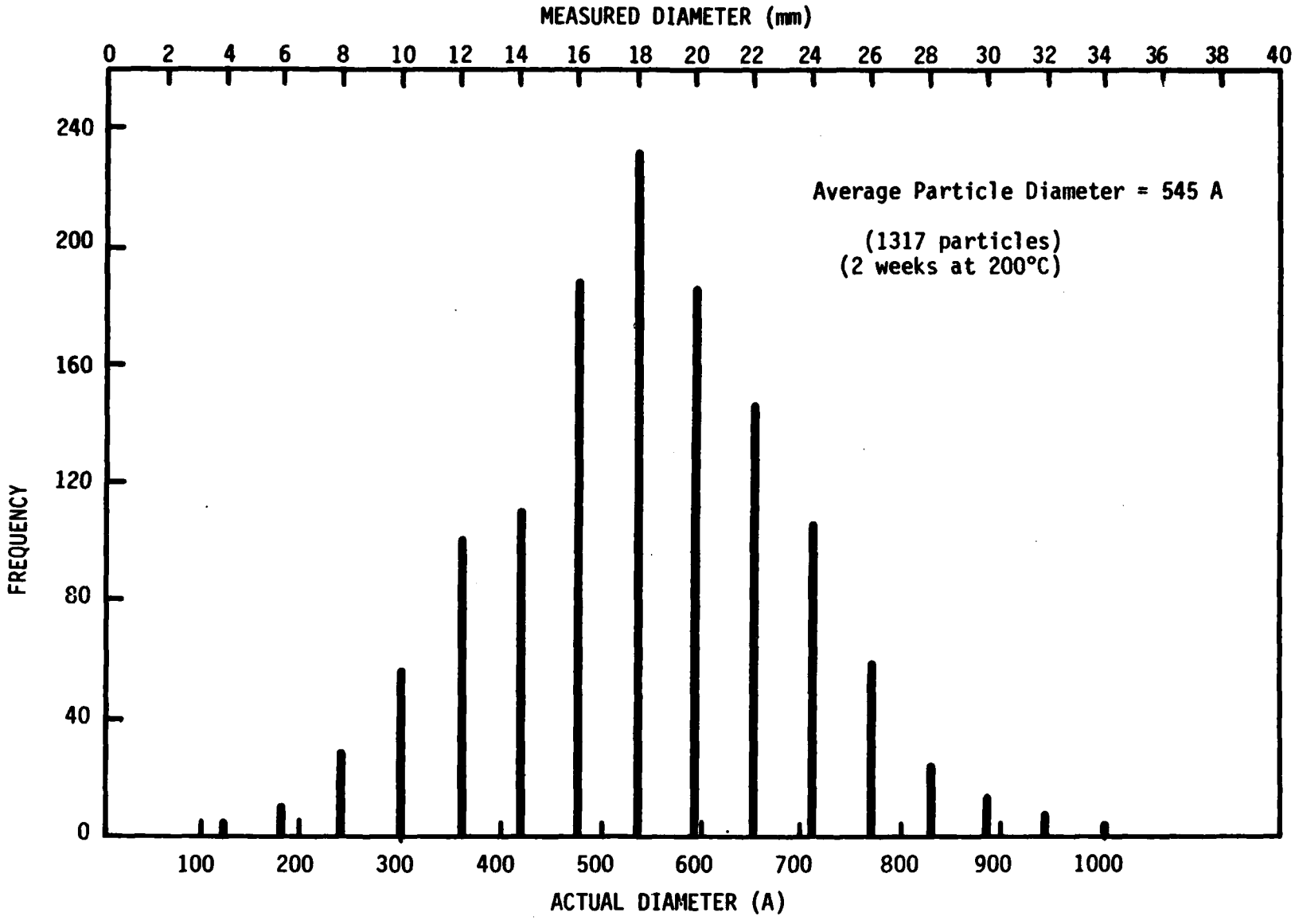

Figure F2. Particle size distribution function with 2mm measurement intervals.

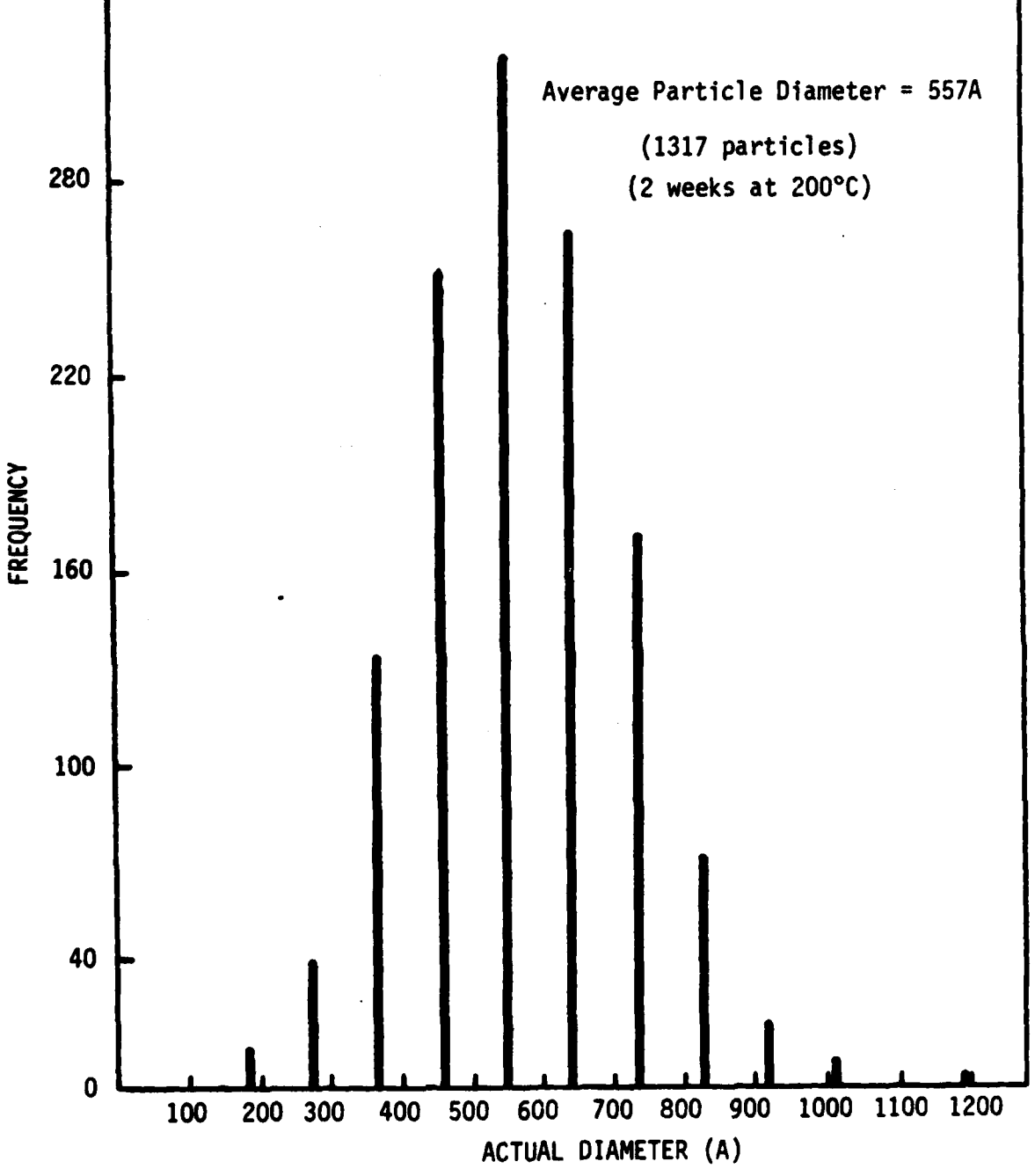

Figure F3. Particle size distribution function with 3mm measurement intervals.

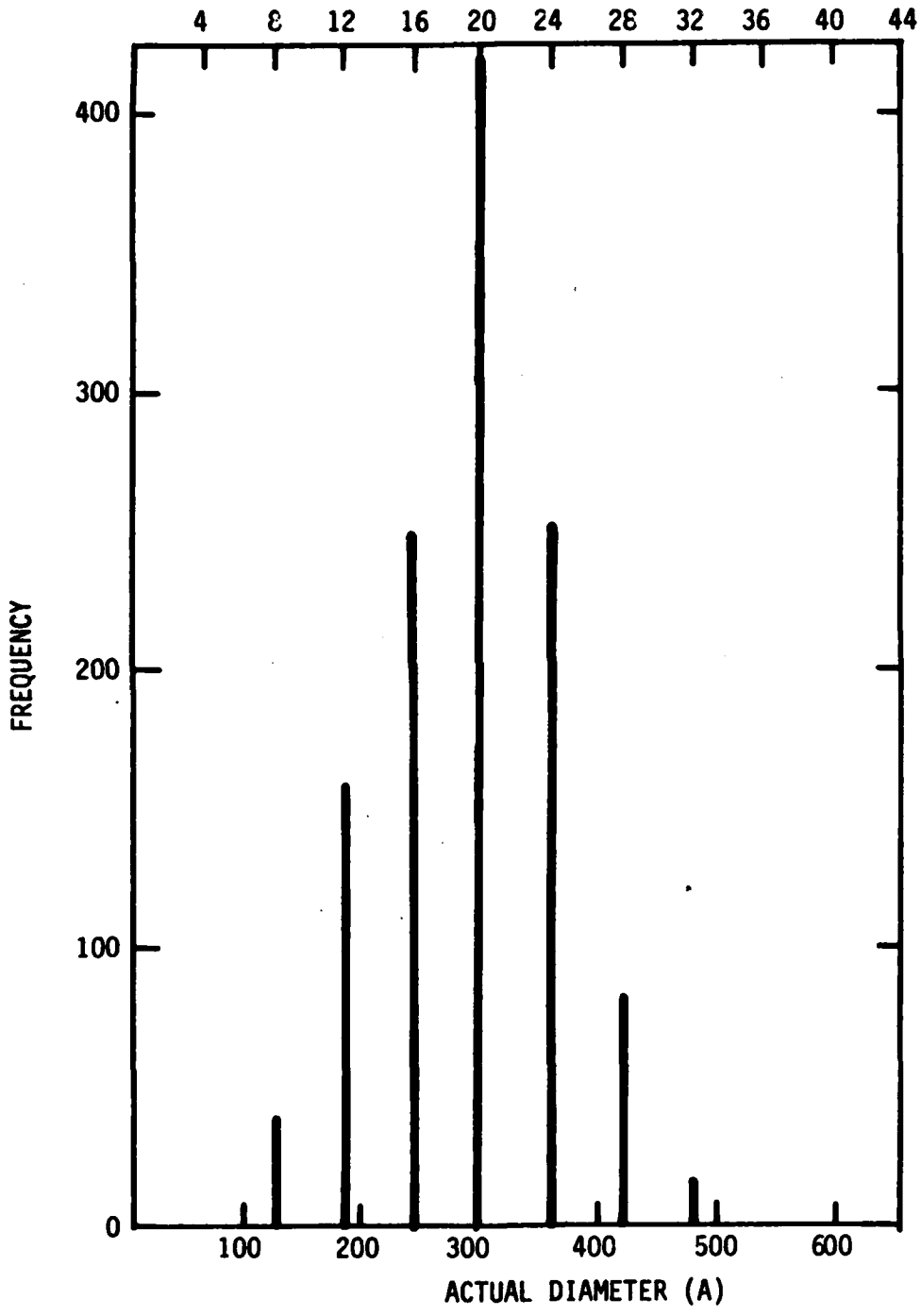

Average Particle Diameter = 579

(1317 particles)
(2 weeks at 200°C)

Figure F4. Particle size distribution function with 4mm measurement intervals.

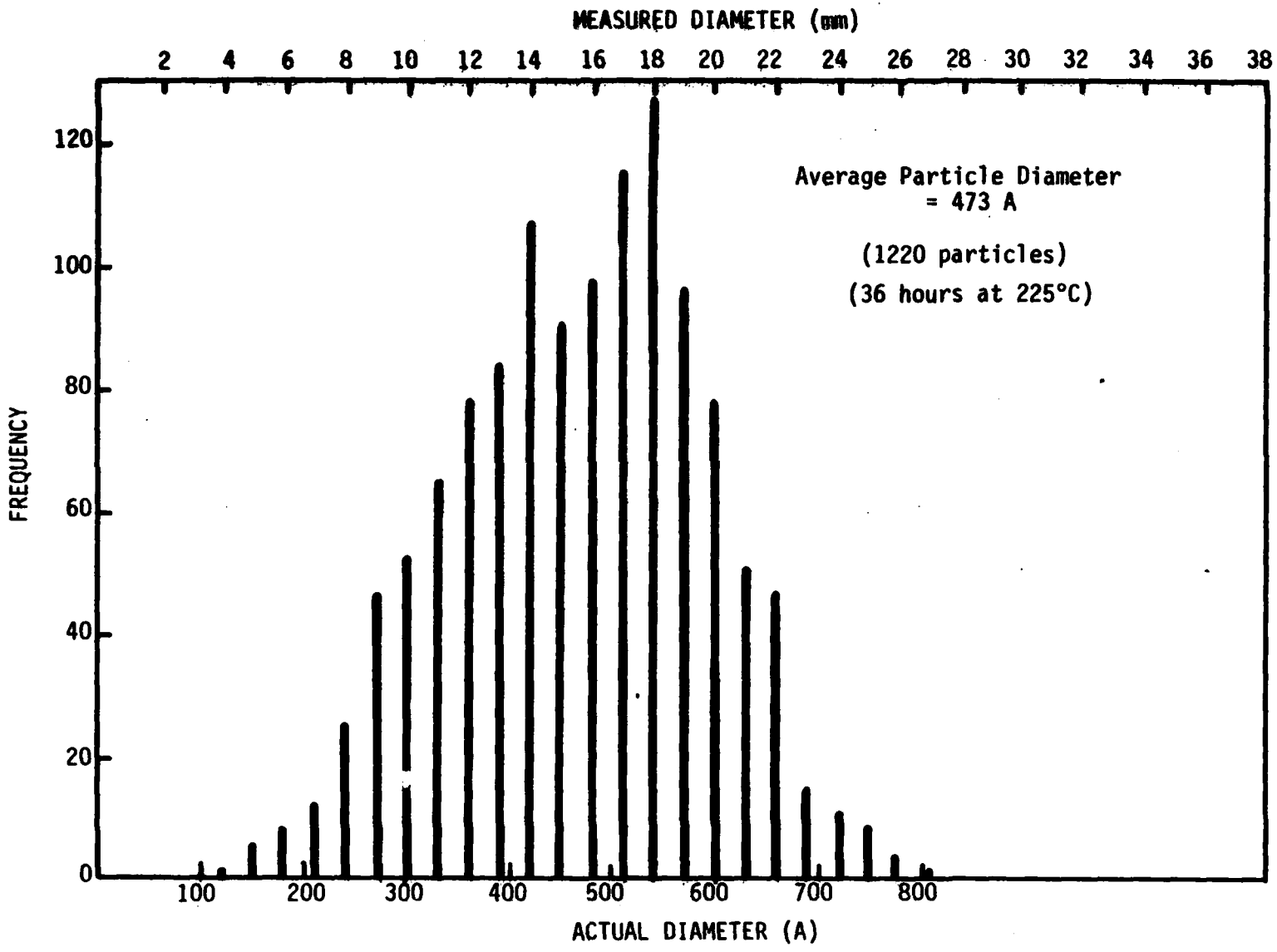

Figure F5. Particle size distribution function with 1mm measurement intervals.

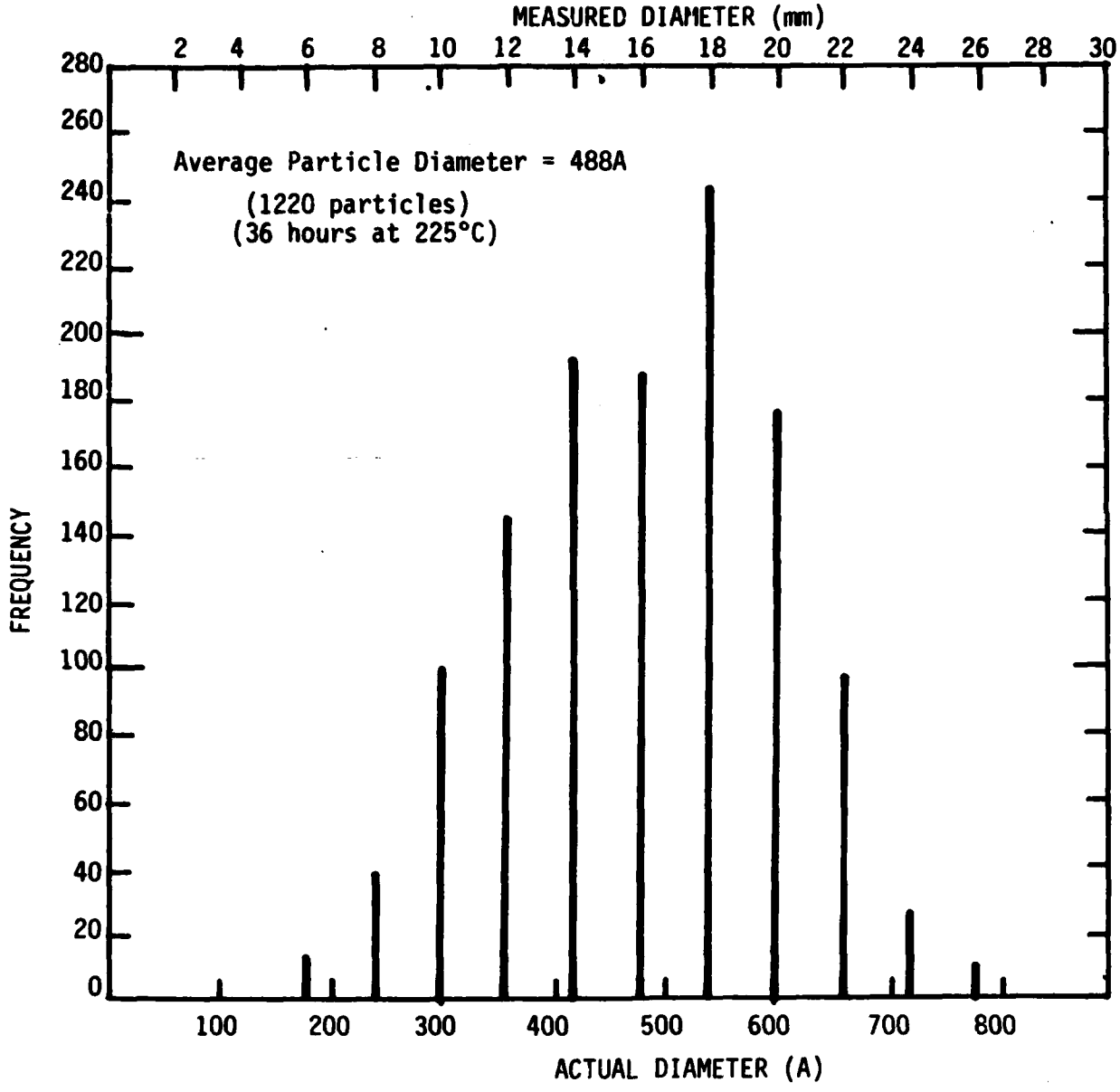

Figure F6. Particle size distribution function with 2mm measurement intervals.

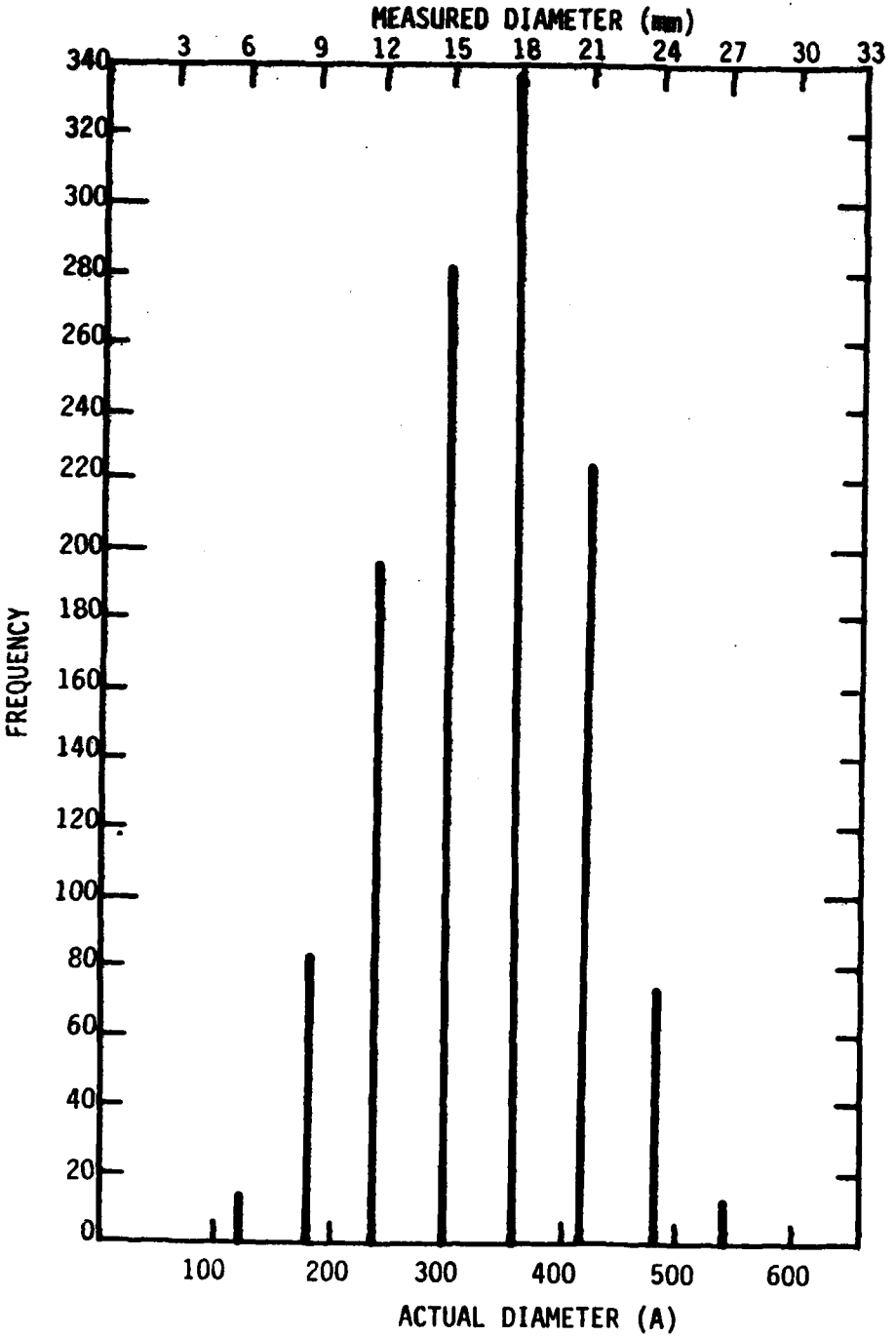

Average Particle Size = 503A

(1220 particles)
(36 hours at 225°C)

Figure F7. Particle size distribution function with 3mm measurement intervals.

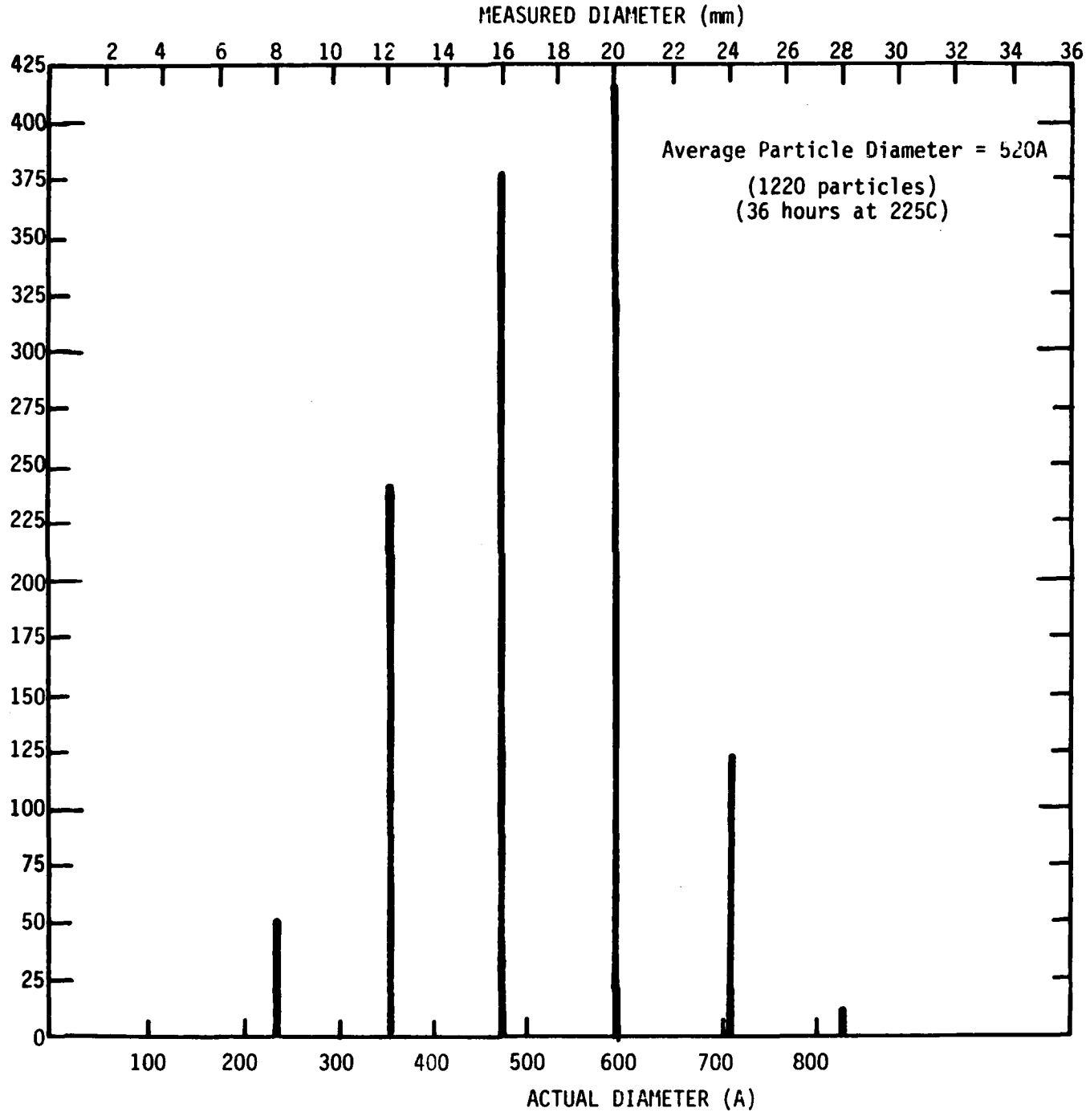

Figure F8. Particle size distribution function with 4mm measurement intervals.

Appendix G

Interval Size for the IAS

To determine an effective interval size for the IAS, the class intervals were combined in a manner similar to Appendix D. Class interval sizes of 1, 2, 3 and 4 units were used as before, with 1 unit representing 1/100 of the length of the standard line utilized for the measurement program of Appendix C. This unit corresponds to a certain length (in Angstrom units) defined by the magnification of the TEM negative, the further magnification of the negative by the video terminal and the entered reference line.

While in all cases a symmetrical PSD was found, the use of the 2 unit interval produced the smoothest results, the results most similar in shape to the hand measurements. The results became smoother as they approached the overall form of a normal curve, with little static in the individual class intervals. This static suggests the interval size is too small for accurate analysis.

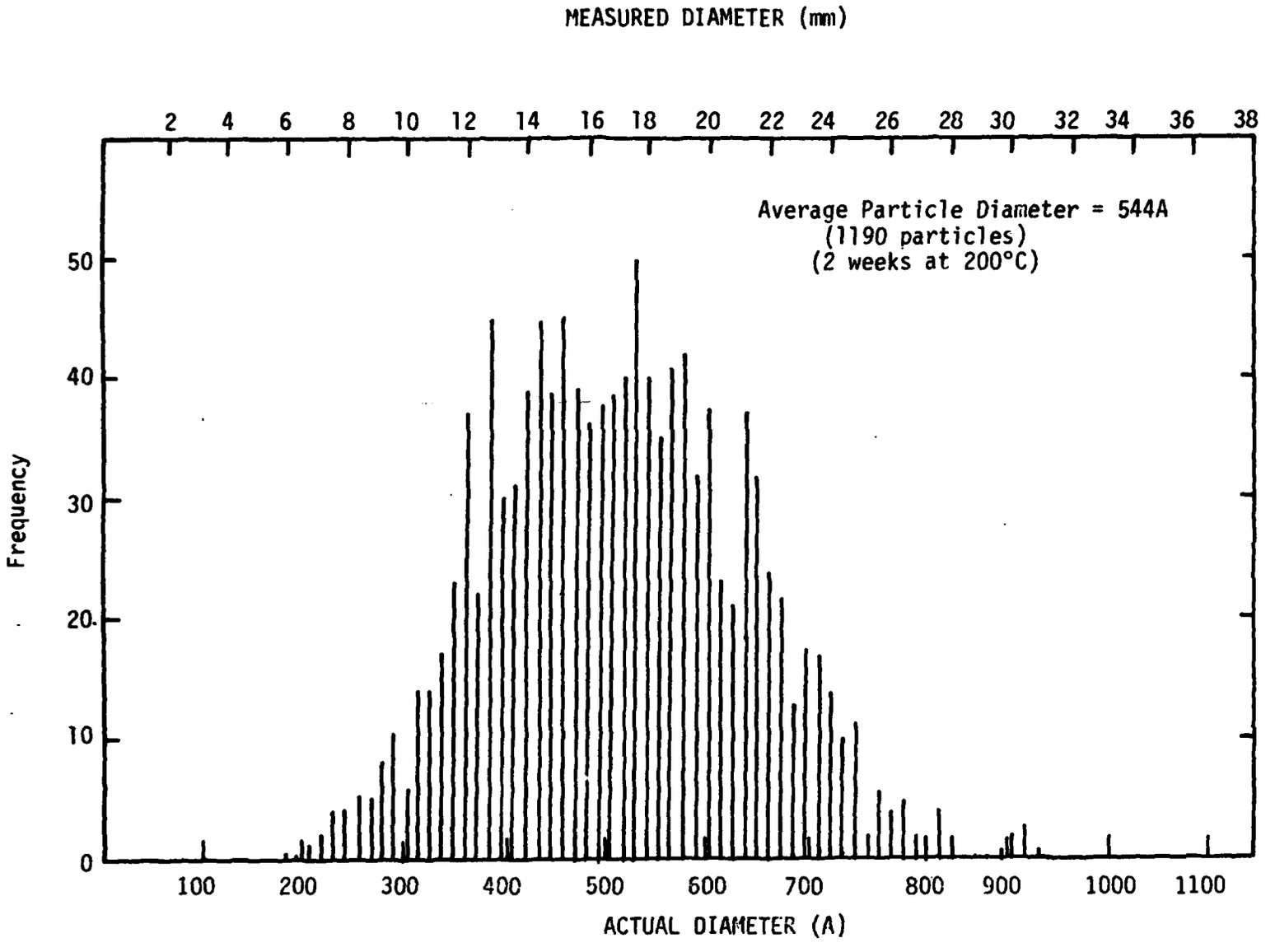

Figure G1. PSD using image analyzer for 1 unit measurement intervals.

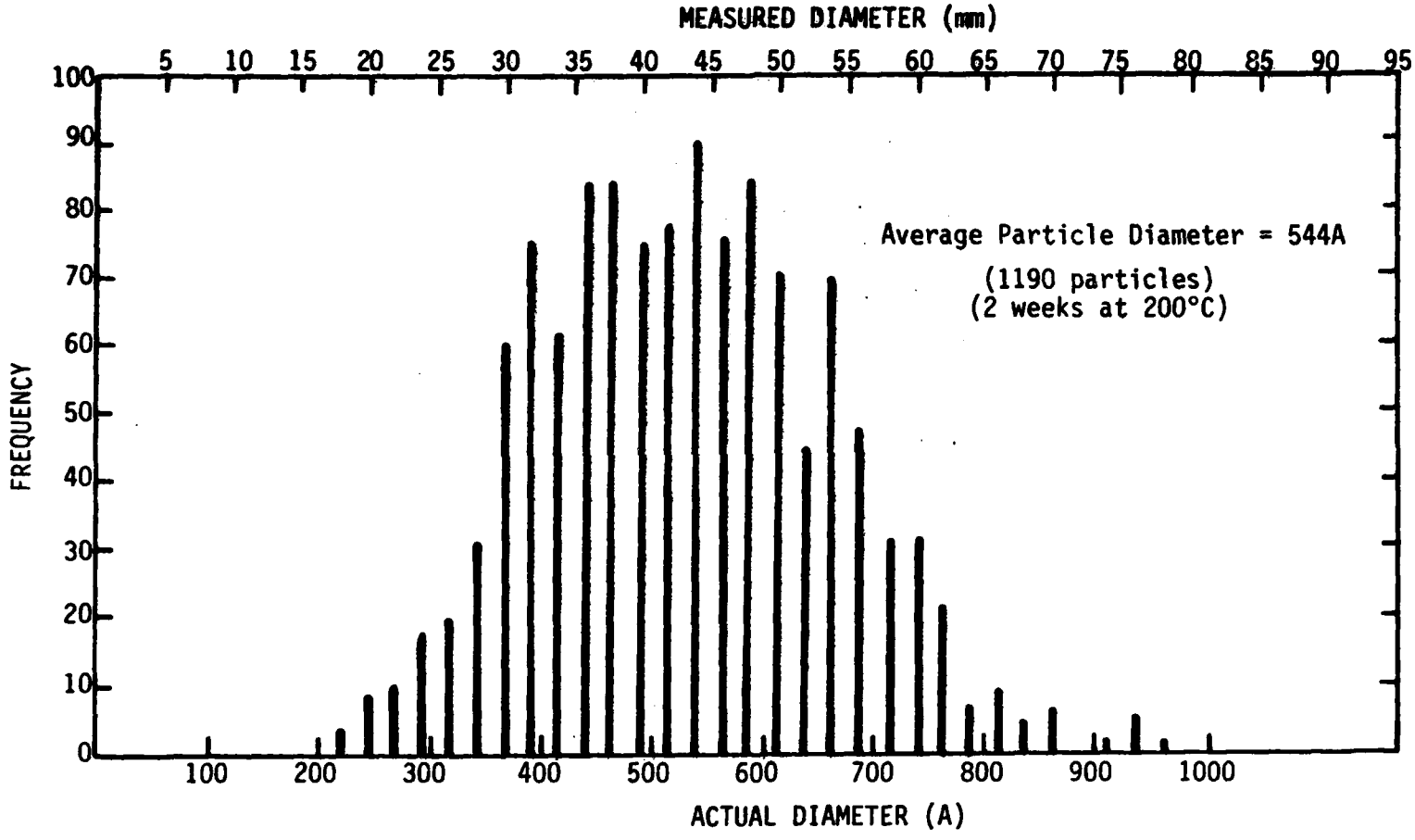

Figure G2. PSD using image analyzer for 2 unit measurement intervals.

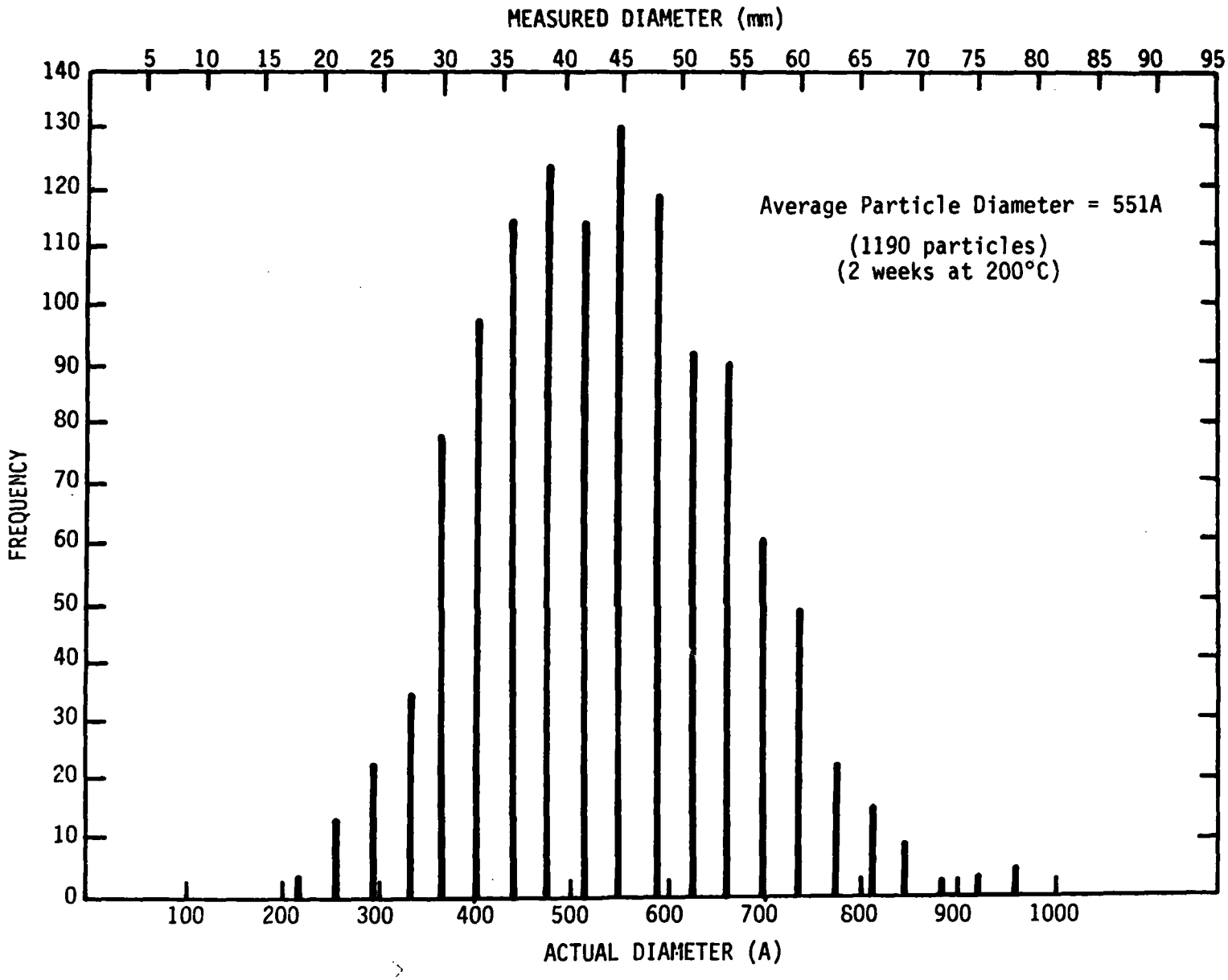

Figure G3. PSD using image analyzer for 3 unit measurement intervals.

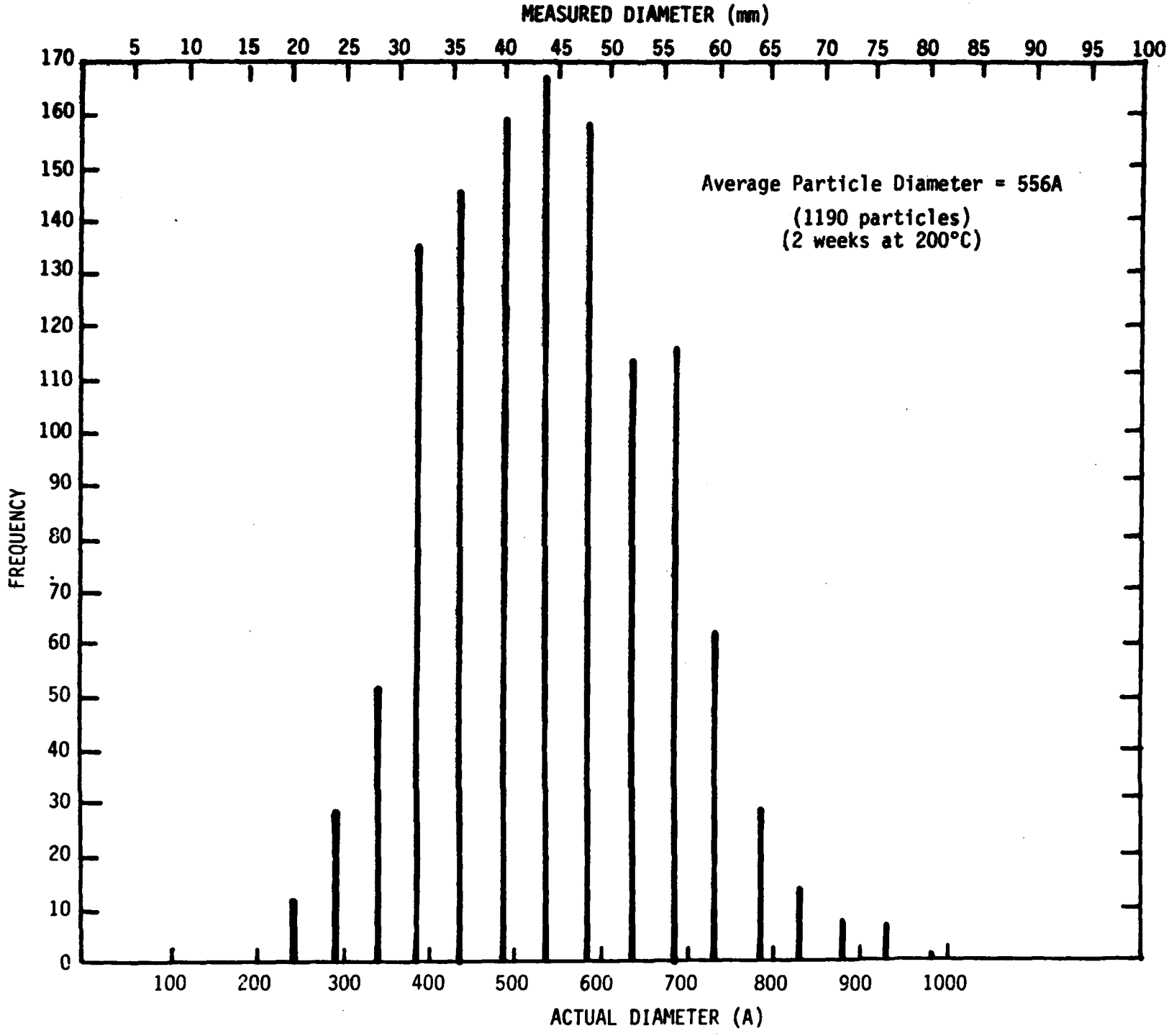

Figure G4. PSD using image analyzer for 4 unit measurement intervals.

Appendix H

Getting on and Using the IAS

The IAS is a system which may be used in either Fortran IV, Basic-11 or Macro-11. Each system has its own compiling program and procedure. Refer to the Introduction to RT-11, Volume 1A for information.

To get on the system, the system must be booted, using floppy disks. The instructions for booting (entering the system) and leaving the system are summarized in Figure H1.

Volume 1A has most of the basic information necessary for simple use of the system. Some simple commands on the IAS are:

- DIR - prints on the terminal the files located on the booted floppy disk.
- PRINT (filename) - prints on the line printer the contents of a file.
- RENAME (filename) - renames a file name from an old name to a new selected name.

Other commands, including the command sequence for copying from one floppy disk to another will be found in instruction manuals located near the system.

To boot the system, the steps are:

1. Turn on the line printer.
2. Turn on the terminal
3. Turn on the disk drive power switch located at the far right. When on this switch should be in the up position.
4. Make sure that the write protect switches for disk 0 located at the top is in down position.
5. Make sure that the row of switches at the bottom of the disk drive are in the up position (this includes the power switch).
6. Open the disk cover for slot 0.
7. Insert the disk in such a way that the label "IBM Diskett" is pointing towards the bottom right.
8. Close the cover.
9. Push the boot switch (located third from left) down and up.
10. The line printer will respond with messages and the system is now booted.

Follow these steps given below to shut off the system:

1. Press the "Enab" switch (located at the first left) on the disk drive down.
2. The line printer will respond with a message.
3. Remove the disk from slot 0.
4. Close the disk cover.
5. Push the "Enab" switch to the up position.
6. Shut off the line printer.
7. Shut off the terminal.
8. Shut off the power for the disk drive.

FIGURE H1. Instructions for operating the image analyzer system.

APPENDIX I

Calibration of DSC

In the DuPont 910 Differential Scanning Calorimeter (DSC) system, each peak area can be converted into heat of reaction by substitution into the following equation.

$$\Delta H = \frac{A}{m} (60\ BE\ \Delta qs)$$

where

- A = peak area in cm^2
- m = sample mass in g
- B = time base setting in min/cm
- E = cell calibration coefficient at the temperature of the experiment in cmW/mV
- Δqs = Y-axis range setting in mV/cm
- ΔH = heat of fusion in J/kg

For the calibration coefficient (E) varied with temperature, its value should be determined as a function of temperature. The calibration coefficient can be determined at any given temperature using a material of which the capacity is known over the temperature range of interest. A sapphire (Al_2O_3) disc was used for this purpose. The calibration run was carried out with the following procedure.

1. The starting temperature and the limit temperature were set to 125°C and 525°C, repectively in the temperature controller.
2. 20°C/min was chosen for heating rate.
3. A "blank" run with empty sample and reference pans was made recording the Y-axis displacement as a function of temperature.
4. The procedure was repeated under identical conditions with a sapphire disc of 65.8 mg in the sample pan.

The results of this run are presented in Figure I1. E was calibrated by measuring the difference in Y-axis deflection between sample and blank curves at any desired temperature, substituting the difference into the following equation.

$$E = \frac{Cp\ Hr\ m}{60\ \Delta qs\ \Delta Y}$$

where

Cp = heat capacity of sapphire in J/g^{o}C
Hr = heating rate (20^{o}C/min)
ΔY = difference in Y-axis deflection between sample and blank at temperature of interest in cm.
m = sample mass (65.8 mg)
Δqs = Y-axis range setting (20 mV/cm)
E = calibration coefficient at the temperature of interest in mW/mV

E versus temperature is plotted in Figure I2.

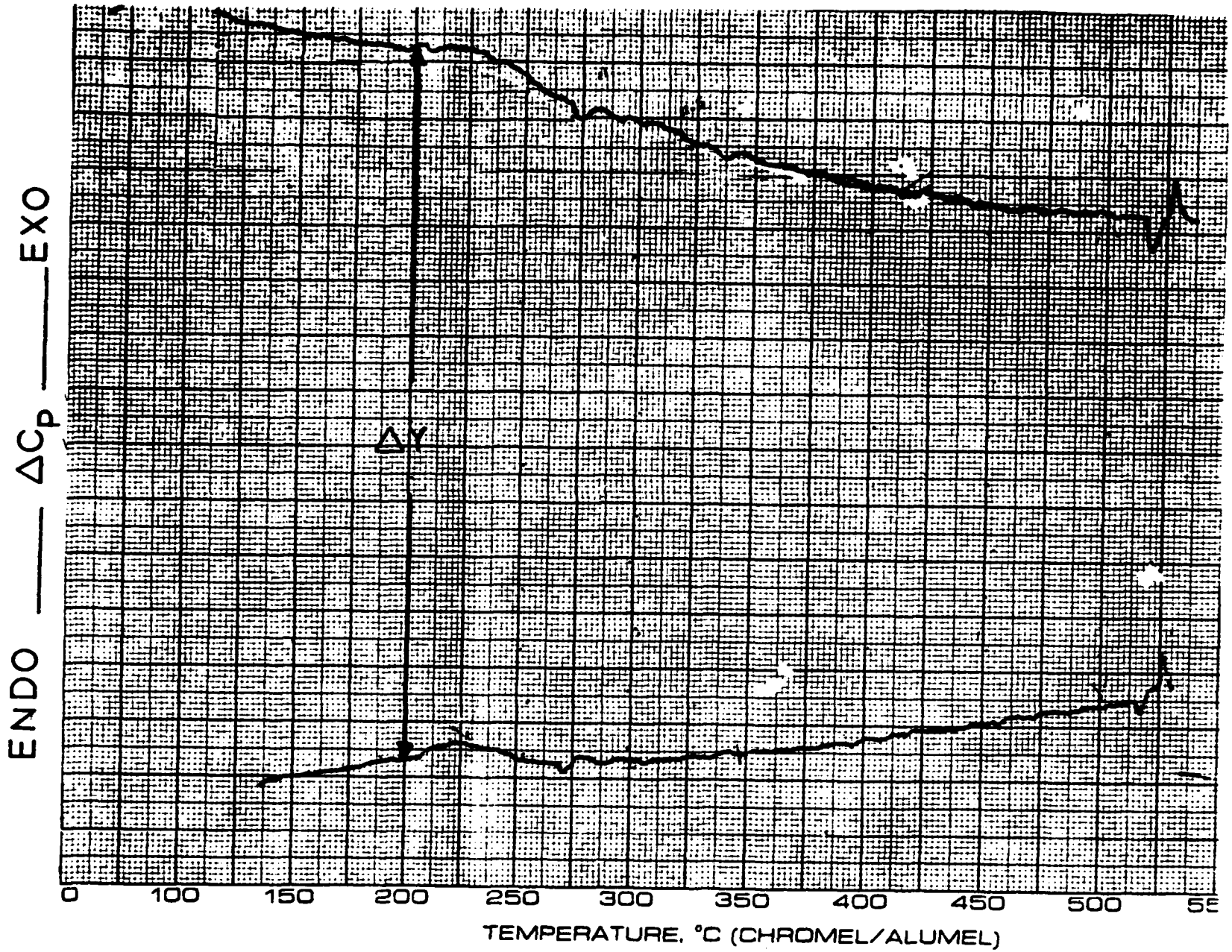

Figure I1. Heat Capacity of Sapphire (Al_2O_3).

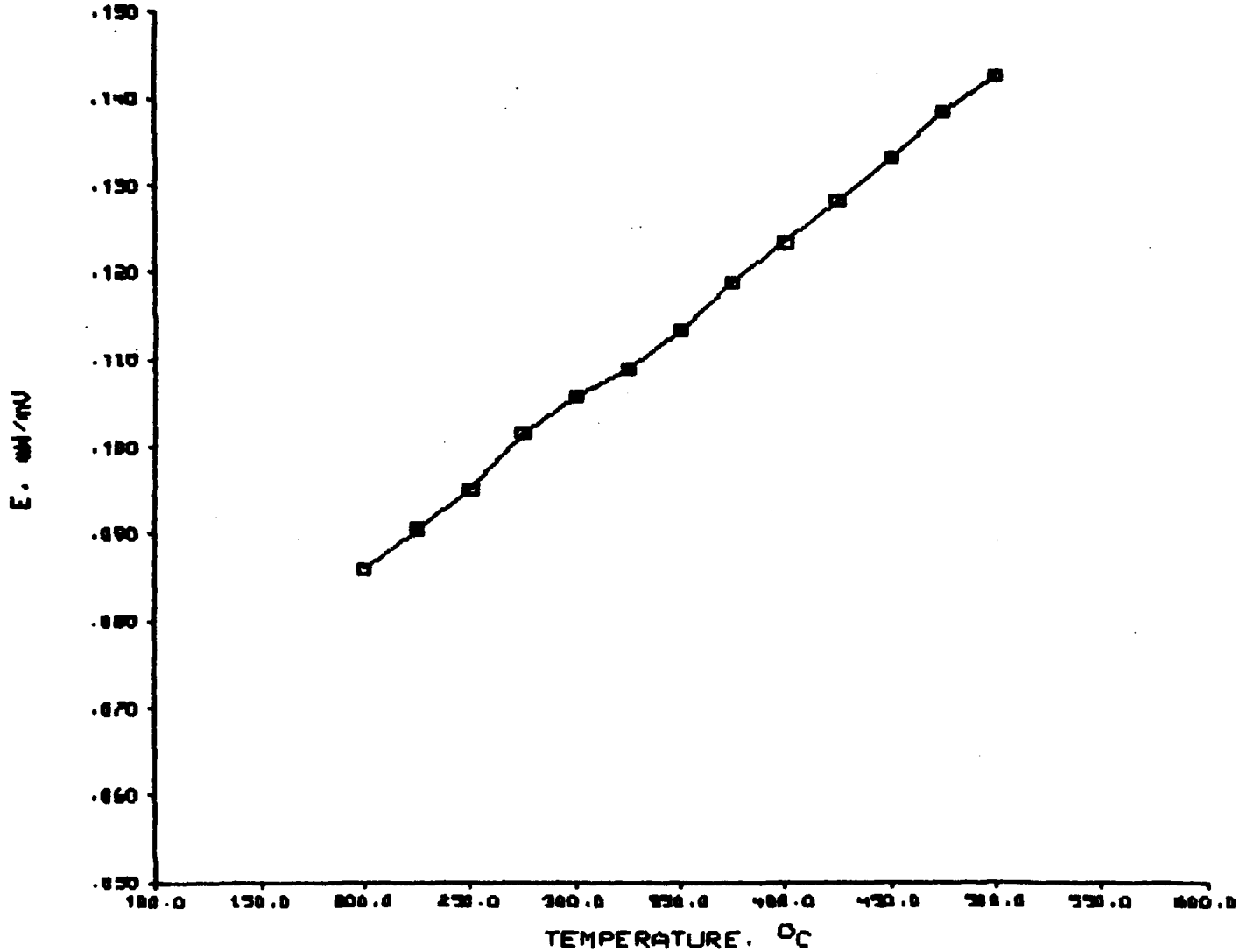

Figure I2. Calibration Coefficient/Temperature Curve.

DISTRIBUTION LIST

DISTRIBUTION LIST

Mr. Michael D. Valentine
AIR-5163C4
Naval Air Systems Command
Washington, DC 20361
(5)

Richard Schmidt
Coade 320A
Naval Air Systems Command
Washington, DC 20361
(2)

A. P. Divecha
R32
Naval Surface Weapons Center
White Oak, Laboratory
Silver Spring, MD 20910

H. M. DeJarnette
R32
Naval Surface Weapons Center
White Oak, Laboratory
Silver Spring, MD 20910

Commander
Naval Air Development Center
(Code 302)
Warminster, PA 18974

Naval Sea Systems Command
(Code 03423)
Department of the Navy
Washington, DC 20360

Naval Ships Research &
Development Center
(Code 2812)
Annapolis, MD 21402

Commander
Naval Surface Weapons Center
(Metallurgy Division)
White Oak, Laboratory
Silver Spring, MD 20910

Director
Naval Research Laboratory
(Codes: 6380, 6490, 6601, 8430)
(1 each)
Washington, DC 20390

Office of Naval Research
The Metallurgy Program
Code 471
Arlington, VA 22217

Dr. T. R. McNelley
Dept. of Mechanical Engineering
(Code 59)
Naval Postgraduate School
Monterey, CA 93940

Commander
Naval Air Systems Command
AIR-954 (2 copies)
DDC (12 copies)
Washington, DC 20361

Dr. Bruce A. MacDonald
Office of Naval Research
800 N. Quincy Street
Code 471
Arlington, VA 22317

Naval Surface Weapons Center
Library - X211
White Oak, Laboratory
Silver Spring, MD 20910
(3)

Wright-Patterson Air Force Base
Ohio 45433
ATTN: C.L. Harmsworth
AFML/MXE

Wright-Patterson Air Force Base
Ohio 45433
ATTN: W. Griffith
AFML/LLS

AFOSR/NE
Bolling Air Force Base
Washington, DC 20332
ATTN: Dr. A. H. Rosenstein

U. S. Army Armament R&D Command
(ARRADCOM)
Dover, NJ 07801
DRDAR-SCM-P, Bldg. 3409

Metallurgy & Materials Science Div.
U. S. Army Research Office
P.O. Box 12211
Research Triangle Park, NC 27709
ATTN: Dr. G. Meyer

Metallurgy & Materials Science Div.
U. S. Army Research Office
P.O. Box 12211
Research Triangle Park, MD 27709
ATTN: Dr. Phillip Parrish

Commanding Officer
Office of Ordnance Research
Box CM, Duke Station
Durham, NC 27706

Army Materials & Mechanics Research Cnt.
Watertown, MA 02172
ATTN: Dr. A. Gorum

M. H. Brennecke
EH 23
Bldg. 4612
NASA
Marshall Space Fight Center
Huntsville, AL 35812

National Aeronautics & Space Admn.
George C. Marshall Space Flight Center
Huntsville, AL 35812
ATTN: Mr. J. G. Williamson
S&E-ASTN-MMC

National Aeronautics & Space Admn.
Langley Research Center
Materials Division, Langley Station
Hampton, VA 23365
ATTN: Mr. H. F. Hardrath
Stop 188M

National Aeronautics & Space Admn.
(Code RWM)
600 Independence Avenue, SW
Washington, DC 20546

National Aeronautics & Space Admn.
George C. Marshall Space Flight Center
Huntsville, AL 35812
ATTN: Mr. J. G. Williamson
S&E-ASTN-MMC

National Academy of Sciences
Materials Advisory Board
Washington, DC 20418
ATTN: Dr. J. Lane

Director
National Bureau of Standards
Washington, DC 20234
ATTN: Dr. E. Passaglia

ERDA Division of Reactor Development
and Technology
Washington, DC 20545
ATTN: Mr. J. M. Simmons, Chief
Metallurgy Section

AiResearch Manufacturing Co. of America
Sky Harbor Aircraft
402 S. 36th Street
Phoenix, AR 85034
ATTN: Mr. Jack D. Tree
Dept. 93-35-5M

Information Department
Bldg. D
Alcoa Technical Center
Alcoa Center, PA 15069
(3)

W. S. Cebulak
Bldg. B
Alcoa Technical Center
Alcoa Center, PA 15069

J. T. Staley
Alloy Technology Division
Bldg. C
Alcoa Technical Center
Alcoa Center, PA 15069

A. K. Vasudevan
Alloy Technology Division
Bldg. C
Alcoa Technical Center
Alcoa Center, PA 15069

Detroit Diesel Allision Division
General Motors Corporation
Materials Laboratories
Indianapolis, IN 46206

Lycoming Division
AVCO Corporation
Stratford, CT 06497
ATTN: Mr. Barry Goldblatt

Avco Space Systems Division
Lowell Industrial Park
Lowell, MA 01851

Battelle Memorial Institute
505 King Avenue
Columbus, OH 43201
ATTN: Mr. Stephan A. Rubin, Mgr.
Information Operations

D. P. Hill
Physical Metallurgy Section
Battelle, Columbus Lab.
Battelle Memorial Institute
505 King Avenue
Columbus, OH 43201

D. N. Williams
Physical Metallurgy Section
Battelle, Columbus Lab.
Battelle Memorial Institute
505 King Avenue
Columbus, OH 43201

The Boeing Company
Commercial Airplane
ORG. 6-8733, MS77-18
P. O. Box 3707
Seattle, WA 98124
ATTN: Cecil E. Parsons

The Boeing Company
Commercial Airplane
ORG. 6-8733, MS77-18
P.O. Box 3707
Seattle, WA 98124
ATTN: A. Lew Wingert

The Boeing Company
Commercial Airplane
ORG. 6-8733, MS7-18
P.O. Box 3707
Seattle, WA 98124
ATTN: Bill Quist

Boeing-Vertol Company
Boeing Center
P.O. Box 16858
Philadelphia, PA 19142
ATTN: Mr. J. M. Clark

Mr. W. Spurr
The Boeing Company
12842 72nd Avenue, NE
Kirkland, WA 98033

Bruch Wellman, Inc.
17876 St. Clair Avenue
Cleveland, OH 44110
ATTN: Mr. Bruce King

Dr. W. C. Setzer, Director
Metallurgy & Surface Technology
Consolidated Aluminum Corp.
P. O. Box 14448
St. Louis, MO 63178

The Dow Metal Products Company
Hopkins Building
Midland, MI 48640

Douglas Aircraft Company
3855 Lakewood Blvd.
Long Beach, CA 90808
ATTN: Mr. Fred Mehe, C1-250

General Dynamics
Fort Worth Division
MZ 5984
P O. Box 748
Fort Worth, TX 76101
ATTN: Mr. E. S. Balmuth

General Dynamics Corp.
Convair Aerospace Division
Fort Worth Operation
P. O. Box 748
Fort Worth, TX 76101
ATTN: Tom Coyle

General Dynamics Convair Div.
P. O. Box 80847
San Diego, CA 92138
ATTN: Mr. Jack Christian
Code 643-10

General Electric Co.
Corporate Research and Development
Bldg. 36-441
Schenectady, NY 12345
ATTN: Dr. J. H. Westbrook, Mgr.
Materials Information Service

General Electric Company
Corporate Research and Development
P. O. Box 8
Schenectady, NY 12301
ATTN: Dr. D. Wood

General Electric Company
Aircraft Engine Group
Material & Processes Technology Lab.
Evendale, OH 45215

General Electric
Missile & Space Division
Materials Science Section
P.O. Box 8555
Philadelphia, PA 91901
ATTN: Technical Library

Dr. Philip N. Adler
Research & Development Center
Grumman Aerospace Corp.
Bethpage, NY 11714

Dr. John M. Papazian
Research Department
Grumman Aerospace Corp.
Bethpage, NY 11714

IIT Research Institute
Metals Research Department
10 West 35th Street
Chicago, IL 60616
ATTN: Dr. N. Parikh

Kaiser Aluminum & Chemical Corp.
Aluminum Division Research Center
for Technology
P.O. Box 870
ATTN: T. R. Pritchett
Pleasanton, CA 94566

Kaman Aerospace Corporation
Old Windsor Road
Bloomfield, CT 06001
ATTN: Mr. M. L. White

Kawecki Berylco Industries
P.O. Box 1462
Reading, PA 19603

Linde Company
Division of Union Carbide
P.O. Box 44
Tonawanda, NY 14152

Lockheed Missile & Space Corp.
Box 504
Sunnyvale, Ca 94088
ATTN: Mr. C. D. McIntyre
Bldg. 182, Dept. 84-13

Lockheed Missile & Space Corp.
Box 504
Sunnyvale, CA 94088
ATTN: Mr. G. P. Pinkerton
Bldg. 154, Dept. 8122

Lockheed-Georgia Company
Marietta, GA 30061
ATTN: E. Bateh

Lockheed-California Company
P. O. Box 551
Burbank, CA 91503
ATTN: Mr. J. M. VanOrden
Dept. 74-71, Bldg. 221, Plt. 2

Lockheed Palo Alto Research Lab.
Materials Science Laboratory
3251 Hanover Street
Palo Alto, CA 94303
ATTN: Dr. Frank A. Crossley
52-31/204

R. E. Lewis
Lockheed Palo Alto Research Laboratory
Dept. 52-31
Bldg. 204
3251 Hanover Street
Palo Alto, CA 94304

Ian Palmer
Lockheed Palo Alto Research Laboratory
Dept. 52-31
Bldg. 204
3251 Hanover Street
Palo Alto, CA 94303

P. R. Mallory & Co., Inc.
3029 East Washington Street
Indianapolis, IN 46206
ATTN: Technical Librarian

Martin Marietta Corporation
P. O. Box 5837
Orlando, FL 32805
ATTN: Dr. Richard C. Hall
Mail Point 275

Martin Marietta Corporation
1450 South Rolling Road
Baltimore, MD 21227
ATTN: Dr. Joseph R. Pickens

Martin Marietta Aluminum
ATTN: Mr. Paul E. Anderson
(M/C 5401)
19200 South Western Avenue
Torrance, CA 90509

McDonnell Aircraft Company
St. Louis, MO 63166
ATTN: Mr. H. J. Siegel
Materials & Processes Dev.
General Engineering Division

Midwest Research Institute
425 Volker Boulevard
Kansas City, MO 64110

Northrop Corporation
Aircraft Division
Dept. 3771-62
3901 West Broadway
Hawthorne, CA 90250
ATTN: Mr. Allen Freedman

Dr. F. N. Mandigo
Olin Metals Research Laboratories
91 Shelton Avenue
New Haven, CT 06515

Pratt & Whitney Aircraft
Division of United Technologies
Florida Research and Development Center
P.O. Box 2691
West Palm Beach, FL 33402

Dr. Howard Bomberger
Reactive Metals, Inc.
Niles, OH 44446

Reynolds Metals Company
Metallurgical Research Division
4th and Canal Streets
Richmond, VA 23219
ATTN: Dr. J. H. Dedrick

Reynolds Metals Company
Metallurgical Research Division
4th and Canal Streets
Richmond, VA 23219
ATTN: Mr. G. Spangler

Reynolds Metals Company
Metallurgical Research Division
4th and Canal Streets
Richmond, VA 23219
ATTN: Dr. D. Thompson

Rockwell International
P.O. Box 1082
1027 Camino Dos Rios
Thousand Oaks, CA 91320
ATTN: Dr. J. Wert

Rockwell International
Los Angeles Division
International Airport
Los Angeles, CA 90009
ATTN: Gary Keller
Materials Applications

Autonetics Division of
Rockwell International
P.O. Box 4173
Anaheim, CA 92803
ATTN: Mr. A. G. Gross, Jr.
Dept. 522-92

Rockwell International
Rocketdyne Division
Canoga Park, CA 91305
ATTN: Dr. Al Jacobs
Group Scientist
Materials Branch

Rockwell International
Columbus Division
Columbus, OH 43216
ATTN: Mr. P. Maynard,
Dept. 75, Group 521

Solar
2200 Pacific Highway
San Diego, CA 92112
ATTN: Dr. A. Metcalfe

Southwest Research Institute
8500 Culebra Road
P. O. Box 28510
San Antonio, TX 78284

Teledyne CAE
1330 Laskey Road
Toledo, OH 43601

Dr. A. I. Mlavsky
Senior Vice President for Technology &
Director of Corporate Technology Center
Tyco Laboratories, Inc.
16 Hickory Drive
Waltham, MA 02145

United Technologies Research Lab.
East Hartford, CT 06108
ATTN: Mr. Roy Fanti

Vought Corp.
P. O. Box 5907
Dallas, TX 75222
ATTN: Mr. A. Hohman

Westinghouse Electric Company
Materials & Processing Laboratories
Beulah Road
Pittsburgh, PA 15235
ATTN: Don E. Harrison

Dr. D. J. Duquette
Materials Engineering Dept.
RPI
Troy, NY 12181

Dr. Charles Gilmore
Tompkins Hall
George Washington University
Washington, DC 20006

Dr. John A. Schey
Dept. of Materials Engineering
University of Illinois at
Chicago Circle
Box 4348
Chicago, IL 60680

Dr. E. A. Starke, Jr.
Dept. of Materials Science
University of Virginia
Charlottesville, VA 22901

Dr. John D. Wood
Associate Professor
Lehigh University
Bethlehem, PA 18015

END

FILMED

12-83

DTIC